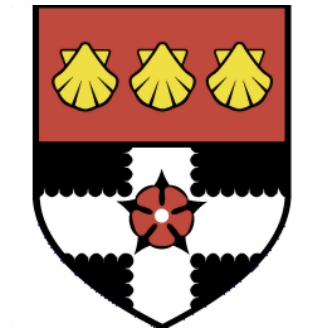# UNIVERSITY OF READING

Department of Meteorology

Multi-scale and upscale interaction of Mesoscale convective systems in the United Kingdom and France

Samantha Clarke

A thesis submitted for the degree of Doctor of Philosophy

December 2017

Declaration

I confirm that this is my own work and the use of all material from other sources has been properly and fully acknowledged.

Samantha Clarke

Abstract

Mesoscale convective systems (MCS) are difficult to forecast due to their inherent unpredictability and small scale. Here the impact of model resolution on MCS structure and downstream forecast evolution are determined.

Four case analyses of European MCSs using output from a 12-km grid-spacing model reveal a consistent potential vorticity (PV) structure with a positive PV anomaly in the mid troposphere (5 PVU) and negative PV anomalies above and to either side of it (-1 PVU). Convection-permitting models produce stronger MCS PV anomalies than convection-parametrizing models in a case study from July 2012. These differences persist after coarse graining to 100-km grid spacing and are largest in the upper troposphere.

The effect of poor representation of MCSs on forecasts is investigated by adding MCS perturbations, calculated as differences from coarse-grained convection-permitting (4.4-km grid spacing) model output, to convection-parametrizing (25-km grid spacing) deterministic and six-member ensemble (with operational initial condition perturbations) model forecasts. Upper-level MCS perturbations have more impact than those at middle levels, though using all levels yields the greatest impact. For the first 30 hours differences grow on the convective scale related to the MCS and a developing UK cyclone, despite perturbation damping. Subsequently, differences grow rapidly onto the synoptic-scale and by five days impact the entire northern hemisphere. The MCS perturbations systematically affect the ensemble forecasts though the differences are smaller than those generated by the initial condition perturbations. MCS perturbations slow the eastward movement of Rossby waves due to ridge amplification. A downstream cyclone deepens by up to 3 hPa after five days and forecast errors (compared to analysis) in mean-sea-level pressure are reduced in most members (by up to 2%).

Thus, perturbing convection-parametrizing models to include PV anomalies associated with MCSs produces alternative realisations to those generated by initial condition perturbations and so could be useful operationally.

Acknowledgements

Firstly, I would like to thank my supervisors Sue Gray and Nigel Roberts. I have had many struggles throughout the course of this research and it has taken a long time to get to this point but you both never gave up on me and offered continued support and guidance to me. I could not have asked for better supervisors and appreciate the time you gave up to help me along the process, particularly with improving my writing. Secondly, I would like to thank my monitoring committee - Peter Clark and Len Shaffrey for their useful discussions regarding my work and thanks to Peter for help with writing the coarse graining code. To Willie and Grenville I can't thank you enough for all the help you have provided me with the UM along the way.

This thesis means more to me than achieving a PhD, it is also about overcoming my own physical and mental health struggles that have come along the way and almost made me give up on the PhD completely on numerous occasions as it felt as if everything was against me achieving it. This thesis is a sign that you can be strong and overcome any set backs that come your way and is a reminder to anyone that doing a PhD is tough but it is doable and you can achieve it! There are too many people that I need to thank for their words of encouragement and support along this journey and I will always be grateful to you all. I particularly want to thank my past and present weight-lifting, running buddies and everyone from 1U07 and 2U06 throughout the years.

Special thanks to a couple of people: Steph - thanks for putting up with me for the past few years. Your belief in me never faded and your positive words of encouragement were most definitely needed on many occasions. Ruari - thanks for putting up with my gruelling weight-lifting and running workouts, for giving me words of encouragement, partaking in tea and coffee breaks with me and for your help with R.

My final thanks is to my family for providing me a place to escape to and for always being supportive of me. Nanna, you are my inspiration and the strongest person I know and you always believe in me; this is the reason I was able to finish this thesis.

Contents

Chapter 1

Introduction and Background

1.1   Introduction and aims

The following Chapter aims to provide a detailed literature review of Mesoscale Convective Systems (MCSs) and discusses the aims of this thesis. The emphasis is upon MCSs occurring (initiating) in western Europe (Spain, France and the UK). However, MCSs occurring elsewhere across the globe are discussed for background purposes.

Maddox (1980) was the first to define the weather system termed Mesoscale Convective Complex (MCC), based on physical characteristics clearly observable in infra-red satellite imagery. Maddox (1980) defined MCCs using a strict size criteria, further characterising them as an amalgamation or organisation of individual thunderstorms into a single cloud system. Maddox *et al.* (1982) states that there are many other mesoscale convective systems which exist that fail to meet the strict size criterion imposed for MCCs. The term Mesoscale Convective System (MCS) was adopted for these systems.

MCSs occur most frequent in Africa, Australia, China, South America and the United States, although they are known to occur over the whole globe except for the Antarctic (Liang and Fritsch, 2000). MCSs are relatively rare in the UK and Europe in comparison to places such as the Central USA and Africa (Liang and Fritsch, 2000). Gray and Marshall (1998) were able to produce a climatology of European MCSs and showed that on average two a year occur in the UK. The UK is also known to be affected by MCSs which are advected from France. Many studies have been conducted into the characteristics of MCSs occurring around the world. They found that, regardless of where they occur, MCSs demonstrate very similar characteristics, namely their size, duration and nocturnal formation on or in the vicinity of land (Miller and Fritsch, 1991; Liang and Fritsch, 1993b; Liang and Fritsch, 1993a; Augustine and Howard, 1991; Maddox, 1980; Velasco and Fritsch, 1987; Browning and Hill, 1984).

MCSs are often associated with extreme weather such as heavy and persistent rain,

large hail, strong winds and occasionally tornadoes (Houze, 2004). This persistent and heavy rain is sometimes slow moving and can often lead to flooding (Gray and Marshall, 1998; Houze, 2004). The extreme weather associated with MCSs makes it important to gain an accurate forecast of such systems.

MCSs may cover only a mesoscale area; however, the convection, and associated latent heating and cooling taking place mean that MCSs are an important link between atmospheric convection and the larger-scale atmospheric circulation (Houze, 2004). Thus, a poor forecast of an MCS is likely to impact on the downstream forecast (Gray, 2001), and could lead to a forecast bust (Rodwell *et al.*, 2013).

Numerical weather prediction (NWP) models have difficulties representing MCSs due to their high unpredictability (Wandishin *et al.*, 2008; Wandishin *et al.*, 2010). Additionally, the initial convection associated with MCSs is often poorly forecast by NWP models due to the representation of convection in the models. The initial convection is sub-grid scale (a single cloud or thunderstorm is around 100 m to a few kms in horizontal extent) and therefore is too small-scale to be explicitly represented by the model.

The unpredictability associated with the forecast of MCSs in NWP models and the importance of forecasting these systems due to their upscale influence on predictability, motivates the research in this thesis. MCSs occurring in the UK and France are the main focus of this thesis since MCSs occurring here have been less well studied (due to their rarity) and the inherent unpredictability of MCSs has led to poor forecasts occurring over this area in the past (Clark *et al.*, 2016). Rodwell *et al.* (2013) found that poor forecasts of MCSs over the USA caused forecast busts in Europe in the days ahead, showing the importance of accurate representation of MCSs, due to their influence on the downstream flow.

MCSs occurring in the UK and France have been studied less than in other areas, where MCSs occur more frequently. As a consequence the MCSs here are not as well understood. Previous studies of MCS cases in western Europe have shown that NWP models can accurately forecast the 'Spanish plume' synoptic environment typically associated with MCS development and the organisation of convective activity, but fail to forecast accurately the position and magnitude of rainfall associated with the MCS (McCallum and Waters, 1993; Young, 1995). Studies have also found that sometimes NWP models do not represent the MCS at all and this can lead to forecast busts downstream

(Rodwell *et al.*, 2013). It is thought that poor forecasts of MCSs over the UK may be related to the current high-resolution Met-Office NWP model not capturing the initial convection associated with an MCS, as they tend to develop over France where the domain of the model does not extend. The NWP models also cannot explicitly represent the initial convection associated with the resulting MCS due to their scale which also hinders the forecasting of these systems.

The aim of this study is to investigate the structure and predictability of MCSs occurring in the UK and France (particularly in terms of potential vorticity), to ultimately assist with improving the short and medium-range forecasting of MCSs in the future over the UK and France. With an improved understanding of MCSs occurring in this region an investigation into the downstream influence of such systems is conducted to determine if accurate representation of MCS events can have a beneficial impact on forecast predictability downstream from the MCS event (through increased ensemble spread). The questions to be addressed by this study, are as follows:

- What are the mesoscale and synoptic-scale structures of PV anomalies generated by MCSs (Chapter 3)?

- How is the forecasting of MCSs affected by the representation of convection in NWP models (whether convection is parametrized or permitted by the model) and what are the associated PV structures produced (Chapter 4)?

- How does the representation of an MCS affect forecast evolution and forecast skill (compared to analysis) for the synoptic-scale forecast downstream from the MCS (Chapter 5 and 6)?

In the remainder of this Chapter the characteristics of MCSs are presented in detail. MCSs are firstly discussed in relation to their occurrence, and the environmental conditions (local environment) associated with their formation. Secondly, the mesoscale features associated with MCSs are described. Lastly, the importance of accurate representation of MCSs is discussed along with a review of the issues surrounding the difficulty in representing these systems in NWP models and the potential downstream impact they have. A brief summary is presented at the end of the chapter. Chapter two describes the Met Office Unified Model which is used for numerical simulations throughout this thesis. Model experiments using different resolutions are described with particular em-

phasis on the use of convection parametrization and representation of convection at each resolution. In Chapter 3, two case studies of MCSs which occurred in the UK are analysed using observational and model data. One of these case studies provides the meteorological framework for numerical modelling experiments for the rest of the thesis. The main results of the thesis are presented in Chapters 4 and 5. Chapter 4 investigates the influence of model resolution on the development of an MCS case from Chapter 3 by simulating convection-permitting and convection-parametrizing forecasts of the MCS. Chapter 5 investigates the downstream impact of an MCS on the larger scale flow. Chapter 6 investigates the predictability of MCSs and the downstream influence they have by using an ensemble approach. Chapter 7 presents the conclusions of the thesis along with an overview of the contributions of this research to the field and plans for future work.

1.2   Characteristics of Mesoscale Convective Systems (MCSs)

1.2.1   Definition of MCSs and MCCs

Maddox (1980) defines an MCC to be a convective cloud system that satisfies the following criteria:

1. has an area of cloud or rainfall greater than 100000 km^2 (50000 km^2 for the inner cloud)

2. has cloud top temperatures $< -32^\circ$C ($< -52^\circ$C for the inner cloud)

3. has a duration of > 6 hours.

Their large area is a consequence of the fact that they are characterised by an amalgamation/ organisation of individual thunderstorms into one single cloud system. This system is typically associated with an area of precipitation 100 km in horizontal extent in at least one direction (the Maddox (1980) definition was updated by Houze (1993) to include this precipitation definition). Maddox *et al.* (1982) states that there still remains other mesoscale convective systems that fail to meet the strict size criteria imposed for MCCs. The term Mesoscale Convective System (MCS) was therefore adopted to describe convective systems of mesoscale size that occur, but may not meet Maddox (1980) strict size criteria. MCS can including squall-lines and bow echoes. This is particularly relevant to MCSs occurring in western Europe which tend to be on a smaller scale than

those that occur in the Central United States of America (USA) (for example). Browning and Hill (1984) states 'MCSs of a size corresponding to the MCCs of Maddox are rare in maritime regions, especially in mid-latitude areas such as the British Isles'. Morel and Senesi (2002b) found that the average size of a European MCS was 9000 km^2, with the largest being 30000 km^2. The smaller European MCSs is a result of less moisture and CAPE developing here in comparison to places such as the USA.

Many different definitions have been used to describe MCSs. Houze (2004) describes an MCS as 'a cumulonimbus cloud system that produces a contiguous precipitation area approximately 100 km or more in at least one direction'. Gray and Marshall (1998) broadened this description for the purpose of producing a climatology of United Kingdom (UK) MCSs and it was later adopted by Lewis and Gray (2010) to extend the climatology. Gray and Marshall (1998) defined an MCS to be a system satisfying the following criteria (which is the criteria adopted for MCSs identified in this thesis):

- wide spread lightning reports covering an area of greater than 100 km in at least one direction (to indicate thunderstorm activity),

- some reports of heavy and/or persistent rainfall (>10 mm) in the storm area,

- high surface temperatures (>$25°C$), to indicate high convective available potential energy may be produced,

- identification of a cold cloud anvil in an infra-red satellite image.

In the UK thunderstorms tend to be more localised, affecting areas of hundreds of kilometres rather than thousands (Gray and Marshall, 1998). In contrast, USA MCSs tend to have longer-lasting convection and tend to acquire larger dimensions (Browning and Hill, 1984). Liang and Fritsch (1997), in a global study of MCSs, found that most of the cloud shield areas were between 2×10^5 to 4×10^5 km^2, with a global average of 354000 km^2 and a duration of 10 hours. MCSs occurring in UK and France were found to have a median size of 50,000 km^2 (Gray and Marshall, 1998). 40% of MCSs in Europe were found to have a duration of 5-8 hours (Morel and Senesi, 2002b) (however, this statistic was calculated using only MCSs larger than 10000 km^2). MCSs which have larger cold cloud shields tend to persist for longer, yielding a positive correlation between size and duration of the MCSs. This correlation is particularly strong in the sum-

mer months at 0.57 (in comparison to 0.32 in autumn and spring months) (Liang and Fritsch, 1997).

Satellite imagery is often used to identify if an MCS exists (for example Maddox, 1980; Bartels and Maddox, 1991; McCallum and Waters, 1993; Morel and Senesi, 2002a; Morel and Senesi, 2002b; Browning and Hill, 1984). Since infra-red satellite imagery can be used to determine the temperature of cloud tops, it can easily be used to see if the area and temperature criteria are satisfied (Figure 1.1). The colder (displayed as whiter) the cloud on infra-red satellite images, the higher the cloud (and/or thicker the cloud) and hence the colder the temperature of the cloud tops (since temperature drops with altitude in the atmosphere). In MCSs the cloud top temperatures are so low because cloud tops often reach tropopause level. The duration can be determined by tracking backwards and forwards in time in satellite imagery to find if the very cold cloud covering a large area exists for 6 hours or more.

As well as satellite imagery, wide-spread lightning reports covering an area of greater than 100 km in at least one direction (an indicator of thunderstorm activity) and some reports of heavy, and/or persistent rainfall ($>$ 10 mm) covering an area greater than 100 km in at least one direction, and last for a period greater than that of a single cell convection ($>$3 hours), can be used to help determine MCS existence (Lewis and Gray, 2010; Gray and Marshall, 1998). Precipitation from radar is also useful for identifying persistent areas of heavy rain which may also indicate the presence of an MCS.

1.2.2   Cloud and precipitation structure of an MCS

The precipitation in an MCS is contiguous across a region at least 100 km in one dimension. Fritsch *et al.* (1986) found that MCSs account for 20–50% of the total rainfall over a region of the Central Plains in the USA, especially in June–August. The large amount of precipitation associated with MCSs is due to stratiform as well as convective precipitation, with stratiform rain accounting for 25–50% of the rainfall in MCSs (Houze, 1993). The associated convective and stratiform precipitation in an MCS is seen in radar echo analyses (Figure 1.2) (Houze, 1977; McAnelly and Cotton, 1989; Houze *et al.*, 1990). Lines of deep convective cells are found within large areas of stratiform precipitation (Houze *et al.*, 1990). Convective precipitation occurs when deep convection creates strong updraughts of several metres per second or greater. These strong updraughts condense
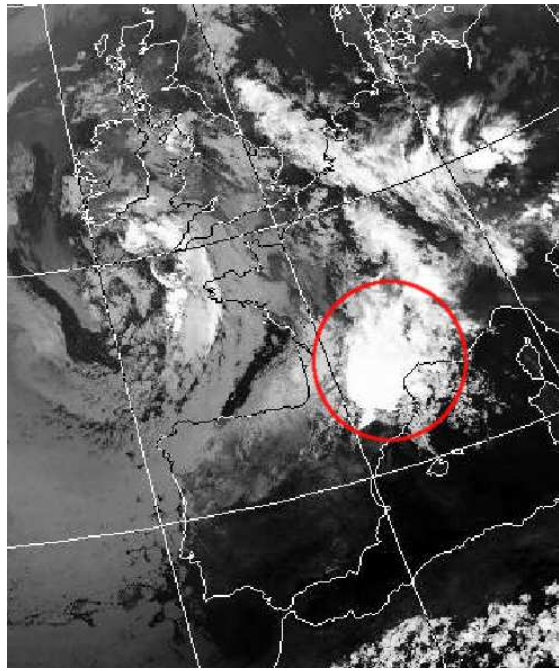
Figure 1.1: Infra-red satellite image from 0230 UTC 5 July 2012 (Case study used throughout the thesis). Circle indicates the location of the MCS. Courtesy of Dundee Satellite receiving station.
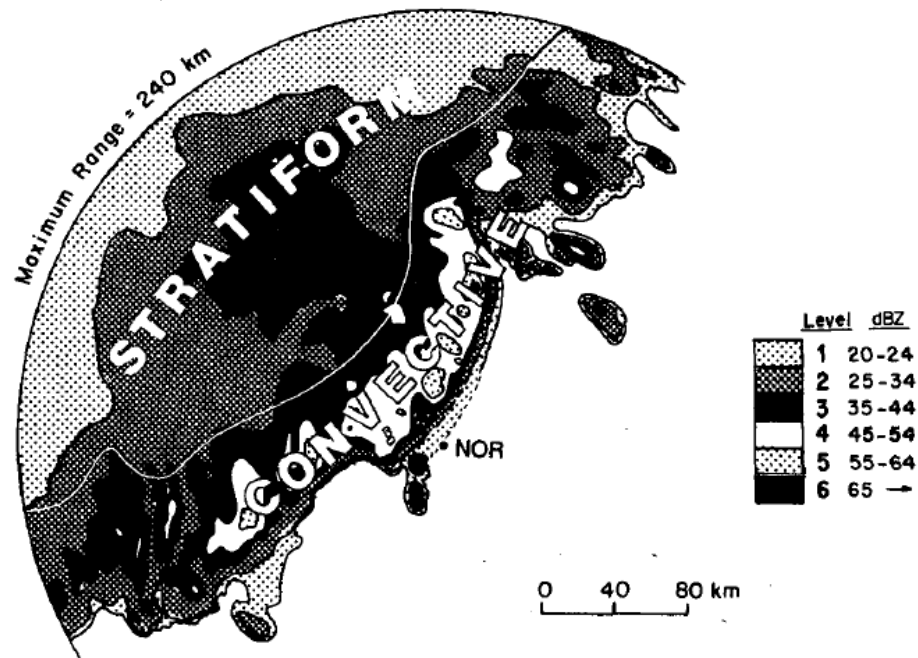
Figure 1.2: Example of a radar echo taken from Houze *et al.* (1990) (figure 5) on 17 May 1982 at 0240 UTC. The partition between stratiform and convective precipitation is shown. ©Copyright American Meteorological Society. Used with permission.

vapour rapidly, producing large concentrations of cloud liquid water (Houze, 1997). Since the bulk of convective precipitation mass falls out within a few kilometres of the updraught centres the radar reflectivity pattern shows concentrated peaks of reflectivity (Houze, 1997). Stratiform precipitation is the precipitation that occurs when convective cells weaken allowing the associated precipitation to develop a layered structure. Stratiform precipitation tends to create highest reflectivity in the regions where convective cores once were vigorous (Houze, 1997).

Although MCSs cover only a mesoscale area the convection and associated latent heating and cooling taking place can have a feedback on the large-scale flow. This is due to the atmosphere surrounding the precipitating convection adjusting to the generation of buoyancy created by latent heating when precipitation occurs. The adjustment is a result of gravity waves which displace mass outside the convective region downward (Mapes, 1993 ; Mapes and Houze, 1995). MCSs are therefore an important link between atmospheric convection and the larger-scale atmospheric circulation (Houze, 2004).

The vertical air motions in the stratiform region, although weaker than the cores, can cover a much larger area than that of the active convective cells (Houze, 1997) and the associated atmospheric adjustments can impact on a large area. The heating profile created by latent heat which is released in convection is affected by contributions from the convective and the stratiform regions of an MCS. The convective region creates deep, fast moving displacement whereas the stratiform region moves much more slowly (Mapes, 1993). Mapes and Houze (1995) found that the response to the large-scale atmosphere is dominated by two distinct modes. The first mode is a faster propagating mode corresponding to the convective-type heating profile. This is characterised by convergence in the lower half of the troposphere and divergence in the upper half of the troposphere. The second mode is a slower mode corresponding to the stratiform-type heating with convergence in middle levels and divergence at lower and upper levels.

The size of an MCS is effectively determined by the growth of the stratiform precipitation region (Houze, 2004) since the stratiform region covers a larger area than that of the convective cells in an MCS (Yuter and Houze, 1998). Houze (2004) describes how a more intense or larger-scale stratiform region may produce different feedbacks to the environment in comparison to a smaller region. A larger stratiform area produces an elevated and intensified vertical profile of heating over a wider area which may ultimately

impact the downstream forecast (Houze, 2004) (and can cause poor forecasts). This fact led Houze (2004) to state that the variability of the MCS population over the Earth is vital in determining global circulation patterns. The stratiform region is associated with a large region of cloud which does not extend deep into the vertical towards the surface whereas the convective region is typified by clouds reaching from the surface to tropopause level due to deep convection. The feedbacks created by the stratiform region are hard to simulate and observe due to the associated vertical air motions being too weak to measure using current methods which leads to underestimates of the effect of the stratiform region on the large-scale environmental flow (Houze, 2004).

1.2.3   Stages of MCS development and decay

Browning and Hill (1984) describes four stages of MCS development and decay, each lasting approximately 3 hours. These stages were developed when looking at the structure and evolution of MCSs in the British Isles and hence should relate to the MCS(s) investigated in this theses. These are:

1. Stage 1: Transition from a region of individual convective shower cells scattered within a convergence zone to a cluster of more vigorous cumulonimbus capped by small cirrus shields at an equilibrium level near the tropopause. Organisation of individual multicellular convection cells into an MCS in Europe usually occurs due to convergence of the outflow associated with the gust front created by downdraughts from the precipitation and updraughts from forced ascent by a weak upper-level trough. MCSs developing around the globe have been found to organise in areas where there is significant vertical wind shear and available CAPE.

2. Stage 2: Rapid enlargement of a combined cirrus shield, accompanying the continued generation of vigorous thunderstorm cells and the formation of an expanding area of moderately heavy, rather uniform, stratiform rain downwind of the convection. New cells of convection generate on the upshear side (due to the gust front).

3. Stage 3: Continued convective activity, but convection less vigorous and a gradual subsidence of the highest cloud; persistence of the large area of moderate-to-heavy stratiform rain, with some thunder. The stratiform rain accounts for at least 70% of

the total rain area, of order tens of thousands of square kilometres.

4. Stage 4: Further decline of the cloud tops and a rapid decrease in the overall area
   and intensity of the rain; new cumulonimbus still forming upwind of the MCS but
   no longer merging with or contributing to the MCS cloud shield. Dissipation of
   the MCS occurs once the MCS moves away from its source of instability or forced
   ascent is no longer able to lift parcels to their lifting condensation level.

The reader is directed to Houze (1993) for further detail.

1.2.4   Spatial and temporal distribution of MCS occurrence

Many studies have been performed that show the existence of MCSs across all parts of
the globe except for the Antarctic (Augustine and Howard, 1991; Velasco and Fritsch,
1987; Liang and Fritsch, 1993a; Liang and Fritsch, 1993b; Miller and Fritsch, 1991; Liang
and Fritsch, 1997). Liang and Fritsch (1997) found that on average 400 MCCs occurred
globally each year (see Figure 1.3). They also found that most MCCs occur over land
(approximately 92%, see Figure 1.4) and are also most intense here, with two thirds oc-
curring in the northern hemisphere (see Figure 1.4). Lightning associated with MCCs
and MCSs is known to occur mostly over land, with the most frequent occurrences in
the tropical and subtropical latitudes (Houze, 2004). Relative to the rest of the world, the
number of MCCs occurring over the whole of Europe is very low with an average of 6 a
year in comparison to South and Central America with an average of 96 each year (Liang
and Fritsch, 1997) (Figure 1.3).

MCCs occur most frequently in Africa, Australia, China, South America and the
United States (Liang and Fritsch (2000), Velasco and Fritsch (1987), Liang and Fritsch
(1997), Miller and Fritsch (1991), Liang and Fritsch (1993b), Liang and Fritsch (1993a),
Maddox (1980)). The small number of MCCs found to form in Europe in comparison to
the rest of the world may be a consequence of interference of the low-level flow by the
mountainous terrain or the fact that the air mass feeding these systems is not as moist as
the air flowing from the Gulf of Mexico, leading to less convective instability (for exam-
ple Liang and Fritsch (1997)). Figure 1.3 shows the frequency of MCCs occurring over
the Globe and shows the relative rarity of MCCs over Europe.

Many more systems occur which do not satisfy Maddox (1980) size criteria therefore

Region/Period of study	Geographic domain	Average No. per season (high–low annual range)	Reference
South, central America, May 1981–Apr. 1983	40°S–30°N, 120°–28°W	96 (47)	Velasco and Fritsch (1987)
Western Pacific region, 1983, 1985	50°S–50°N, 90°E–170°W	82 (14)	Miller (1990)
United States, 1986–87	25°–50°N, 130°–70°W	51 (14)	Augustine and Howard (1991)
Africa, 1986–87	40°S–35°N, 45°W–45°E	97 (7)	Laing (1992)
Indian subcontinent, Apr.–Dec. 1988	0–50°N, 45°–110°E	49	Laing (1992)
Europe, 1986–87	35°–55°N, 20°W–45°E	6 (1)	Added in current study
Total		381 (83)	

Figure 1.3: MCC populations (Table 2 from Liang and Fritsch (1997)).

Location	Fraction of global population (%)
Land	91.6
Ocean	8.4
Northern hemisphere	66.5
Southern hemisphere	33.5

Figure 1.4: MCC populations over land (Table 3 from Liang and Fritsch (1997)).

are termed MCSs. Morel and Senesi (2002b) studied MCSs occurring over Europe which had a cloud shield of at least 10000 km^2 and found that around 6 MCSs occur per year in France, with 2 in the UK. Schiesser *et al.* (1995) found that the convective instability was weaker in Europe and systems are not as well organised as those in Central plains of the USA. MCCs and MCSs observed in Europe are also less intense than MCCs and MCSs observed in other places and are smaller.

MCCs have been found to be sensitive to the large-scale flow patterns (Augustine and Howard, 1991; Fritsch *et al.*, 1986). For example, Velasco and Fritsch (1987) found that the number of MCCs in mid-latitude South America doubled during an El Nino year since an El Nino has an effect on the large-scale flow and that affects MCC occurrence. It is thought that the El Nino event can lead to the production of an upper-level anticyclonic circulation which would result in an intensification of the upper-level jet or even a shift in the location of the jet maximum. This would lead to a large-scale impact on the environment in mid-latitudes and cause an affect on the MCC production (Velasco and Fritsch, 1987). Anderson and Arritt (2001) found that the El-Nino caused more MCC events due to the infrequent cold air flow from the north which led to more MCCs developing.

MCSs are predominantly nocturnal across the globe (Liang and Fritsch, 1997). In general, over the globe, the initial thunderstorms develop in mid-to-late afternoon and by sunset they have organised into a mesoscale structure (Liang and Fritsch, 1997) (see Figure 1.6). Liang and Fritsch (1997) found over the Globe that MCSs tend to be mature in the early hours of the morning (greatest frequency 00–01 UTC over the globe, over the ocean maturity happens later with the greatest frequency at 03 UTC; Figure 1.6). Liang and Fritsch (1997) found noticeable exceptions in that southern hemisphere MCSs initiate and decay slightly later and oceanic MCSs decay much later in the morning than over land (Figure 1.6). These differences led the authors to conclude that the life cycle of these MCSs is not dependent on the diurnal radiation cycle.

Liang and Fritsch (1997); Maddox (1983) and Chen and Li (1995) found that a nocturnal low-level jet was present in most cases of MCSs which developed in mid-latitudes and provided a continuous supply of air with high equivalent potential temperature (discussed later) to the intense and long-lived convection. This low-level jet is a consequence of terrain related differential radiative processes and decoupling of daytime well-mixed boundary layers, due to solar radiation diminishing (for example, Bleaker and Andre, 1951; Bonner, 1968). This nocturnal jet is important as Liang and Fritsch (1997) found that most MCSs occur downwind of significant terrain features.

Most European MCSs were found to initiate corresponding to diurnal heating of the atmosphere with a marked peak in initiation at 11 Local solar time (LST; with 12 being when the sun is highest in the sky) which reaches a maximum at 14 LST and then decreases until 9 LST (Morel and Senesi, 2002b). Morel and Senesi (2002b) did find though that 20% of MCSs initiated between 2 LST and 9 LST, indicating that the diurnal destabilisation of the atmosphere is not always necessary to produce an MCS. In these cases they found that the MCSs were triggered by frontal systems, cold pools at mid-levels or outflows from other systems. Morel and Senesi (2002b) found that European MCSs tend to have a peak in initiation at 14 LST, however the average global population of MCSs generally tend to form in the evening (18 to 24 UTC) (Liang and Fritsch, 1997).

MCSs over the northern hemisphere tend to form in summer months from May to September (Liang and Fritsch, 1997). This is due to higher surface temperatures in the summer, allowing for a large build up of convective available potential energy (CAPE) required for MCS development. Additionally, the late afternoon triggering of MCSs

allows for larger amounts of CAPE to develop. Most of the European MCSs studied by Morel and Senesi (2002b) lasted on average for 5.5 hours with 38% lasting for 5–8 hours.

This study will focus on MCSs occurring in western Europe (France, Spain and the UK). The UK is the main focus since the aim is to improve understanding of MCSs that either occur in the UK or reach the UK thus have an impact here. Gray and Marshall (1998) identified 32 MCSs occurring over the UK in 17 years from 1981–1997, an average of only 2 MCSs each year, indicating their rarity here. Although MCSs are rare here, the flood risk and high wind threat that these MCSs pose mean that accurate forecasting is extremely important. Gray and Marshall (1998) found all of the 32 systems that occurred in the UK between 1981–97 happened between May and September, with the greatest frequency in August. Gray and Marshall (1998) found that most MCSs in the UK occur in the south of England with most occurring overnight (being mature at this time, triggering in late afternoon), similar to findings by Liang and Fritsch (1997) for the global occurrence of MCSs. Four of the 32 MCSs were defined as meeting the MCC size criteria; however these did not last for the 6 hours required to meet the duration criteria of Maddox (1980).

Gray and Marshall (1998) found that most of the MCSs that occurred in the UK advected in from France. This is due to the associated synoptic environment which generally forms the prerequisite to MCS formation in western Europe (southerly flow gives warmer conditions which helps develop the MCS). It is possible that the MCSs that affect the UK trigger later than the European MCSs studied by Morel and Senesi (2002b), where they found most MCSs in Europe trigger at 14 LST, as most of these MCSs triggered much further south than the UK where higher surface temperatures were present before diurnal heating. Therefore, it did not require as much surface heating during the day to enable triggering to occur. Thus, MCSs triggering in the UK require more surface heating before triggering of convection occurs hence they develop later on in the day.

1.2.5 Environment conducive for MCS formation

Moist convection can only occur in regions with either conditional or potential (convective) instability and can be triggered by solar heating or a lifting mechanism (Griffiths *et al.*, 2000). Therefore, moisture, instability and a lifting mechanism are required for

deep, moist convection to occur. For European MCSs the most common lifting mechanism is forced ascent by a weak upper-level trough or due to forced ascent due to orography. This section defines the stability measures and terms that are used to describe various aspects of the convective instability of the storm environment.

Definitions

Below is a list of definitions related to environmental stability:

- Wet-bulb potential temperature (θ_w): the temperature an air parcel would have if cooled adiabatically to saturation and then brought back to the surface along the moist adiabat to 1000 hPa.

- potential temperature (θ): the temperature an unsaturated parcel of air would have if lowered to the surface (1000 hPa).

- level of free convection (LFC): the level at which a parcel moves from being negatively buoyant to positively buoyant (i.e. the parcel will rise of its own accord although things such as mixing in of dry air or drag from rain may prevent ascent).

- level of neutral buoyancy (LNB): the level the parcel is able to rise to from the LFC until it becomes cooler than the environment and is no longer buoyant then.

- lifting condensation level (LCL):The level marking where the parcel becomes saturated and condensation occurs forming cloud.

- conditional instability: instability that is conditional on saturation occurring after a finite displacement of a parcel (Ambaum, 2010)

- Potential Instability: an unsaturated layer of air in which θ_w decreases with height.

- Convective Available Potential Energy (CAPE): energy released when a parcel moves between the LFC and LNB. It is the amount of energy a parcel has to rise.

- convection inhibition (CIN): energy required to lift a parcel from the starting level (LCL) to the LFC (lifting against negative buoyancy).

- convective cap/lid: a layer of high static stability (high $\frac{d\theta}{dz}$) (usually with drier air above) that causes an ascending parcel of saturated air to become negatively buoyant and stop rising.

Conditional instability: CAPE

Conditional instability is instability that is conditional on saturation occurring after a finite displacement of a parcel (Ambaum, 2010). The parcel is therefore stable until it becomes saturated after a lifting mechanism occurs to lift the parcel to its LCL. An indication of the stability of a parcel is given by considering the difference between the temperature of a parcel of air and its surrounding ambient environmental temperature (CAPE). Conditional instability can be indicated through convective available potential energy (CAPE) being allowed to build to large amounts before it can then be released to create deep convection. A finite displacement of the parcel is required to lift the parcel to its LCL to overcome CIN and allow the parcel to become positively buoyant. CAPE is given by the following (Emanuel, 1994):

$$CAPE = \int_{p_{LFC}}^{p_{LNB}} R(T_p - T_a)d(lnp), \tag{1.1}$$

where p_{LNB} is the pressure at the level of neutral buoyancy (where the parcel of air would stop rising); p_{LFC} is the level of neutral buoyancy; the level the air moves from being negatively buoyant to positively buoyant; T_p and T_a are the parcel and ambient temperatures; and p is the pressure. CAPE has the units Jkg^{-1}. CAPE is the energy that would be released if a parcel of air was lifted above its level of free convection (LFC) to the level of neutral buoyancy. CAPE is a necessary, but not sufficient, condition for the onset of convection (Ambaum, 2010) with high levels of CAPE not necessarily meaning that convection will occur, just that it can occur (a triggering mechanism is required to release this energy before the convection can occur). Before the parcel reaches the LFC, it needs to be lifted against a negative buoyancy. The energy required to lift the parcel from the starting level (so 1000hPa for this study) to the LFC is known as the convective inhibition (CIN) (Ambaum, 2010):

$$CIN = \int_{p_{START}}^{p_{LFC}} R(T_p - T_a)d(lnp), \tag{1.2}$$

where p_{START} is 1000 hPa. CIN has the same units as CAPE.

Potential Instability

Potential instability indicates an area where convection may occur if a suitable lifting mechanism takes place, such as passage of an air parcel over a mountain range or dynamical lifting due to positive vorticity advection. Lifting allows the unstable layer of air to rise, overcoming the convective cap (created when an unstable layer of air is unable to rise as it is prevent from doing so due to being overlaid by a layer of stable air) created by the stable air overlying the unstable air. Wet-bulb potential temperature (θ_w) can be used to determine if potential instability is occurring and it is the temperature a parcel of air which has been lifted to saturation and is brought down to 1000 hPa while maintaining saturation (i.e. following a moist adiabat).

A decrease in θ_w with height means that the parcel of air is moister and/or warmer at lower levels and is thus less dense than the air above and wants to rise: This is known as potential instability (also termed convective instability). The layer is potentially unstable because θ_w of the layer is higher than θ_w of another layer above it. This depends on the layer above being drier meaning that θ_w is lower thus θ_w decreases with height. If a lower layer of air has a higher θ_w but lower θ than the layer above it (cooler but moister layer of air than the layer above it) then if this layer of air is lifted it will cool slower along the moist adiabat (as upon saturation latent heat is released which mean the layer cools more slowly). The layer above it which is drier will cool along the dry adiabat which cools more quickly. This will result in the moist layer cooling more slowly and eventually being warmer than the layer that originate above it and thus it will be more buoyant and will be able to continue rising. Therefore the moist layer of air will no longer have potential instability as it has been lifted which has allowed it to overcome the drier, warmer capping layer of air.

1.3 Relationship to MCSs

Prior to the formation of MCSs large amounts of CAPE (over 1000 Jkg^{-1}) can build up and the air can be potentially unstable, with a higher wet-bulb potential temperature (θ_w)

at lower levels than the levels above, and is prevented from rising by a 'convective cap'. This cap is often created when warm, moist air is overlaid by drier, warm air (with higher θ). In western European MCSs, this is often described as a 'tongue of warm, dry air', with a minimum in θ_w at around the 900–800 hPa level (can be higher) (Browning and Hill, 1984) which prevents a layer of moist air (with a maxima in θ_w, which is also increased by solar heating of the the ground) underneath it from rising. In this case CAPE may only be released upon lifting occurring. This causes many MCSs to initiate in the afternoon after sufficient diurnal heating has occurred to remove or weaken the 'convective cap' and initiate the convection. This situation allows for convection to occur to tropopause level (if the troposphere is unstable to this height) which manifests as MCSs showing up as very white cloud on satellite imagery, due to cold cloud temperatures at this level.

Tephigrams are a useful tool for finding the lifting condensation level (LCL) of a parcel of air. This is useful as it is at this level where the cloud base will form. Once this level has been determined on a tephigram it is then also possible to determine whether CAPE (convective available potential energy) or CIN (convective inhibition) are present (see Figure 1.7 which shows in this case 792 Jkg^{-1} of CAPE was available). CAPE is a measure of how much energy a parcel of air has to rise whereas CIN is a measure of the energy required to lift the parcel to its level of free convection. If there are large amounts of CAPE present it often suggests that there is instability present, however, there may be CIN present as well preventing the instability from being realised. CAPE is therefore a necessary but not sufficient condition for convection.

Tephigrams can also be used to find the layers of dry and moist air associated with the MCS formation. Figure 1.7 shows all the usual conditions that occur in the environment prior to deep convection. There is a large amount of CAPE (792 Jkg^{-1}), a layer of dry, warm air at 900hPa with a moist, cooler layer below it (which is still warm with a temperature of 25°C, typical of MCS development). There is also CIN available which is preventing the moist layer from rising. Air is unable to break through the lid to start with at night and may break through the lid upon surface heating which makes the near-surface layer much warmer and will either weaken or remove the CIN allowing the air to rise.
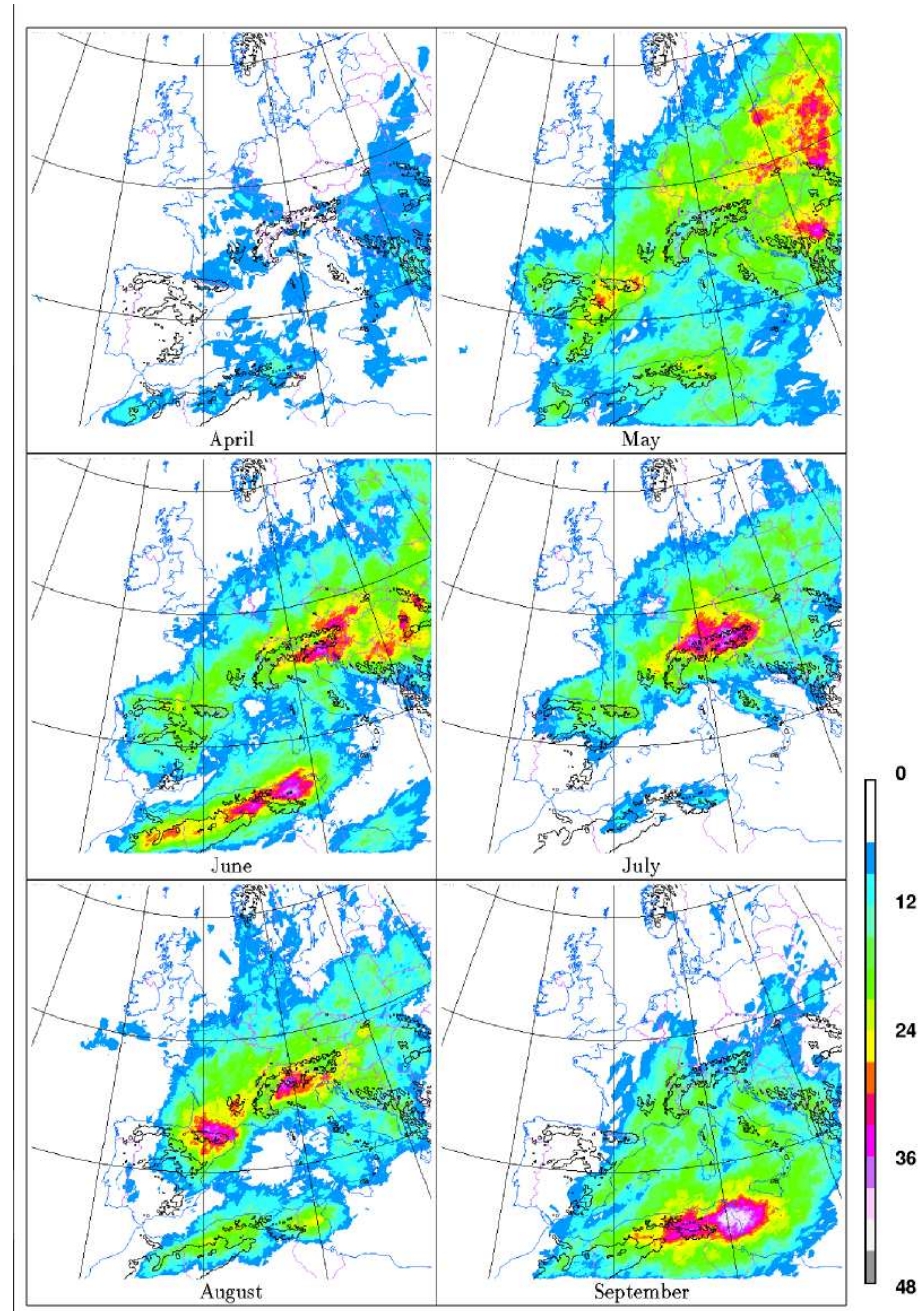
Figure 1.5: Monthly density maps of MCS occurrance (in number of MCSs occurring per pixel) taken from Morel and Senesi (2002b).
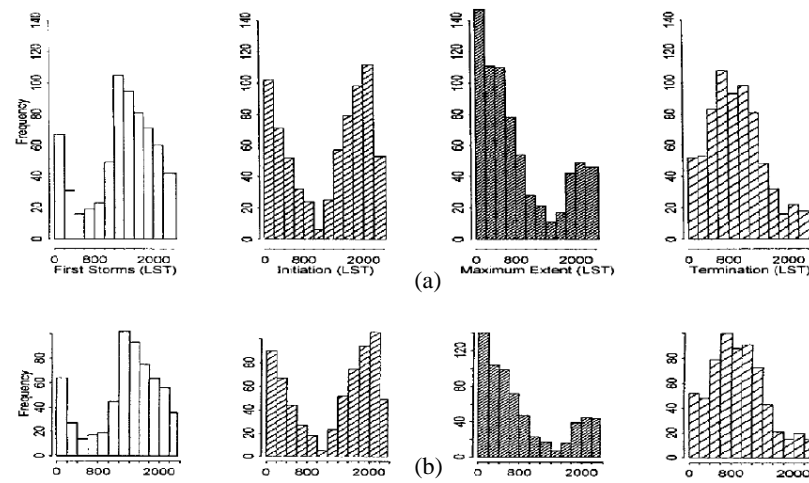
Figure 1.6: Life-cycle of MCCs for (a) the global population and (b) land population. From first storms, initiation, maximum extent, and termination stages. Local time is used (LST) to show the diurnal cycle of systems observed globally (Figure 5 from Liang and Fritsch (1997)).
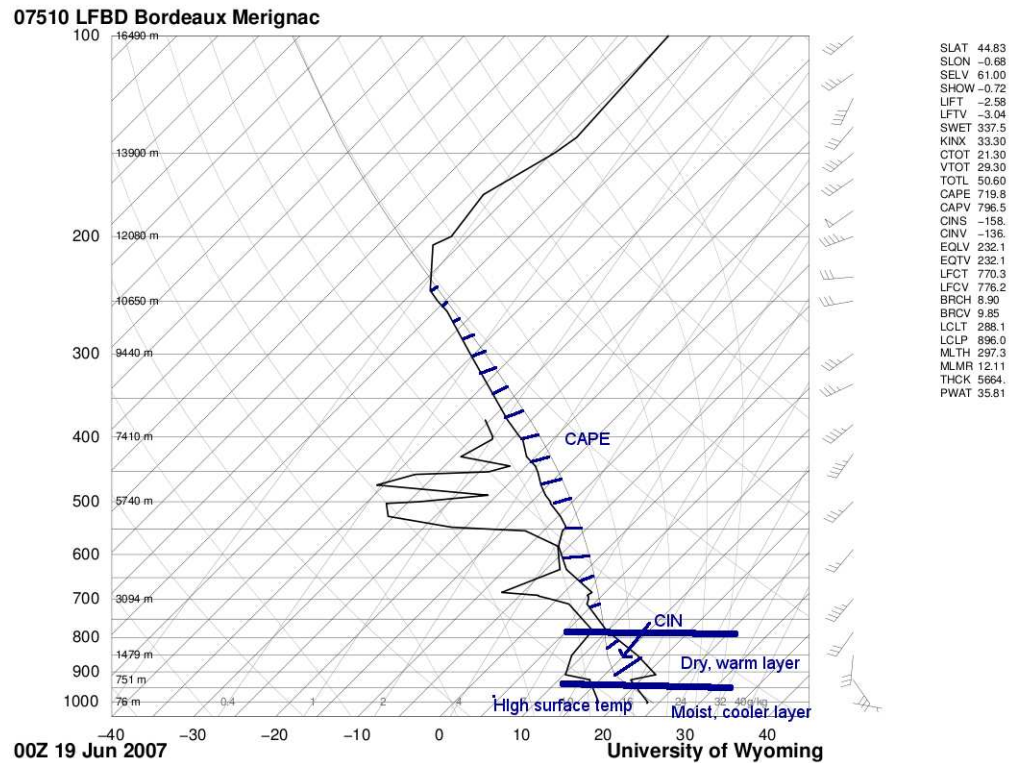
Figure 1.7: Tephigram for an MCS 19 June 2007 (same tephigram as used in Lewis and Gray (2010)). Layer of moist, warm air and layer of dry, warmer air is marked on the tephigram. The areas of CAPE and CIN are also marked.

1.3.1   Generic synoptic environments associated with MCSs initiation

Many studies have noted that MCS development and evolution is sensitive to the pre-convective environment in which the MCS forms (e.g Rotunno *et al.* (1988), Cohen *et al.* (2007)). Liang and Fritsch (1997) state that there must be thermodynamic and/or dynamic conditions that are conducive to organisation of deep convection into MCS mode (vertical wind shear and CAPE). MCSs have a clear tendency to occur in certain regions of the world (Liang and Fritsch, 1997) . Typically, MCSs occur in the lee of elevated terrain (Figure 1.8). MCSs form due to a combination between instability (which may be enhanced in the lee of high terrain) and the effects of strong vertical shear.

Many studies have been conducted into the environments associated with MCSs in the United States and have shown that characteristic mesoscale and synoptic-scale dynamical features are generally present (Liang and Fritsch, 2000). Maddox (1983), Kane *et al.* (1987), Cotton *et al.* (1989), Augustine and Howard (1991) and Smull and Augustine (1993) all found that a weak short-wave upper-level trough, quasi-stationary east-west frontal zone and a pronounced low-level jet coupled with strong lower-tropospheric warm advection are typically present in the area where MCSs form. Maddox (1983) also noted that a moist potentially unstable environment is required. These conditions provide sufficient vertical wind shear to produce deep convection because the shear allows constructive organisation of updraughts and downdraughts.

The large-scale environments associated with MCSs occurring in Africa, Australia, China, South America and the United states (the five places where MCCs occur most commonly) were found to be very similar (Liang and Fritsch, 2000). A local maximum in absolute humidity and a local minimum in static stability mark the favoured region for formation of the MCSs (Liang and Fritsch (2000)).

1.3.2   Synoptic environments associated with initiation of MCSs that affect the UK - the Spanish plume

Due to the relative rarity of MCSs occurring in western Europe, the environment associated with their occurrence here has been less well studied. Although studies have shown that MCSs occurring in USA, Africa, Australia, China and South America all had similar synoptic environments present at the time of initiation of the MCSs, the precise details
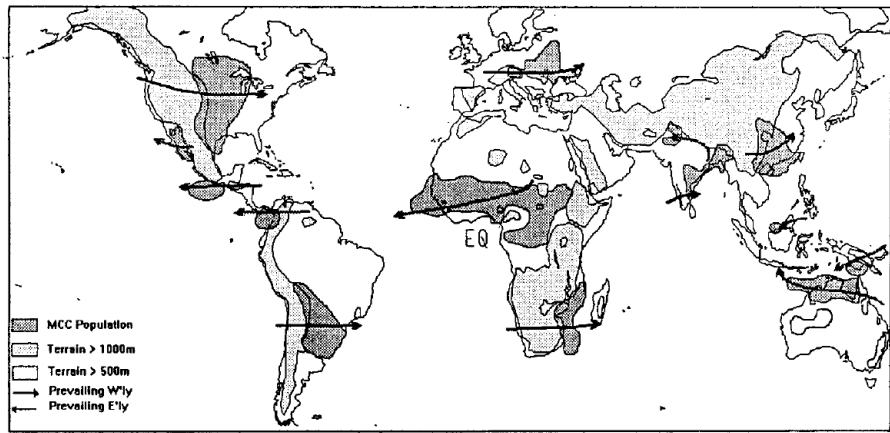
Figure 1.8: Relationship amongst MCC population centres, elevated terrain and prevailing mid-level flow (taken from Liang and Fritsch (1997))

depend on the country or continent concerned. Since the UK is a maritime country the dominant processes leading to convective initiation may be different in comparison to elsewhere (Bennett *et al.*, 2006).

MCCs are rare in Europe so Morel and Senesi (2002b) used criteria for MCSs to build a database of MCS systems occurring in Europe. Figure 1.9(a) and (b), taken from Morel and Senesi (2002b), provides a density map of MCS triggering in Europe, where triggering is indicated by the system reaching a cloud top temperature of $< -45°C$ and covering an area of 10000 km^2. Morel and Senesi (2002b) showed that most MCSs triggered due to orography (this can be seen in Figure 1.9(a) where most MCSs triggered where the elevation exceeded 1000 m) and a maxima in density occurs around mountain ranges in Europe. They also show a limited number of MCSs triggered over the UK and suggest it is due to a lack of strong diurnal heating in the summer months here. There is also limited elevated dry air from high ground in this region too because there is only the sea/ocean upstream (the exception being the Spanish plume situation).

The Spanish plume synoptic situation occurs more sporadically than the synoptic conditions occurring elsewhere over the globe that allow favourable conditions for MCS development. Portugal and western and southern Spain also show limited triggering of MCSs which is hypothesized to be because of low humidity (these areas are very dry in summer) and a lack of mountain ranges (Morel and Senesi, 2002b). Most of the European systems move in a east-north-east direction (Morel and Senesi, 2002b). Figure 1.5 shows that most MCSs trigger over France in August due to a northward shift in MCS activity at this time (due to the higher temperatures in France in August). This suggests that MCSs

are more likely to affect the UK at this time if they advect towards the UK from France. MCSs over the UK are likely to be influenced by land sea roughness contrasts, local orography and the interaction between maritime and continental air masses (Bennett *et al.*, 2006).

In the UK and France a synoptic situation known as a Spanish plume (Morris, 1986; Carlson and Ludlam, 1968) is in most cases found to be the prerequisite to MCS formation; this has been documented by Carlson and Ludlam (1968), Gray and Marshall (1998), Morris (1986) and Bennett *et al.* (2006). However, Lewis and Gray (2010) also identified cases that were not linked to a Spanish plume environment. Gray and Marshall (1998) found that 25 of their 32 MCSs studied occurred in Spanish plume conditions.

A Spanish Plume is the description for the advection of a potentially unstable plume of warm air from Spain towards the UK (Figure 1.11). For a Spanish Plume to occur there are two main precursors that tend to occur. Firstly, an upper-level trough causes a southwesterly upper-level flow over Iberia and Biscay. Secondly, warm temperatures at low-levels over Iberia. These two conditions are favourable for the development of potential (convective) instability.

In the classical Spanish plume case documented by Carlson and Ludlam (1968) the Spanish plume is indicated as a plume of dry, warm air in the middle troposphere (due to the height of the Iberian Peninsula reaching up to 3500 m) which tends to be stable (high θ, lower θ_w than the air below) creating a so called "lid" to a layer of air which is moist (high θ_w) in the lower troposphere. This layer of air at low-levels with high θ_w usually travels from the south east in the classic case (from the Mediterranean) and upon reaching France the plume of potentially very warm air from Spain found aloft over southwest France acts as a "lid" to confine small-scale convection to a layer which is 1 to 2 km deep (Carlson and Ludlam, 1968). This allows for a rise in θ_w values in this lowest layer during a sunny summer day and may allow for θ_w values to become abnormally large which may allow for the formation of intense deep convection if a triggering mechanism occurs. The warm humid air below the lid is unstable, but it is unable to rise due to the stable layer preventing it from doing so. This creates a large temperature gradient which allows large levels of CAPE to develop as the air moves northwards towards France and the UK. The development of intense deep convection is favoured not only by high θ_w near the surface but on the forward side of large-scale

(a)

(b)
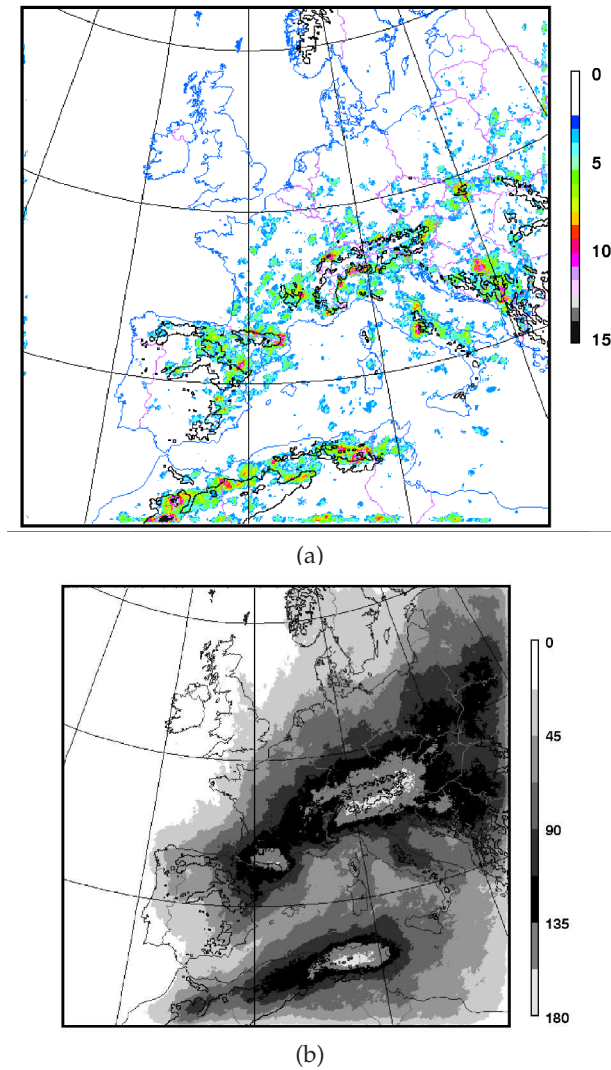
Figure 1.9: Figures 2 and 4 of Morel and Senesi (2002b) for (a) Density map of MCS triggering for the trajectories (in number of MCSs over each pixel), contours of 1000m elevation are marked and (b) Density map of MCS occurrence for the whole database (in number of MCS occurrences over each pixel).

troughs and by wind shear being present allowing for the generation of new cells of convection (Carlson and Ludlam, 1968).

Spanish plumes provide all the same ingredients as are needed for MCSs occurring elsewhere over the globe; however, the upper-level trough seems to be more important for western European MCS formation than elsewhere with its strength and dynamics playing a more key role (Lewis and Gray, 2010). An important feature of the Spanish plume is that the elevated warm dry layer 'capping' the moist, cooler layer can be created through advecting air north over France since northern Spain is elevated. Spanish Plumes can occur at any time of the year, however it is only in the summer months, when

there are higher temperatures and more moisture, that thunderstorms tend to develop which can lead to MCSs.

A triggering mechanism is required for the CAPE to be released through the weakening of CIN which leads to weakening or removal of the cap/lid. Triggering can occur through positive vorticity advection (PVA) which causes large-scale lifting created by the upper-level trough (Gray and Marshall, 1998) and can be explained by the Omega equation:

$$\sigma \left(\bigtriangledown^2 + \frac{{f_0}^2}{\sigma} \frac{\partial^2}{\partial p^2} \right) w = f_0 \frac{\partial}{\partial p} \left[\vec{V_g} \cdot \bigtriangledown \left(\zeta_g + f \right) \right] + \bigtriangledown^2 [\vec{V_g} \cdot \bigtriangledown \left(-\frac{\partial \phi}{\partial p} \right)], \qquad (1.3)$$

where σ is the static stability, $\bigtriangledown^2$ is the laplacian, p is the pressure, w is the vertical velocity, f_0 and f are the Coriolis force, $\vec{V_g}$ is the geostrophic wind, ζ_g is the geostrophic relative vorticity and ϕ is the isobaric coordinate (Martin, 2006). The left hand side of Equation 1.3 is essentially a 3D Laplacian term and a local maximum (minimum) in $\bigtriangledown^2 w$ implies a local minimum (maximum) in w itself. Thus, whenever the right hand side of Equation 1.3 is positive (negative), then $\bigtriangledown^2 w$ is positive (negative) implying that w is negative (positive), corresponding to upward (downward) vertical motion Martin (2006). In addition to this, the first term on the right hand side represents the vertical derivative of geostrophic vorticity advection. Therefore, if the environment is characterised by geostrophic cyclonic vorticity advection increasing (decreasing) with height, then this term is positive (negative) which implies that the environment is characterised by upward (downward) vertical motion. Thus, when there is a low-pressure at the surface geostrophic vorticity advection occurs above the surface low and is large and positive so that the column of air experiences upward-increasing cyclonic vorticity advection and thus upwards vertical motions. See Figure 6.7 from Martin (2006) for an explanation of the areas associated with the high and low pressure systems which are associated with positive and negative vorticity.

Triggering can also be created along the edge of a cold front or by ascent over hills. The steep gradient created by the cold front creates favourable conditions for the warm moist air to rise as the cold air from the cold front pushes into the unstable air mass, allowing CAPE to be realised and creating clouds along the gradient between the cold front and this warmer air mass. Many MCSs occur ahead of the cold front though. Once

this CAPE is released it allows all the energy and moisture to develop into a thunderstorms. Strong vertical wind shear (due to the synoptic pattern) allows these individual thunderstorms to organise into an eventual MCS. Lewis and Gray (2010) identified that there are three types of Spanish plume which occur. These three types are now discussed.

1.3.2.1   Types of Spanish plume

Lewis and Gray (2010) identified three types of Spanish plume synoptic situations in which MCSs they studied formed: classical Spanish plume (Figure 1.11), modified Spanish plume and European easterly plume (Figure 1.12). However, they also found cases which did not fit any of these three types. Each of these types of Spanish plumes is different; however, all three have the ingredients required for MCS formation (Morris, 1986).

Each of the three Spanish plumes identified has a different synoptic configuration, leading to differences in the evolution of the plume and triggering of the MCS (Lewis and Gray, 2010). Figure 1.10 provides a summary of the three synoptic environments associated with UK MCSs. All three configurations of the Spanish plume had organisation of convection due to the interaction of an upper-level disturbance with a low-level region of warm advection.

A classical Spanish plume (Figure 1.11) is associated with an upper-level trough which is north-south tilted to the west of the UK and Ireland and an open wave frontal system with a broad warm sector extending over western Europe.

A modified Spanish plume is associated with a cut-off upper-level feature to the north west of the Bay of Biscay (Figure 1.12). This upper-level feature often leads to a greater advection of warm air (through a mature frontal system) to the north than in the classical or European plume. This creates MCSs that tend to affect western and northern regions of the UK more than for the classical Spanish plume (Figure 1.11), which typically reaches the UK on the south or east coast (Lewis and Gray, 2010).

The European easterly plume is characterised by a weak upper-level disturbance over north west Europe and a high amplitude omega block (a high pressure system blocked between two low pressure systems) over Central Europe (Figure 1.12); Lewis and Gray (2010) state that the European easterly plume environment most closely resembles that of the formation of MCCs in the United States in Maddox (1983). The European

easterly plumes are associated with weak ascent forced by positive vortcity advection due to a weak upper-level trough feature (weak as in it is slow moving so there is less forced ascent ahead at the upper-levels), with the primary reason of the development of the MCS being strong low-level warm advection.

The mean sea level pressure and geopotential height structure for the modified Spanish plume and European easterly plume can be seen in Figure 1.13 which shows the low-pressure system to the west of the UK which influences the modified Spanish plume (tilted to the north west whereas the classical plume is more north-south orientated) and the equatorward stretching of the geopotential height contours in the European easterly plume.

Feature	Classical Spanish plume	Modified Spanish plume	European Easterly Plume
Baroclinic wave life cycle	LC1	LC2	No baroclinic cyclone
Upper-level flow pattern	N–S orientated trough approaching from E Atlantic	Stretched NW–SE tilted trough (possible cut-off)	High amplitude omega block over Scandinavia
Low-level flow pattern	Cyclone centred south of Iceland (left jet entrance) with trough extension over Ireland/UK	Cyclone centred over Bay of Biscay (occluded fronts, left jet exit)	Strong Scandinavian anticyclone
Low-level plume origin	Iberia	Iberia	Northern continental Europe
Mean MCS propagation	NE across SE England	N across W and N England	NW across S England

Figure 1.10: Synthesis of the three Spanish plume environments associated with UK MCSs (taken fromLewis and Gray (2010)).
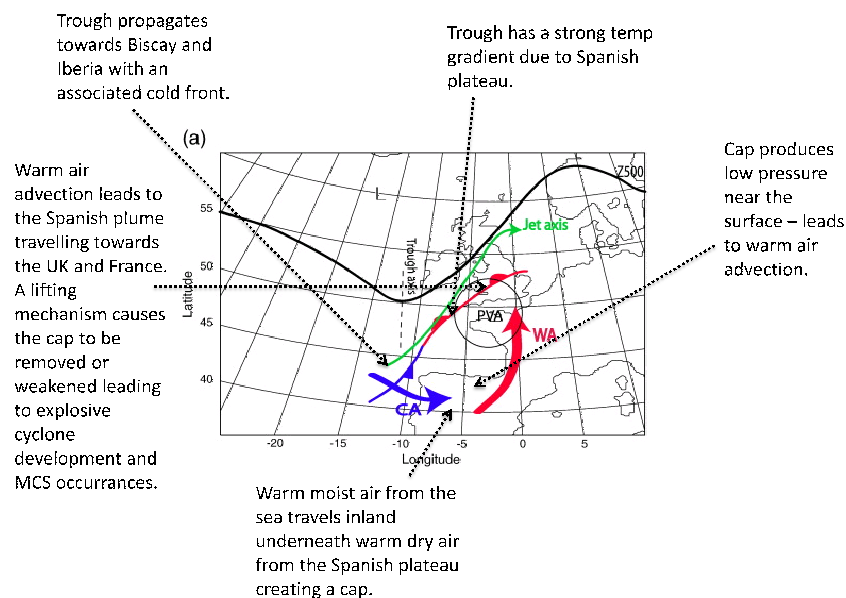
Figure 1.11: Schematic of a Classical Spanish plume (Adapted from Lewis and Gray (2010))
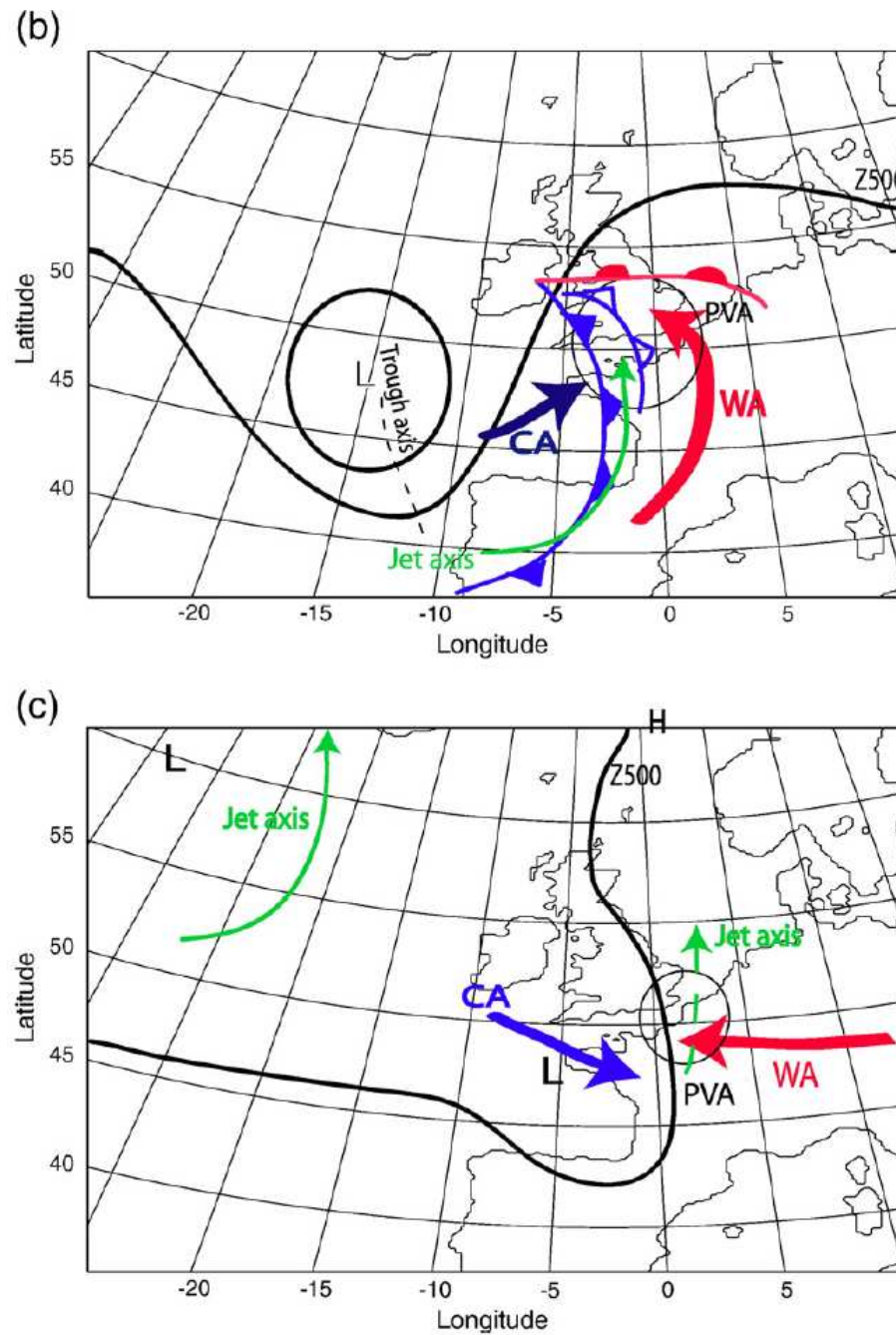
Figure 1.12: Schematics of Modified Spanish plume and European easterly plume taken from Lewis and Gray (2010).)
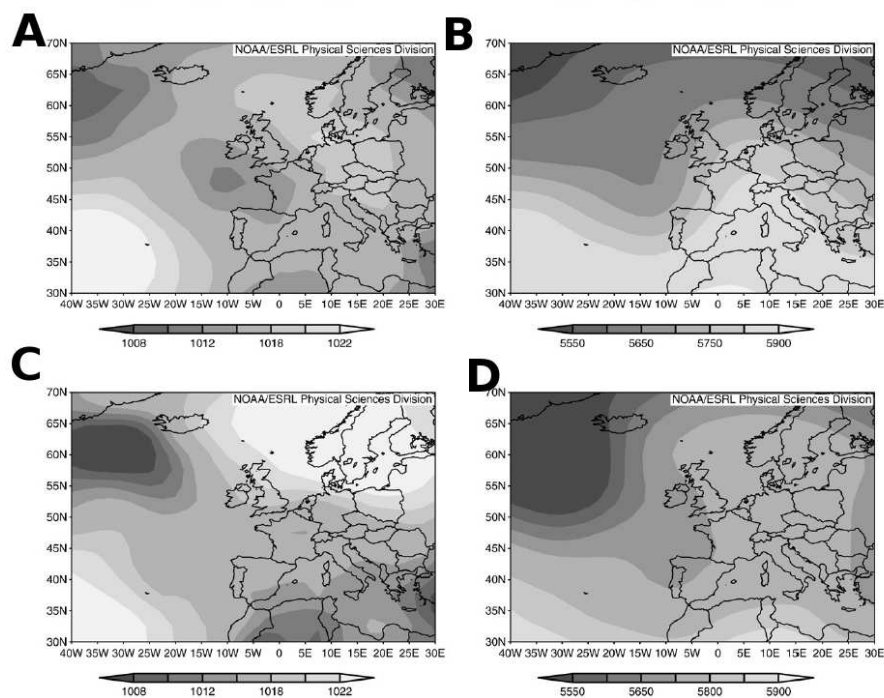
Figure 1.13: Composites of mean sea level pressure (hPa, left column) and 500hPa geopotential height (gpm, right column) for (a),(b) modified Spanish Plume and (c),(d) european easterly plume (taken from Lewis and Gray (2010)).

1.3.3   Potential vorticity structure of MCSs

1.3.3.1   Potential vorticity (PV) definition

Potential vorticity (PV) is a useful diagnostic for characterising midlatitude weather systems such as MCSs because it is conserved in adiabatic frictionless motion (PV can be used to track features and also redistributes in association with diabatic heating). Ertel (1942) defined PV as

$$PV = \frac{1}{\rho}\underline{\zeta} \cdot \nabla\theta. \tag{1.4}$$

where ρ is the density, $\underline{\zeta}$ is the absolute vorticity and θ is the potential temperature. Equation (1.4) shows that PV is essentially a relationship between the static stability (since $\nabla\theta$ is dominated by the vertical gradient in θ) and the absolute vorticity of an air parcel. PV is zero on the equator in the climatological average, as $\underline{\zeta}$ in Equation (1.4) is dominated by the vertical component of planetary vorticity, $f = 2\omega\sin\phi$, known as the Coriolis parameter, where ω is the angular speed and ϕ is the latitude. A strong vertical gradient in PV occurs at the tropopause as static stability is much stronger in the stratosphere. $\nabla\theta$ is thus much larger in the stratosphere. PV is also useful as it can be inverted upon a suitable balance assumption and boundary conditions to determine the associated balanced winds and temperature variables (Beare *et al.*, 2003; Hoskins *et al.*, 1985).

1.3.3.2   Vertical PV structure in MCSs

Changes in PV occur through frictional generation or diabatic heating (latent heat release). Latent heat release in an MCS changes the thermodynamic structure of the atmosphere locally. Convection causes air to rise, and upon reaching the level of free convection, condensation occurs and clouds are formed. When this process happens latent heat is released. This causes the cloud that is formed to become warmer than the surrounding environment producing a warm anomaly. This warm anomaly is associated with a tightening in θ isentropes (Figure 1.14). A higher θ means a bigger vertical gradient in θ just below where the latent heating occurs and a slacker gradient just above it thus since the equation of PV includes $\nabla\theta$ PV is changed. If cloudy air continues to be warmer than its environment it will continue to rise causing heating in a column. It is important to note that the friction or diabatic heating redistributes PV - it does not create or destroy it

(Thorpe and Emanuel, 1985). This produces PV anomalies (Figure 1.14).

The changes to PV can be related to Equation (1.4). Positive PV anomalies are created when either or both of the static stability or the vorticity is increased. Alternatively, negative anomalies are formed when either or both of the static stability or vorticity are decreased. Since usually the MCS is long-lived, with continued convection, any positive PV anomalies that form are eventually stretched to extend into a 'pv tower'. As diabatic heating takes place, isentropes (of θ) are squeezed closer together increasing the static stability (see positive PV region in Figure 1.14). This has associated cyclonic circulation leading to increased vorticity. These together produce an increase in PV through ascent stretching vortex lines and moving PV up into a tower. Conversely, the air above the diabatic heating is cooler and isentropes (of θ) are stretched further apart leading to decreased static stability (see Figure 1.14). Low PV above the latent heating is stretched out at tropopause level. This has associated anti-cyclonic circulation and decreased vorticity. These together produce a decrease in PV. These changes to the PV structure can also be thought of in terms of the redistribution of mass. Cumulus convection predominantly acts to transport mass across isentropic surfaces; evacuation of mass from a layer will decrease the mass and increase the PV (Raymond and Jiang, 1990). This mass is then deposited above creating a decrease in PV.

1.3.3.3 Evidence for the existence of Mesoscale Convective Vortices (MCVs)

Positive PV in mid-levels is associated with diabatic heating from convection and negative (or near-zero) PV in upper-levels from divergence is the typical PV structure known to occur in MCSs (Bosart and Sanders, 1981, Fritsch and Maddox, 1981, Menard and Fritsch, 1989, Smull and Houze, 1985, Raymond and Jiang, 1990) and can be seen in Figure 1.15. Figure 1.16 (Fig 1. of Pomroy and Thorpe (2000)) shows this pattern of PV generated by a steady heating source (one which continues for time periods similar to the vertical advection), such is the case for MCSs. Figure 1.15 shows a schematic of the vertical PV structure of an MCS in the USA. It shows that in upper-levels, in the MCS, there is an associated near zero PV and anticyclonic circulation, a warm core PV maximum in middle layers with associated cyclonic rotation and a cold pool at the surface. This cold pool is formed by cold air generated by downdraughts (due to precipitation, evaporative cooling and melting associated with the MCS) in individual convective cells in an

MCS spreading out at the surface and combining to form a large mesoscale cold pool below the MCS (Houze, 2004). Due to the cyclonic nature of the positive PV anomaly in mid-levels, air tends to rise to the east ahead of the motion of the system and sinks to the west of the system.
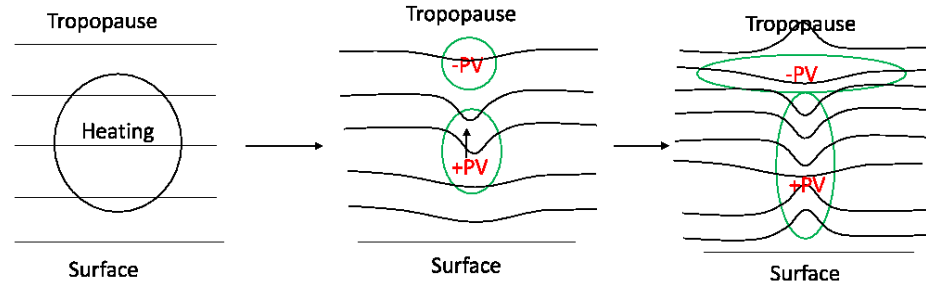
Figure 1.14: Schematic of the PV structure created by an MCS; from initiation to maturity. Lines of θ are given showing that a region of positive PV is associated with a large gradient in θ ang negative PV is associated with a slack gradient in θ.
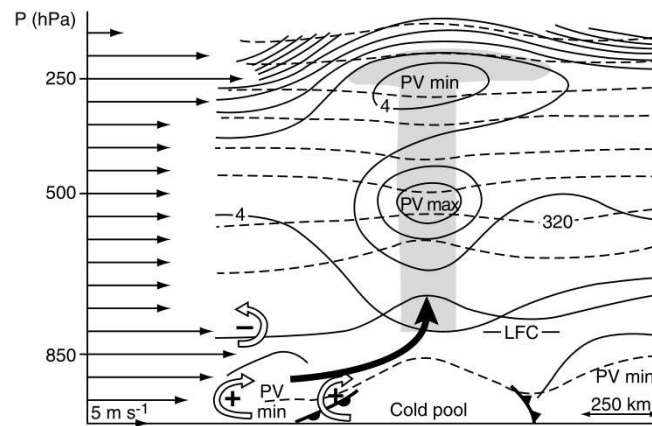
Figure 1.15: Schematic of the PV structure of an MCS at its most intense, in the USA (taken from Houze (2004), but was originally in Fritsch *et al.* (1994)). Dashed lines are potential temperature (5K intervals) and solid lines are PV. ©Copyright American Meteorological Society. Used with permission.

Menard and Fritsch (1989) and Zhang and Fritsch (1988) discovered during modelling studies that an MCS can develop a middle level mesoscale vortex in its mature and decaying stages. There are three mesoscale circulations that are consistently associated with mature mesoscale convective systems (e.g. Maddox, 1983; Menard and Fritsch, 1989; Liang and Fritsch, 2000). At tropopause level, a large, cold divergent anticyclone occurs (Maddox, 1983; Fritsch and Maddox, 1981; Fritsch and Brown, 1982; Brown, 1979), which is short-lived and shallow (Menard and Fritsch, 1989). The mid-levels of the tro-
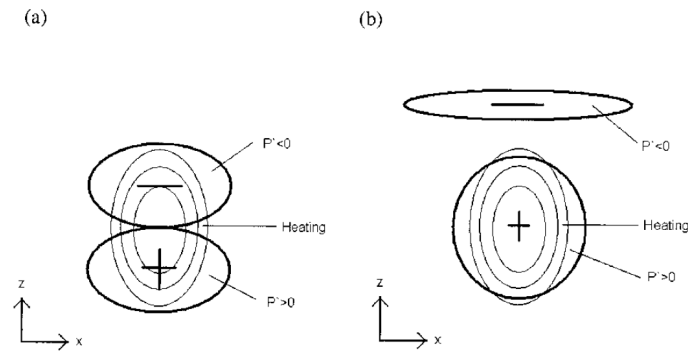
Figure 1.16: PV created in (a) an impulsive heating source and (b) a steady-state heating source (such as an MCS) (taken from Pomroy and Thorpe (2000)). ©Copyright American Meteorological Society. Used with permission.

posphere are characterised by cyclonic vortices (Menard and Fritsch, 1989; Johnston *et al.*, 1989) within a mesoscale updraught due to latent heating and convergence (Smull and Houze, 1985). Johnston (1981) was the first to find observational evidence of the cyclonic circulations in mid-levels using film loops of visible satellite imagery of MCCs. He concluded that these mesoscale convective vortices (MCVs, rotation created around the PV anomalies produced by the MCS) originated somewhere in the MCS, were in the 700–500 hPa layer and had an average diameter of 50–100 km. MCVs have since been used as a term for the mid tropospheric circulations associated with long-lived MCSs.

MCVs are hard to identify using infra-red and satellite imagery since documentation of them is affected by several factors including satellite viewing angle, timing of the dissipation of the parent cloud and the presence of higher-level clouds which obscure it (Bartels and Maddox, 1991). However, Bartels and Maddox (1991) managed to identify a lifecycle for MCVs based on cloud features and patterns through the use of radiosonde soundings at the 500 hPa level. Using this they estimated that MCVs have typical dimensions of 100–300 km in the horizontal (which was larger than found by Johnston (1981)). These MCVs are often several kilometres deep and sometimes span most of the troposphere (Fritsch *et al.*, 1994; Davies and Trier, 2007). MCVs usually maximise between 500–600 hPa (4–6 km altitude) (Zhang 1992; Fritsch *et al.* 1994 ; Bartels and Maddox 1991 and Davies and Trier 2007). It has now been established that the cyclonic circulation develops within the stratiform precipitation region of the MCS (Johnston 1981; Zhang and Fritsch 1988; Chen and Frank 1993; Houze (1977); Zhang and Fritsch (1987); Johnson and Bartels (1992); Brandes (1990); Smull and Houze (1985) and Smull and Houze (1987)) in the area of maximum convergence (Houze, 2004). Figure 1.17 shows a schematic of an

MCS and its mesoscale vortex.
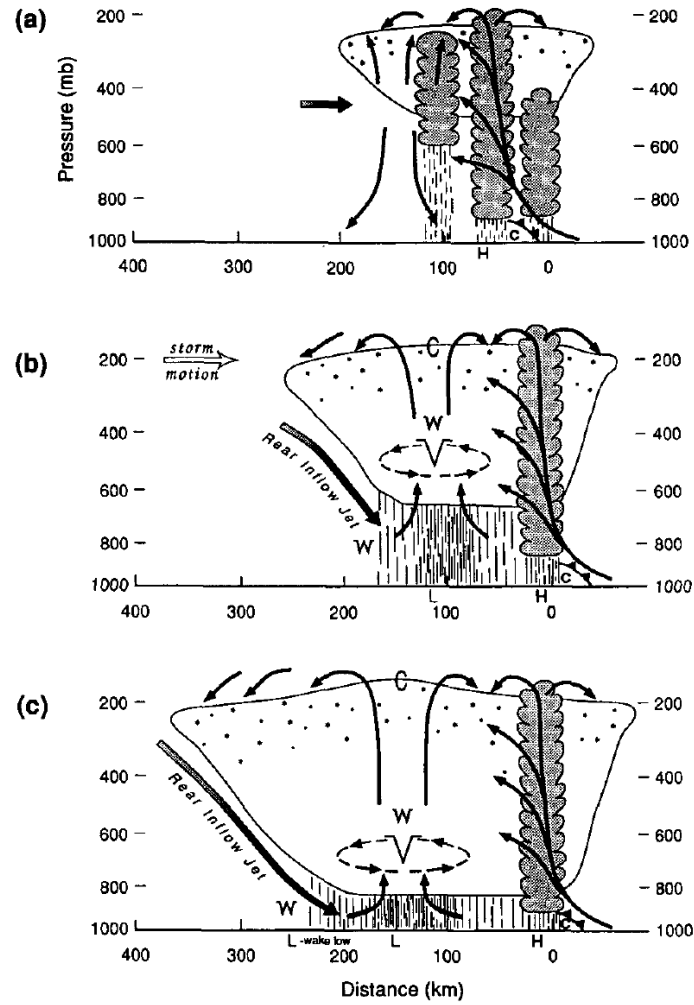
Figure 1.17: Schematic diagrams of the structure of an MCS with the leading convective line (dark shading) and the trailing stratiform region (outlined) and the associated mesovortex at (a) initial stage, (b) mesovortex genesis stage and (c) mesovortex intensification stage. The solid arrows represent that mesoscale circulation. The shaded arrows indicate the location of a rear inflow. Here W and C represent the locations of positive and negative temperature anomalies, respectively; V and dashed arrows denote a mid-level mesoscale vortex. Taken from Chen and Frank (1993) Fig. 21. ©Copyright American Meteorological Society. Used with permission.

1.3.3.4   Horizontal PV structure in MCSs

Along with the vertical dipoles of PV created in association with the MCS, horizontal dipoles also exist. Chagnon and Gray (2009) show that horizontal dipoles of PV originate due to heating from moist processes inside clouds in an environment containing horizontal vorticity (associated with vertical wind shear). The horizontal dipoles of PV can only be represented by high resolution, convection-permitting simulations. Hori-

zontal dipoles of PV on the storm-scale represent a more 'primative' evolutionary stage of the MCS than the vertical MCV structure that typically occurs when the MCS is fully developed. This evolutionary stage is not well represented (or is not represented at all in coarse NWP models. The MCV can also be poorly represented when convection parametrization is operated due to the large scale of the grid boxes. It is hypothesised that this will impact the forecast of the mature MCV stage of the MCS (Chagnon and Gray (2009)), ultimately producing a different forecast than would occur in a higher resolution model.

A higher resolution model which is able to resolve the storm-scale system will generate both vertical and horizontal dipoles. In this instance the vertical dipoles will also have more detail and be stronger. It is likely that the increased intensity of the PV anomalies and the horizontal component of their structure will have a downstream influence on the environmental flow, similar to the influence vertical dipoles have been previously documented to generate (Gray, 2001).

1.3.3.5   The importance of MCVs

MCVs are important as they have been found, in some cases, to lead to the development of subsequent MCSs (Fritsch *et al.*, 1994). Raymond and Jiang (1990) proposed a mechanism by which PV anomalies associated with long-lived MCSs can interact with environmental shear and induce regions of mesoscale ascent in which favourable conditions for MCS development are created. Figure 29 of Fritsch *et al.* (1994) (Figure 1.15) shows a conceptual model of the structure and redevelopment mechanism of the mesoscale warm core vortex in middle levels, which clearly shows the maximum in PV at midlevels with a minimum directly above it at tropopause level.

The representation of MCVs in numerical weather forecasts and their associated PV anomalies are important as they have the ability to persist after the associated convection from which they arise has dissipated. PV anomalies associated with MCSs can affect the environmental flow (clouds and precipitation) far downstream of their origin (Davis and Galarneau, 2009). In their dissipating phase the MCS may degenerate into a remnant MCV (Bartels and Maddox, 1991). The resulting MCV may travel with the mid-level flow with a different velocity to that of the cold pool or active convection surrounding the MCS. This MCV may then generate a new cycle of convection (Bosart and Sanders, 1981;

Fritsch *et al.*, 1994). These subsequent MCSs often form within the pre-existing vortex providing further evidence of the need to accurately forecast these mesoscale circulations (Fritsch *et al.*, 1994). Gray (2001) found that the mid-level MCV can lead to influences downstream 48 hours after the MCS, including deepening a low-pressure system by up to 6 hPa.

Representation of the circulations in MCSs is difficult. The circulations themselves are much smaller than the cloud shield associated with the parent MCS. Thus, although the model may be able to accurately represent the MCS, it may not be able to represent the embedded circulations. Additionally, if the forecast of the initial convection is poor then it is likely that the subsequent forecast of the MCV will also be poor. Some MCVs penetrate to the surface (Bosart and Sanders, 1981; Fritsch *et al.*, 1994; Rogers and Fritsch, 2001). In MCVs over land, this penetration may have consequences in forming surface fronts and organising precipitation (Galarneau and Bosart, 2009). Davies and Trier (2007) observed strong vertical wind shear in the lowest few kilometres in cases of MCVs with little or no signature at the surface. The factor determining the vertical penetration of an MCV to the surface is how strong the shear is near the surface. In cases where there was little shear near the surface, the MCVs penetrated to the surface and were strongest. They also helped lead to the development of further secondary convection downshear of the original MCV where there is high equivalent potential temperature air and the MCV is able to enhance the vertical shear (Trier and Davies, 2007).

1.3.3.6   The importance of upper-level negative PV anomalies in MCSs

The negative PV anomalies created at upper-levels in the MCS have divergent anticylonic circulations associated with them that can influence the environment flow. Fehlmann and Davies (1997) found that misforecasts of PV at tropopause level (usually corresponding to jet stream level) and mid-levels causes errors in the forecast of a low-level cyclone. When these PV structures were introduced into the model the development of the cyclone was much better represented in the model and more consistent with reality. Thus, Fehlmann and Davies (1997) concluded that the pattern and structure of PV distributions is key to achieving a successful forecast of the low-pressure centres in cyclones for some cases. Thus, not only representation of convection associated with MCVs in NWP models is important, but also the tropopause-level flow patterns since

convectively-generated PV anomalies at this level can influence the downstream flow patterns.

Previous studies have shown the importance of accurately representing moist processes in large-scale flow modification (e.g. Rodwell *et al.*, 2013; Davies and Didone, 2013; Grams and Archambault, 2016), particularly at upper-level jet stream level since it is this level which dominates the midlatitude flow patterns. Zhang *et al.* (2007) and Selz and Craig (2015) also found errors grow rapidly in the presence of convective instability and latent heat release at tropopause level (as happens in MCSs). This stage is followed by the perturbations expanding in spatial scale and then growing onto a synoptic scale. Negative PV anomaly outflow at upper-levels in tropical cyclones and extratropical cyclones has been shown to lead to downstream influences on the flow, particularly in slowing the eastward progression of the flow and amplifying the ridges downstream (Grams and Archambault, 2016; Quinting and Jones, 2016; Riemer *et al.*, 2008). These negative PV anomalies at upper-levels created in MCSs are therefore an important link between the mesoscale MCS and the large-scale flow. However, Gray (2001) showed that mid-level PV anomalies associated with MCSs have the largest influence on the downstream forecast, more so than the upper-level anomaly.

1.3.3.7 The impact of PV anomalies on the surrounding flow

An important property of PV; due to being conserved under adiabatic and frictionless flow, is that upon a suitable balance condition and boundary conditions the PV can be inverted to find out the winds and temperatures (vorticity and static stability) associated the PV anomaly itself. This is known as PV inversion. PV invertibility provides a means of quantifying the importance of features in terms of the strength of their associated circulations and their ability to enhance the development of other features (Davis and Emanuel, 1991).

Through PV inversion it can be shown that PV anomalies have action-at-a-distance whereby the PV anomaly impacts the flow surrounding it, just as a charge would produce an electric field. A positive PV anomaly has cyclonic circulation associated with it along with increased static stability, or just one of the vorticity and static stability can be increased (a warm anomaly is created above the anomaly and a cold anomaly below it). A negative PV anomaly has anti-cyclonic circulation associated with it and decreased

static stability, or just one of the vorticity and static stability can be decreased (a cold anomaly develops above the PV anomaly and a warm anomaly develops below it).

Away from the PV anomalies themselves Bishop and Thorpe (1994) note that for quasi-geostrphic (QG) PV inversion a positive PV anomaly has increased static stability with anticyclonic vorticity in one region but decreased static stability and cyclonic vorticity in another region showing the action-at-a-distance influence of a PV anomaly (see Figure 2 from Bishop and Thorpe (1994)). For a single-cell meridional circulation, free PV charges are displaced to create a local dipole of vorticity anomalies. This causes further meridional advection to occur around the original dipole due to the charge inducing a field (Bishop and Thorpe, 1994). This causes further PV charges to be displaced and leads to the propagation of a wave-train of alternating PV charges.

Pomroy and Thorpe (2000) in a study of PV anomalies produced by a cyclone, determined through PV inversion that upper-level reduced or negative PV anomalies cause instantaneous impacts on the wind and temperature perturbations which are at least comparable in magnitude and extent to those induced by a similar positive PV anomaly at middle levels. For a negative PV anomaly at upper-levels Pomroy and Thorpe (2000) found that the warm region below the anomaly penetrates less far away (approximately 4 km deep) than the cold region above the anomaly (extends approximately 7 km upwards in the vertical). This greater penetration of the cold above the PV anomaly is due to the higher PV in the stratosphere acting to increase the penetration of the perturbation into the stratosphere. The negative PV anomaly produced a characteristic anticyclonic circulation however the effect of the tropopause on the wind field was even more pronounced with the wind anomaly having hardly any penetration into the stratosphere despite the anomaly occurring so close to it at tropopause level (Pomroy and Thorpe, 2000) (see Figure 4 of Pomroy and Thorpe (2000)). In the horizontal, the meridional winds penetrate outwards from the anomaly approximately 10 degrees longitude in both directions (for an upper-level negative PV anomaly which extends 10 degrees longitude in the horizontal).

When Pomroy and Thorpe (2000) studied an upper-level negative PV anomaly which was stronger magnitude the penetration of the warm and cold regions surrounding the anomaly were similar magnitude in this case which they concluded was due to the positioning of the stratosphere since this upper-level negative PV was in the troposphere

but the previous weaker magnitude negative PV anomaly was surrounded by the stratosphere on three sides. Again though, the wind field hardly penetrated into the stratosphere but had a similar horizontal extent of influence of the wind field surrounding the PV anomaly (see Figure 7 of Pomroy and Thorpe (2000)).

For a middle-level positive PV anomaly the characteristic region of cold air below and warm air above develops. The vertical extent of the warm anomaly is greater and reaches throughout the troposphere due to the cold anomaly being restricted by the surface. The magnitude of the cold and warm temperatures are similar though. The wind field for the positive PV anomaly shows positive cyclonic rotation with the influence of the winds surrounding the anomaly stretching throughout the troposphere (see Figure 13 of Pomroy and Thorpe (2000)). Pomroy and Thorpe (2000) concluded that upper-level negative PV anomalies induce larger perturbations than lower-tropospheric positive PV anomalies.

The atmospheric response to upper-level negative PV anomalies and lower-tropospheric positive PV anomalies was investigated by Pomroy and Thorpe (2000). When the upper-level negative PV anomaly was removed reduced anticyclonic curvature in the upper-level ridge allowed the trough to broaden eastward of approximately 400 km. This broadened trough allows for coupling between upper and lower levels to be enhanced due to the troughs new position relative to the depression. The removal of the lower-tropospheric positive PV anomaly associated with a cyclone led to decreases in the low-level circulation and the depth of the depression. The positive anomaly rapidly reformed though which minimised any potential effects due to its removal from the simulation.

Pomroy and Thorpe (2000) state "upper-level negative PV anomalies create non-negligible perturbations to the geopotential height field, which are at least equal magnitude to diabatically produced increased lower-tropospheric PV anomalies". However, Pomroy and Thorpe (2000) found that the influence over time in their case study was small but the maximum impact occurred upon the initial development of the low of the cyclone and thus can play a vital role in the long-term development of the cyclone. This finding was in direct contrast to the positive PV anomaly which had most influence in the later stages of the cyclone development.

There are significant nonlinear error growth around PV perturbations associated

with an extratropical cyclone for a moist case (Beare *et al.*, 2003) but linear growth for a dry case. Stronger vertical velocity perturbations develop associated with a positive PV perturbation 48 hours after initiation in a moist case compared to the dry case however the spatial scale of influence of the winds is similar in both cases (Beare *et al.*, 2003) (approximately extending 4000 km). The most sensitive region to error growth are in the regions of the steering level and the cold and warm fronts. When a mesoscale positive PV perturbation is input (200 km horizontal scale) the instantaneous impact is to force ascent to the east and descent to the west. The vortex created advects eastwards by the large-scale flow and interacts with the large-scale dynamics. The initial impact is that the pressure perturbation grows in both magnitude and scale impacting the synoptic-scale after 48 hours showing upscale cascade from mesoscale to synoptic-scale (Beare *et al.*, 2003). Error growth in the moist case is larger and more nonlinear than the dry case due to it modifying the heating which is inherently nonlinear in nature. Beare *et al.* (2003) also found that mesoscale PV perturbations give a deepening of a low centre associated with the cyclone.

As discussed in the previous Sections, MCSs are characterised by a vertical dipole of PV with a positive PV anomaly at middle levels and a negative PV anomaly at upper-levels. If PV anomalies are sufficiently strong enough then localised regions of negative PV are generated which can result in mesoscale circulations which are anticyclonic in nature. Horizontal dipoles of PV can also be produced by individual storm cells generated by heating in a vertically sheared environment compared to vertical PV dipoles which are produced when heating occurs in an atmosphere containing some background vertical vorticity (Chagnon and Gray, 2009). The dipole orientation becomes more horizontal as the shear increases relative to the Coriolis parameter (Chagnon and Gray, 2009).

Chagnon and Gray (2009) shows that for MCS scale heating in a weak shear environment generates primarily a vertical PV dipole, increasing the shear causes a tilting of the PV dipole axis towards the horizon. Chagnon and Gray (2009) concluded that for the initial PV dipole generation as the heating width is decreased the dipole orientation becomes more horizontal and the relative vorticity becomes more dominant (see Figure 2 Chagnon and Gray (2009)). Additionally, when the shear is increased the dipole orientation becomes more horizontal. In the balanced state the PV anomaly resides almost entirely in relative vorticity or heating on the cumulus scale whereas for heating

on the MCS scale the latent stretching vorticity component is the dominant term, with relative vorticity being of secondary importance (Chagnon and Gray, 2009). Chagnon and Gray (2009) found that the adjustment time-scale for cumulus-scale heating is approximately 0.5 hours and concluded significant conversion of latent to relative vorticity occurs during the lifetime of a cloud. Horizontal dipoles tend to be tilted in the direction of environmental shear and can only be represented in convection-permitting simulations (Chagnon and Gray, 2009).

The generation of vertical motion precedes the generation of PV by heating implying that relative vorticity after a rapid adjustment to PV anomaly generation can persist beyond the lifetime of an updraught (Chagnon and Gray, 2009). Chagnon and Gray (2009) found that horizontal dipoles of PV were produced in a 1 km simulation as they originate from moist processes on the cloud scale which cannot be represented in larger grid spacing models whereas in a 12 km simulation only vertical dipoles were produced. When these 1 km simulations were coarse grained to a 12 km grid the horizontal structure of the dipoles was preserved but their magnitude was reduced. Horizontal dipoles tend to have larger magnitude of order 10 PVU than the vertical dipoles of order 1 PVU however the horizontal dipoles tend to be made up entirely of relative vorticity dipoles even though they are generated by heating from moist processes in clouds (Chagnon and Gray, 2009).

The horizontal dipole may induce a very different velocity field compared with a vertical dipole. A large wind perturbation could be produced in the upshear direction between vortices produced by the dipoles (Chagnon and Gray, 2009). A particular influence on the flow is that relative vorticity anomaly produced by PV can be maintained beyond the lifetime of the individual updraught. Chagnon and Gray (2009) concluded that the impact of horizontal PV dipoles appears to be local to the storms themselves but discussed the need to examine the implications of storm-scale PV on synoptic-scale error growth. Although dependant on the scale of the model used, Chagnon and Gray (2009) showed the horizontal influence of horizontal PV dipoles was approximately 10 km, with the vertical extent varying but in some cases extended throughout the whole troposphere. The main point to note from Chagnon and Gray (2009) is that cumulus scale heating induces PV dipoles which are more horizontally orientated than those created by mesoscale heating thus induce different impacts on the wind field.

A connection between vertical penetration above and below the PV anomaly with the amplitude of the PV anomaly was found by Davis and Galarneau (2009) but was dependant on the amount of rotation occurring. Middle level positive PV perturbations have increased wind and pressure perturbations as the Rossby number increases (with the opposite for negative anomalies) (Davis, 1992). However, Davis (1992) concluded that nonlinear effects will be mostly manifested by large amplitude positive PV anomalies.

The studies discussed above suggest that it is likely that the PV anomalies produced by MCSs with a vertical positive PV column at middle levels and a divergent negative PV lens at upper-levels (steady-state heating) will have a different impact than PV anomalies produced by instantaneous heating. The impact may be that the PV anomalies produced by MCSs will have a greater range of influence due to their larger scale and magnitude. In addition, it is likely that the positive PV anomaly column in middle levels will have a different impact on the flow than the upper-level negative PV anomaly due to differences in the wind and temperatures that these anomalies have associated with them.

The negative PV lens created at upper-levels in an MCS should produce larger perturbations of wind and temperature than the positive PV at middle levels (Pomroy and Thorpe, 2000) largely due to the background winds being stronger at tropopause level. The negative PV lens will produce anticyclonic circulations whereas the positive PV column will produce cyclonic circulations which will both act on the flow surrounding the anomalies. Chagnon and Gray (2009) suggested that dipoles of PV since they are on the small-scale act locally to the storm itself therefore these dipoles of PV may be less important than say the column of positive PV and lens of negative PV produced by steady state heating in an MCS as the momentum flux and therefore gravity waves produced by these will likely be larger thus producing more dynamical impacts on the flow.

1.4   Numerical modelling of MCSs

Numerical weather prediction (NWP) models are used to generate weather forecasts by predicting the future state of the atmosphere. Producing a forecast using an NWP model requires a numerical approximation to be produced from five mathematical equations (see Section 2.1.1 for details on these). To produce forecasts, information about the present state of the atmosphere is required. To do this a previous short forecast is adjusted to be closer to recent observations using the mathematical process of data assimilation. NWP models split the forecast area into grid-boxes. Each grid-box in the forecast domain requires information (in the form of prognostic variables) being discretised onto a grid. The size of the grid-box determines the resolution of the NWP model.

'Fine' resolution models with horizontal grid lengths of order 1 km are termed convection-permitting and tend to be used for smaller regional domains that represent convective motions directly (explicitly). 'Coarse' resolution models, that are unable to represent convective motions directly (explicitly) require the use of parametrized convection due to their larger-scale grid-spacing and are often used for global forecasts because it would be too expensive to run at a finer resolution over the whole globe. These grid boxes are too large to enable convection to be represented by the model grid and hence are called convection parametrizing as a convection scheme is required in the model (discussed further in Chapter 2).

Regardless of the grid spacing being used, the equations can only represent atmospheric processes at the scales allowed by the grid. Atmospheric processes can only be properly resolved in the NWP model over four to six grid-boxes (Lean *et al.*, 2008) this is because it requires this many grid boxes to accurately represent a sine wave. Any process that occurs at scales close to or smaller than the grid spacing cannot be represented by the NWP model. Parametrization schemes are therefore required to represent the effect of these processes which are important because they influence the atmospheric flow and the weather of the boundary layer, convection, cloud processes and cloud microphysics. Parametrization schemes are also required so that the equations used in the model do not become unstable and grid-box storms do not form. Parametrization schemes are essentially a model inside the large-scale NWP model to represent the effect of things which cannot be explicitly represented by the model. See Section 2.1 for details on each of these schemes.

Higher resolution NWP models (with smaller grid spacing) may not require all these parametrizations though if the model is able to represent processes explicitly on the grid. For example, the Met Office uses a Global NWP model, which is called the Global Met Office Unified model (MetUM). This model has about 25 km grid-spacing (meaning that each grid box is 25 km apart - so can resolve processes which are about 100 to 150 km in horizontal size). This resolution is relatively 'coarse' and is 'convection-parametrizing' meaning that convection cannot be resolved over this scale so a parametrization scheme is used. In 2017 the Met Office upgraded to a 10 km grid spacing Global NWP model but at the time of this study the Global model was 25 km grid spacing. The Met Office also has a 1.5 km UK MetUM model called the UKV (Tang *et al.*, 2013), which has a 1.5 km grid-spacing, which is able to represent convection explicitly on the grid at scales around 6–8 km. Hence the model is called 'convection-permitting'. The rest of this Section will discuss the representation of convection in NWP models and the importance of this before discussing the predictability of MCSs.

1.4.1   Representation of convection in the Met Office Unified Model

NWP models with a grid spacing of greater than a few kms require convective parameterisation to represent deep convection as they are unable to sensibly represent the size, location, intensity and propagation of convection on the grid because the grid is too coarse. The purpose of convective parametrization is to represent most, or all, of the convective-scale motion to prevent a build up of convective instability and an unstable growth of cloudy structures on the grid (Clark *et al.*, 2016).

Convection-permitting and convection-parametrizing NWP models often give different looking forecasts. These differences arise due to the way convection is represented in each of the models. Convection-permitting models are usually able to represent convection and hence the model produces localised heating due to diabatic processes. On the other hand, convection-parametrizing models are unable to represent convection explicitly as it is usually too small-scale for the grid-spacing of the model. This requires a convection scheme to be used in order to simulate convection in the model. The convection scheme used in coarser-resolution models produces convection which simulates the average effect of a convective cloud over an entire grid box. This produces convection which is not localised because it is effectively a grid square mean and is often of a lower

intensity in comparison to the convection-permitting models. These differences in the forecasts are often due to the heating profiles created by the convection simulated in the models. The non-localised convection in the parametrizing models, in comparison to the localised diabatic heating profile created in the permitting models, leads to variations in the circulation patterns created in the forecasts.

Although convection-permitting models are able to explicitly represent convection, realistic structures still cannot be developed by the model as it is unable to represent the sub-grid scale turbulent mixing in the clouds along with other sub-grid scale structures. This often creates stronger convection in the models than actually occurs in reality as the turbulent mixing generally slows down the updraughts.

Convection-permitting models allow for the formation of actual showers with an initiation, decay and propagation phase which creates local rain, heating and outflows unlike in the convection-parametrizing models which do not create showers on the grid and instead represents the average effect of convection over the grid square and assumes a steady state whereby there is no memory of there being rainfall. Thus, this can influence the downstream environmental flow causing the forecasts to vary between the models.

Although convection should be represented more realistically by the convection-permitting models, there is the disadvantage that individual showers are not predictable at these small-scales and that errors can grow rapidly (Lorenz, 1969). This is because it is impossible to predict every small detail of the initial conditions or physical processes required to make an accurate forecast at this size of grid spacing. Observations are often too sparse at these scales which puts errors into the initial conditions.

Convection acts on a much faster timescale than that of the large-scale atmosphere (Arakawa and Schubert, 1974) and therefore errors grow more quickly producing short predictability times for the small-scale structures (Lorenz, 1969). The choice of whether to include a convection parametrization in NWP models is determined by how large the convection is in comparison to the grid-scale of the model (for example, a convection scheme is required if a Global Met UM model is used which has 25 km grid-spacing). NWP models, are as a consequence, poor at developing convection at the correct location and time due to the small scales involved in triggering the convection (Kain and Fritsch, 1992; Stensrud and Fritsch, 1994). A convection scheme is required but is not designed

to represent individual storms, only the average effect on larger scales. Individual deep convective clouds tend to span a distance around 10 km (Bryan *et al.*, 2003), this is small in comparison to the distance convection associated with an MCSs spans (MCSs are defined as an amalgamation of individual convective clouds). Bryan *et al.* (2003) proposed that grid spacing on the order of 100 m should be used to represent small-scale turbulent eddies in order to properly model convective events. Additionally, however, they found that resolving the majority of properties of a convective cloud may be possible when using a 1 km grid spacing, although the representation of some micro-physical processes will still be unresolved at this resolution. Currently, the highest resolution used operationally by the Met Office for weather forecasting is 1.5 km grid spacing (for the UK area) due to the computational costs of using higher resolutions and because computer time is also spent on an ensemble 2.2 km MOGREPS-UK forecast (discussed in Section 2.5).

The initial convection associated with the growth of an MCS cannot be resolved explicitly by the convection-parametrizing or convection-permitting models; however, the convection is likely to be resolved by the convection-permitting models when the MCS is organised and the convection is no longer sub-grid scale. Stein *et al.* (2015) found that 200 m grid-spacing performed best for all diagnostics, life-cycle of the storm, storm morphology and convective updraughts, however, they did find that the results were dependent on the mixing length used in the sub-grid turbulence model. This causes problems in the forecasting of MCSs because if the representation of the initial convection is poor then the subsequent forecast of the MCS is likely to be inaccurate in location, intensity and size and may not even develop in the forecast at all.

A MetUM model with 4.4 km grid spacing (called the Euro 4 km) uses a convective parametrization but also allows convection to develop explicitly. The model uses a modified version of the convection scheme used for lower resolution models, to essentially restrict the convection scheme (Roberts, 2003). This scheme allows the model to generate convection explicitly when convection and the associated showers are large enough that they can be resolved on the grid but, alternatively, convective parameterisation can be utilised if convective clouds are weak and cannot be resolved on the grid (Roberts, 2003). When convective parametrization is used in this configuration of the Met UM the scheme varies from the regular convection scheme in that it restricts the activity of the scheme. Representing convection at 4 km grid spacing, the so-called grey-zone where

clouds are partially resolved, provides a major research challenge (Gerard *et al.*, 2009; Yu and Lee, 2010; Arakawa and Wu, 2013), but the approach of using modified convection parametrization in the 4 km model gives better results than running without the convection parametrization (Clark *et al.*, 2016). Despite this, Lean *et al.* (2008) found that the Euro 4 km model produces showers that are too few, too intense and too organised.

A 1.5 km grid spacing MetUM model resolves convection explicitly as it generally has a small enough grid length to be able to represent deep convective clouds thus can be run without a convection scheme. However, this is still a relatively coarse grid scale in comparison to the size of typical convective plumes so showers produced tend to still be under-resolved (Bryan *et al.*, 2003; Hanley *et al.*, 2015) and, although they can look realistic in comparison to radar, they are often produced in the wrong location as convection initiation is very sensitive to the initial and boundary conditions.

Lean *et al.* (2008) found that a model with a 12 km grid tends to initiate convection and precipitation 1-2 hours too early, whereas the 4 km and 1 km models are closer to reality. Additionally, Lean *et al.* (2008) found that the 4 km and 1 km models tended to have too large peak rainfall rates, too large cells (4 km model) or too many small cells (1 km model) compared to reality. 'One km models' often look very realistic when compared to rainfall radar since they are able to represent some of the small-scale rainfall cells that coarser models cannot represent. These small-scale cells are still too smooth in comparison to reality though since the 1 km model is still coarser than reality, thus the small showers are still under-resolved (Clark *et al.*, 2016).

The Global model is unable to represent the small-scale cells though and instead predicts widespread precipitation which gives little indication of any areas which may get heavier or lighter rainfall (Clark *et al.*, 2016). How to best verify high resolution model precipitation is still an issue though. Studies have found that the models on the order of 1 km grid spacing typically produce rainfall that looks more like reality in structure but is often in the wrong location. This means that typical verification techniques end up giving the forecast a bad skill score. Barrett *et al.* (2016) found that for four localised precipitation events, from 2.2 km and 1.5 km models, the models were able to represent the structure, intensity, location and duration of the precipitation in each case but never all of them satisfactorily in a single case. Barrett *et al.* (2016) also found that the accuracy of the model representation of the large-scale environment upstream of the precipita-

tion event was strongly correlated with the accuracy of the precipitation forecast in the convection-permitting runs. This indicates the importance of forecasting the large-scale environment accurately for an MCS case.

Unlike convective-parametrizing models, convection-permitting models allow for unstable growth of convective clouds in the model (Clark *et al.*, 2016). Latent heat is released through condensation, allowing the air parcels to become buoyant in this region in respect to their surroundings, producing vertical circulations (Clark *et al.*, 2016). Clark *et al.* (2014) reported an MCS case which was well forecast by the UKV model but was not well forecast by the Global model, which produced hardly any rainfall due to no MCS being represented in the Global model. The circulations related to the PV anomalies created by MCS formation are therefore likely to be poorly represented by convection-parametrizing models, especially if the PV anomalies themselves are not represented. This may impact the large-scale forecast since variations to the PV structure in the upper-levels (jet stream) can lead to significant downstream changes to the static stability and large-scale circulation patterns (Gray, 2001).

Models which explicitly represent convection tend to have a delay in initiation of convection in comparison to observations, but in some cases the convection is too advanced when compared to observations (Lean *et al.*, 2008; Kain and Coauthors, 2008). This is due to the models not being able to reproduce the very small initial convective plumes (Clark *et al.*, 2016). However, Petch (2006) showed that when explicit convection is used a 1 km grid scale model initiates convection more quickly than a 4 km model as initiation time decreases as grid length is reduced. Lean *et al.* (2008) found that 1 km models initiate more quickly than 4 km and 12 km models. Larger grid length models are generally unable to erode convective caps effectively as the effect of convection is less concentrated at one point (Lean *et al.*, 2008). This is of importance when modelling MCSs which tend to initiate after the erosion of a convective cap that has allowed for CAPE to build up to a sufficient amount that it creates "explosive" convection when triggered by the removal of the cap.

Although the UKV configuration has high enough resolution that it could explicitly represent the initial convection associated with an MCS, its domain does not extend far enough south to cover the area in which the majority of MCSs affecting the UK initiate (see Section 2.1.2). Warner and Hsu (2000) and Lean *et al.* (2008) found that the repre-

sentation of convection in the model providing the boundary conditions for the high resolution model has a large effect on the representation of convection in the high resolution model. The UKV operationally uses boundary conditions generated by the Global model therefore, if the Global model was unable to represent the MCS, then it is likely that the subsequent forecast created by the UKV model will be poor also. The model providing the boundary conditions is known to begin to dominate the forecast after approximately a day for the UKV model (Clark *et al.*, 2016).

Convection-permitting models tend to produce cloud which is larger, more widely spaced and slower moving than real cloud (Clark *et al.*, 2016), but produce a better representation than the convection-parametrizing models. Pearson *et al.* (2014) found that individual storms can fail to organise into larger systems in NWP models due to their small-scale, however, when a MetUM 1.5 km model is used (configured over Africa so not the UKV configuration) there tends to be improvement in the diurnal cycle of convection. Stein *et al.* (2015) found that in 1.5 km UKV configuration short-lived storms are not represented well and thus the precipitation produced in these cases was much less than was observed. Storms which lasted too long in the model though overestimated precipitation in comparison to observations (which could be important for MCSs). Stein *et al.* (2015) found that the optimal grid spacing for convection representation is approximately 200 m.

1.4.2   Importance of representing convection for modelling MCSs

Inadequate resolution, an inability to represent convection properly and uncertainty in initiation (due to errors in initial and boundary conditions) are the major issues leading to poor forecasts of MCSs. The difficulties in forecasting these small-scale processes cause a misrepresentation of the initial development of convection. Fine-scale models can realistically represent convection but can get the location and development wrong and in some respects are still too coarse resolution to represent some processes and can lead to wrong outflows or rainfall rates along with secondary development (convection feedbacks on the large scale and can have an impact on the subsequent forecast causing errors which can grow quickly in the model).

The difficult nature of observing the mesoscale environment surrounding the convection initiation can cause initial development of convection to be poorly represented,

partly due to inadequate understanding of the mechanisms of convective cell initiation (Bennett *et al.*, 2006). Additionally, the details of the mesoscale structures involved in the initiation of deep convection are known to be important for accurate forecasts (Zhang and Fritsch, 1987; Stensrud and Fritsch, 1994). Accurate representation of MCSs is known to be sensitive to the mesoscale features present in the initial conditions used in a model run (Stensrud and Fritsch, 1994). These mesoscale features include frontal zone, dry line and convective outflow. Stensrud and Fritsch (1994) found that a simulation that included the outflow produced a more realistic evolution of events. Their initial condition sensitivity tests showed that incorrect representation of the mesoscale features, in terms of timing and location in comparison to observations, can produce a simulation that quickly diverges from observations when parametrized convection is used in the numerical model.

1.4.3   Predictability of MCS events

Since NWP models rely heavily on the initial conditions from observations input into the model before it is even run, it is essential that these be as accurate as possible. This is extremely difficult, impossible in fact. Observations themselves have their own errors and accuracy issues (user error and equipment error) which, when these observations are put into the NWP model, grow over time as the forecast is simulated. Observations tend to be sparse over some parts of the Earth which poses a problem. The atmosphere itself is also inherently unpredictable so it is impossible to predict every little detail that will occur on that day to create a completely accurate forecast. Since errors grow over time within the forecast, Lorenz (1969) found that after around 7–14 days of a forecast the errors have grown so much that the forecast no longer has enough skill. This 14 day period can be considerably shorter though if the atmosphere is particularly unpredictable. MCSs have a predictability of less than 24 hours due to the difficulties in representing them in NWP models. It may be possible to determine however that an MCS will occur due to a favourable environment for formation from around 5 days ahead. Subgrid variations in the model can also be an important factor in the errors produced in forecasts.

Initial condition errors can be input into the model to begin with and then, if the initial convection is poorly represented by the NWP model due to inadequate resolution, large errors can occur in the PV anomalies produced by the MCS along with errors in

other variables in the model. This can eventually lead to growth of errors over time due to the continued inadequate resolution and cause an upscale feedback producing large-scale errors. If small-scale errors develop in forecasts then over time these can grow substantially and cause large-scale errors to develop.

Errors are created by parameterisation of convection, therefore more accurate forecasts of precipitation (timing and location) are produced when explicit convection is used only (Lean *et al.*, 2008). This is not possible for coarse models though since they are unable to resolve the convection involved however eventually instability will build up and produce grid-point storms. If coarse-resolution models do produce precipitation they tend to predict widespread precipitation (rather than localized rainbands or small-scale cells of rainfall) without much indication of an area which could receive larger rain rates (Clark *et al.*, 2016). The representation of propagation and upscale growth associated with mesoscale organisation in a mesoscale model is a great challenge as the upscale growth will be represented explicitly to some extent.

In a study by Done *et al.* (2006) when simulating an MCS in a 12 km grid spacing NWP model a negative lens of PV developed at tropopause level associated with the MCS when convection parametrization was switched off. This lens of negative PV did not develop in the simulation when convection was parametrized. This resulted in a feed back on the surrounding wind and temperature profile in the simulation that developed the negative PV lens at tropopause level suggesting the importance that the representation of convection has on the representation of MCSs in NWP models.

1.4.3.1   Ensemble forecasting of MCSs

Since it is difficult to get completely accurate observations to input into the NWP models to provide initial conditions to the forecast, ensembles are used whereby slightly different initial conditions (perturbed conditions) are put into a number of models (to take into account the error in the observations). The perturbations used must be small enough to be within the limits of observational uncertainty, but large enough to lead to significant divergence between ensemble members through the forecast period (Inness and Dorling, 2013). Predictability of the atmosphere at convective-scale is different to at the synoptic scale with error growth rates growing ten times larger (Hohenegger and Schlar, 2007). Leoncini *et al.* (2010) states that poor convective-scale predictability is likely due to

significant nonlinearities of the atmosphere at smaller scales: microphysics, turbulence, radiation and flow dynamics are strongly coupled and can act to amplify model and observation uncertainties. Doing ensemble forecasts is a way to access the predictability of the atmosphere at that time. If all the models diverge considerably from each other than the atmosphere is deemed to be highly unpredictable. This allows forecasters to convey how confident they can be in their forecast for that day. If all the ensemble members have a very similar forecast then the forecasters can be more confident that that is what the forecast will be for that day.

The difficulty of numerical representation of convection is only part of the problem with forecast accuracy of MCSs. Uncertainties arise from errors created due to model physics along with uncertainties due to having to parametrize sub-grid scale processes such as the initial convection and turbulence in clouds. Lorenz (1969) showed how predictability of the environment is affected by the uncertainty in modelling processes involved. Past studies (Romero *et al.*, 1998; Lean *et al.*, 2008) have shown that the precise location and timing of convection is often poorly represented by models of varying resolutions and convection schemes. Ensemble forecasts are therefore now used to predict the future state of the atmosphere by running many different forecasts with varying initial conditions to sample the uncertainty involved. Usually the mean of the ensemble forecasts is taken to be the most representative forecast of the system. It has been shown though that ensemble forecasts do not always lead to improved forecasts; Stensrud *et al.* (2000) showed no members of their ensemble were able to trigger an MCS that occurred. Brooks and Doswell (1993) suggest that using a large number of simulations at mesoscale resolution to create an ensemble forecast is advantageous as it recognises and makes use of the uncertainty in the model initial conditions. Using ensemble forecasts are peferable as one high resolution simulation has a high probability of providing no useful information if the forecast is inaccurate due to deficiencies in model physics and/or the model initial conditions (Stensrud and Fritsch, 1994). Stensrud and Fritsch (1994) suggested that producing ensemble forecasts using a combination of different initial conditions and different convective parameterisation trigger functions was optimal for producing the best overall forecast of an MCS. Their 'high resolution' modelling used a grid spacing of 25 km which is the same as the grid spacing of the global model used during this study.

1.4.3.2 Error growth in MCS forecasts

Wandishin *et al.* (2008) and Wandishin *et al.* (2010) produced 100 ensemble members (using the North American Model (NAM) with 1 km grid-spacing) each with slightly different perturbations in windspeed, relative humidity and instability (CAPE), based on the 24-hour forecast error. They found that reducing the 24-hour forecast errors by half increased the success rate of forecasting an MCS within 100 km of the control run simulation (for a two day forecast) from 70% to 90%, but only for some of the ensemble members. However, their study almost guaranteed convective initiation which is a major forecast concern as errors in the model often causes convection not to trigger or to trigger in the wrong location. The reduction in the forecast errors for windspeed, relative humidity and instability were not consistent and cannot be generalised, but all had a substantial impact on the forecast uncertainties (for an idealised 2D 1 km model, Wandishin *et al.* (2008)). All three perturbations (windspeed, CAPE and relative humidity) needed reducing in the idealised 1 km 3D run to have an improvement on the success rate of producing an MCS (Wandishin *et al.*, 2010). They conclude that, although high-resolution models are appealing since they can produce realistic looking fields, their study had shown that there is a gap between producing realistic-looking MCSs and producing a skilful forecast of an MCS (Wandishin *et al.*, 2010). This indicates the challenges faced when predicting MCSs. Not only do the 24-hour forecast errors (in the initial conditions) need to be greatly reduced to improve forecasts of such systems, but the uncertainty of convective initiation will also need to be improved.

A study of downstream forecast busts in Central USA by Rodwell *et al.* (2013) suggests that initial errors appear to be created and potentially increased by MCS events. Fifty ensembles were simulated using the European Centre for Medium Range Weather forecasts (ECMWF) forecast model. The authors also suggest that how quickly errors develop in the forecast of an MCS has an impact on the time-scale on which they begin to affect the larger-scale forecast. Rodwell *et al.* (2013) suggest that to reduce errors, improving the accuracy, availability and usage of relevant observations along with an improvement of the representation of MCSs in the models is necessary. Model uncertainty is also important as it was found initial errors were in some cases caused by MCS events or were magnified by them. Rodwell *et al.* (2013) found that if the initial convection is forecast poorly then it often means that a subsequent MCS is poorly forecast and

has the potential to lead to downstream forecast busts. This is because small-scale errors can grow rapidly (Lorenz, 1969), particularly in regions where convection occurs. Zhang *et al.* (2002) found that mesoscale forecast errors grow rapidly particularly in areas where moist processes are active and can eventually infect larger scales throughout the domain (Zhang *et al.*, 2003).

Done *et al.* (2012) investigated the predictability of two MCS cases using a 12 km hydrostatic MetUM configuration. They found when running 12 ensemble members alongside a control forecast for two cases that small-scale perturbations added to the system showed some predictability in the location and intensity of convective precipitation. During their study they left the large-scale unperturbed with the aim of investigating variations to the small-scales which are unobserved. However, the nature of the predictability was different between the two cases. The two cases used were one convective equilibrium case and one convective non-equilibrium case. In convective equilibrium CAPE generally remains small and fairly constant throughout the convective life cycle and the environment is uniform over a region large enough to contain many convective elements (Done *et al.*, 2006). In convective non-equilibrium large amounts of CAPE build up over time before being released when convection triggers. The model used during this study was a 12.5 km grid spacing MetUM model. The small-scale perturbations were in temperature and humidity. Done *et al.* (2012) found that both cases had some, but not complete, predictability in the location and intensity of the convective precipitation, but the nature of the predictability varied between the two cases. In the equilibrium case, the total precipitation over the convective region was not impacted by the perturbations, but the exact number and location of the convective storms varied. This led to a large ensemble spread. In the non-equilibrium case, the ensemble members all produced storms in the same locations (the observed storm location was actually produced in two of the ensembles). The total precipitation varied a lot between each of the ensemble members though (Done *et al.*, 2012). This study was conducted before the MetUM used a non-hydrostatic formulation of the equations, so they suggested that this could have had an impact on the results.

Roberts and Lean (2008) showed that spatial scales of predictability vary widely between different forecasts of convective events. They ran MetUM configurations with 12-km, 4-km and 1-km grid spacing with each being given initial states from a 12-km

MetUM simulation. Since the 4 km and 1 km models were spun up from a 12 km model, this had an impact on the first few hours of the forecast for these models. The results showed that the 1 km model is more skilful than the 12 km model (when comparing fraction skill scores after the spin up period). The improvement is from more accurate distributions of the rain along with a better prediction of high accumulations. They did find that there is an over prediction of rainfall amounts though. The 4 km model was found to have inherent difficulties in convection representation and thus the same improvements did not occur in this model.

Zhang *et al.* (2007) and Selz and Craig (2015) both studied upscale error growth and although not related to MCS events they found that errors initially grow rapidly in the presence of convective instability and latent heat release (errors grew particularly in areas where precipitation occurred). This was followed by a stage where the perturbations expand in spatial scale and then these perturbations grow at the synoptic scale. Zhang *et al.* (2003) and Tan *et al.* (2004) found that initial error growth in models with parametrized convection is much slower than in high-resolution models that resolve convection. These models with parametrized convection do not account for convective-scale uncertainty. Previous studies (of extratropical cyclones and tropical cyclones) have shown the importance of accurately representing moist processes due to the effects it has on large-scale flow modification (e.g. Rodwell *et al.*, 2013; Davies and Didone, 2013 and Grams and Archambault, 2016). Grams and Archambault, 2016 found diabatic processes associated with strong latent heat release are crucial in yielding a highly amplified mid-latitude upper-level Rossby wave flow pattern. They also showed that the flow pattern is substantially less amplified in cases where there is an absence of strong latent heat release and moisture transport. For tropical cyclones transitioning into extra-tropical cyclones the downstream impact can be over an entire ocean basin, predominantly causing a retardation in the eastward movement of the large-scale flow (Grams and Archambault, 2016; Quinting and Jones, 2016; Riemer *et al.*, 2008) which indicates the importance of accurate forecasting of moist processes.

In summary, the studies discussed above show the difficulty of representing MCSs in NWP models due to their scale and the grid-spacing of the model utilised. MCSs are importance to represent accurately though due to the large-scale flow modification they produce due to the impact the associated PV anomalies have on the circulation patterns

particularly at upper-levels.

1.4.3.3   PV-based consideration of predictability

A study by Gray (2001) which added MCS PV anomalies at mid-levels and upper-levels (taken from PV inversion to input the horizontal wind fields and θ as perturbations) to four cases where an MCS occurred in observations but was not represented in the model was used to determine the impact of MCS PV anomalies on the forecast. Gray (2001) showed that including PV anomalies associated with an MCS in a Global (80 km grid spacing) NWP model led to large differences in the forecast evolution (in two out of the four cases studied; smaller differences in the other two cases were found) in comparison to the control forecast (without the anomalies), suggesting that it is important to represent these PV anomalies when forecasting MCSs. Gray (2001) found that the mid-level MCV associated with MCSs (2 PVU) had the biggest impact on the NWP (compared to the upper-level low PV anomaly with the value 0.1 PVU) forecast due to the circulations associated with the positive PV anomaly, creating ascent and decent around the MCV.

Lack of representation of the PV anomalies associated with the MCS is a cause of model and analysis error (Gray, 2001). If the PV anomalies are formed they can still be formed in the wrong location or at the wrong time though, which is also likely to impact the forecast. It was found that including the anomalies led to a slight decrease in forecast errors through the deepening of a downstream low pressure system (by approximately 6 hPa at least 48 hours ahead) that for one of their cases produced a forecast which matched reality more closely (and reduced the root mean square error values). The authors concluded by stating that MCVs are important PV structures that can influence the subsequent downstream flow and thus improvements in the representation of MCVs in NWP models could lead to increased forecast accuracy. The downstream influence could be related to the fact that differences in the mean sea-level pressures were found when the PV anomalies associated with the MCS were included in the model in comparison to when they were not. These differences varied in magnitude between the simulations though.

As a consequence of the study by Gray (2001), due to the downstream influence found due to the PV anomalies associated with the MCSs a stochastic physics scheme was added to the MetUM ensemble forecasting (Bowler *et al.*, 2008). The purpose of this

scheme was to simulate the PV anomalies associated with MCSs to account for error produced through misrepresentation of the PV anomalies associated with MCSs. This was later retired though as it was found to have little improvement on the forecasts.

Stensrud *et al.* (1999) also found that when cold pools are included in the initial conditions the location and total amounts of precipitation are improved in the five MCS events they studied. Davies and Didone (2013) found that using a PV-based metric of forecast error is a meaningful way to assess forecast performance. However, data assimilation in NWP models may not capture the details of key PV features at tropopause elevations in the initial analysis which is likely to impact on low-level forecast errors since these errors have been found to be collocated to errors in the PV field at tropopause level (Davies and Didone, 2013).

Although their study did not focus on MCS events Fehlmann and Davies (1997) and Fehlmann *et al.* (2000) found that for some weather events the pattern and structure of the PV distribution at tropopause elevations was key to achieving a successful forecast which may be important to MCSs since they produce PV anomalies at this level. Additionally, it has been shown that the PV error pattern and errors based on the PV structure at tropopause level provide an insight of the nature of the forecast error and its evolution for MCS events (Dirren *et al.*, 2003; Rodwell, 2006). Clark *et al.* (2016) states that larger-scale errors in convective rain are often associated with mesoscale features in the mid- and upper-level wind and temperature pattern (upper-level potential vorticity anomalies) or in the low-level thermodynamics, especially in the moisture distribution.

Roberts (2000) showed that the track of an upper-level vortex in a NWP model is important. He found that even if an upper-level vortex originates in the correct location it may diverge from reality with time and have a subsequently large impact on the rainfall forecast accuracy. For the larger-scale flow to be correct it is important to have a good representation of the vorticity as it is important for subsequent storm formation. This unpredictability makes forecasting of MCSs difficult and is due to the fact that MCSs begin as cloud-scale systems and develop into mesoscale systems that are then able to be resolved by NWP models.

Beare *et al.* (2003) found that the development of extratropical cyclones was sensitive to the mesoscale PV anomalies (200 km horizontal scale mid-level anomaly). A large degree of nonlinear error growth occurred associated with these mesoscale PV anomalies

in the moist case which did not occur for a dry simulation.

PV anomalies associated with MCSs are important structures to represent in NWP models due to their associated impacts on the wind patterns and temperatures. These changes in the wind patterns and temperatures have an inherent impact on the flow patterns around the MCS and downstream from the MCS itself. The studies discussed above show evidence for the impact of PV anomalies associated with MCSs and the current difficulties in representing them in NWP models. The studies suggest that misrepresentation of these anomalies can potentially lead to forecast busts downstream along with pressure patterns that diverge from reality.

1.5   Summary

Mesoscale convective systems form when there is an amalgamation of many individual thunderstorms into one large convective system. MCSs occur all over the globe (except for the Antarctic) and mostly over land. They are associated with heavy rain, strong winds and have been known to produce flooding. MCSs tend to form when large amounts of CAPE develop due to CIN associated with an inversion layer (sometimes called a convective 'lid' or 'cap'). This instability is unable to be released until a triggering mechanism occurs and then convection forms. For western Europe MCSs often develop in a synoptic environment called a Spanish plume which provides the moisture, instability and lifting mechanism which favours deep, moist convection. MCSs are rare in the UK, but this does not take away from the need for forecast accuracy since they are associated with a flooding risk and have an impact on the downstream forecast due to the heating and convection which occurs.

MCS events are difficult to forecast due to their inherent unpredictability and the nature of their scale, meaning that they start off at sub-grid scale in all models before becoming large enough to be explicitly represented by the convection-permitting models. This has been shown in the past to lead to forecast busts in association with MCS events not being represented in the model. This study aims to determine the impact of, not only model resolution on the forecast of MCSs, but also the impact that MCSs have on the large-scale environment and thus on the forecast produced and the predictability of the downstream forecast. Previous studies have found that MCSs can have an

impact on the downstream flow due to the PV anomalies associated with them. There-fore, if these PV anomalies are not represented in the model then it is likely that a very different downstream forecast would be produced. By determining the PV structure as-sociated with MCSs in western Europe and the differences in these structures between convection-permitting and convection-parametrizing models an investigation into the predictability of the downstream forecast after an MCS event can be conducted. The impact that the PV anomalies associated with MCSs have on the downstream flow is in-vestigated to determine if these PV anomalies can have a beneficial effect on the forecast spread.

Chapter 2

Methodology

The purpose of this Chapter is to discuss the methods used for the research conducted throughout this study. An overview of the Met Office Unified Model (MetUM) is given along with the most relevant parametrization schemes used in the models for this research. Details of the different model configurations used in this study are then given followed by details of the diagnostic code (NDdiag) which is used to produce diagnostics from the MetUM output. Information on a coarse graining technique will then be given; this technique is used in Chapters 4, 5 and 6 of this study. The final section is on ensemble methods used in Chapter 6 of the study.

2.1 The Met Office Unified Model

The Met Office Unified Model (MetUM) is a numerical model used to simulate the atmosphere (and oceans) produced by the Met Office in the UK. The purpose of the MetUM is to predict the weather (through numerical weather prediction) and climate (through climate models), over a range of time and space scales and geographical regions. This is achieved by the use of different configurations of the same model. The differences required in each configuration depend on the intended purpose of the model. The model configurations are produced to best represent processes required on the time and space scales required. The MetUM is known as a unified model meaning that the same model can be used for all space and timescales with only a few variations and additions required. The use of a seamless model allows model development to be more efficient with greater flexibility.

For the purpose of this study the MetUM was used to produce numerical weather prediction (NWP) forecasts at high resolution in a "limited area" mode for domains covering parts of western Europe as well as forecasts on the full global domain for forecasts lasting from a few hours to a few days. Version 8.2 of the MetUM, which uses the New

Dynamics dynamical core (Davies *et al.*, 2005), is used throughout this study in Chapters 4, 5 and 6. NWP models are generally run to produce a forecast for a few hours to several days. The following section provides details of the MetUM dynamical core and physical parametrization schemes used in the model for this study. The dynamical core is the part of the MetUM model which is required for every NWP forecast made which solves the equations of motion on the grid. This is the part of the model that simulates the larger-scale processes that can be resolved by the model. Coarser resolution NWP forecasts may then require additional physical parametrizations in the model to account for things which are too small-scale for the model to resolve. Higher resolution models need less parametrization schemes because more small scales motions are represented on the grid however some processes may occur on scales too small to be directly represented on the grid (such as convection and cloud microphysics) and these need to be parametrized separately. For further detail on the MetUM the reader is advised to read the model documentation papers on the National Centre for Atmospheric Science Computer Modelling Services (NCAS-CMS) website (http://cms.ncas.ac.uk/wiki/Docs/MetOfficeDocs).

2.1.1 Dynamical Core

The MetUM is non-hydrostatic meaning that it takes into account the vertical motions in the atmosphere rather than assuming vertical accelerations are negligible (i.e. a vertical equation of motion is required). The model is also compressible meaning that as the pressure changes the atmosphere responds with a change in density. The MetUM uses spherical polar coordinates (λ, ϕ, r), where λ is longitude, ϕ is latitude and $r = a + z$ being the distance to the Earth's centre, a is an assumed constant for the Earth's radius and z is the height above mean sea level. The MetUM has a number of equations which it must solve; the equations of motion, continuity (conservation of mass) and thermodynamic equations. These equations provide what is known as the 'prognostic' variables (the model must solve mathematical equations via integration in order to find a solution of the variables). The prognostic variables required by the MetUM are the wind velocity, **u**, which has three components (u, v, w); potential temperature θ; density ρ_x (where x can be dry, water vapour (vap), cloud water (cl) and cloud ice (ci)); pressure p (which for the atmosphere is defined by the Exner function $\Pi = (\frac{p}{p_0})^\kappa$, where p is the pressure, $p_0 = 10^5 Pa$ the reference pressure at sea-level and $\kappa \equiv \frac{R_{dry}}{c_p}$ where R_{dry} is the gas constant

for dry air and c_p is the specific heat at constant pressure for dry air); and the mixing ratio of moist quantities. Mixing ratios are given by water vapour (m_v), liquid water (m_l) and ice (m_i). Mixing ratios are then defined to be $m_x = \frac{\rho_x}{\rho_{dry}}$ where x is any of the vapour, water or ice phases. The potential temperature $\theta \equiv \frac{T}{\Pi}$ where T is the temperature.

To solve for these prognostic variables the equations of motion for the three dimensional wind **u**, the thermodynamic equation for θ, the continuity equation (mass conservation) for ρ, the transport equation for m and the equation of state for p are all required. These equations are used with the main priority of NWP models being to make sure that conservation of mass, momentum, energy and water occurs, as these create the large-scale dynamics of the model. The equations of motion are all expressed in spherical polar coordinate form (λ, ϕ, τ) over a deep atmosphere (change with height is important; the difference between r and a is considered important), with the Earth's centre being the origin:

$$\frac{Du}{Dt} = 2\Omega \sin \phi v - 2\Omega \cos \phi w + \frac{uv \tan \phi}{r} - \frac{uw}{r} - \frac{c_p \theta_v}{r \cos \phi} \frac{\partial \Pi}{\partial \lambda} + P_u, \tag{2.1a}$$

$$\frac{Dv}{Dt} = 2\Omega \sin \phi u - \frac{u^2 tan\phi}{r} - \frac{w}{r} - \frac{c_p \theta_v}{r} \frac{\partial \Pi}{\partial \phi} + P_v, \tag{2.1b}$$

$$\frac{Dw}{Dt} = 2\Omega \cos \phi u - \frac{u^2 + v^2}{r} - g - c_p \theta_v \frac{\partial \Pi}{\partial r} + P_w, \tag{2.1c}$$

$$\frac{D\theta}{Dt} = P_\theta, \tag{2.2}$$

$$\frac{D\mathbf{m}}{Dt} = P_m, \tag{2.3}$$

$$\frac{\partial \rho_{dry}}{\partial t} + \nabla \cdot (\rho_{dry} \mathbf{u}) = 0, \tag{2.4}$$

The equation of state ($p = R_{dry} \rho T_{vap}$) can be written as

$$k \Pi \rho \theta_v = \frac{p}{c_{p_{dry}}}. \tag{2.5}$$

Here, Ω is the angular speed of rotation, Π is the Exner pressure, p is pressure, g is

the gravitational acceleration, ρ is the total air density and is defined as $\rho = \rho_{dry}(1 + m_{vap} + m_{cl} + m_{ci})$. P is used to represent the tendencies from the physics parameterisation schemes used in the model. The material derivative for the spherical polar coordinates is given by

$$\frac{D}{Dt} = \frac{\partial}{\partial t} + \frac{u}{r\cos\phi}\frac{\partial}{\partial\lambda} + \frac{v}{r}\frac{\partial}{\partial\phi} + w\frac{\partial}{\partial r}. \tag{2.6}$$

Although these equations 2.1-2.5 must be satisfied by the model, they cannot be solved and instead the equations are advanced forward in time to create an approximate solution at a future time, producing a forecast. The equations are advanced forward in time through the use of a Semi-Lagrangian (SL) scheme. The SL scheme finds the location from which air will arrive at a grid square. The advantage is that air can travel further than a grid square in a time step, allowing a longer time step and allowing it to be run faster (however this has some loss of accuracy when compared to some higher-order Eulerian methods). The continuity equations needs to be re-adjusted after advection leaving imbalances and is the most expensive part of the scheme. SL integration (or advection as it is also known) is used as it combines the regular resolution of a Eulerian scheme with the added stability of a Lagrangian scheme (Staniforth and Cote, 1991) (a Eulerian scheme solves the equations at a set point and advances with time whereas a Lagrangian scheme follows the flow as it advances in time). SL uses different particles at each time-step chosen so that they arrive at the exact location of the points on the regular Cartesian grid (Staniforth and Cote, 1991). A Eulerian form for the continuity equation is used though as it gives mass conservation. The other prognostic variables are in semi-Lagrangian form though, with sufficient stability (Davies *et al.*, 2005).

The five equations are integrated by performing a two time-level semi-implicit semi-Lagrangian advection scheme for the prognostic variables except for density which as previously mentioned undergoes Eulerian scheme to conserve mass. The two time-level semi-implicit semi-Lagrangian scheme is also an off-centred scheme (needed to retain stability) as this can drive the solution to an appropriate simplified model allowing it to adjust to inputs from the physical parametrizations or when data assimilation is used (Cullen, 1999). The semi-implicit semi-Lagrangian method used in the model to find the prognostic variables is described below. For a full and more detailed description of the scheme see UM Documentation Paper Number 15 (Staniforth *et al.*, 2006).

A prognostic equation is written in the form

$$\frac{D\mathbf{V}(\mathbf{x},t)}{Dt} = \mathbf{L}(\mathbf{x},t,\mathbf{V}) + \mathbf{N}(\mathbf{x},t,\mathbf{V}), \tag{2.7}$$

where $\mathbf{x}$ is position, $\mathbf{V}$ is the prognostic variable (m_x, θ, u, v, w) and $\mathbf{L}$ represents terms linear in $\mathbf{V}$, and $\mathbf{N}$ represents terms nonlinear in $\mathbf{V}$. For some of the prognostic variables the right hand side of the equation may be zero. The two time-level semi-implicit semi-Lagrangian scheme when applied to Equation 2.7 gives the following:

$$\frac{\mathbf{V}^{n+1} - \mathbf{V}_d^n}{\Delta t} = \alpha(\mathbf{L}+\mathbf{N})^{n+1} + (1-\alpha)(\mathbf{L}+\mathbf{N})_d^n, \tag{2.8}$$

where n is the time-level, Δt is the time step, and d subscript denotes evaluation at the departure point $\mathbf{x}_d$ and α is a time-weighting coefficient. The equation may be rearranged to form

$$\mathbf{V}^{n+1} - \alpha\Delta t \mathbf{L}^{n+1} = [\mathbf{V} + (1-\alpha)\Delta t(\mathbf{L}+\mathbf{N})]_n^d + \alpha\Delta t \mathbf{N}^{n+1}. \tag{2.9}$$

This equation needs to be solved for each of the prognostic variables. For the MetUM a predictor-corrector scheme is used to do this. In the predictor step, when time-level n+1 terms are needed, time-level n values are used instead in Equation (2.9). These are then replaced in the corrector step by better estimates for these terms. The resulting scheme is written as follows:

$$\mathbf{V}^1 = \mathbf{V}_d^n + (1-\alpha)\Delta t(\mathbf{L}+\mathbf{N})_d^n + \alpha\Delta t(\mathbf{L}+\mathbf{N})^n, \tag{2.10}$$

$$\mathbf{V}^2 - \alpha\Delta t \mathbf{L}^2 = \mathbf{V}^1 + \alpha\Delta t(\mathbf{N}^1 - \mathbf{N}^n - \mathbf{L}^n), \tag{2.11}$$

where the numbered subscripts indicate successive estimates of $\mathbf{V}$. The predictor step is given by Equation (2.10) and the corrector step by Equation (2.11). The resulting equation from combining Equation (2.10) and Equation (2.11) is

$$\mathbf{V}^2 - \alpha\Delta t \mathbf{L}^2 = [\mathbf{V} + (1-\alpha)\Delta t(\mathbf{L}+\mathbf{N})]_d^n + \alpha\Delta t \mathbf{N}^1, \tag{2.12}$$

which gives an approximation to Equation (2.9). The term $\mathbf{V}^2$ is $\mathbf{V}^{n+1}$, the vector at time-level $n+1$. Equation (2.10) and Equation (2.11) are the simplified symbolic repre-

sentation of the semi-implicit semi-Lagrangian scheme applied in the MetUM. To solve for the prognostic variables in the model a three-dimensional, elliptic (Helmholtz) equation, for which the Exner pressure increment is required (as this can be solved and back-substituted to find the other prognostic variables) is given by

$$\Pi' = \Pi^{n+1} - \Pi^n, \tag{2.13}$$

where the primed superscript denotes differences between time-level n values and the latest estimators, for example, $\Pi' = \Pi^2 - \Pi^1$. Equation (2.13) is solved using a generalized conjugate residual (GCR) iterative solver (Eisenstat *et al.*, 1983 ; Smolarkiewicz and Margolin, 1994) with additional appropriate preconditioning. The preconditioning used depends on the configuration of the model. Limited Area Models (LAMs) have a relatively uniform horizontal grid so vertical preconditioning is sufficient whereas Global models have a decrease in grid-spacing towards the poles in a longitudinal direction so an alternating-direction-implicit (ADI) preconditioner is required for the vertical and longitudinal directions (see Skamarock *et al.*, 1997). Once a solution to Equation (2.13) is obtained, back-substitution can be performed in the other equations to retrieve solutions for the other variables.

In the horizontal Arakawa-C grid staggering (Arakawa and Lamb, 1977) is used with a regular latitude-longitude grid whereby pressure is held at the edges of the grid but wind values are held at the centre. This allows for the best geostrophic adjustment properties for atmospheric flows (Davies *et al.*, 2005). Terrain-following coordinates are used in the vertical for the model. This means that near the surface the model follows the contours of the topography to take into account the fact that in reality the air would flow around obstacles such as mountains instead of going through them, which would be the case if the model just had horizontal heights for all vertical levels of the model. The model levels gradually flatten out with height. This terrain-following height is given by the coordinate η. If z is the regular height above sea-level then η is defined to be zero at $z = h(\lambda, \theta)$ where $h(\lambda, \theta)$ is the height of orography above $r = a$ (where a is the Earth's mean radius). $\eta = 1$ at $z = z_T$ where z_T is a fixed height indicating the model lid. For $\eta > 0$ then z is related to η by choice of how the flattening is specified and is given by the following relationship:

$$f(z) = \begin{cases} \eta z_T + h \left(1 - \frac{\eta}{\eta_{flat}}\right)^2 & 0 \leq \eta < \eta_{flat} \\ \\ \eta z_T & \eta_{flat} \leq \eta \leq 1, \end{cases} \tag{2.14}$$

where η_{flat} indicates the height where the terrain following finishes and the coordinate becomes flat. Vertical grid spacing in η has higher resolution (more levels) near the surface to more accurately resolve the boundary layer since vertical gradients and fluxes are large here (Davies *et al.*, 2005). As a consequence the grid spacing is chosen to be irregular (Davies *et al.*, 2005). To give this higher resolution at the boundary layer a quadratic function is used: η at level k is given by $\eta_k = \left(\frac{k}{N}\right)^2$ where N is the total number of vertical levels in the model. Hence layers thicken gradually towards the model top. This places the lid so that it is well above any feature in the model that is important to accurately depict, allowing the top level to be very high without needing lots of levels where they are not needed. Thus the quadratic equation is only used to a certain height; above this height gradual thickening of the layers occurs according to $\eta_{k+1} = \eta_k + \beta(\eta_k - \eta_{k-1})$ where $\beta_k > 1$ is a factor that increases as k increases. Once the values of η and z_T have been chosen Equation (2.14) can be used to find the value of z at every point.

In the vertical Charney-Phillips grid-staggering is used (Charney and Phillips, 1953): potential temperature (θ) and w are held on the same vertical levels known as θ-Levels. u, v, ρ and Π are held on ρ-Levels which are halfway between the θ - Levels. Once the dynamical core has integrated forward a timestep the so-called physics of the model must be run. These are the other processes which occur in the atmosphere on smaller scales which are important to the evolution of the atmosphere but cannot be represented by the dynamics. This is done through the utilisation of parameterisation schemes with the choice of the schemes used dependant on the model configuration. The different model configurations used throughout this thesis will now be discussed before the important parametrizations are described.

2.1.2 Model Configurations

The MetUM can be run at different resolutions by varying the model configuration and changing the parameterisation schemes required or not required. For this study the operational versions of the MetUM are used along with a model configuration developed

by the author for the purpose of the study. The models used are as follows:

- Global Model - 25 km grid-spacing (operational)

- North Atlantic European (NAE) Model - 12 km grid-spacing (operational at the time of study but retired now)

- Euro 4 km Model - 4.4 km grid-spacing (operational)

- UKV Model - 1.5 km grid-spacing (operational)

- France 1.5 km - 1.5 km grid-spacing (developed for this study)

- Met Office Global and Regional Ensemble Prediction System (MOGREPS-G) - 60 km (operational)

For all models the Global model provides the boundary conditions since it is too expensive to use convection-permitting models to provide the boundary conditions. For longer forecast times (for the UKV at the order of one day) the Global model begins to dominate the forecast (Clark *et al.*, 2016). In each of the models no data assimilation is used and hence this is not detailed here. Each of the models therefore relies on down-scaling where forecasts are spun-up from larger-scale model conditions (in this case from the Global model). The spin up from these smooth initial conditions is unphysical but tends to last only a few hours (Clark *et al.*, 2016). The smooth flow given by the boundary conditions spins up as it enters the forecast domain though (Clark *et al.*, 2016). This is one of the main reasons why variable resolution is used for the UKV model at the domain boundary. These model configurations are now described in more detail.

Global Model

At the time of this study the Global model used a 25 km grid-spacing (the Global model is now 10 km resolution operationally; since 2017). The Global model is called a 'coarse-resolution' model, in comparison to convection-permitting resolutions. The large grid-spacing used means that the model requires convection to be parametrized (see Section 2.1.4). In the horizontal it has 1024×769 grid boxes with a spacing of approximately 25 km. It has 70 vertical levels (80 km lid).

MOGREPS-G

MOGREPS-G is the Met Offices global ensemble forecasting configuration. At the time of this study the MOGREPS-G was 60 km grid-spacing which was later reduced to 33 km grid-spacing and is now 20 km grid-spacing. This model is set-up as the Global model just with increased grid-spacing and is used for ensemble forecasts as it is too costly to run at the same resolution as the Global model as 24 members of the ensemble are simulated. It has 70 vertical levels (80 km lid). Ensemble forecasting is described in further detail in Section 2.5.

NAE Model

When this study began the NAE model was an operational MetUM regional 12 km model with a domain covering Europe and the north Atlantic used by the Met Office to create daily weather forecasts. It was later decommissioned though as further advances in resolution occurred in the Global model. For this study NAE operational data is analysed in Chapter 3. The author did not simulate any forecasts using the NAE domain and just analysed NAE analysis files. When NAE data was used in Chapter 3 it was taken from a T+6 operational forecast model. The NAE model uses a rotated latitude-longitude grid with $0.11° \times 0.11°$ horizontal grid boxes ($0.11°$ is equivalent to 12 km at this latitude). The NAE model is too coarse to explicitly represent convection and hence a convection parameterisation scheme is used (see Section 2.1.4). The NAE model has 70 vertical levels.

Euro 4 km Model

This model has a horizontal grid length of 4.4 km with 1100×1000 grid squares and 70 levels in the vertical with a lid at 40 km. It covers much of Europe and extends to the north Atlantic on a rotated latitude-longitude grid. The rotated North Pole latitude is $41°$ and the longitude is $193°$. The first longitude of the grid boxes is $337.0°$ and the first latitude is $-18.7°$ in rotated co-ordinates (Figure 2.1). The grid spacing means that convection can be explicitly represented if it is large enough and lies in the "grey" zone in which smaller showers should still be parametrized as they are too small scale to be

explicitly represented. Since convection partially begins as small clouds that are very small scale in comparison to the resolution of the model, these are unlikely to be re-solved if no convection parametrization is implemented. This can lead the model to develop convection later than expected and cause precipitation to be much larger than expected as it will all occur very quickly developing grid-point storms in some cases. Alternatively though, once convection has developed and is of grid-scale magnitude it is likely that if a convection parametrization is being used that the scheme will remove instability in the model too quickly and result in little to no precipitation developing the model. To try to combat this issue the Euro 4 km model can be run either without any convection parametrization, with regular convection parametrization or, with a convec-tion parametrization that has been formulated for use in the 4.4 km model specifically where the activity of the scheme is reduced. The latter parametrization uses the scheme of Gregory and Rowntree (1990), but can run with a CAPE closure scheme that restricts the cloud-base mass flux to stop the scheme removing instability from the model too early (this is discussed further in Section 2.1.4). For the Euro 4 km model the Global model is used to provide boundary conditions at each forecast hour.

UKV Model

For the UKV model the boundary conditions are obtained from the Global 25 km model. The UKV has 1.5 km grid spacing with 744×928 grid boxes. Although the grid spacing in the interior is 1.5 km the outside boundary of the model varies between 1.5 km and 4 km grid spacing, with 4×1.5km in the east-west and 1.5×4km in the north-south (see Figure 2.2). It has a 1.5 km grid spacing over the UK, which stretches to 4 km at the boundaries, as this variable resolution was found to be beneficial to the forecast (Tang *et al.*, 2013). This is thought to help with the model transition from the 25 km Global boundary conditions to 4 km boundaries and then to the 1.5 km grid spacing of the model. The rotated first latitude of the model is $-5.5932°$, and the first longitude is $353.0525°$. The rotated North Pole latitude is $37.5°$ and longitude $177.5°$. The model has 70 vertical levels with a lid at 40 km. The UKV model is deemed to have a high enough resolution that it does not need a convection parametrization as it can explicitly represent convection. The UKV model is still in the "grey zone" whereby small scale showers cannot be explicitly represented but larger scale showers can. This is not as

severe as the Euro 4.4 km model. It is still unable to resolve small-scale convection as small scale turbulent mixing still cannot be represented but the forecast is better without a convection scheme. Even at 1.5 km grid spacing the model is still unable to represent sub-grid scale turbulent mixing so unrealistic convection develops. As the grid spacing of models drops to 1 km or less a new grey-zone develops related to turbulent mixing. Small turbulent eddies cannot be explicitly represented so a parametrization scheme is required but large scale eddies can be represented (Stein *et al.*, 2015).

France 1.5 km Model

For the France 1.5 km model boundary conditions are taken from the 25 km Global model every hour. The model has 1.5 km grid spacing with 744×928 grid boxes and has uniform grid spacing unlike the UKV. The first rotated latitude is $-7.0°$ and longitude is $355.0°$. The North Pole latitude is $43°$ and longitude is $177.5°$. It has 70 levels in the vertical with a lid at 40 km. The resolution is high enough that the convection parametrization is not required so is switched off in the model runs. The domain of the France 1.5 km model can be seen in Figure 2.3.
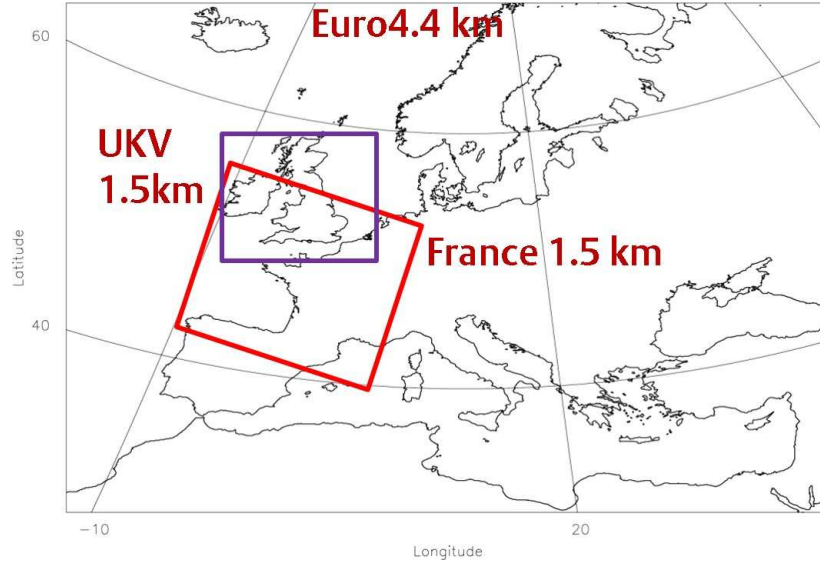

Figure 2.1: Domains of the convection-permitting MetUM simulations. The outside domain is the 4.4 km grid-spacing Euro 4 km model (operational). The purple box indicates the domain of the 1.5 km grid-spacing UKV model (operational). The red box indicates the domain of the 1.5 km grid-spacing France 1.5 km model simulation (non-operational; developed for this study).
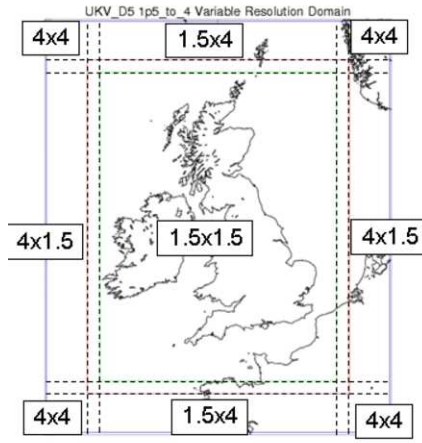
Figure 2.2: Varying grid spacing of the UKV model (Taken from metoffice.gov.uk)
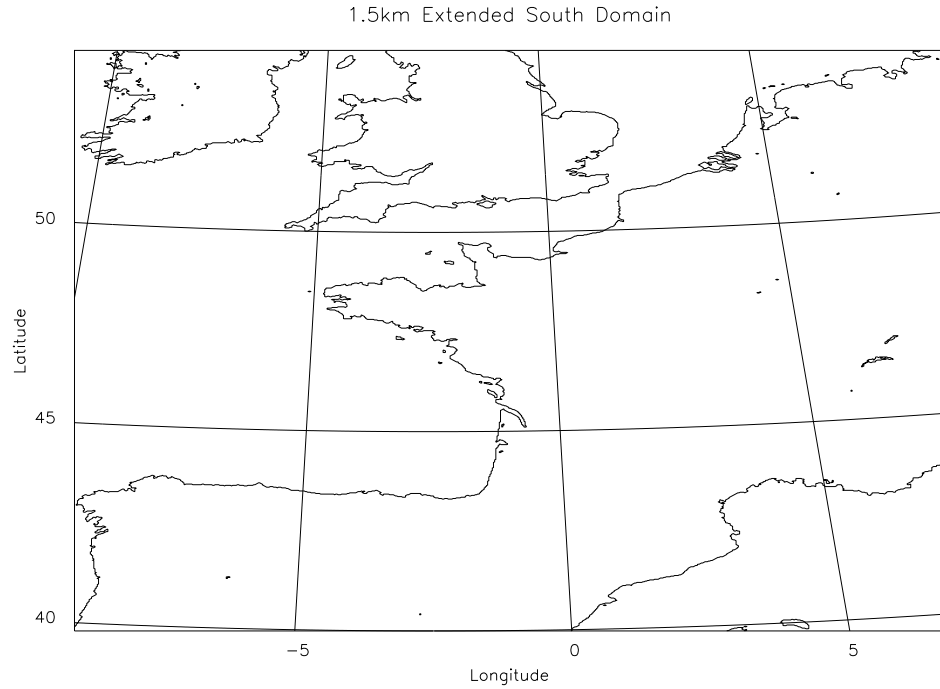
Figure 2.3: Domain of the Extended South MetUM simulation with 1.5 km resolution (France 1.5 km)

2.1.3 MetUM model simulations

For this thesis, five MetUM model configurations have been simulated. These are, a Global 25 km grid-spacing convection parametrizing model, MOGREPS-G 60 km grid-spacing Global model which is convection parametrizing, a European 4.4 km grid-spacing convection parametrizing and permitting model, a UK 1.5 km grid-spacing convection resolving model (UKV) and a 1.5 km grid-spacing model covering France, which is convection resolving (see Figure 2.3 for this domain). From now on this model will be

referred to as the 'France 1.5 km'. The NAE configuration was also used to analyse analysis files and was not simulated. The domains of the Euro 4 km, UKV and France 1.5 km models can be seen in Figure 2.1. The France 1.5 km model domain was chosen by the author in order to capture the area of initiation of the MCS (France), with the other models being standard configurations used operationally at the Met Office. Although, the UKV model is high enough resolution that it can accurately represent the convection involved in MCSs and their initiation, the domain of the UKV does not extend far enough south to capture where most MCSs initiate when they eventually impact the UK. This may impact on the forecast of the MCS as it has been found that the model which provides the boundary conditions for the higher resolution models (UKV model for example) can impact the subsequent forecast. For example, if the Global model providing the boundary conditions for the UKV model does not represent the MCS well because of insufficient resolution then it is likely that it will not be represented accurately in the UKV model. Therefore, it is hoped that extending the higher resolution 1.5 km grid spacing southwards to include the area of initiation of the storms may help to improve the forecast of the MCS and the downstream forecast.

Chapter 3 uses NAE operational model analyses. In Chapter 4 for consistency, the Euro 4 km, UKV and France 1.5 km models were all set-up to use Global start dumps and boundary conditions (every hour). All four of the model configurations were run for 24 hours (Global, Euro 4 km, France 1.5 km and UKV) starting at 00 UTC 5 July 2012 and ending at 00 UTC 6 July 2012. The UKV, Euro 4 km and France 1.5 km are simulated from 03 UTC (T+3) since the Global model is simulated for 24 hours to produce boundary conditions for the convection-permitting models. The convection-permitting models are then simulated from T+3 (to avoid spin up issues) using the boundary conditions and initial conditions produced from the Global model simulation. Chapter 5 and 6 utilise the MOGREPS-G, Global and Euro 4 km models.

2.1.4   Atmospheric Physics - Parameterization schemes

If atmospheric processes occur over smaller length-scales than approximately 4–6 grid lengths of the grid-spacing of the MetUM model in use then the process cannot be explicitly represented by the model and must be parametrized (the process is termed sub-grid scale). Parameterisation of these processes assumes that the overall effect of the process on the resolved scale can be predicted by using a parametrization operating on the large-scale fields in the model (UM basic user guide version 8.2). There are many different parameterisation schemes currently utilised by the MetUM; however, parametrization schemes such as aerosols and river routing, for example, are not required during this study. Only the parameterisation schemes used during this study are discussed below.

Convection Scheme

It is important to simulate convection in Global NWP models as it has an important impact on the large-scale circulation patterns. In limited area models it is important to represent convection to get realistic rainfall and diurnal cycles. Unfortunately though, the convection (except for when very large scale storms occur) is sub-grid scale for coarse resolution models (models which have grid-spacings over a few km's) and so cannot be represented explicitly by the model. It is thus necessary for a convective parameterisation scheme to be implemented to represent the net effect of a group of convective (cumulus) clouds upon the atmosphere using grid-scale parameters to do so (Gregory and Rowntree, 1990). The aim of the parameterisation scheme is to do two things:

- Predict the net convective energy release and hence stabilise the atmosphere appropriately. This is done in terms of large-scale variables that the model can represent and is called the closure problem. The closure is when the chain of events related to the changes occurring are known but the magnitude of those changes are having to be assumed.

- Ensure that in the vertical, the atmospheric structure (together with other physical parametrizations used) and the distribution of the released energy are realistic.

The MetUM uses the mass-flux convection parametrization scheme of Gregory and Rowntree (1990) with some additions. A brief overview of the convection scheme is

given here. For a full description of the scheme see UM Documentation Paper 27 (Stratton *et al.*, 2012). The convective parameterisation scheme diagnoses shallow, deep and mid-level convection. These are defined as follows by Stratton *et al.* (2012):

- Shallow: Convection (resolved-scale vertical velocity) starting in the boundary layer (below 850 hPa) and stopping below the freezing level or below an inversion (with only weak large-scale ascent above or descent).

- Deep: Convection beginning in the boundary layer, but continuing on into the free troposphere (i.e. not shallow convection), meaning that the cloud depth is large.

- Mid-Level: Convection that starts above the boundary layer or above shallow or deep convection.

The convection scheme works in three stages:

1. Diagnosis of the convection to determine if convection is possible from the boundary layer and if so, also diagnosing if convection is deep or shallow. This is fed back to the boundary layer scheme then convection is developed.

2. A call to mass flux scheme. Either the deep or shallow scheme depending on whether deep or shallow convection is diagnosed in stage 1.

3. A call to the mid-level convection scheme for grid points where instability occurs that starts either above the boundary layer top or above the level of shallow or deep convection.

Once the model has determined that convection is possible, it then must diagnose if the convection is shallow or deep thus must first work out if there is an unstable layer near the surface. To do this the surface buoyancy flux, the lifting condensation level (LCL) and the level parcel ascent are calculated. This helps to diagnose if there is an unstable layer and, if there is, what levels the parcel of air would lift to before condensing to form cloud and would stop ascending (to determine if the convection is shallow or deep). The convective available potential energy (CAPE) of the parcel is also calculated as part of the parcel ascent diagnosis. If the top of the parcel ascent is greater than or equal to 3000 m the ascent is assumed to be deep cumulus. If a cumulus capped boundary layer is diagnosed then further tests are done to determine whether the convection is shallow or deep.

A mass-flux approximation (Swann, 2001) is used to parametrize convection. This approximation depends on the convection (either upwards or downwards) being over a small area relative to the size of the grid square whilst the vertical velocities associated with the convection are large relative to large-scale vertical velocity (and that mass flux associated with convection is in equilibrium with the larger scale). A bulk cloud model is used to produce a model for the mass flux and the magnitude of the up and downdraughts in the convective plumes. The bulk cloud model is named 'bulk' because it relies on the use of an ensemble of convective cloud models with different characteristics to produce an approximation of the bulk of the characteristics of the convective plumes. This applies for all types of convection whether it be shallow, mid-level or deep. The bulk characteristics include effects of entrainment of environmental air, detrainment of cloudy air through turbulent mixing at the edge of cloud, forced detrainment as the cloud ascends (used to only occur at cloud top, but adapted forced detrainment was added to the model and so now this can occur lower in the ascent). The bulk cloud model also takes into account transport of momentum and tracers by the updraughts. Both the up and downdraughts effect the environment through entrainment and detrainment of heat, moisture and cloud liquid water.

In the convection scheme, precipitation initiates when condensed water is over a certain value (in the past it also used to take account of cloud depth and whether the cloud was over land and sea, to take account of the differences in aerosols, as it impacts the cloud condensation nuclei number impacting the formation of precipitation however; the model now includes a distribution of aerosols so this adjustment has been dropped). Precipitation created by the updraughts is assumed to have a portion that falls through the downdraughts where it undergoes evaporation and sublimation. The rest of the precipitation falls through cloudy air and undergoes evaporation and sublimation when it falls below cloud level. The parametrization used for evaporation and sublimation is described fully in Gregory (1995); however, the downdraughts are assumed saturated and maintaining negative buoyancy through the evaporation and sublimation process.

The cloud models differ depending on the type of convection that has been diagnosed and the main difference is the closure scheme used to define the cloud-base mass flux (assumed to be in equilibrium, no life cycle). A CAPE closure scheme (described in Fritsch and Chappell, 1980) is used for deep and mid-level convection. This scheme

is based upon CAPE being reduced to zero over a given timescale. Originally when the CAPE closure scheme was developed, a single CAPE timescale was required. Now the CAPE timescale must be longer than the convection time step to maintain stability of the model.

There are variations to the CAPE closure scheme. The most commonly used is the vertical velocity based CAPE closure in which a threshold vertical velocity is defined and is dependent on the model resolution in the horizontal and vertical and the time-step. Higher resolution models can support higher vertical velocity thresholds. Maximum large-scale vertical velocity is evaluated before convection and, if this value exceeds the threshold vertical velocity, then the CAPE timescale is reduced, but it must still be greater than or equal to the convection model time step. If the CAPE timescale is shorter then it means that convective instability is removed more quickly so convection will stop sooner. The second variation to the CAPE closure scheme is the relative humidity based CAPE closure. If the mean relative humidity in the convective layer is greater than 60%, then the CAPE timescale is reduced.

For shallow convection different entrainment and detrainment rates are used (described in Grant and Brown (1999)). For shallow convection a closure scheme described by Grant (2001) is implemented. This scheme has cloud base mass flux proportional to the sub-cloud convective velocity scale.

Convective cloud is created in the convection scheme by the use of an anvil scheme (Gregory, 1999). This scheme changes the height of the anvil in the vertical to account for radiative effects of convective anvils. This anvil scheme is only applied when deep convection is specified by the model. The anvil base is defined as the freezing level. The convective cloud for radiation scheme (CCRad) allows for the occurrence of multiple clouds in a model grid square. For CCRad the anvil scheme is applied to each of the contiguous clouds in the vertical profile allowing for the representation of the effect of multiple clouds occurring over the same vertical area e.g., where mid-level convection occurs over deep or shallow convection.

The mass-flux approximation breaks down as resolution of the model increases because the area of the deep convective plumes may now become large in comparison to the size of the grid box. When the grid spacing gets as fine as 1–2 km the convection may fill a whole grid square and can be resolved by the model (or at least partially), so

the parametrization scheme for convection may no longer be required. However, for a 4 km grid spacing the convective parametrization scheme is still required. This scheme however has a different closure for mid-level and deep convection. This closure scheme is called the grid-box area scaled CAPE closure (Roberts, 2003). The closure scheme essentially restricts the cloud-base mass flux. The cloud-base mass flux would normally get bigger for higher CAPE but this is restricted in this case. This allows for a partial representation of the convection allowing the rest to be represented on the grid. This closure scheme allows the model to produce convection explicitly when showers are large enough to be resolved, but then allows the convection scheme to represent the effects of weaker convection where the showers would be small and not resolved by the model (so would be missed altogether without a convection scheme). If the convection scheme is turned off in the 4 km model then it often creates too few but too intense precipitation cells and tends to initialise precipitation late (Lean *et al.*, 2008). If the regular CAPE closure scheme is used in the 4 km model then it can cause the instability to be removed too quickly and then no precipitation may develop or it may be severely underdeveloped. This can also cause large horizontal gradients in humidity and or temperature which can feedback on the large-scale dynamics. Thus, the grid-box closure scheme was developed which allows for longer CAPE timescales so that the instability is not removed too quickly. A downside is that initiation can be delayed even more on some occasion (Lean *et al.*, 2008).

Boundary Layer

The MetUM uses the boundary-layer scheme of Lock *et al.* (2000). The purpose of the scheme is to parametrize sub-grid scale vertical turbulent transports of heat, moisture and horizontal momentum. For a full description of the scheme see Lock and Edwards (2012). For conserved scalar variables χ, the rate of change of the vertical contributions of turbulence and from other processes other than boundary layer turbulence (given the term **S**) can be expressed as

$$\frac{d\partial \chi}{\partial t} = -\frac{1}{r^2 \rho} \frac{\partial}{\partial z} \left(r^2 \rho \overline{w' \chi'} \right) + \mathbf{S}, \tag{2.15}$$

where $\overline{w'\chi'}$ is the vertical turbulent fluxes to be parametrized. The primes indicate turbulent fluctuations and the overbar indicates the mean of an ensemble of gridboxes. The rate of change of the vertical contributions of turbulence (and other processes given the term **S**) must also be computed for the horizontal momentum (u and v wind components) by the following:

$$\frac{d\partial \mathbf{u}}{\partial t} = \frac{1}{r^2\rho}\frac{d}{dz}(r^2\tau) + \mathbf{S}, \tag{2.16}$$

where τ is the vertical turbulent flux to be parametrized. The scalar variables χ that are approximately conserved under moist adiabatic ascent are given by

$$\theta_l = T - \frac{L_v}{c_p}q_l - \frac{L_s}{c_p}q_f + \frac{g}{c_p}z, \tag{2.17}$$

$$q_t = q_v + q_l + q_f, \tag{2.18}$$

where T is temperature, q_v, q_l and q_f are the vapour (specific humidity), liquid and ice (frozen) water contents respectively, $L_s = L + L_f$ is the latent heat of sublimation, and L_f is the latent heat of freezing. A first order closure is used to parametrize the turbulent fluxes. This closure is given by

$$\overline{w'\chi'} = -K_h\frac{d\chi}{dz} + K_h^{surf}\gamma_\chi, \tag{2.19}$$

$$\tau = K_m\frac{d\mathbf{u}}{dz} + \tau^{nl}, \tag{2.20}$$

where K_h is the eddy diffusivity for scalar variables χ and K_m is the eddy diffusivity for momentum. $K_h^{surf}\gamma_\chi$ represents a non-local flux in an unstable boundary layer, is only non-zero when $\chi = \theta_l$ and is only applied for transport arising from surface driven turbulence (K_h^{surf}). Equations 2.19 and 2.20 then become a parametrization problem of determining what K_m, K_h, τ^{nl} and γ_χ are. To do this the first step is to determine the boundary-layer type which is dependent on the stability of the parcel of air and whether or not cumulus cloud is present. Currently there are seven classifications used:

1. Stable boundary-layer (with or without cloud),

2. Stratocumulus over a stable boundary layer (a decoupled stratocumulus layer),

3. Well mixed boundary-layer which may be cloud topped,

4. Unstable boundary-layer (well mixed) with a decoupled stratocumulus layer not over cumulus,

5. Boundary-layer with decoupled stratocumulus over cumulus,

6. Cumulus capped boundary-layer,

7. An additional boundary layer option is: shear dominated unstable boundary-layer (wind shear may allow for deeper turbulent mixing in the unstable boundary-layer).

The eddy diffusivities are calculated at each level for the local and non-local mixing, given by the terms K_χ^L and K_χ^{NL}, respectively. For the local mixing a first-order mixing-length closure scheme is computed.

$$K_m = L_m^2(S + S_d)f_m(Ri),\tag{2.21}$$

$$K_h = L_h L_m(S + S_d)f_h(Ri),\tag{2.22}$$

where L_m and L_h are the neutral mixing lengths for momentum and scalar variable respectively and S is the resolved vertical shear of the horizontal wind components given by $S = |\frac{d\mathbf{u}}{dz}|$. Wind shear generated by drainage flows in complex terrains can also be included and is given by S_d (not described here). Ri is the Richardson number: Ri is < 0 for unstable boundary layers and Ri is > 0 for stable boundary layers. f_m and f_h are stability functions dependant on the local Richardson number for momentum and scalar variables. For non-local mixing it only occurs in unstable environments and is called non-local because it is not dependent on any local properties of the mean profile at that height, but only on the magnitude of the turbulence forcing at that height. Non-local turbulence consists of two processes: surface-driven turbulence (surface heating) and cloud-top driven turbulence (from radiative or evaporative cooling at the top of the stratocumulus cloud). These two processes are represented using eddy diffusivity terms: K_χ^{surf} and K_χ^{Strato}, where χ is the momentum and scalar variable combined. These terms are given different vertical representations depending on the boundary-layer profile type. The total non-local eddy diffusivity then becomes

$$K_\chi^{NL} = K_\chi^{surf} + K_\chi^{strato}.\tag{2.23}$$

This means that the overall eddy diffusivity calculated for both the local and non-local mixing is as follows:

$$K_\chi = max[K_\chi^{surf} + K_\chi^{strato}, K_\chi(Ri)], \qquad (2.24)$$

suggesting that under stable boundary layers, where only local mixing occurs, the mixing is only related to the Richardson number. At the top of the boundary layer entrainment fluxes are parametrized to ensure entrainment mixing is included; this scheme follows Lock (2001). Above the boundary-layer top only local mixing occurs so $K_\chi^{NL} = 0$ and the mixing is related to the Richardson number only. In the decoupled stratocumulus layer $K_\chi^{NL} = K_\chi^{strato}$ as $K_\chi^{surf} = 0$. The model's convection scheme performs the mixing in layers where cumulus convection is diagnosed because K_χ is then set to zero. This only occurs for models where a convection scheme is active though and not for models which are of high enough resolution that convection can be explicitly resolved (so no convection scheme is used), or if the convection scheme is switched off (as can be considered for the 4 km resolution models).

Microphysics - Precipitation

The microphysics scheme, or precipitation scheme as it is also known, is used to model the significant atmospheric microphysical processes resulting from the downward transfer of water in the atmosphere (precipitation) and the associated phase changes between water vapour, liquid water and ice water, for example, by condensation, evaporation, sublimation, ice crystal growth and droplet collection. The scheme is based on the mixed-phase precipitation scheme of Wilson and Ballard (1999). A full description of the scheme is found in UM Documentation Paper 26 (Wilkinson, 2012). Water is split into four variables: water vapour, liquid water droplets, rain and ice. Ice is split into three types. These three types are large-ice category (aggregates), small-ice category (crystals) and graupel (precipitation that forms when supercooled droplets freeze onto falling snowflakes, also known as soft hail). The model has the option to treat both large and small ice variables as prognostic variables and either treat them separately and then recombine them or treat them both separately in the model. The latter option was not used in the model runs in this thesis. The model also allows the graupel to be used as an additional prognostic treatment for ice. Graupel was included in the model runs for

the Euro 4 km, UKV and France 1.5 km but not in the Global model as graupel should only form in clouds with high enough vertical velocities which the Global model cannot produce. This is because the option of more detailed microphysical calculations is intended for high resolution models only. The large-scale precipitation scheme works by splitting the model into columns. Within each model column the scheme calculates the transfer of moisture between each of the vapour, liquid, ice and rain categories through modelling the microphysical processes that take place in the atmosphere resulting in the transport of water downwards, meaning that the scheme works from the top down. All of the model runs in this thesis utilise the 3D version of the Wilson and Ballard (1999) scheme since the 3B version was retired as of Version 7.7 of the UM and thus is not detailed here. In the 3D scheme, for the four phases of water (vapour, liquid, ice and rain) the following microphysical processes are represented, leading to changes in the mixing ratio of any of the phases of water within a grid box:

1. The fall of ice and rain under gravity (also known as sedimentation),

2. Heterogeneous and homogeneous nucleation of ice,

3. Deposition and sublimation of ice,

4. The collection of ice particles by other ice particles (aggregation),

5. Collection of cloud droplets by ice (riming),

6. Falling ice particles collect rain to produce more ice content,

7. Melting of ice particles,

8. Evaporation of rain,

9. Collection of cloud droplets by rain droplets (accretion),

10. Cloud water converted into rain to produce rain and drizzle (autoconversion).

This is not a complete list of microphysical processes that take place in reality, but the neglected processes are deemed less important than the ones mentioned and thus are not represented by the model to save computational power and expense. Condensation and evaporation of cloud droplets are also not represented in this scheme, but instead are represented by the cloud scheme.

In the Global model rain is treated as either a diagnostic or prognostic variable. The diagnostic case represents the flux of rain (or the rain rate) in each model level. For the diagnostic treatment of rain there is no advection of rain horizontally in the model so any rain that occurs only falls between levels in a column. Additionally, any rain generated by the model must reach the surface in one time-step; it is assumed that all rain will have fallen to the surface as no rain is retained between time-steps by the model. For the Global model used in this thesis and in higher resolution models (Euro 4 km, UKV, France 1.5 km) the rain is treated as a prognostic variable and is represented by the mixing ratio of rain. The difference is that advection occurs to represent the downwards movement of rain in the column and is thus more costly to compute. Although it is costly this representation has the benefit of being able to advect rainfall across horizontal grid boxes as it falls which could be advantageous for storms which remain stationary for periods of time or the interaction of the rainfall with the updraughts or downdraughts is important. Additionally, it allows evaporation or formation of cold pools in shear. The prognostic approach is also known to delay the onset of rainfall in the model (takes time to fall) as the dynamics may not respond instantly.

The size of the particles of each water phase is given by $N_p(D)$, where D is the particle diameter and subscript p represents either rain, aggregates, ice crystals and graupel. D is defined by a gamma function

$$N_p(D) = N_{0P}D^{\alpha_p}e^{-\lambda_p D}, \tag{2.25}$$

where N_{0P} is the intercept parameter, λp is the slope parameter and α_p is the shape parameter. The intercept parameter is assumed to be constant and to be a simple function of λ given by

$$N_{0p} = N_{ap}\lambda_p^{N_{bp}}, \tag{2.26}$$

where N_{ap}, N_{bp} and α_p are constants for the large-scale precipitation scheme. The slope parameter is calculated from the mixing ratio (for the prognostic variables) and the diagnostic flux of rain.

Rain is assumed to be spherical and with density equal to liquid water 1000 kgm^{-3}. Graupel is assumed to be spherical with a density of 500 kgm^{-3}. For ice species the

density is assumed to be found through a relation of the mass to the diameter:

$$M_p(D) = a_p D^{b_x}. \tag{2.27}$$

To solve for microphysical transfer rates, the particle size distribution must be inferred from the mixing ratios and fluxes. The rain fall velocity of the model is represented differently depending on whether diagnostic or prognostic rain is used in the model. For diagnostic rainfall all the rain is assumed to fall out in one time step, unrelated to droplet size so changing the fall speed has limited impact. The code examines the difference in fall velocity between the Sachinananda and Zrnic (1986) and Abel and Shipway (2007) relations, with the ratio of the two velocities found being used to enhance the evaporation rate. This is so that light drizzle is evaporated more quickly while heavier rain rates are unaffected. For prognostic rainfall, the Abel and Shipway (2007) fall velocity is used throughout to determine how long the rain remains in each layer so allowing it to remain in the column longer before evaporation.

Cloud droplets are not allowed to settle over more than one vertical grid box at each timestep. No assumption of cloud fraction is used, but the scheme assumes that there is uniform settling of cloud droplets settling into the grid box below.

The precipitation scheme divides the grid boxes into eight regions. These regions represent all the combinations of the presence or absence of ice, cloud liquid water, and rain. This is because there are $2^3 = 8$ options available because each of the three phases (ice, cloud and liquid water, either present or absent) has two options. To determine the size of these eight regions the scheme uses the cloud volume fractions for ice (C_i), liquid cloud fraction (C_l) and the rain fraction along with how all three overlap. The microphysics scheme uses information on C_i, C_l and the total cloud fraction, C, taken from the cloud scheme. Using this information it is then possible to determine their overlap:

$$C_{mixed phase} = C_i + C_l - C \tag{2.28}$$

The cloud scheme assumes there is minimum overlap between cloud ice and cloud water. The microphysics scheme then calculates the rain fraction and its overlap with the cloud ice, liquid and mixed phase.

Radiation

Radiative transfer is an important process in the atmosphere and thus needs modelling in a forecast. The sun emits short-wave radiation and the Earth and atmosphere emit long-wave radiation. Short- and long-wave radiation need modelling separately. A brief description of the radiation scheme used in the MetUM will be given below, however, for a full description of the radiation code the reader is directed to UM Documentation Paper 23 (Edwards, 1996; Edwards and Slingo, 1996). For the short-wave radiation the calculation begins by determining the amount of short wave radiation which reaches the top of the atmosphere. Scattering is very important for short-wave (solar) radiation whether by Rayleigh scattering by molecules or scattering by aerosols, water droplets and ice crystals. Reflection from the surface is also important. For long-wave (terrestrial) radiation, radiation is emitted from the surface and the atmosphere. The radiation code is used to calculate the radiative fluxes in order to find heating rates and other related quantities. A two-stream approximation is used where fluxes in the vertical (upwards and downwards directions) are considered. The fluxes of short-wave and long-wave radiation for each of the grid-boxes are represented as the sum of the upward and downwards diffuse fluxes plus a direct flux from the solar (short-wave) radiation.

The frequency ranges of the short- and long-wave radiation are split into spectral bands and are treated as having properties that are independent of frequency except for the gaseous mass absorption coefficient. The total flux is then the summation of the fluxes from each of the distinct spectral bands. The flux in each band is found by dividing the spectral bands into quasi-monochromatic regions, each with a constant gaseous absorption coefficient. For each of the quasi-monochromatic regions the fluxes are calculated taking into account gaseous absorption and continuum absorption. The scheme also takes into account absorption and scattering by aerosols, ice crystals and water droplets and Rayleigh scattering. The radiation scheme is very expensive to run and thus is not performed at every time step in the model and is often split into prognostic and diagnostic radiation timesteps. When a prognostic timestep occurs full radiation calculations are computed. Diagnostic radiation calculations are used when further calls to the scheme are required. Due to the expense of the radiation scheme, approximate scattering in the long-wave region can be used as the scattering occurring here is not as important as in the short-wave region. Spectral degradation can also be implemented

where short- and long- wave radiation calculations are only computed at every other grid point with interpolation used to determine the short- and long-wave radiation at the grid points where radiation calculation did not occur. On the next time-step, the points for which interpolation occurred in the previous time step will now have a full radiation calculation, whereas, the points from the previous time step, where the full calculation occurred will now have interpolation performed. This approach tends to be implemented for higher resolution models. For the radiation scheme the heating rates at each level and the net fluxes at the surface are used to advance the rest of the model, with the heating rates being calculated using the net flux at the surface.

Cloud Scheme

The main purpose of the cloud scheme is to calculate the amount of condensation at each time-step (from water vapour to liquid water or vice versa) and to calculate or update the cloud fractions for use in the radiation, large-scale precipitation or other physics schemes. There are two cloud schemes. A diagnostic scheme of Smith (1990) and a prognostic scheme introduced by Gregory *et al.* (2002) known as PC2 (prognostic cloud fraction and condensate). The PC2 scheme is not used in the models run during this study so will not be described here. Full details of these schemes can be found in UM Documentation Paper 29 (Wilson and Morcrette, 2011).

Cloud fields are determined by the distribution of water, temperature and pressure within the model grid box. The diagnostic scheme deals with the condensation and evaporation of cloud liquid water associated with changes within the grid-box in relative humidity. Where locally water vapour content exceeds saturation content condensation will occur. Evaporation of any liquid water droplets occurs if the vapour content is less than saturation. Due to fluctuations in moisture and temperature within the grid box, mean water vapour content does not need to exceed the saturation specific humidity to produce cloud somewhere in the grid box. Cloud liquid water may be parametrized by finding the fluctuations in the moisture and temperature within the grid boxes, as knowledge of the combined liquid and vapour content can be used to find vapour and liquid contents and liquid cloud fractions. Since these variables are unchanged during the condensation process it is useful to write the cloud scheme in terms of these variables.

Considering only liquid condensate we can write, assuming that when a cloud becomes supersaturated it removes the excess water content, that

$$q_{cl} = q_T - q_{sat}(T, P),$$

(2.29)

assuming $q_T > q_{sat}(T, p)$. q_T is the local total water content, which is equal to the sum of the condensate, cloud liquid water content (q_{cl}) and the water vapour content (q_v, specific humidity), T is the temperature, p is the pressure and $q_{sat}(T, p)$ is the saturation specific humidity at temperature T and pressure p with respect to liquid water. Temperature can be written in terms of liquid water T_L to give

$$T_L = T - \frac{L}{c_p} q_{cl},$$

(2.30)

where L is the latent heat of vaporization and c_p is the heat capacity of air. T_L is not dependant on changes in phase between vapour and liquid. Taylor expansion can be used to expand $q_{sat}(T)$ about $q_{sat}(T_L)$ to give

$$q_{cl} = a_L(q_T - q_{sat}(T_L, p)),$$

(2.31)

where a_L is given by

$$a_L = \left(1 + \alpha \frac{L}{c_p}\right)^{-1},$$

(2.32)

and where $\alpha = \frac{dq_{sat}}{dt}$ at constant pressure. Thus local total water content (q_{cl}) has been rewritten in terms of conserved variables q_T and T_L as they are conserved during condensation and evaporation. Equation (2.31) can now be written in terms of gridbox mean and variation from gridbox mean:

$$q_{cl} = a_L\left(\overline{q_T} - \overline{q_{sat}(T_L, p)} + q_T' - q_{sat}(T_L, p)'\right),$$

(2.33)

where overbars indicate the grid box mean and primes indicate fluctuations from these means. Since we have assumed that α and a_L are independent of temperature and that the rate of change of q_{sat} is independent of pressure we can write Equation (2.33) as

$$q_{cl} = a_L\left(\overline{q_T} - q_{sat}(\overline{T_L}, \overline{p})\right) + a_L\left(q_T' - \alpha T_L' - \beta p'\right),$$

(2.34)

where $\beta = \frac{dq_{sat}}{dp}$ at constant temperature. Equation (2.34) can be written as

$$q_{cl} = Q_c + s, \tag{2.35}$$

where $Q_c = a_L(\overline{q_T} - q_{sat}(\overline{T_L}, \overline{p}))$ and is related to the mean properties of the gridbox and $s = a_L(q_T' - \alpha T_L' - \beta p')$ and is related to deviation of the local conditions from the mean. To find an expression for the cloud fraction volume C within the gridbox we use the assumption that cloud water content must be greater than zero (where $s > -Q_c$). Therefore if we integrate over the area $s > -Q_c$ within any particular gridbox for s then we produce a function such as

$$C = \int_{s=-Q_c}^{\infty} Grid(s)ds, \tag{2.36}$$

with the expression for mean condensate being

$$\overline{q_{cl}} = \int s = -Q_c^{\infty}(Q_c + s)Grid(s)ds. \tag{2.37}$$

If we can parametrize $Grid(s)$ then we can find a solution for C and $\overline{q_{cl}}$ (find the liquid cloud fraction and the condensation required for the large-scale cloud scheme) without needing to find the distribution of individual variables q_T, p, T_L since the distribution is in terms of s. This parametrization is done using Smith (1990) (and the PC2 scheme which is not described here). The Smith scheme parametrizes the $Grid(s)$ distribution by using a symmetric triangular probability density function (PDF) of s. As s represents the deviations from the gridbox mean, and the PDF must be normalised, the PDF must satisfy $\int_{s=-\infty}^{\infty} sGrid(s)ds = 0$ and $\int_{s=-\infty}^{\infty} Grid(s)ds = 1$. This means that only the width of the triangle is needed to close the symmetric triangular PDF. The half-width of the distribution is given by the term b_s (the distance in s space from where $Grid(s) = 0$ to $s = 0$). b_s is defined so that the condensation in the grid-box occurs when the gridbox relative humidity (RH) equals a specified critical value of relative humidity termed RH_{crit}:

$$b_s = a_L q_{sat}(\overline{T_L})(1 - RH_{crit}), \tag{2.38}$$

with $RH_{crit} < 1$ being the critical relative humidity value. This is the value for which saturation first occurs and is the grid-box mean humidity. The whole grid box does not

need to be saturated for cloud formations to occur on scales smaller than the grid-box (subgrid scale). Since α depends on T, iteration must be used to find new values of α. A weighted average is used to speed up convergence. Estimates of a_L, b_s, q_{cl}, T all follow on from the new approximations of α at all computations. New gridbox mean temperature and specific humidity can also be computed. The value of RH_{crit} varies with model resolution (being larger typically for finer resolution models to give an all or nothing cloud fraction appropriate for when updraughts fill grid squares) and also varies with vertical height in the model. The value of RH_{crit} decreases with height as the volume between each layer increases due to the increase in vertical grid spacing thanks to the terrain following coordinate height.

The grid box volume which contains liquid cloud can easily be found by integrating the PDF of s. Ice cloud must be treated using the prognostic ice microphysics scheme of Wilson and Ballard (1999). Although this scheme makes ice content prognostic it still requires a parametrization of ice cloud from the large-scale cloud scheme. Ice cloud fraction may vary dependant on cloud depth. The ice cloud and liquid cloud are then combined to give a total cloud volume fraction. The clouds are assumed to be uniformly distributed in the vertical within a grid-box, but not in the horizontal, and RH_{crit} values are chosen for each grid-box. The area cloud fraction is calculated by dividing each grid-box into three layers. The cloud volume calculations are computed for an array of $3x3$ gridboxes at a time as it is assumed that relating these grid boxes for variability and moisture in the horizontal can be used to determine the variability within the grid-box. The maximum value of these nine cloud fractions are used after determining if any outliers exist.

2.2   NDdiag

Throughout this study the NDdiag (New Dynamics Diagnostics) FORTRAN program is used to calculate several diagnostics from MetUM output (Panagi and Dicks, 1997). The diagnostics are computed on pressure levels after interpolating from model levels used in the model run. Diagnostics can be computed for any horizontal or vertical resolution, for data on a spherical grid. These computed diagnostic variables are then viewed using JPLOT (Panagi and Dicks, 1997) to be able to plot the data and produce figures that are

used throughout this study. NDdiag requires the following basic prognostic variables from the Unified Model to calculate other variables:

- Surface Pressure

- Orography

- Temperature

- Wind in the u direction

- Wind in the v direction

- Rate of change of pressure

- Specific humidity

The variables are held on model levels that are terrain following near the surface and become pure height levels higher up. Met-Office specific model output is created called "pp-format".

2.2.1   Potential Vorticity

As discussed previously in Chapter 1, PV is an important atmospheric variable in relations to MCSs as PV anomalies form when diabatic heating occurs. Due to the importance of PV anomalies in MCSs this variable was analysed extensively throughout the remaining Chapters of the thesis and was calculated using NDdiag. Potential Vorticity is defined by Holton (1992) as

$$PV = \frac{1}{\rho} \zeta \cdot \nabla \theta. \tag{2.39}$$

To calculate PV using NDdiag the potential temperature (θ) and absolute vorticity (ζ) are required. Since NDdiag computes diagnostics on pressure levels the PV equation becomes

$$PV = -g \left[-\frac{1}{a \cos \phi} \frac{dv}{dp} \frac{d\theta}{d\lambda} + \frac{1}{a} \frac{du}{dp} \frac{d\theta}{d\phi} + \frac{d\theta}{dp} \zeta \right] \tag{2.40}$$

2.2.2 Convective Available Potential Energy (CAPE) and Convective Inhibition (CIN)

As discussed in Chapter 1, MCSs are associated with large amounts of CAPE developing. CAPE can be calculated using NDdiag along with CIN. CAPE and CIN are calculated as lifting from the surface (1000 hPa) in 50 hPa intervals for every hour of the model run. CAPE is calculated using a pseudo-adiabatic ascent (Emanuel, 1994)

$$CAPE = \int_{p_{nb}}^{p_{lift}} R(T_p - T_a)d(lnp), \tag{2.41}$$

where p_{nb} is the pressure at the level of neutral buoyancy where the parcel of air would stop rising; p_{lift} is the level the air parcel is lifted from, which for this study was 1000 hPa. T_p and T_a are the parcel and ambient temperatures, respectively, and p is the pressure.

CIN is calculated by NDdiag as follows:

$$CIN = \int_{P_{LFC}}^{P_{lift}} R(T_p - T_a)d(lnp), \tag{2.42}$$

where P_{LFC} is the level that free convection takes place.

2.3 Coarse Graining and averaging

Coarse Graining is a method implemented in Chapters 4, 5 and 6 of this study. Coarse graining means to take high resolution model output and average it to a lower resolution grid. The purpose of it is to make the output from all models the same resolution (by statistically averaging model data) to be able to directly compare the output from all the models with each other. For this study the lower resolution grid averaged onto to make a direct comparison between all the models in Chapter 4 is 100 km grid spacing. A 100 km grid spacing is utilised as this is large enough grid spacing (coarse enough) to smooth out the global model data when averaged, but is not so large (coarse) that the data became over smoothed (this happened when a trial of 150 km was done). The coarse graining was implemented by using a series of IDL scripts. In order to do this a number of steps are required:

1. A higher resolution global land-sea mask file is required (higher resolution than

      the resolution of the finer model whose data is being coarse grained).

2. This mask file is a very large file so a domain subsection is required to continue with the process. This subsection must be larger than that of the domain of the higher resolution model that is to be coarse grained.

3. The relevant fields from the high resolution model data must then be re-gridded onto this higher resolution global subsection land-sea mask created.

4. The Global model data must be coarse grained onto a lower resolution grid (in this case 100 km grid spacing) so that it can be compared to the coarse-grained higher resolution data. To do this a 100 km grid spacing land mask file must be produced which will be the final coarse-grained grid.

5. Average the high-resolution fields (from step 3) onto the 100 km grid.

6. The same process can be completed for the Euro 4 km, UKV and France 1.5 km data once it has been re-gridded on the high resolution global land mask to average it onto the 100 km global coarse-grained grid.

7. Once all the models have been averaged onto the same 100 km Global coarse-grained grid they can then be compared.

For this study a comparison of the higher resolution models to the Global model is performed in Chapter 4, so the differences between the coarse-grained Euro 4 km, UKV or France 1.5 km and the coarse-grained Global model are calculated. It must be noted that only one variable at a time can be coarse grained using the IDL scripts. In Chapter 5 and 6 the difference between the coarse-grained variables of the Euro 4 km model (coarse grained to 25 km grid spacing) and the Global model (the original 25 km grid-spacing not the coarse grained Global model) are combined into a single file, called an IAU file, to create an MCS perturbation file that could be added to the MetUM Global simulations.

2.4   MetUM - Incremental analysis update file

In Chapter 5 and 6 MCS perturbations are calculated from the difference between Euro 4 km variables coarse-grained to 25 km grid-spacing and the Global variables which are 25 km grid-spacing. The variables used are the zonal (u) and meridional (v) components

of wind, and θ. Using these three variables a so called perturbation file is created. The MCS perturbation file is a UM fields file (also known as an ancillary file) and forms what is known as an IAU file (Incremental analysis update file) which can be added to a MetUM simulation. For the purpose of this research Global model simulations are run for five days starting at 18 UTC 5 July 2012 with and without the inclusion of IAU perturbation files (MCS perturbations) and the difference between the two forecasts produced is analysed in Chapter 5 and 6. The IAU scheme is described briefly below, for a more detailed description see UM documentation paper No.31 (Clayton, 2012).

The IAU scheme allows increments to be added gradually over a series of timesteps with the fraction added at each timestep being determined by a (discrete) IAU weighting function $g(t)$ (Bloom *et al.*, 1996). The gradual insertion is to prevent some of the spurious noise that would otherwise be created. The following is a summary of the mathematics involved in the IAU scheme and is taken from Clayton (2012). Suppose the IAU insertion period starts at time $t_{-N} = -N\Delta t$ and ends at $t_N = -N\Delta t$, where Δt is the model timestep. During this time the evolution of the background state $\mathbf{x}^b$ is given by

$$\mathbf{x}^b_{j+1} = M_j[\mathbf{x}^b_j], \tag{2.43}$$

where $\mathbf{x}^b_j = \mathbf{x}^b(t_j)$ and M is the time-dependant model operator. The evolution of an increment $\delta\mathbf{x}$ with respect to the background evolution is given by

$$\delta\mathbf{x}_{j+1} = M_j[\mathbf{x}^b_j + \delta\mathbf{x}_j] - M_j[\mathbf{x}^b_j]. \tag{2.44}$$

If the increment is assumed to be small, this can be approximated by introducing a time-dependant tangent-linear operator $\mathbf{M}$:

$$\delta\mathbf{x}_{j+1} \simeq \mathbf{M}_j\delta\mathbf{x}_j, \tag{2.45}$$

where

$$\mathbf{M}_j = \frac{\partial M_j}{\partial \mathbf{x}}\big|_{\mathbf{x}^b_j}. \tag{2.46}$$

If the evolution of the model state during the insertion period is assumed to make little

difference to the evolution of the increment then it becomes approximately,

$$\delta \mathbf{x}_{j+1} = \mathbf{M}_0 \delta \mathbf{x}_j, \tag{2.47}$$

where $\mathbf{M}_0$ is the tangent-linear operator relative to the background state $\mathbf{x}_0^b$ valid at the centre of the insertion period. During an IAU run, a fraction g_j of the analysis increment $\delta \mathbf{x}_0^a$ is added to the model state at each time t_j within the insertion period. If the IAU increments are assumed to evolve linearly according to Equation 2.47 then

$$\delta \mathbf{x}_{-N}^{IAU} = g_{-N} \delta \mathbf{x}_0^a, \tag{2.48}$$

$$\delta \mathbf{x}_{j+1}^{IAU} = \mathbf{M}_0 \delta \mathbf{x}_j^{IAU} + g_{j+1} \delta \mathbf{x}_0^a, -N \le j < N, \tag{2.49}$$

where $\delta \mathbf{j}^{IAU}$ is the cumulative effect of the increments added up to and including time t_j. For Chapter 5 and 6 the IAU increments are added over a 60 minute period at the start of the model run (at 18 UTC 5 July 2012). The increments are added uniformly over the 60 minute period for this case. Currently, direct incrementing is supported for u, v, w, θ, pr^2 (scaled density), Π (exner), q_{cl} (liquid cloud), q_{cf} (ice cloud), murk (aerosol) and ozone.

2.5   Ensemble Methods

The Met Office Global and Regional Ensemble Prediction System (MOGREPS) is used in Chapter 6 of this study. MOGREPS is designed to provide short to medium range ensemble-predictions (with forecasts out to seven days operationally). At the time of this study MOGREPS utilises a Global, regional (North Atlantic European) and higher-resolution (2.2 km grid spacing UK) domain but for the purposes of this study only the Global domain is used, called MOGREPS-G. MOGREPS-G was run operationally at 60 km grid-spacing at the time of the case analysed (2012) but has since been upgraded to 33 km grid-spacing (2014) and further to 20 km grid-spacing (2017), each running with 70 vertical levels. The grid-spacing of the MOGREPS-G model is chosen to be approximately half that of the corresponding Global model (which is 25 km grid-spacing for this study, but in 2017 was upgraded to 10 km grid-spacing). At the time of this study MOGREPS-G ran with 24 ensemble members every 6 hours: 23 are perturbed

using initial condition and model perturbations and one member is a control forecast run at the same resolution as the other members but with no perturbations. Initial condition perturbations are chosen to quantify the errors in analysis and to be sufficiently large to capture errors in short-range forecasts. Initial condition perturbations for MOGREPS are generated using an ensemble transform Kalman filter (ETKF) (Bishop *et al.*, 2001). The ETKF produces a set of perturbations which are added to the Met Office four dimensional variational data assimilation (4D-Var) analysis to provide the initial states for ensemble members (Bowler *et al.*, 2008). 4D-Var is a method used to estimate a set a parameters (initial conditions for example). This is performed by adjusting the model variables until the analysis optimizes the observations with the first guess (Goodliff *et al.*, 2015) (for a full description of 4D-Var the reader is directed to Talagrand and Courtier (1987)). The perturbations created by ETKF are added at the start of the forecast as an IAU file in the MetUM simulation. Ensemble forecasts at the Met Office use random parameters scheme to account for errors due to parametrization schemes used in the model. Ensemble Kalman fliter and 4D-Var are now discussed in more detail below.

2.5.1 Ensemble Kalman filter

The Kalman filter (Kalman, 1960) uses certain conditions to find an optimal estimate of the state of the system. The filter maintains this estimate of the true state, which is updated by a forecast of the state from the previous time and by observations (Bowler *et al.*, 2008). This filter provides an optimal data-assimilation system if the model and observation operator are linear and all the errors are Gaussian, conditions not met by the atmosphere (Bowler *et al.*, 2008). In NWP models an ensemble Kalman filter (EnKF) is therefore used as an approximation to the Kalman filter (Evensen, 1994). The EnKF allows the data assimilation to be computed assuming a limited ensemble size. The EnKF requires an ensemble of forecasts of the current state. The ETKF is related to the EnKF allowing for a rapid calculation of the analysis perturbations (Bowler *et al.*, 2008). The reader is directed to Bowler *et al.* (2008) for details of the mathematics involved in calculating the filters.

2.5.2   4D-Var

Four dimensional variational data assimilation (4D-Var) is a way of estimating unknown parameters in the forecast model, for example, initial or boundary conditions through optimizing the fit between the solution of the model and a set of observations which the model is meant to predict. The method is called 4D-Var due to it using the three-dimensional space and the time domain. This produces a solution which is a trajectory. The reader is directed to Bannister (2007) for a through description of 4d-Var and the mathematics involved.

2.5.3   Ensemble diagnostic methods

In Chapter 6 two sets of ensembles are simulated and an analysis is completed. To perform this analysis of the ensembles the following three verification techniques are utilised:

2.5.3.1   Root mean squared differences (RMSD)

Root mean squared differences (RMSD) are a measure of the differences between values. For this study the RMSD is a measure of either the differences between the members of the ensemble and the control of the ensemble, the differences between the member of one ensemble to the corresponding member of the second ensemble or the differences between the members of the ensemble and the ensemble mean. RMSD is calculated using the following equation:

$$\sqrt{\frac{\sum_1^{n_i} \sum_1^{n_j} (x - y)^2}{n_i n_j}}, \tag{2.50}$$

where n_i and n_j are the number of grid points in the i and j direction on the grid, x is data value of the member from an ensemble and y is either the value from control or ensemble mean of that ensemble or the value from the corresponding member from another ensemble. Therefore, to calculate the RMSD, for example between the ensemble members and the control, the first step is to find the sum of the squared differences between values on each point on the model grid for the member and the control, then find the average squared difference by dividing by the number of data points and then the square root. RMSD is used as a measure of the spread and variability of an ensemble. The mean of the

RMSD taken over all members gives a measure of the ensemble spread. In this study the RMSD between each of the members and the ensemble mean (or the control member) are computed individually and displayed graphically. The differences between the individual RMSD values gives a measure of the ensemble variability. Variability indicates how different the RMSD values are between the different ensemble members (i.e. the range of RMSD values). An analysis of the variability in RMSD values between member–control and member–ensemble mean is conducted in Chapter 6. In Chapter 6, member–member RMSD calculations are also performed. This diagnostic is no longer a measure of spread or variability within the ensemble, but is a measure of differences between the members of the two ensembles.

Root mean square error (RMS error) calculations are performed in Chapter 6. RMS error is the same as the RMSD calculations, however the error indicates that the ensemble members are compared to analysis or observations. In this study the ensemble members are compared to forecast analyses for times of interest. Therefore, RMS error becomes a measure of the forecast errors.

2.5.3.2   Correspondence ratio (CR)

The correspondence ratio (CR) is a measure of the spread of an ensemble. A lower CR value indicates an ensemble with a larger spread. The CR takes a value between 0 and 1. In Chapter 6 the correspondence ratio is used as in Gebhardt *et al.* (2011) to measures how much each grid point in the model corresponds to a grid point from another ensemble member for a particular variable.

$$CR = \frac{N(GP_{all})}{N(GP\geq 1)},\tag{2.51}$$

where $N(GP)$ and $N(GP_{\geq 1})$ denotes the number of grid points. The index "all" denotes the grid points where the event is forecast by all ensemble members and the index "≥ 1" denotes the grid points where the event is forecast by at least one ensemble member. The event is defined by the exceedance of a given threshold for a particular variable. The CR was initially described by Stensrud and Wandishin (2000), however, they included an observation in their CR so it was purely a measure of forecast quality rather than forecast spread.

2.5.3.3   Fraction of common points

The fraction of common points (FCPs) is between two ensemble members (this could be between an ensemble member with the control member or a member–member comparison) using a particular threshold depending on the variable. Firstly, all the points where precipitation exceeds the chosen threshold (for example, 1 mm per hour) in both members are found and then the fraction of common points is found by dividing this by the total number of grid points where there is precipitation (exceeding the threshold) in the two members (using the same threshold). This gives the following calculation:

$$F_{common} = \frac{N_{12}}{N_1 + N_2 - N_{12}}, \tag{2.52}$$

where N_{12} is the number of common points between members 1 and 2 at which the threshold is exceeded. N_1 is the number of points exceeding the threshold in member 1 and N_2 is the number of points exceeding the threshold in member 2. The calculation requires N_{12} points to be taken away in the denominator to avoid double counting of the points (Flack *et al.*, 2017). F_{common} gives the fraction of common points and is always a value between 0 and 1. An F_{common} value of 1 means that both members are identical and a 0 value means there are no common points between members. For the FCP calculations computed in Chapter 6 the corresponding ensemble members are compared to each other, as well as comparing members to their control.

Chapter 3

Case Studies

This chapter presents an analysis of the synoptic and mesoscale features of two case studies of mesoscale convective systems (MCSs) that occurred over western Europe. Observations and North Atlantic European (NAE) operational forecast model data are analysed for each case to determine the synoptic environments and lifecycles of the MCSs. The two case studies were chosen as, after a brief analysis of the observations, they appeared to be MCS cases. The second case study forms the basis of numerical simulations conducted throughout the rest of this thesis. Each case is compared to MCSs that have been described in previous literature. The Chapter closes by comparing and contrasting the two case studies to two case studies presented in Lewis and Gray (2010), before conclusions are presented.

3.1   Methodology

Observational data is analysed for each case to determine if an MCS is occurring. This includes infra-red satellite imagery, Met Office synoptic charts and precipitation radar. The meteorological fields associated with each case are analysed using Met Office Unified Model (MetUM) data from the NAE configuration of the operational forecast model (as this was the operational European configuration at the time of this study). The following time periods are used for the cases: 18 UTC 6 May 2011 – 09 UTC 7 May 2011 and 00 UTC 5 July 2012 – 12 UTC 6 July 2012. The NAE model simulations are initialised using data taken from a T+6 operational forecast model. The NAE model uses a rotated grid with $0.11° \times 0.11°$ horizontal grid boxes ($0.11°$ is equivalent to 12 km grid spacing at this latitude). The NAE model is too coarse to resolve convection explicitly and hence a convection parameterisation scheme is used. This parametrization could affect how the MCS is produced in the model forecast in comparison to reality.

Identification of the mesoscale-scale features occurring in an MCS event using the

NAE forecast model data can help identify why the MCS occurred in that particular location and at that time. However, due to the limitations of the NAE model and its 12 km grid spacing the forecast could fail to produce an MCS at all, produce an MCS which is stronger or weaker than occurred in reality, produce an MCS which is in a different location than occurred in reality and/or has a different track to what occurred in reality. The representation of convection associated with the MCS could also impact the PV anomalies produced.

The observational data and NAE operational forecast data will be used answer a number of sub questions to investigate the initial question posed in Section 1.1: What are the mesoscale and synoptic-scale structures of PV anomalies generated by MCSs? These sub questions are:

1. Are the synoptic conditions conducive to MCS formation?

2. Do MCSs satisfying the criteria from Gray and Marshall (1998) form (see Section 1.2.1)?

3. What led to the triggering of the MCSs?

4. What is the PV structure of the MCSs?

To determine the answers to the above questions a determination of whether the operational NAE model analyses produce an MCS that corresponds well to reality is required. Therefore, as well as finding out information about the environmental conditions associated with the MCSs in both cases, the aim is to determine if the model produces the following:

• an MCS in the correct location in comparison to reality as determined from the location of rainfall;

• an MCV structure typical of an MCS with related PV anomalies;

• the expected conditions related to Spanish plume and instability;

• CAPE and CIN in amounts necessary for an MCS;

• a similar track of the system in comparison to reality.

A MCS case study from 6-7 May 2011 is now described followed by a MCS case study from 5-6 July 2012. The Chapter closes with a comparison of these two MCS case studies with two MCS case studies from Lewis and Gray (2010).

3.2   Case study 1: 6-7 May 2011

The synoptic conditions leading to the MCS event are analysed followed by an analysis of the observational data associated with the MCS, including rainfall radar, lightning reports (sferics) and satellite imagery. The MCS life-cycle is related to the stages discussed in Section 1.2.3 then the structure and evolution of the MCS is investigated using operational NAE model data. The section concludes by relating the case study to the stages of Browning and Hill (1984) using the NAE model analysis, followed by a short case summary.

3.2.1   Synoptic overview of the MCS event

In the days preceding the development of the MCS a cut-off low-pressure system moving eastwards develops and strengthens to the west of the UK. A high pressure system to the east of the UK also strengthens. This allows the following conditions to form which were favourable for deep, organised convection:

- On the morning of 6 May 2011 pressure falls over Spain and Central Europe (as an omega block - area of high pressure between two areas of low pressure; moves eastwards away from Germany) and is marked by a low pressure trough line in Figure 3.1(a) over Spain. Additionally, a further cut-off upper-level disturbance develops and strengthens during 6 May 2011 to the west of Spain (Figure 3.1(b)). These together produce a strengthening easterly airflow (Figure 3.2(a)).

- Two weak omega blocks were present: over Scandinavia and Germany. These blocking high pressures along with an upper-level trough to the west allows for strong zonal flow of air from the Mediterranean region as the omega block over central Europe pushes the upper-level jets southwards.

- A cold front to the southwest of Spain creates a temperature gradient whereby cold air advection occurs (Figure 3.2(a) shows this colder air to the southwest with

$\theta_w = 280$ K, with warmer air to the east of it, with $\theta_w = 288$ K). The air at lower-levels (850 hPa and below) is warmer than the air above. This is seen in Figure 3.2(b) where at 850 hPa the air over Spain has a θ_w temperature of 292 K whereas at 500 hPa the temperature is $\theta_w = 286$ K (Figure 3.2(a)).

- A warm front is associated with a temperature gradient (Figure 3.1(a) shows this warm front to the west of Spain at 00 UTC 6 May 2011).

- During 6 May 2011 a weak low develops over Spain and moves north towards France. Figure 3.1(b) shows this as a trough line to the north of Iberia. At 600 hPa warm air is forced up from Africa/ Mediterranean Sea (Figure 3.3). Movement of air at 600 hPa is in a north east direction (Figure 3.2(a)) with air at this level being warm and dry due to it originating from north Africa. Figure 3.3 shows that the air at lower-levels (700 hPa) travels inland towards the Iberian peninsula over the Atlantic ocean on an easterly track whereas air at 600 hPa travels from the southwest, with a shorter oceanic track over the Mediterranean sea. Therefore, the air at 700 hPa is moister than the air at 600 hPa. At 950 hPa, the air is in a north westerly direction over Spain and is warm and dry due to surface heating (Figure 3.3, 3.2(b)).

- The strengthening of a weak low pressure system over Spain allows for weakly upper-level forced ascent on 7 May 2011 (not shown). Due to the weak upper-level disturbance (shown as a trough line in Figure 3.1(b) which tracks along with the MCS) the upper-level winds are weak and thus a small MCS occurs.

- The synoptic situation occurring on 6 May 2011 caused airflow from a north east direction over Spain (Figure 3.2(a)) therefore an MCS (with initialisation at 18 UTC) tracked north east towards France from the Iberian Peninsula (where it initialised).

- The weak easterly movement of air and weak forced ascent with blocking Scandinavian anti-cyclone resembles a European Easterly plume as described by Lewis and Gray (2010). However, in this case a blocking high over Central Europe meant that airflow was forced in a much more southerly direction towards the UK than is typical for a European Easterly Plume (these tend to create MCSs over northeastern France). This case also differs from that of a European Easterly plume due to the existence of an upper-level trough to the west. This, along with the blocking

highs, allowed for the more southerly movement of air than is typical. Similarly to a European easterly plume though the dry air was from eastern continental Europe Lewis and Gray (2010) did find that some of their cases did not fit into any of the three Spanish plume categories and this case is one of those. If the geopotential height for this case (Figure 3.2(a)) is compared to that of the geopotential height for Lewis and Gray (2010) for the different types of Spanish Plume events (Figure 1.13) it can be seen that this case actually appears more like a typical modified Spanish plume event in terms of geopotential height, but with contours stretched further south than is usual.

(a)	(b)
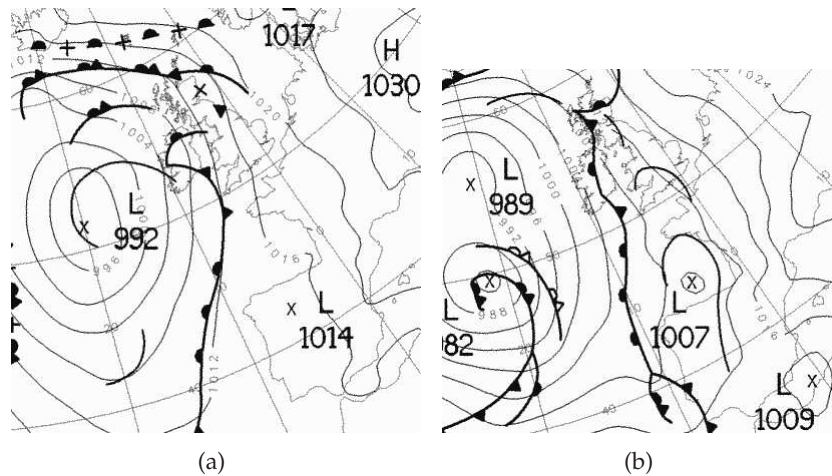
Figure 3.1: Met Office surface analyses for (a) 00 UTC 6 May 2011, (b) 00 UTC 7 May 2011 (Archived by www.wetter3.de).

3.2.2 Initial Development and track of the MCS

In the preceding days to the MCS development the airflow (at low-levels, below 700 hPa; Figure 3.3) had been from the Mediterranean region under largely cloudless skies and created a warm air parcel over Spain. As the airflow changed to a more easterly direction during 6 May 2011, it allowed air to flow inland over Iberia (at 700 hPa). This created a layer of warm, moist air capped by warm, drier air from the Mediterranean region (at 600 hPa). This case was unusual in that there was a very warm, dry layer at 950 hPa due to strong surface heating as the air moved from eastern Europe towards Spain. The moist, warm layer at 700 hPa was therefore above a stable dry layer at 950 hPa but was capped below a dry, cooler layer at 600 hPa.
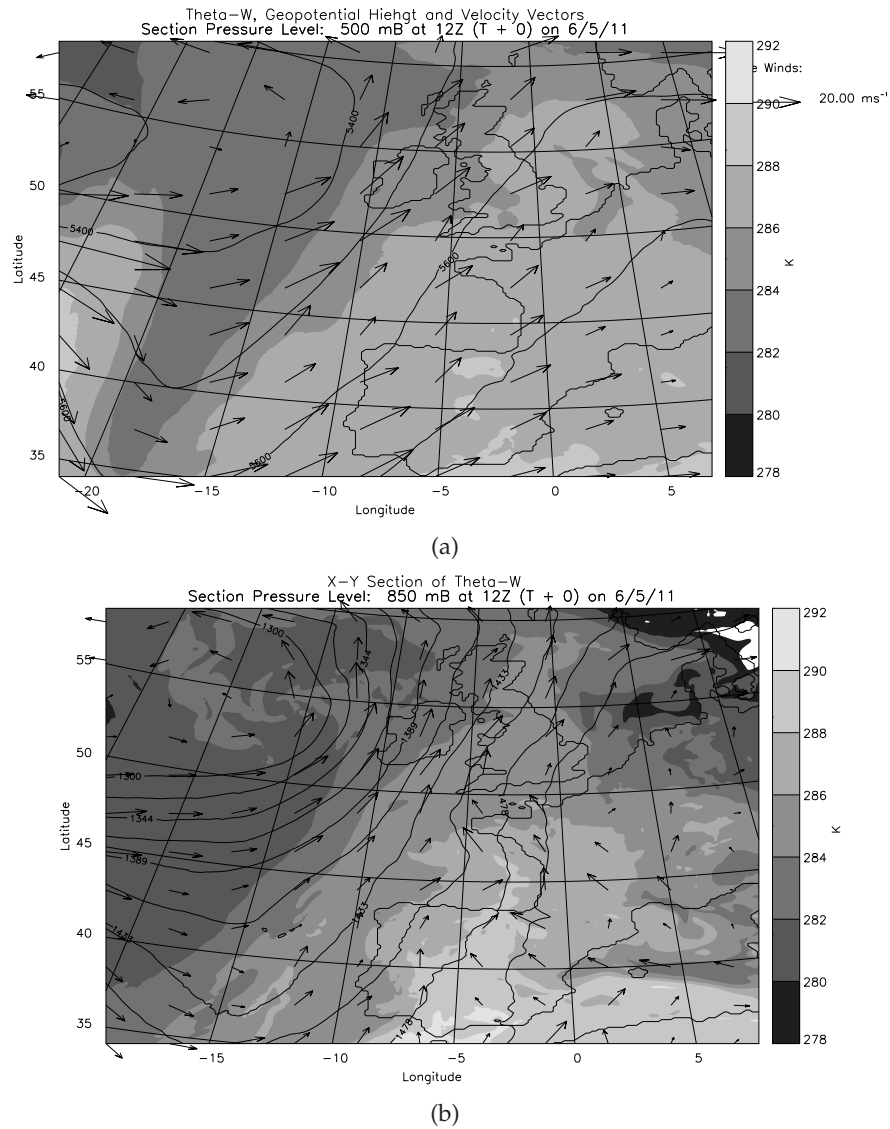
(a)

(b)

Figure 3.2: Geopotential height (black contours), θ_w shaded and velocity vectors (scale velocity $20\,\mathrm{ms}^{-1}$) at 12 UTC 6 May 2011 for (a) 500 hPa and (b) 850 hPa.

Cloudless skies allowed strong surface heating to occur over Spain, Germany and France in the preceding days. This allowed temperatures to reach between low $20^\circ C$– high $20^\circ C$. Large amounts of surface heating particularly took place over Spain with temperatures reaching $30^\circ C$ over areas of the Spanish plateau (not shown here). Air at levels below 950 hPa is thus very warm due to surface heating over Spain.

Instability grows during 6 May 2011 as strong surface heating takes place to the moist, warm parcel of air at low-levels (950 hPa to 700 hPa). Deep convection develops to the north of Spain around 18 UTC due to forced ascent by a weak low pressure trough and air passage over the elevated Spanish plateau. Deep convection develops
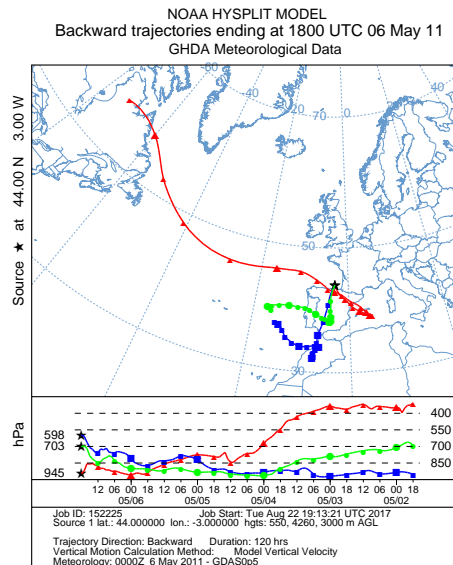
Figure 3.3: Backwards trajectory starting at 18 UTC 6 May 2011 (at the location of MCS initiation) and ending at 00 UTC 2 May 2011. Blue line is 600 hPa and red line is 950 hPa and green line is 700 hPa (HYSPLIT computed using www.arl.noaa.gov). It should be noted that the ascents and descents suggested by the HYSPLIT trajectory calculations may not be very accurate due to the trajectories being calculated using the resolved winds and the scale of the grid spacing used being large.

over the Bay of Biscay to the north of Spain, as a result of larger-scale ascent associated with convergence in the lower troposphere (see the wind arrows at 850 hPa in Figure 3.2(a) and ascending trajectories in Figure 3.3).

Orography leads to the development of convection through forced lifting of the air enabling instability to be released. On the leeside of the mountains instability is increased and a surface low pressure develops which allows for a convergence between the ascending air associated with the low pressure and the gust front associated with convection. This often gives the organisation mechanism for MCS development. An alternative organisation mechanism is in the form of positive vorticity advection by a weak upper-level trough converging with the gust front of individual convective cells. In this case both organisation mechanisms took place to cause the MCS to develop.

Deep convection begins to cluster and can be seen in Figure 3.4 at 0139 UTC 7 May 2011 as a large area of very white, cold cloud. The initial deep convection creates a small area of rainfall to the north of Spain at 18 UTC 6 May 2011 and can be seen in Figure 3.5(a). Over time this convection organises into a large area of light rainfall with smaller areas contained within, with very intense rainfall (shown in Figures 3.5(a) - 3.5(f)). This is typical for an MCS which by definition has precipitation across a region of at least 100 km

in one dimension (Gray and Marshall, 1998), with this rainfall being split into small areas of very intense convective rainfall surrounded by light stratiform rain (Houze, 1977; Houze *et al.*, 1990; McAnelly and Cotton, 1989).

As convection develops at 18 UTC 6 May 2011, lightning is reported in the same area (Figure 3.6(a)). These lightning reports track along with the rainfall and show that, as the convection organises and develops, it moves from the Bay of Biscay to north western France before reaching the southwest of the UK (Figure 3.5(a)- 3.5(f) and Figure 3.6(a)-3.6(f)). The MCS is mature by 00 UTC 7 May 2011 and has a large area of rainfall associated with it by this time, along with many lightning reports (Figure 3.5(c) and Figure 3.6(c)). The MCS maintains it strength until 05 UTC 7 May 2011 when the number of lightning reports decreases along with the rainfall weakening (not shown here). After 05 UTC 7 May the MCS begins to decay but as it passes from France to the UK it gains some strength again with the rainfall increasing. By 11 UTC 7 May 2011 the MCS has decayed, but a large area of weak stratiform rainfall remains (Figure 3.5(f)). There are no longer lightning reports associated with the system and no intense rainfall (Figures 3.6(f) and 3.5(f)).
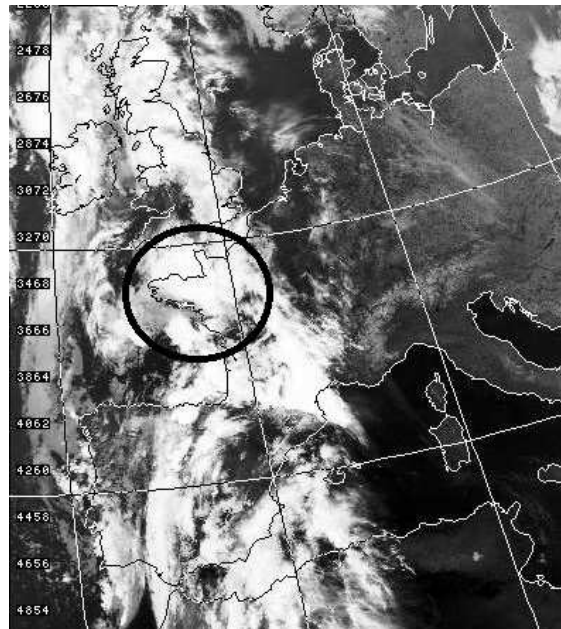
Figure 3.4: Infra-red satellite image for 0139 UTC 7 May 2011. Convection associated with the MCS is indicated by a black circle (Archived by Dundee Satellite receiving station).
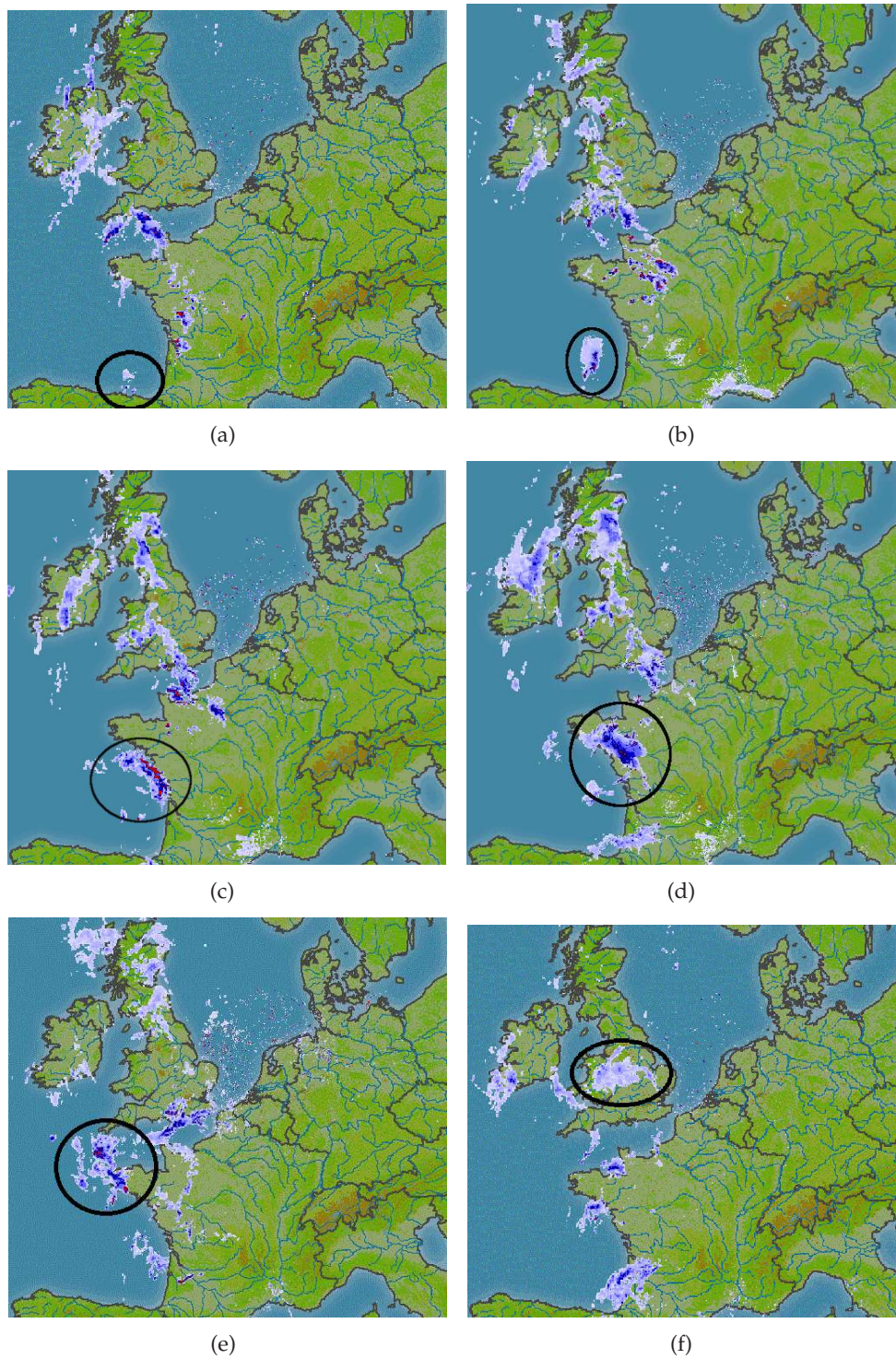
Figure 3.5: Radar precipitation for (a) 18 UTC 6 May 2011 (MCS initiates), (b) 21 UTC 6 May 2011 (MCS developing), (c) 00 UTC 7 May 2011 (MCS mature) and (d) 02 UTC 7 May 2011 (sustained MCS maturity), (e) 06 UTC 7 May 2011 (MCS is decaying but gains some strength due to orography) and (f) 11 UTC 7 May 2011 (MCS decayed). The circles marked on each figure indicate the convection of interest. Blue colours signify <10 mmhr^{-1} rain and red signifies >10 mmhr^{-1} (archived by www.Meteox.com).

3.2.3 Comparison to Browning and Hill (1984)

Browning and Hill (1984) describes four stages of MCS development and decay, each lasting approximately three hours (see Section 1.2.3). These stages were based on observational analysis. A direct comparison to the case study in Browning and Hill (1984) is not possible, however, analysis of rainfall radar, satellite imagery, lightning reports and synoptic charts are used to make an approximation for the 4 stages of MCS formation and decay for this case, similarly to Browning and Hill (1984):

- Stage 1 MCS initiates: 18 UTC–22 UTC - A region of individual convective showers develops and begins to joins up with more convective cells to form an increasing area of rainfall. The rainfall is mostly weak, but is beginning to become more intense (Figure 3.5(a), 3.5(b)). This is accompanied by increasing ascent and thickness of cloud cover along with sustained high cloud at tropopause level (Figure 3.13(a) shows this cloud cover at 20 UTC 6 May 2011). Lightning reports also increase within this time period (Figure 3.6(a) and 3.6(b)). Organisation of individual convective cells begins to occur due to convergence of ascent associated with an upper-level trough with the gust front of the individual convective cells.

- Stage 2 MCS mature: 23 UTC–02 UTC - Rapid enlargement of the rainfall area and intensity of rainfall (Figure 3.5(c) and 3.5(d)). This is accompanied by an increase in lightning reports (Figure 3.6(c)) and cloud cover (thickness and area increases, Figure 3.4).

- Stage 3 MCS sustained and beginning to decay: 03 UTC–06 UTC - The intensity of the rainfall begins to diminish (Figures 3.5(d) and 3.5(e)). The area of rainfall remains sustained though. At 03 UTC the cloud at high levels begins to break up indicating that the MCS is beginning to decay as further thunderstorms created are no longer joining up with the MCS (seen in satellite imagery, not shown here). Lightning reports decrease in frequency (Figure 3.6(c) and 3.6(d)).

- Stage 4 MCS decaying: 07 UTC–11 UTC - The magnitude of rainfall decreases dramatically (Figure 3.5(f)). There is also a break up in the cloud cover at high levels. In this case however there is an increase in ascent at 06 UTC – 09 UTC: this may be due to orography effects which in turn may account for the slight increase in rainfall rates and cloud thickness from 06 UTC onwards until around 08 UTC. It

appears as if orography increases ascent slightly from 06 UTC leading to a slight increase in rainfall rates after this time (Figure3.5(f)). However, any new cumulonimbus cloud which is formed is not joining with the MCS cloud and hence the MCS cloud continues to decay suggesting why there is a complete lack of sferics by 10 UTC (Figure 3.6(f)) indicating that the MCS has completely decayed.
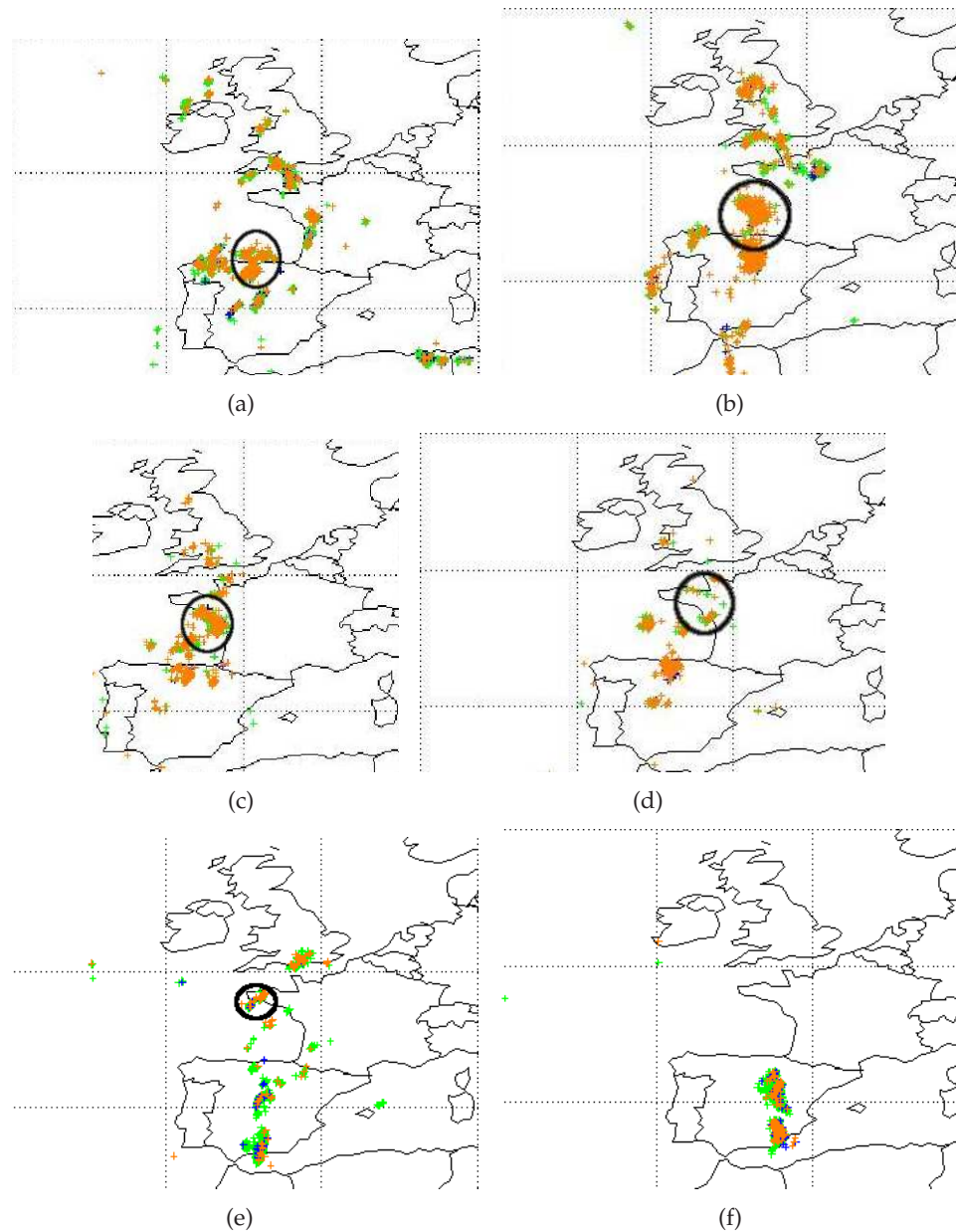
Figure 3.6: Sferics data (Met Office lightning detection reports) for (a) 18 UTC 6 May 2011, (b) 21 UTC 6 May 2011, (c) 00 UTC 7 May 2011, (d) 02 UTC 7 May 2011 (e) 06 UTC 7 May 2011 and (f) 11 UTC 7 May 2011 (Sourced by Nigel Roberts; Met Office).

3.2.4 Structure and Evolution of the MCS determined using operational NAE model forecasts

For this Section operational six-hourly analyses from the North Atlantic European model are used with their intermediate hourly forecasts for the period 18 UTC 6 May to 12 UTC 7 May 2011. This 20 hour period is deemed long enough to include the initiation, maturity and decay of the MCS and to track the movement of the system, as forecast by the model. The NAE operational forecast is used to analyse the PV structure of the MCS, precipitation, cloud cover and convective instability. The following time line of development of the MCS is used throughout the analysis due to the 4 stages discussed in the previous section:

- 18 UTC 6 May 2011: Initiation of convection,

- 20 UTC 6 May 2011: Further trigging of convection,

- 02 UTC 7 May 2011: MCS is mature,

- 05 UTC 7 May 2011: MCS is decaying,

- 11 UTC 7 May 2011: MCS fully decayed.

3.2.4.1 Precipitation

Most of the rainfall produced by the model is associated with the convective parametrisation scheme (not shown here). The rainfall produced by the model compares well to the location and track of rainfall observed in reality; however, the intensity of the rainfall produced in the model is weaker (comparing figures 3.7(a)- 3.7(e) to Figures 3.5(a) - 3.5(e)). This weaker rainfall is due to the parametrization scheme producing the average effect of convection over an entire grid box and has been shown to cause lower rainfall rates than in reality, early initiation of convection and unrealistic structure to showers compared to rainfall radar (Lean *et al.*, 2008).

The model in this case appears to initially produce rainfall at the same time as observed (18 UTC 6 May 2011); however, the location of the rainfall in the model is slightly west of the observed rainfall (Figure 3.7(a) compared to Figure 3.5(a)). This perhaps suggests that the NAE model develops the initial convection too late or in the wrong location.

3.2.4.2 Environmental convective stability

Initial convection takes place at 18 UTC over the sea (Figure 3.5(a)) as air is travelling northwards over the Iberian peninsula (Figure 3.2(a) and 3.2(b)). The effects of orography cause some convection and light rainfall to be produced, however, the MCS is not triggered until 20 UTC 6 May 2011 when CAPE is released due to forcing by a weak upper-level trough (approximately 1000 Jkg^{-1}: Figure 3.8) allowing strong convection to occur from 950 hPa (below this level is a layer of warm, dry stable air) and deep clouds begin to form (Figure 3.9(a)). Figure 3.10(a) shows a sharp increase in θ with height until 950 hPa at 20 UTC 6 May 2011 where triggering occurs.

Larger-scale ascent by a weak upper-level trough causes weakening of the capping stable layer (strong vertical gradient in potential temperature; Figure 3.10(a)) that was separating the warm moist lower-tropospheric air from the air above with lower wet-bulb potential temperature (Figure 3.9(a)). Once the capping stable layer had been sufficiently weakened convective clouds could were able to break through and extend up to the upper troposphere (see vertical velocity contours on Figure 3.9(a)).

The stable layer corresponds to a peak in temperature (23$^\circ C$, seen at 950 hPa, Figure 3.11(a)) and an associated minima in θ_w indicating that there is a 'tongue' of warmer, drier air at the 950 hPa level. This is followed by a layer of air between 950 hPa–700h Pa which increases in relative humidity until reaching saturation at 700 hPa, where there is then a layer of air which decreases in relative humidity to 600 hPa (Figure 3.9(a)). This can be explained using the trajectories found in Figure 3.3 along with Figure 3.2(a) and 3.2(b), which show that at 600 hPa the air travelled from the south where the air was warmer and moister but it lost most of the moisture whilst travelling northwards over Spain as large amounts of rainfall occurred in the days preceding the MCS (not shown here).

The air at 950–700 hPa however, travelled from the east where the air was cooler but more moist due to its continued passage over the Atlantic ocean. Figure 3.3 shows that at 700 hPa the air moves from the Atlantic and is stationary over Spain for much of the previous five days retaining the moisture. The air below 950 hPa at this time had a long track over the Atlantic but in the two days before the MCS initiation this layer of air tracks from the Mediterranean sea inland west over the Spanish Peninsula where it is affected by surface heating due to the elevation here. At 00 UTC 950 hPa is

approximately 600 m height. The Spanish plateau has elevations at this 600 m level. This indicates that warm, dry air at 950 hPa is from the Spanish plateau and is warmer and drier due to surface heating on the plateau. For this case the convective cap is 700 hPa due to a layer of warm air from 950 hPa to 700 hPa which increases in relative humidity until saturation at 700 hPa.

For a typical Spanish plume case the relative humidity below the convective cap should be higher than that above as the air is typically moister at lower levels since it has travelled from the sea, whereas air at higher levels is from the dry Spanish plateau. When the convective cap is removed the air will be moister in all levels. For this case, relative humidity decreases from the surface to 950 hPa (Figure 3.10(b)). There is then an increase in relative humidity from 950 hPa to 700 hPa (Figure 3.10(b)) this corresponds to where θ_w also decreases with height suggesting a layer of unstable air (Figure 3.9(a)). Above 700 hPa the air is 50–60% relative humidity indicating a drier layer of air. It has 100% humidity at upper-levels above 450 hPa signifying the high-level cloud that was already present due to the orography effects. As the MCS intensifies, relative humidity behind and beneath the system is much drier. This is due to downdraughts behind the MCS (not shown).

As the MCS develops, clouds develop from 750 hPa to tropopause height, marking the height of the unstable layer of air. The tephigram at 00 UTC 7 May 2011 shows this saturation from 750 hPa to tropopause level (Figure 3.11(b)). Figures 3.9(a)– 3.9(c) show that ascent is occurring from the 950hPa level suggesting that below this level the atmosphere is stable due to the warmer, dry air.

At 20 UTC 6 May 2011 θ_w decreases with height where the storm is developing (Figure 3.9(a)) indicating a region of instability. At this time high clouds are already occurring due to initial convection created by the effects of passing over the Spanish plateau (see black contours on Figure 3.9(a)). This instability begins to be released through triggering due to the effects of upper-level forcing by a weak low pressure system in this area (it could also be caused by cooling from precipitation since there is some weak rainfall at this time, Young (1995) described this happening in MCS cases), with convection occurring at this time (see green contours of ascent on Figure 3.9(a)).

By 21 UTC 6 May 2011 convection has begun to form deeper cloud as the instability continues to be released (Figure 3.9(b), with green contours showing an increase in con-

vection) . By 22 UTC 6 May 2011 (Figure 3.9(c)) strong convection has created very deep cloud with CAPE having been released (see black contours on Figure 3.9(c)).

In summary,

- Triggering of convection occurs at 20 UTC after some weak initial convection occurs at 18 UTC due to the elevation of the Spanish plateau.

- There is an unstable layer of air between 950 hPa and 700 hPa which increases in relative humidity until saturation at 700 hPa. This layer is capped by a warmer and drier layer of air above it to 600 hPa.

- Below 950 hPa there is a layer of air which is dry and very warm and this is due to the air being from the Spanish plateau where surface heating has made it very warm.

3.2.4.3   Potential vorticity structure in the MCV

As the MCS matures a positive PV anomaly develops and strengthens in mid-levels (600 hPa is the approximate middle of the positive PV that forms and exists throughout the life span of the MCS; seen in Figure 3.12(a) - 3.12(f)). The positive PV anomaly at 600 hPa strengthens over time (Figure 3.12(a) - 3.12(f)). Negative PV anomalies also develop at upper-levels either side of the maximum in PV and above it to tropopause level (Figure 3.13(a) – 3.13(d)). As well as spreading outwards from the top of the positive PV anomaly (approximately 400 hPa), the negative PV anomalies spread downwards either side of the positive PV anomaly at mid-levels. A similar PV anomaly structure associated with MCSs was also found in a study by Done *et al.* (2006) using this 12 km grid-spacing model however their simulation was hydrostatic and did not include parametrized convection. There is also a negative PV anomaly below the positive anomaly. This negative PV anomaly occurs below 850hPa due to downdraughts created by the system, producing a cold pool (Figure 3.13(a)–3.13(d)).

The positive PV anomaly occurs slightly south of the location of the system when viewed in observations, this is due to rainfall developing to the north of the MCV typically but also could be due to misplacement of the MCS in the model simulation. The positive PV anomaly at mid-levels begins to develop at 20 UTC 6 May 2011 which corresponds to the time of initiation of the MCS (Figure 3.12(a)). Deep convection can be seen

with ascent occurring from 850 hPa-250 hPa (tropopause level) (Figure 3.13(b)). Descent occurs behind the system suggesting evidence for downdraughts (not shown here). Although the ascent weakens around 05 UTC 7 May 2011 the PV at mid-levels remains until the MCS is decayed.

The areas of ascent, positive PV signature (Figure 3.12(a)–3.12(f)) and high relative humidity (Figure 3.10(b)) all approximately correspond, however the location of the positive PV anomaly appears to be occurring slightly west of these (this corresponds to Raymond and Jiang (1990) that found ascent tends to form to the east of PV anomalies). When comparing with reality the NAE forecast appears to produce the system slightly too south-west (comparison of Figures 3.5(a)– 3.5(f) to Figures 3.12(a)– 3.12(f)); however, there are the correct features present in the forecast to suggest an MCS is occurring. Although the NAE forecast uses a parametrization scheme for convection, in this case it still produces an MCS but with weaker precipitation than in reality.

Ascent intensifies at 22 UTC 6 May 2011, corresponding to the strengthening of a positive PV anomaly at mid-levels. At 00 UTC 7 May 2011 a clear horizontal PV and ascent structure forms (Figure 3.12(c)) this then tracks north eastwards until 05 UTC (not shown here) when a localised 'oval' of positive PV and ascent forms and tracks northwards across the UK; it is this that forms the MCS over the UK. By the time it reaches the UK (around 06 UTC) the MCS has begun to decay. This corresponds to the decrease in lightning reports and rainfall after 06 UTC (not shown here). Ascent moves from being collocated with the PV band to being ahead of the PV band and focused on the western edge of the PV anomaly (Figure 3.12(a)– 3.12(f)).

Analysis of north–south vertical sections of vertical velocity from 18 UTC 6 May 2011 – 09 UTC on 7 May 11 (not shown here) shows

- A clear movement of weak updraughts measuring 1–6 cms^{-1} to the north of the positive PV tower.

- The vertical velocity appears to have weakened by 05 UTC with the largest velocities measuring 4 cms^{-1}.

- The vertical extent of the stronger vertical velocities appears to cover from 750 hPa-250 hPa at all times except 06 UTC when it is 900 hPa–250 hPa due to orography causing further triggering. The strongest velocity at this time only reaches 3 cms^{-1}

though and occurs at the 300 hPa level. At all times there are downdraughts occurring behind the updraughts (associated with negative vertical velocity).

- The weak updraughts seem to initialise at 18 UTC 6 May 2011. Before this time there are no updraughts appearing on the charts.

The maximum vertical velocity is quite weak in this case and is largely due to the weak low pressure system which forces the ascent. The vertical velocity does show that the MCS as expected has deep convection occurring to heights of 250 hPa (tropopause level) due to the large amounts of CAPE built up before initialisation.

3.2.5   Comparison to Browning and Hill (1984) using NAE model analyses

In Section 3.2.3 the 4 stages of MCS development and decay for this case study were discussed. This section aims to add to these 4 stages through an analysis of the PV structures found in the NAE model analyses. It must be noted though that in previous studies it has been shown that the MCV persisted after the MCS had decayed (Bartels and Maddox, 1991).

- Stage 1: 18 UTC–22 UTC: Weak positive PV begins to develop at 600 hPa (Figure 3.13(a) and Figure 3.12(a) and 3.12(b): 3 PVU magnitude). This is accompanied with a development of an MCV (PV anomalies with associated circulations around it) structure which is increasing in vertical extent and magnitude. Ascent develops at upper-levels and relative humidity reaches 90% from 700 hPa up to tropopause level.

- Stage 2: 23 UTC–04 UTC: The MCV structure intensifies in magnitude up to 5 PVU at the strongest, with negative PV (-2 PVU) above the positive PV tower and to either side (Figure 3.13(b) and 3.13(c)). This is also associated with an increase in the intensity and vertical extent of the convection and a deep layer of cloud (by analysing relative humidity). The positive PV at 600 hPa also increases in horizontal area as the MCS increases in size and more thunderstorms join up and the MCS becomes mature (Figure 3.12(d) and 3.12(e)). The area and intensity of precipitation also increases within this time frame (Figure 3.7(d)).

- Stage 3: 05 UTC–07 UTC: Convection continues but the intensity and vertical extent decreases. At 03 UTC the cloud at high levels begins to break up indicating that the MCS is beginning to decay as further thunderstorms created are no longer joining up with the MCS (Figure 3.13(c)). Although cloud cover begins to break up at upper-levels after 03 UTC the MCV structure continues to intensify until 04 UTC suggesting that the MCV structure continues to develop after the MCS begins to decay. This could also be due to the NAE model not representing the MCS timing as reality.

- Stage 4: 08 UTC–11 UTC: The MCV structure decays away until it no longer exists (Figure 3.13(d)). Rainfall decreases in intensity (not shown) and the cloud cover becomes broken up along with ascent diminishing to nothing (not shown).

After an analysis of the PV structure in the NAE model the times related to each stage were varied slightly to that in 3.2.3 due to the MCV structure intensifying after the end of the mature stage.

3.2.6 Case Summary

- The synoptic situation does not appear to fit exactly into any one particular Spanish plume category, but is somewhat similar to that of a European easterly plume. However, usually for this type of Spanish plume, the MCS develops further east over central Europe before tracking northwards affecting the east of the UK. In this case a strong upper-level trough to the west and a blocking high to the east caused the movement of air strongly from the south. An MCS develops which affects the south of the UK and initiated out over the sea, north of the Spanish coast.

- A deep convective feature with associated PV anomalies exists in the NAE model forecast and corresponds to the area of lightning reports and large area of rainfall in observations (Figure 3.13(b), Figure 3.5(d) and Figure 3.6(d)).

- Below 950 hPa the air is dry and very warm. From 950 hPa to 700 hPa there is a layer of air that increases in relative humidity until saturation at 700 hPa. Above 700 ha there is a layer of air which is warm but dry until 600 hPa (Figure 3.9(a)).

- This case appears to be of the correct size and duration to satisfy the definition by Gray and Marshall (1998) indicating that it is an MCS (see Section 1.2.1).

- Initial convection occurs at 18 UTC 6 May 2011 due to effect of the elevated Spanish plateau, but triggering that creates deep convection and allows for the organisation of thunderstorms into an MCS does not occur until 20 UTC due to weak forcing from an upper-level trough. The MCS is fully developed around 22 UTC on 6 May 2011, with strong convection occurring leading to thick cloud cover, intense rainfall and the development of anomalous positive PV at mid-levels and negative PV at tropopause level and either side of the positive anomaly.

(a)

(b)

(c)

(d)

(e)
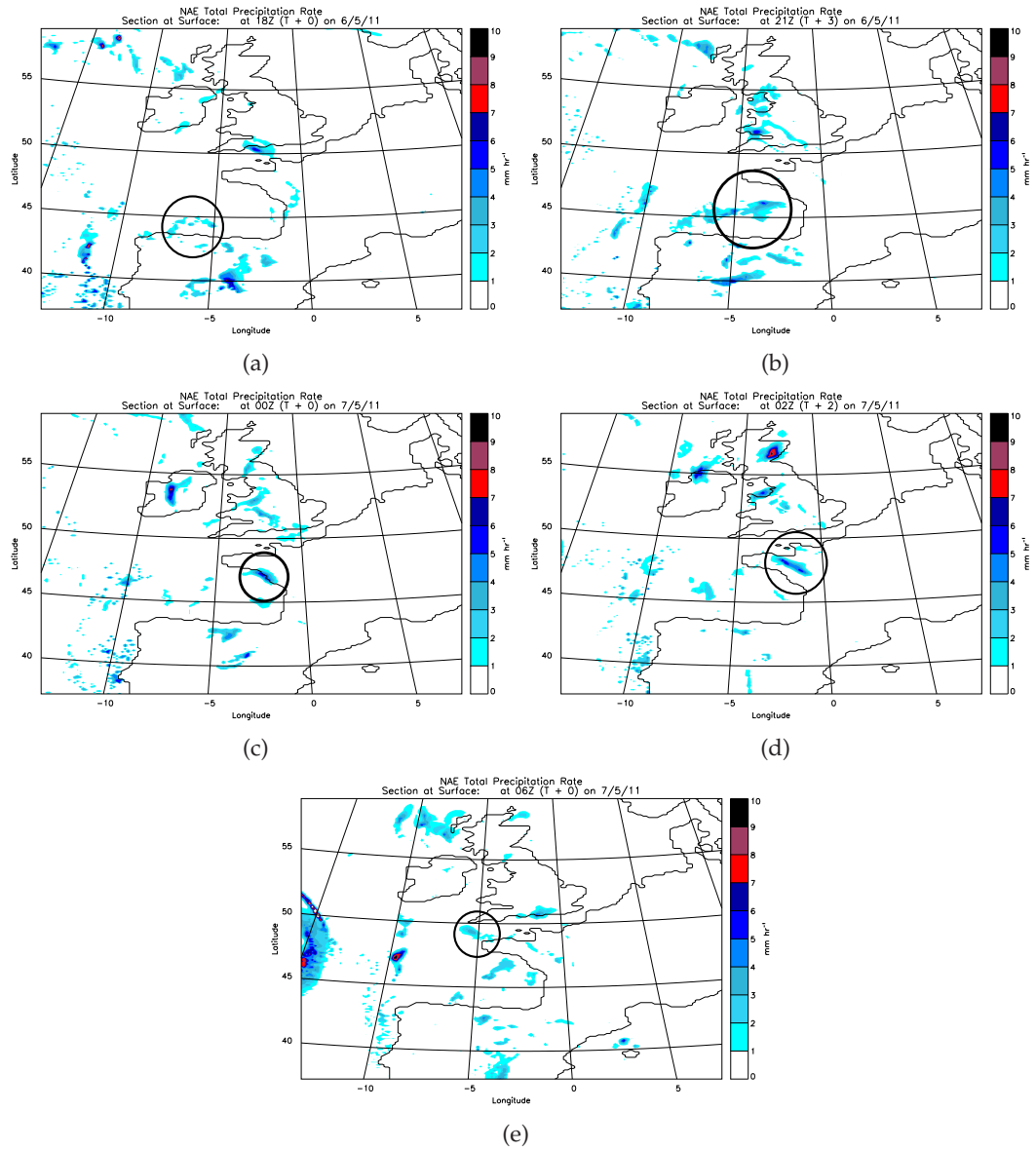
Figure 3.7: NAE total rainfall rate (convective and large-scale rainfall rates combined) for (a) 18 UTC 6 May, (b) 21 UTC 6 May, (c) 00 UTC 7 May, (d) 02 UTC 7 May and (e) 06 UTC 7 May 2011. Black circle indicates the MCS location.
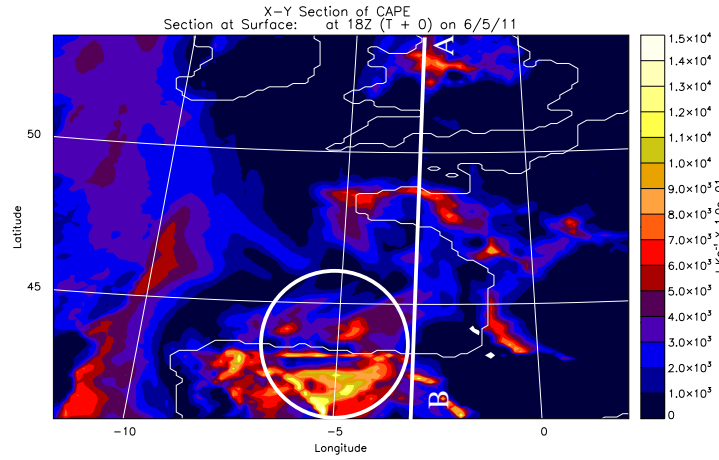
Figure 3.8: CAPE at 18 UTC 6 May 2011 from the operational NAE model, calculated from lifting from 1000 hPa. The white circle indicates the CAPE associated with the triggering MCS. White line A-B shows the cross-section used for Figure 3.9(a)– 3.9(c), Figure 3.10(a) and Figure 3.10(b).

(a)

(b)

(c)
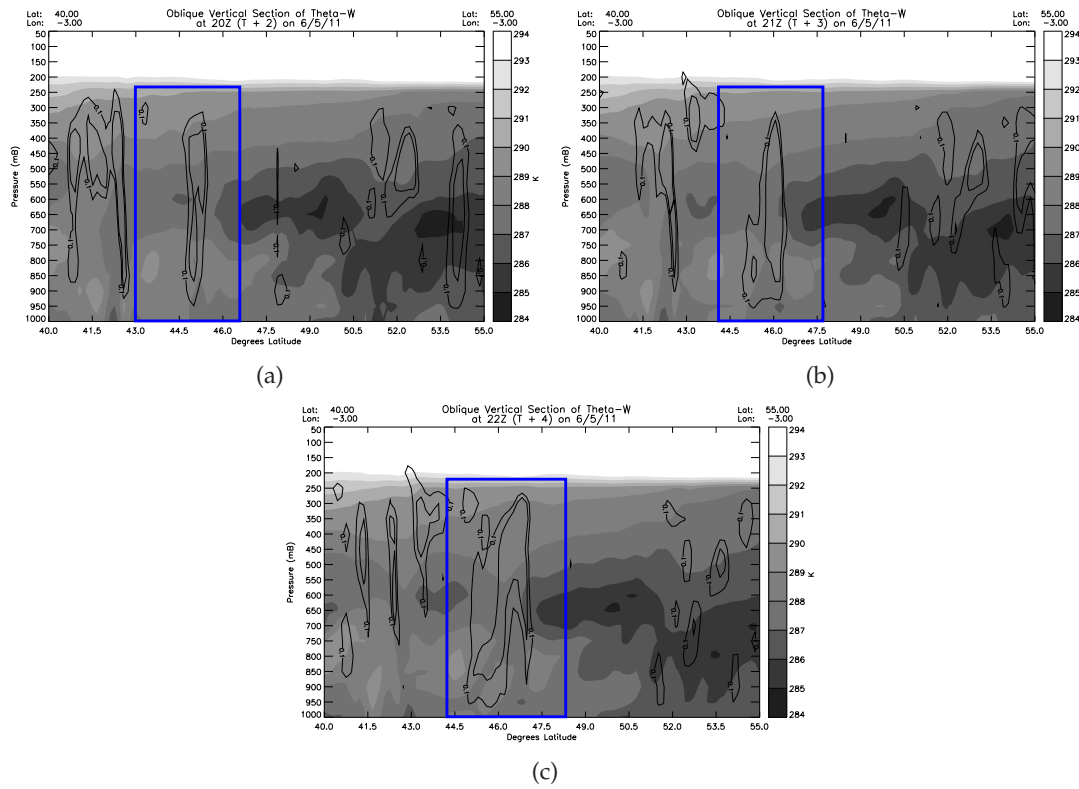
Figure 3.9: Vertical cross-sections of θ_w from NAE forecast model to identify when the convection initialises. (a) For 20 UTC 6th May 2011, (b) For 21 UTC 6th May 2011 and (c) For 22 UTC 6th May 2011. In all figures the black contours show regions of ascent larger than 0.1 ms^{-1}. The blue rectangle indicates the region of the MCS.
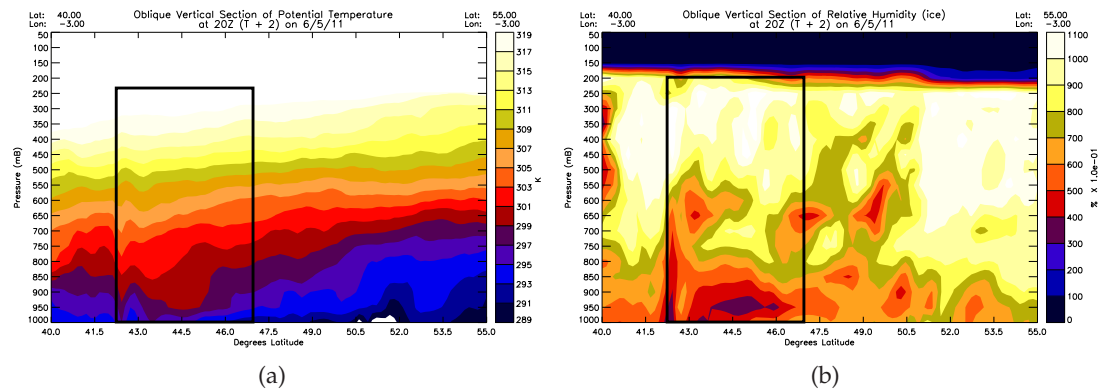
Figure 3.10: Vertical cross sections at 20 UTC 6th May 2011 as the MCS triggers for (a) θ and (b) relative humidity. The black rectangle indicates the location of the developing MCS.
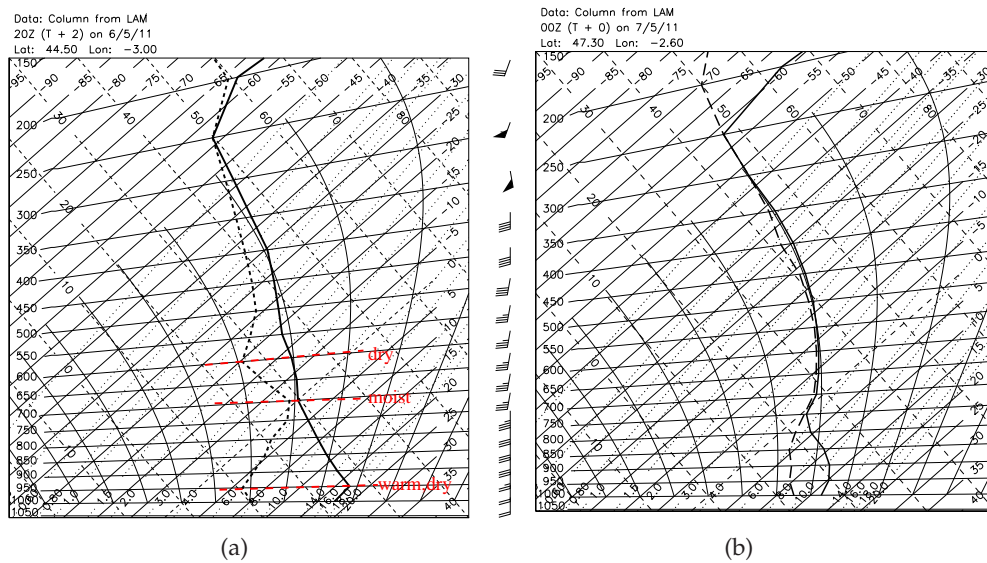
Figure 3.11: Skew-T tephigrams at (a) 20 UTC 6 May 2011 for -3°W and 44.5°N with red lines indicating the different layers of air that occurred and (b) 00 UTC 7 May 2011 at -2.60°W and 47.30°N. Both locations taken where the storm is centred at that time.
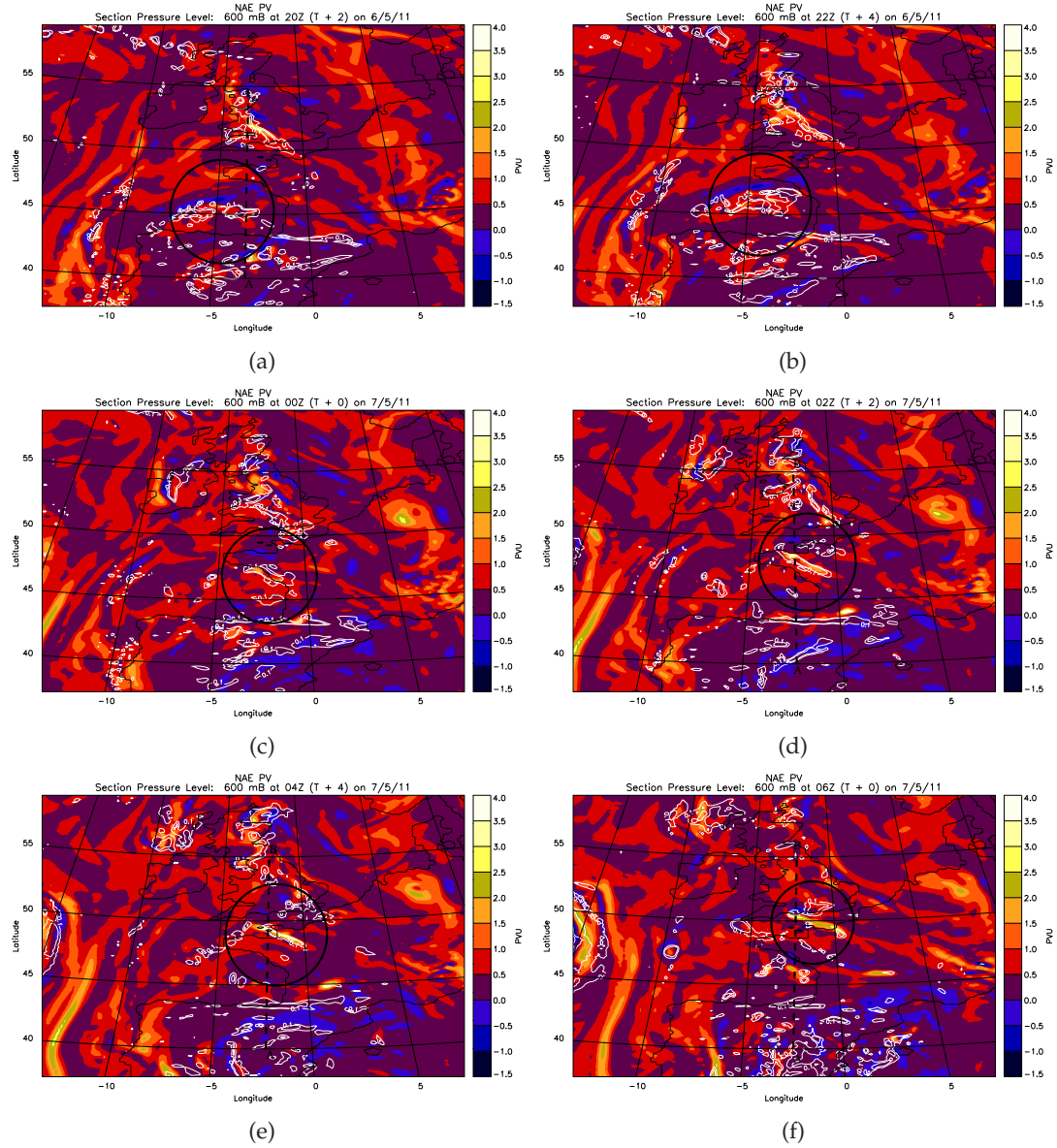
Figure 3.12: NAE model forecast plots for horizontal cross-section of PV (units $Km^2Kg^{-1}s^{-1}$ is equivalent to PVU) at 600 hPa for times (a) 20 UTC 6 May 2011, (b) 22 UTC 6 May 2011, (c) 00 UTC 7 May 2011, (d) 02 UTC 7 May 2011, (e) 04 UTC 7 May 2011 and (f) 06 UTC 7 May 2011. White contours show ascent greater than $0.1ms^{-1}$. Cross-sections A-B marked on the figures indicate the cross-sections used for Figure 3.13(a)– 3.13(d).
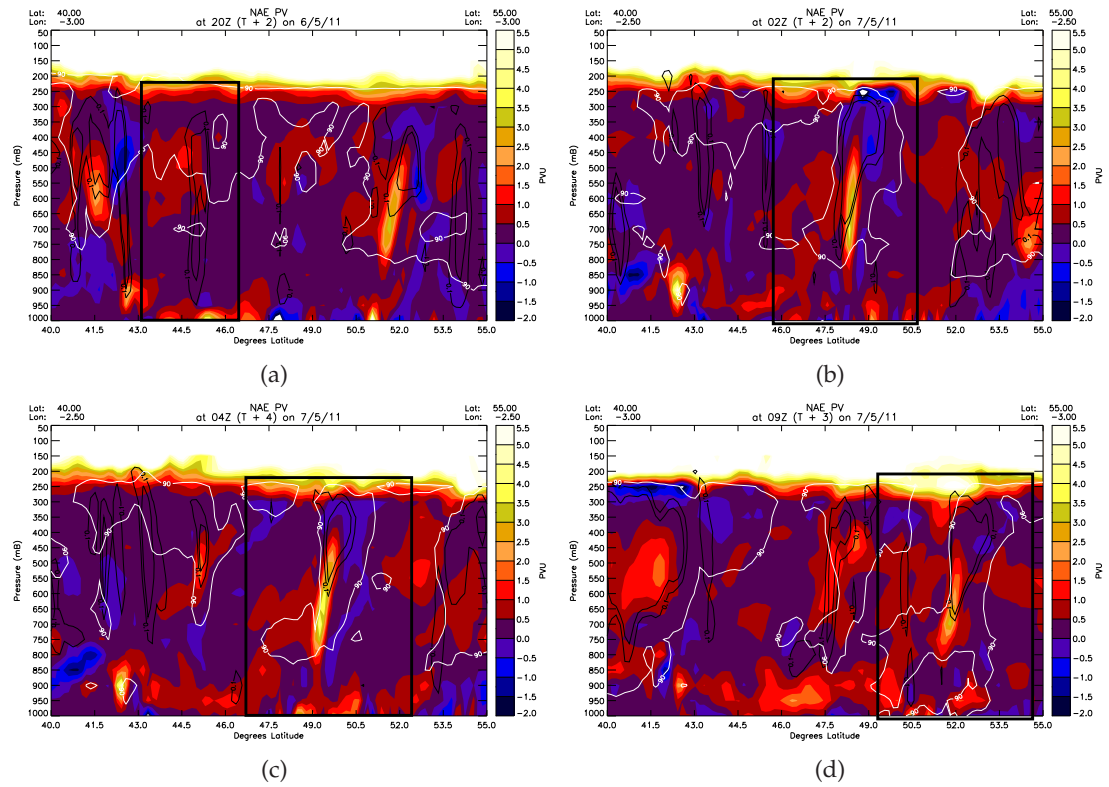
Figure 3.13: NAE model potential vorticity with contours of 90% relative humidity (white) and vertical velocity (black: at 0.1 and 0.2 ms^{-1}) plotted on top for (a) stage 1: 20 UTC 6 May 2011 (b) stage 2: 02 UTC 7 May 2011 (c) stage 3: 04 UTC 7 May 2011 and (d) stage 4: 09 UTC 7 May 2011. Rectangle indicates the MCS location.

3.3 Case Study: 5-6 July 2012

The synoptic conditions leading to the development of an MCS are analysed followed by an analysis of the observational data associated with the MCS, including rainfall radar, lightning reports and satellite imagery. The MCS life-cycle is related to the stages discussed in Section 1.2.3 then the structure and evolution of the MCS is investigated using operational NAE model data. The section concludes by relating the case study to the stages of Browning and Hill (1984) using the NAE model analysis, followed by a short case summary.

3.3.1 Synoptic Overview of the MCS event

Prior to the development of the MCS a cut-off low-pressure system to the west of the UK is almost stationary for four days. This is due to a blocking weak low-pressure system over Spain and France, along with high pressure to the east of the UK over Scandinavia. This allowed for the following conditions to form which were favourable for deep, organised convection:

- An upper-level trough occurs to the southwest of the UK and forces airflow from Spain northeastwards over France before turning west to hit the UK (Figure 3.14(a)). This is accompanied by a weak upper-level trough over the northeast of Spain and the south of France. This allows warm, moist air to move inland from the Atlantic over the Iberian Peninsula.

- After comparison to Lewis and Gray (2010), this case study appears similar in synoptic conditions to a modified Spanish Plume. Modified Spanish Plumes are classified as having an upper-level trough that is stretched equatorwards creating a cut-off upper-level trough to the northwest of the Bay of Biscay (Lewis and Gray, 2010) (Figure 1.13). They also found that modified Spanish plumes tend to have cold fronts associated with them which causes warm air advection from Iberia. It can be seen that this is the case here too (see Figure 3.14(a) and 3.15(a)).

- This case also has a weak, but well developed, low pressure system associated with it, thus, is already an organised system rather than one which develops as the MCS initiates and matures, which is generally the case for the Classical Spanish Plume.

In the modified Spanish Plume the frontal system is usually the cause of the MCS developing. The synoptic charts show a trough line which appears to track the evolution of the MCS from initiation to maturity (Figure 3.14(c)). This signifies an area of instability and corresponds with where convection occurs.

- The blocked low-pressure system allows for large amounts of instability to grow and thus many MCSs developed (around the time of the MCS of interest), but only this one reached the UK. Throughout the course of this case study a second MCS can be seen developing over south France and nothern Spain.

- A slack pressure gradient across Iberia and France allows for the development of warmer temperatures (Figure 3.14(a)).

- A cold front running through the centre of France creates a temperature gradient that has a weak low pressure trough associated with it (marked on Figure 3.14(a)-3.14(c)). This temperature gradient and weak upper level trough creates the necessary triggering mechanism for the deep convection in this case through frontal circulation.

- After 00 UTC 6 July 2012 the decaying MCS begins to wrap up within a developing frontal cyclone over the UK (Figure 3.14(e)-3.14(h)).

- Convective instability results from the moist, warm air (high θ_W) being capped by warm, dry air above. Figure 3.15(b) shows that where the MCS initiates there is a layer of moister, warmer air (high θ_w temperature) below a layer of dry, warm air which has lower θ_w temperatures at 500 hPa (Figure 3.15(a)). Instability is released through forced ascent by a weak upper-level trough and could have been developed due to the elevated Massif Central mountainous region. Figure 3.16 shows that air at 950 hPa has a long track over the Mediterranean sea in the days preceding the MCS and has relative humidity around 90% (not shown here). Although the layer of air at 900 hPa has a similar track as that of the layer at 950 hPa this layer has relative humidity around 75% similar to the layer above at 750 hPa. At 750 hPa there is a layer of air which is warm and dry due to the long track over Spain in the days before the MCS. This air caps the moist layer at 950 hPa.

3.3.2   Initial development and track of the MCS

Initial convection occurs around 00 UTC 5 July 2012 due to passage of the airmass over the Pyrenees and the individual convective cells can be seen in Figure 3.17(b). Further triggering of convection occurs at 09 UTC 5 July 2012 due to weak surface heating and lifting in front of a weak upper-level trough which produces deep convection. The convection is also helped by the weak upper level trough being in front of a cold front which creates a temperature gradient with cold air behind it. The weak-upper level trough, temperature gradient created by the cold front and the weak surface heating all help to lift the moist layer near the surface. This convection develops into a large area of very white cloud and is sustained between 12 UTC to 21 UTC 5 July 2012 (Figure 3.17(c) and 3.17(d)).

The MCS then begins to decay and starts to be influenced by a developing frontal cyclone over the UK (Figure 3.17(e)). This leads to an increase in the area of cloud cover, as the frontal systems produce cloud and rainfall too; however, the cloud appears more grey on the satellite imagery indicating that it does not reach as high up into the atmosphere or is not as deep. This is typical of cyclone development as the low-pressure leads to a tropopause fold, whereby, the tropopause level is brought downwards, therefore, cloud only develops to this level. It will be seen later on in this Chapter that although the PV structures that occurred within the MCS still exist at this point, the system is now a cyclone and not an MCS.

Rainfall radar show the existence of an area of rainfall that intensifies (over 10 mmhr^{-1}) and grows in size throughout the day (Figure 3.18(a)- (d)) and is also accompanied by an increase in lightning reports (Figure 3.19(a)-(d)). At 18 UTC 5 July 2012 the MCS is fully mature and it begins to move west towards the UK. By 00 UTC 6 July 2012 the rainfall has begun to decrease in intensity, but the weak stratiform rainfall (1–2mmhr^{-1}) is maintained (Figure 3.18(e). This change also corresponds to a decrease in the number of lightning reports (Figure 3.19(e)). The area of stratiform rainfall then increases as the system becomes wrapped up in a developing cyclone, but the intensity of the rainfall decreases (Figure 3.18(f)-(h)). As the MCS is impacted by the cyclone the number of lightning reports continues to decrease until there are none reported at 18 UTC 6 July 2012 (Figure 3.19(f)–(h)).

Rainfall radar also show the development of a second MCS over the south of France

around 18 UTC 5 July (Figure 3.18(d)) with a large number of lightning reports associated with it (Figure 3.19(h)). This MCS is not the focus of this study though since it does not impact the UK. This second MCS travels in an easterly direction towards Italy and Germany and dissipates by 12 UTC 6 July 2012.
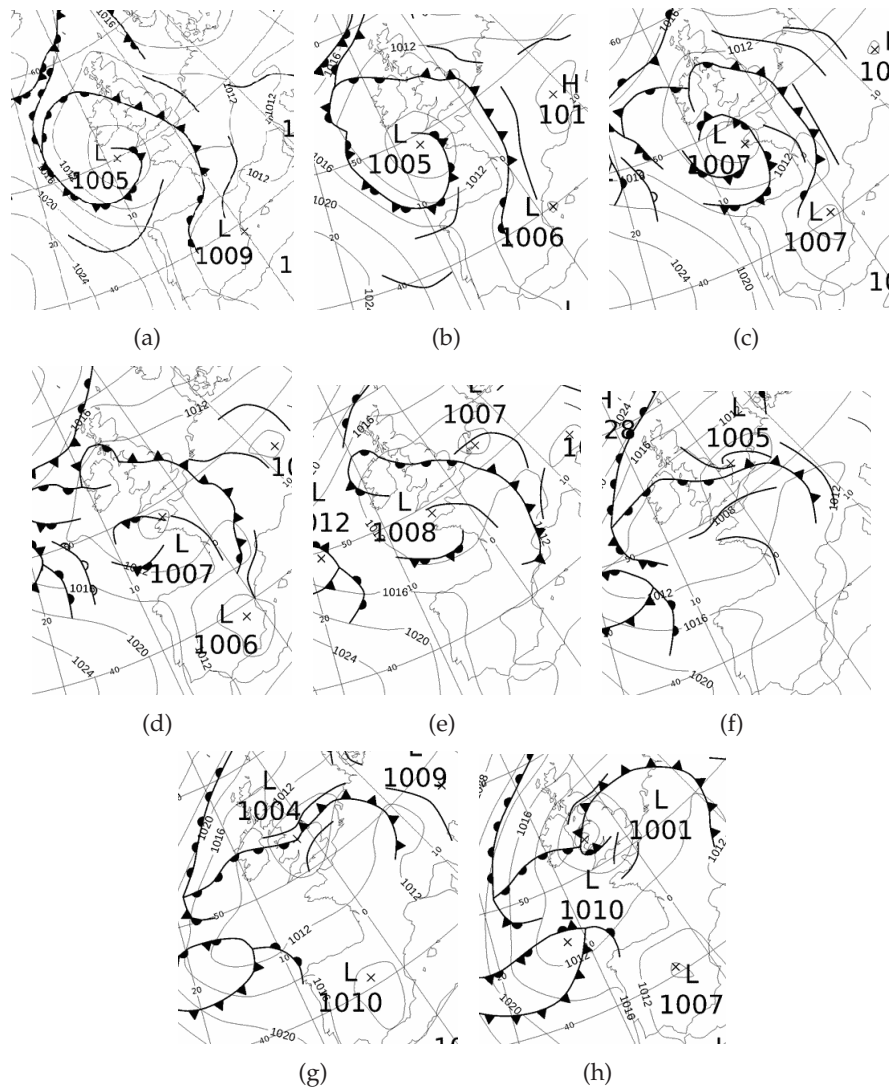

Figure 3.14: Synoptic analysis charts for (a) 00 UTC 5 July 2012 (initial convection), (b) 06 UTC 5 July 2012, (c) 12 UTC 5 July 2012 (secondary triggering of convection), (d) 18 UTC 5 July 2012 (MCS mature), (e) 00 UTC 6 July 2012 (MCS decaying), (f) 06 UTC 6 July 2012, (g) 12 UTC 6 July 2012 and (h) 18 UTC 6 July 2012 (Archived by www.wetter3.de).

Additionally to analysing the precipitation radar, precipitation data and surface temperature observations and rainfall amounts were investigated (using www.wunderground.com). Large amounts of CAPE were able to develop over northern Spain during 4 July 2012 as warm surface temperatures ($25°C$) occurred (Figure 3.24(a) and 3.24(b)). During the day on 5 July 2012, areas of north east France and Belgium
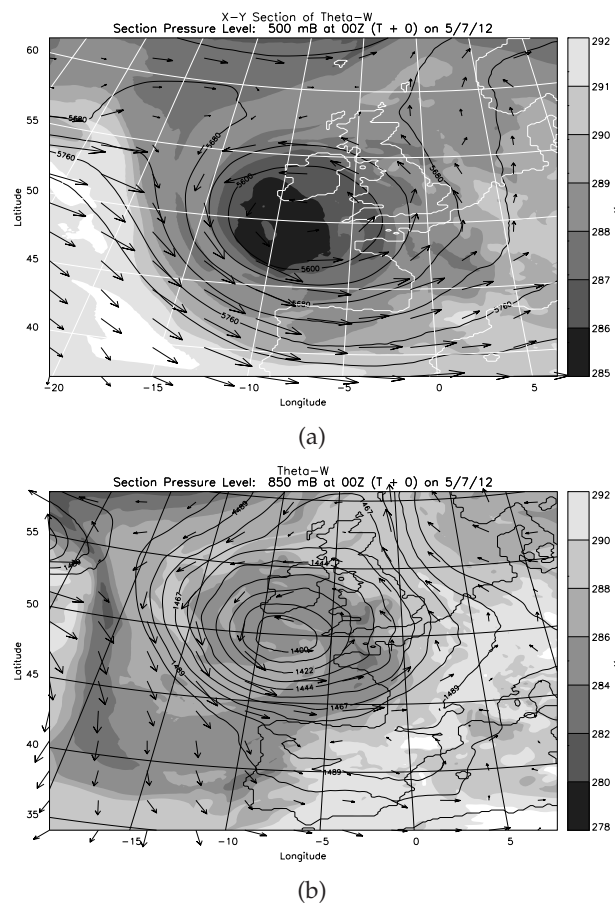
(a)

(b)

Figure 3.15: Geopotential height (black contours), θ_w shaded and velocity vectors (scale velocity $20\,\mathrm{ms}^{-1}$) at 00 UTC 5 July 2012 for (a) 500 hPa and (b) 850 hPa.
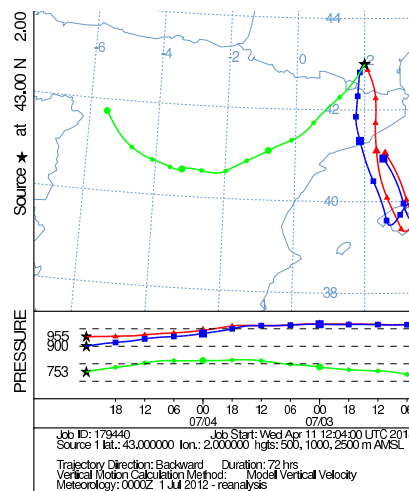

Figure 3.16: Backwards trajectories of air at the location of the MCS at 750 hPa (green line), 900 hPa (blue line) and 950 hPa (red line) levels starting at 00 UTC 5th July 2012 (HYSPLIT computed using www.arl.noaa.gov). It should be noted that the ascents and descents suggested by the HYSPLIT trajectory calculations may not be very accurate due to the trajectories being calculated using the resolved winds and the scale of the grid spacing used being large.

experienced surface temperatures of $25^\circ C$ (not shown here, but favourable for MCS occurrence as allows instability to grow). This will have allowed for large CAPE to develop in these areas. Between 18 UTC and 20 UTC 5 July (when the MCS was deemed most active) Luxembourg experienced 10 mm precipitation along with wind speeds up to 63 kmhr^{-1} (not shown here). Antwerp in Belgium also experienced 17 mm rainfall between 17 UTC and 18 UTC. Areas of north eastern France experienced 1–2 mm rainfall whilst this heavy rainfall was occurring over areas of Belgium (not shown). Lowestoft and Norwich, along with other areas of East Anglia had heavy rain from 2 UTC until 10 UTC 6 July (specific numbers cannot be found though). Light rainfall continued to effect much of the South of UK during the 6 July 2012 as the cyclone developed and progressed westward.

A second MCS develops over southern France between 12 UTC and 18 UTC 5 July 2012 with large CAPE (1600 Jkg^{-1}; Figure 3.17(d), Figure 3.18(d) and Figure 3.19(d)) being triggered due to passage over the Pyrennes and a temperature gradient due to a cold front causing forced ascent. This MCS moves towards eastwards towards Germany and Italy and has a similar PV anomaly structure as the MCS which impacts the UK.

Synoptic and observational summary

After an analysis of the synoptic environment and observational data for 5–6 July 2012 the following has been determined:

- Synoptic conditions conducive to MCS development were present on 5 July. An upper-level trough to the west of France and the UK created the necessary flow of air inland over the Iberian Peninsula. This air then moved on a north-easterly trajectory due to the low-pressure systems.

- Air from the Mediterranean sea which was warm and moist due to the long track (below 950 hPa) moved inland underneath dry, warm air (900 hPa to 600 hPa) which had a long track over Spain (see Figure 3.16). This creates convective instability.

- The cold front allows for the organisation of individual thunderstorms, due to the vertical shear, into an organised system creating the MCS.

- Areas where precipitation are observed exceed 10 mmhr^{-1}. A large surrounding stratiform area experiencing 1–2 mmhr^{-1} precipitation also occurs. There are also associated lightning reports, covering an area large enough to satisfy the MCS criteria (see Section 1.2.1).

The operational NAE forecast will now be used to investigate the small-scale features associated with this MCS and the stages of MCS development are discussed related to Browning and Hill (1984).

3.3.3   Comparison to Browning and Hill (1984)

As previously discussed in Section 3.2.3, Browning and Hill (1984) describes four stages to MCS development and decay. Each of the four stages are now discussed related to this case study.

- Stage 1 MCS initiates: 00 UTC–11 UTC 5 July 2012 individual convective cells are present with rainfall increasing (Figure 3.18(a) – 3.18(c)) and convection developing and organising. There is also a corresponding increase in lightning reports (Figure 3.19(a) and 3.19(b)). Deep convection is triggered at 09 UTC in the warm air ahead of the cold front along with weak surface heating and forcing by a weak upper-level trough (cold front and trough seen on Figure 3.14(b)).

- Stage 2 MCS developing: 12 UTC–17 UTC 5 July 2012 convective cells begin to join with a corresponding increase in rainfall area (Figure 3.18(c)) and increased area of lightning reports (Figure 3.19(c)). Cloud cover area increases and cloud deepens (Figure 3.17(c)).

- Stage 3 MCS mature: 18 UTC–03 UTC 6 July 2012 rapid enlargement of the rainfall area and intensity (Figure 3.18(d)). Lightning reports increase and cover a much larger area (Figure 3.19(d)). Intensity of rainfall begins to decrease after 00 UTC (Figure 3.18(e)) and less lightning is reported (Figure 3.19(e)). MCS begins to decay. Cloud cover begins to break up (Figure 3.17(e)).

- Stage 4 MCS decaying: 03 UTC–12 UTC 6 July 2012 MCS fully decays and begins to wrap around a developing cyclone that is effecting the UK. The rainfall becomes less intense, but more widespread, as ascent occurs in association with the cyclone

(Figure 3.18(f)–3.18(h)). Lightning reports decay until there are none at 18 UTC 6 July 2012 (Figure 3.19(f)–3.19(h)). Cloud cover extends to cover a larger area but is not as deep so appears more grey on satellite imagery (Figure 3.17(f)–3.17(h)).
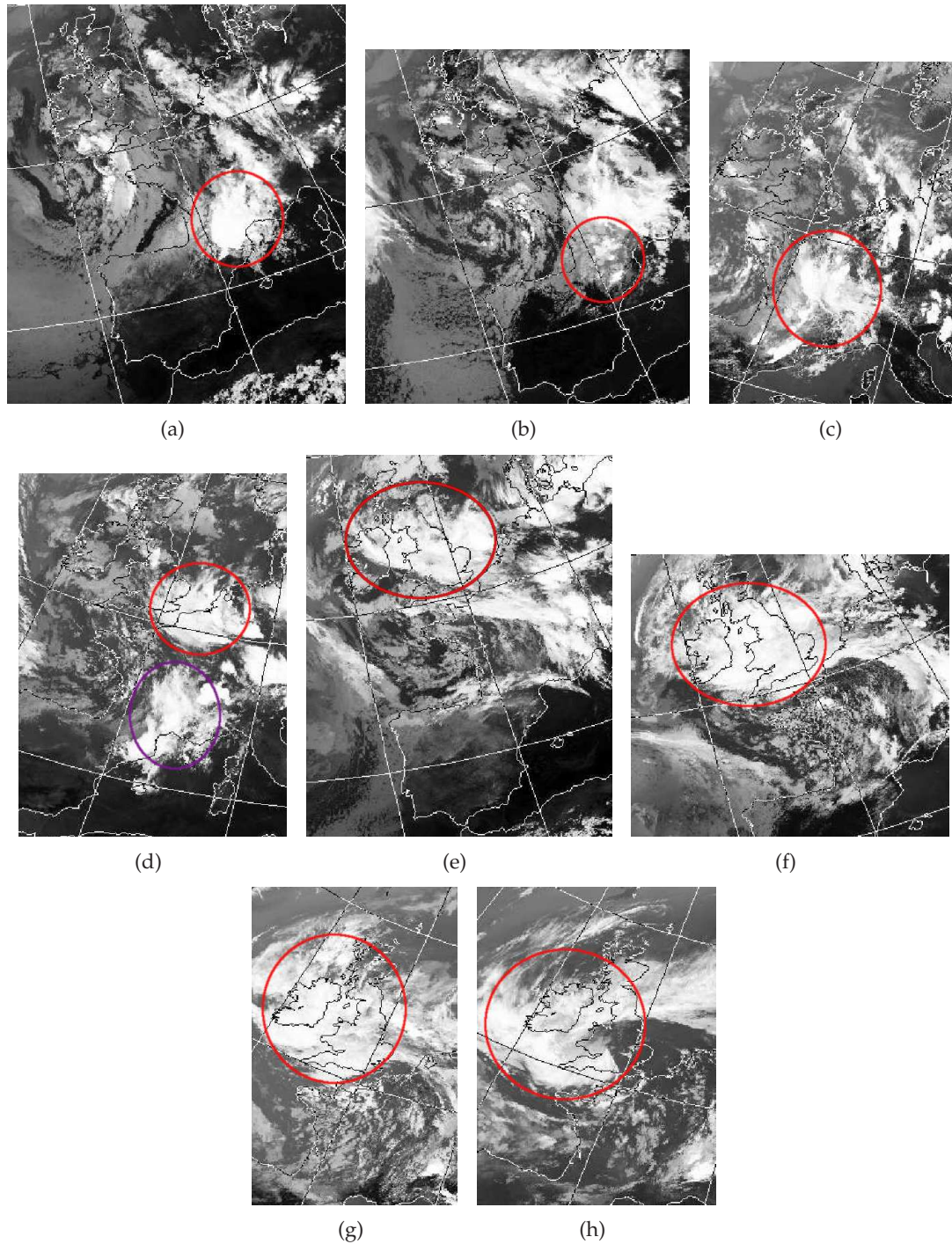
Figure 3.17: Infra-red satellite images for (a) 0230 UTC 5 July 2012, (b) 0942 UTC 5 July 2012, (c) 1224 UTC 5 July 2012, (d) 1936 UTC 5 July 2012, (e) 0220 UTC 6 July 2012, (f) 0930 UTC 6 July 2012, (g) 1214 UTC 6 July 2012 and (h) 1924 UTC 6 July 2012 (Courtesy of Dundee satellite receiving station).
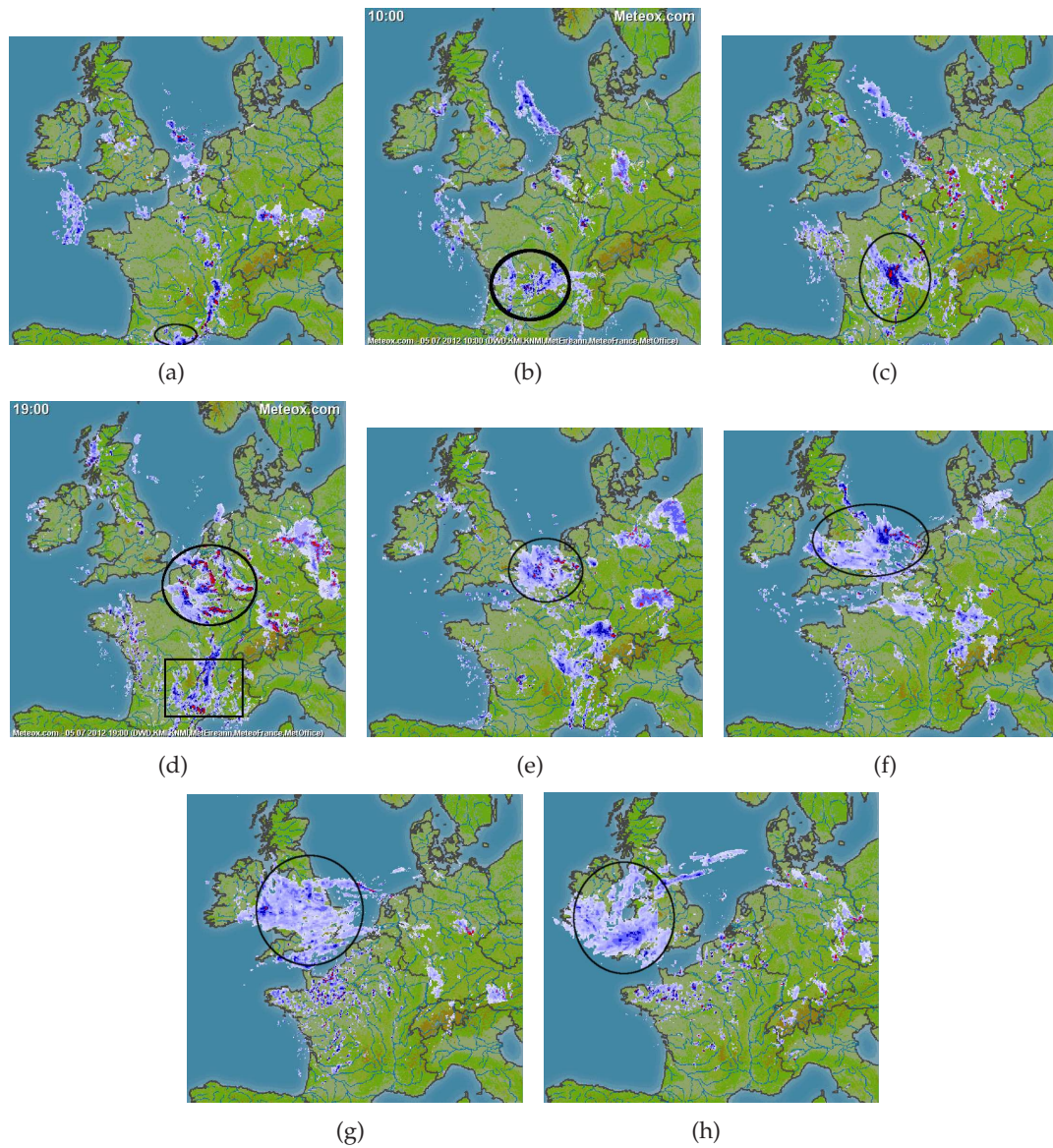
Figure 3.18: Precipitation radar for (a) 00 UTC 5 July (Initiation of convection due to passage over Iberian Peninsula) (b) 09 UTC 5 July (deep convection triggers) (c) 12 UTC 5 July (MCS present) (d) 18 UTC 5 July 2012 (MCS mature), (e) 00 UTC 6 July 2012 , (f) 06 UTC 6 July 2012, (g) 12 UTC 6 July 2012 and (h) 18 UTC 6 July 2012 (Archived by www.meteox.co.uk) Red indicates >10 mmhr^{-1} rainfall. Dark blue is 5–10 mmhr^{-1} rainfall. Light blue is >0 mmhr^{-1} but <5 mmhr^{-1}. The circle indicates the location of the developing over northern France MCS. The rectangle indicates a second MCS which developed over the south of France.
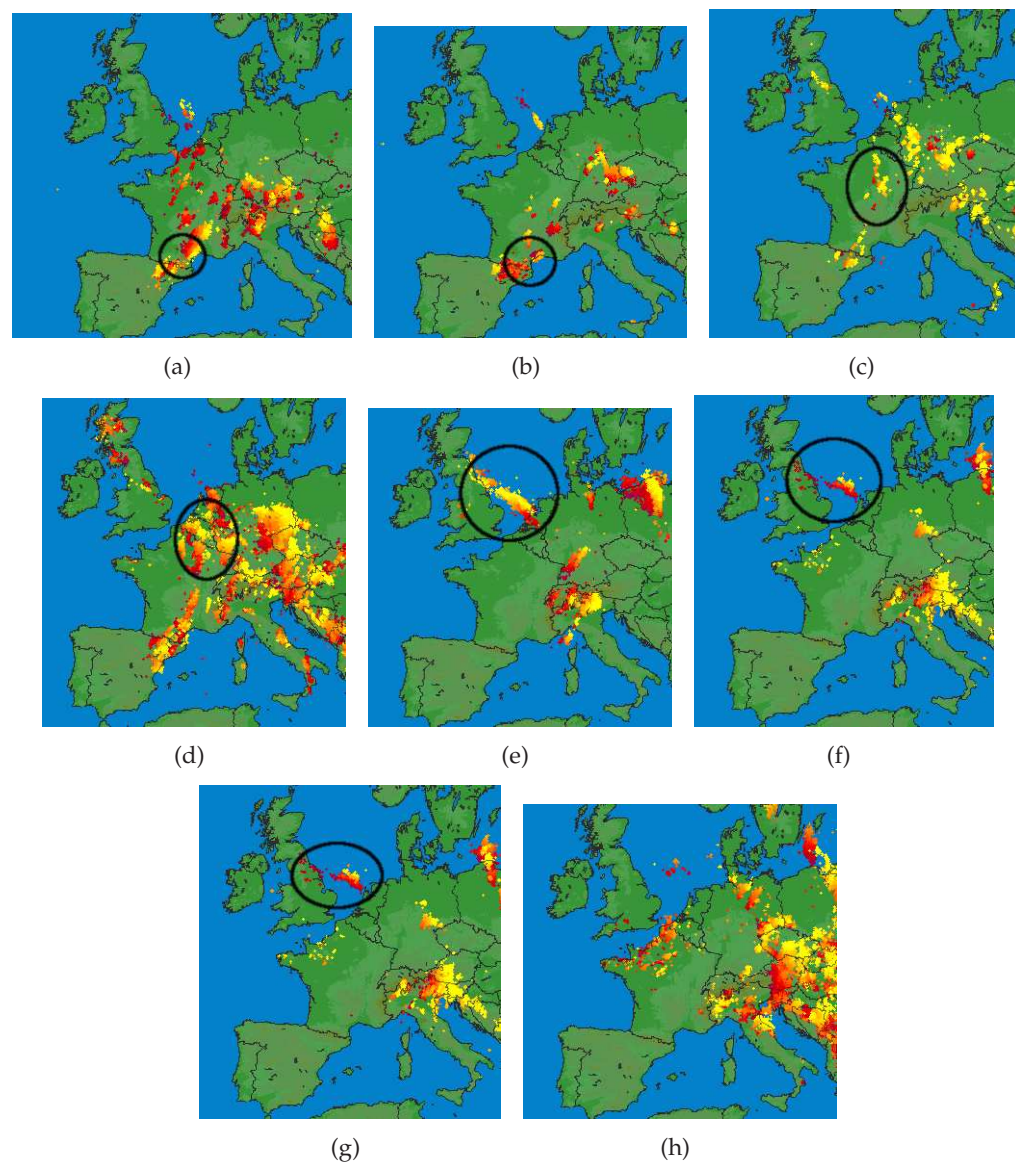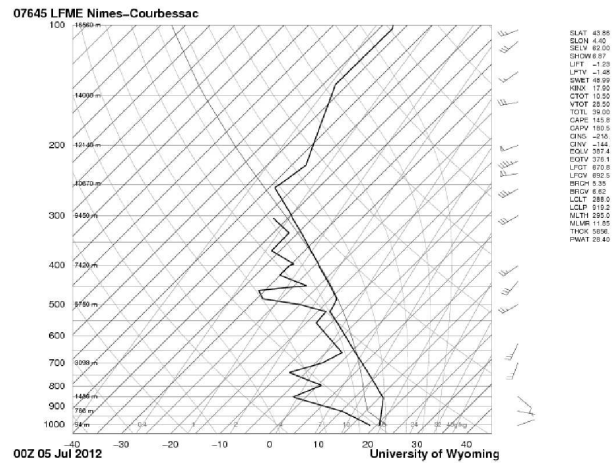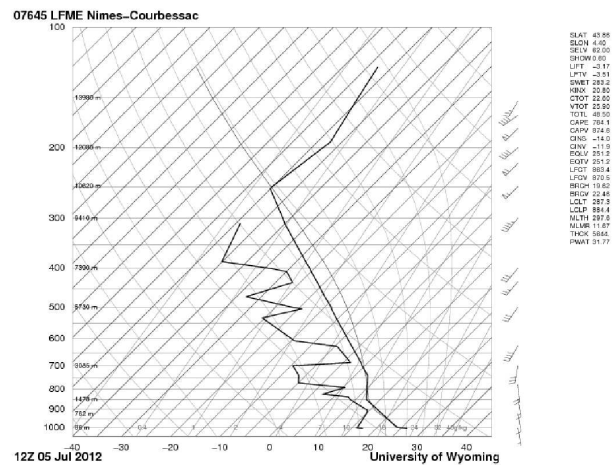
Figure 3.19: Lightning reports every 6 hours starting at 00 UTC 5 July 2012 and ending at 18 UTC 6 July 2012. Taken from www.lightningmaps.org

(a)

(b)

Figure 3.20: Atmospheric profiles (skew-T plots) from the radiosonde ascents at NimesCourbessac for (a) 00 UTC 5 July 2012 and (b) 12 UTC 5 July 2012. Courtesy of University of Wyoming.

3.3.4 Structure and evolution of the MCS determined using operational NAE Model Forecasts

For this Section operational six-hourly analyses from the North Atlantic European model are used with their intermediate hourly forecasts for the period 00 UTC 5 July to 12 UTC 6 July 2012. This 36 hour period is deemed long enough to include the initiation, maturity and decay of the MCS and to track the movement of the system, as forecast by the model. The NAE operational forecast is used to analyse the PV structure of the MCS, precipitation, cloud cover and convective instability. The following time line of development of the MCS is used throughout the analysis due to the 4 stages discussed in the previous section:

- 00 UTC 5 July 2012: Initiation of convection,

- 09 UTC 5 July 2012: Deep convection is triggered

- 12 UTC 5 July 2012: MCS identified

- 18 UTC 5 July 2012: MCS is mature

- 00 UTC 6 July 2012: MCS is decaying

- 06 UTC 6 July 2012: decaying MCS is beginning to be influenced by a developing frontal cyclone

- 12 UTC 6 July 2102: Cyclone is present; no longer an MCS.

3.3.4.1 Precipitation

Precipitation begins to develop at 00 UTC 5 July 2012 (Figure 3.21(a)) similarly to in the rainfall radar (Figure 3.18(a)). The location and intensity of the developing rainfall matches well between the observations and NAE forecast. In the radar images precipitation is seen to increase from 00 UTC to 18 UTC and this is also the case for the NAE forecast (comparison to Figure 3.18(a)-3.18(d) and Figure 3.21(a)-3.21(c)). For this case, the rainfall became more intense with time as the MCS developed, with rainfall amounts increasing from 2 mmhr^{-1} to around 10 mmhr^{-1} from 00 UTC (Figure 3.21(a)) to 18 UTC (Figure 3.21(c)). The rainfall radar shows rainfall rates of >10 mmhr^{-1} for the MCS at

18 UTC 5 July 2012 (Figure 3.18(d)) suggesting the NAE model produces rainfall which is too weak.

At 00 UTC 6 July 2012 the MCS beings to decay indicated by a weakening of the most intense rainfall and most of the rainfall now being <5 mmhr^{-1} (Figure 3.21(d)). This again corresponds well with the rainfall radar (Figure 3.18(e)). After this time the area and intensity of rainfall grows as the cyclone begins to develop (Figure 3.21(e)). In the rainfall radar the area of rainfall increases, but the intensity does not. There is a line of intense rainfall that occurs that corresponds to the lightning reports at the same time (Figure 3.18(f) and Figure 3.19(f)). In the NAE model, as the cyclone develops the rainfall intensity increases and becomes too strong in relation to the rainfall radar.

3.3.4.2 Environmental convective instability

Initial triggering of convection occurs at 00 UTC 5 July 2012 above 700 hPa. This is because the convection is developing in a region of more moist air than the surrounding conditions and initial triggering occurs due to the elevated orography of the Pyrenees (elevated at 3000 m; Figure 3.22(a)). South of this convection though there is a region of instability that is present with a layer of moist air (high θ_w, Figure 3.22(a) and high relative humidity, Figure 3.23(a), due to a long track over the Atlantic ocean) trapped beneath around 900 hPa. A layer of dry air from 900 hPa to 600 hPa occurs, due to the air at this level having a long track over Spain over the preceding days. Instability grows in the moist, warm layer trapped beneath the dry, warm layer and tracks northwards, with storms developing above the layer of instability with cloud developing from 750 hPa to 250 hPa (Figure 3.22(b)).

The MCS develops above this layer of dry air after initially developing to the north of it as the air at lower levels is moving quicker. Now the convection is only able to occur from 700 hPa level as the instability in the lower levels has yet to be released. By 09 UTC secondary triggering occurs as instability in lower levels is released due to lifting by the combination of the cold front, the weak upper level trough, passage over the Massif Central mountains and the weak surface heating (not shown here) and breaks through the dry air at 900–750 hPa with convection developing at all levels (Figure 3.22(b) and Figure 3.22(c)). Convection develops in the warm air in front of the cold front and larger scale lifting is occurring in the mid troposphere due to an ascending warm conveyor belt

(ascent ahead of the upper-level trough). This secondary convection, which leads to the release of further instability, allows the organisation of individual thunderstorms into a developing MCS with both cloud cover and ascent increasing (Figure 3.22(b) and Figure 3.22(c)). The dry layer of air can be seen in the radiosonde ascent in Figure 3.20(a) with temperature increasing with height up to 850 hPa and the largest difference between the dew point temperature and temperature of the air at this height indicating a warm, dry layer.

There is considerable amounts of CIN at 00 UTC 5 July indicating why convection only occurs above this level. There is CAPE in the profile above this level though to tropopause level (as it is above the dry layer) again indicating why ascent occurs. At 09 UTC, when secondary convection occurs, the dry air at lower levels still exists but the CIN has been removed to allow triggering of convection from lower levels (Figure 3.20(b)). At 00 UTC 5 July 2012 there is approximately 1000–1600 Jkg^{-1} CAPE available where the MCS begins to develop (Figure 3.24(a)) but there is considerable CIN present preventing convection from lower-levels (300 JKg^{-1}). By 09 UTC there is around 1800 JKg^{-1} CAPE (not shown) and after secondary triggering occurs at 09 UTC the CAPE reduces to 800 JKg^{-1} at 12 UTC. At 09 UTC, the CIN is removed so strong convection occurs from near the surface (Figure 3.24(b)). The second MCS which forms over south France has 1600 Jkg^{-1} CAPE associated with it before it triggers (Figure 3.24(b)).

At 00 UTC relative humidity is high (>80%) in all levels where the convection is occurring (Figure 3.23(a)). Behind the convection the relative humidity is very different. Here the layer of dry air can be seen as a distinct layer of lower relative humidity (50%), with a layer of high relative humidity below it (>80%, under 900 hPa). At this time there is only a small area of deep cloud since all the instability has not been released (this happens later at 09 UTC 5 July 2012; Figure 3.23(b)). By 18 UTC when the MCS is fully mature, it can be seen that there is a large area of high relative humidity (>80%) indicating the presence of a large area of deep cloud (Figure 3.23(c)).

3.3.4.3 Potential Vorticity structure in the MCV

Horizontal cross-sections at 600 hPa show there to be an area of anomalous positive PV with associated ascent, where the MCS is developing (Figure 3.25(a)). This positive PV anomaly appears to grow in strength from 00 UTC 5 July to 11 UTC 5 July 2012 (growth

between 00 UTC and 09 UTC can be seen in Figures 3.25(a), Figure 3.26(a), Figure 3.25(b) and Figure 3.26(b)) then remains at a sustained strength from 12 UTC 5 July 2012 until around 21 UTC 5 July (Figure 3.26(c) and Figure 3.25(c)) when the positive PV region begins to break up and becomes less intense (Figure 3.26(d) and Figure 3.25(d)).

The positive PV anomaly tracks northeast from northern Spain at initiation at 00 UTC 5 July 2012, then from 07 UTC 5 July the positive PV anomaly tracks northwards until 00 UTC 6 July. After this time it then breaks up and tracks northwest across England and northern Ireland before wrapping back around to affect the Midlands due to the cyclone that forms. The largest positive PV anomaly value remains consistently around 4–4.5 PVU. Small amounts of negative PV with a magnitude of -1 PVU occur in upper-levels, either side of the positive PV anomaly and above it (see Figures 3.26(a)-3.26(e)).

The MCS is deemed mature at 18 UTC 5 July 2012 as there is a large area of deep cloud cover, a strong positive PV anomaly at mid-levels and deep convection occurring (Figure 3.26(c) and Figure 3.23(c)). At 18 UTC 5 July 2012 a further positive PV anomaly begins to form in mid-levels associated with a second MCS. The MCS is deemed to be decaying after 21 UTC 5 July 2012 as the positive PV anomaly in mid-levels begins to weaken (not shown here). By 00 UTC 6 July 2012 the positive PV that has been tracked during this analysis has weakened, with ascent decreasing and cloud cover breaking up (Figure 3.26(a)).

After 00 UTC on 6th July it becomes difficult to determine the location of any positive PV anomaly in the model associated with this MCS since it begins to wrap up with positive PV associated with the developing cyclone over the UK. The cyclone causes the development of a tropopause fold (Figure 3.26(e)). Between 06 UTC 6 July 2012 and 12 UTC 6 July 2012 the positive PV anomaly almost fully decays and ascent begins to weaken, as the cyclone strengthens (Figure 3.26(f)).

This case was interesting as the jet stream was very far south and hence interacted with air passing over the Iberian Peninsula. This interaction may have fed the development of the positive PV anomaly by allowing convection to be initialised as the air passed over the mountains here at 00 UTC 5 July 2012.

3.3.5   Comparison to Browning and Hill (1984) using NAE model analyses

In Section 3.3.3 the four stages of MCS development and decay are given for this case study. In this section the stages are updated to include information gathered from the NAE model analyses.

- Stage 1: 00 UTC–12 UTC 5 July 2012: CAPE is 1000–16000 JKg^{-1} as some convection is initiated due to the orography of the Spanish plateau at 00 UTC. Deep cloud develops and is indicated by high relative humidity from the surface to tropopause level which initially was from 700 hPa to tropopause level. A positive PV anomaly starts to develop at mid-levels and strengthens over time. Deep convection occurs at 09 UTC which removes most of the CAPE and allows for the development of further individual thunderstorms which being to organise into an MCS.

- Stage 2: 12 UTC–21 UTC 5 July 2012: The amplitude of positive PV at mid-levels increases up to a maximum of 4–4.5 PVU at 600 hPa. The horizontal and vertical extent of the positive PV increases, along with the amount of negative PV occurring at upper-levels increasing. Deep convection occurs and is sustained with a magnitude of $0.2ms^{-1}$.

- Stage 3: 21 UTC–03 UTC 6 July 2012: MCS begins to decay. Positive PV anomaly at mid-levels begins to weaken and break up.The vertical extent of the PV tower decreases. Cloud cover begins to break up. Convection is sustained but precipitation is weaker.

- Stage 4: 03 UTC–12 UTC 6 July 2012 MCS fully decays and begins to wrap around a developing cyclone that is affecting the UK. Positive PV at mid-levels weakens further but further positive PV anomalies develop in association with the cyclone. A clear tropopause fold associated with the cyclone can be seen from 06 UTC.

3.3.6   Case Summary

- The synoptic situation was similar to that of a modified Spanish plume. Large amounts of instability grew across Spain and France preceding the MCS due to the almost stationary low-pressure system over the Atlantic in the days before.

- A deep convective feature with associated PV anomalies exists in the NAE model forecast and corresponds to the area of lightning reports and large area of rainfall which initiate at 00 UTC 5 July 2012. CIN is present at this time though so convection only occurs from an elevated layer around 700 hPa.

- There are two distinct layers of air masses. Below 900 hPa the air is warm and moist. From 900 hPa to 700 hPa there is a layer of dry, very warm air. Initial triggering of convection occurs to produce convection above 700 hPa.

- Further triggering of convection occurs at 09 UTC as weak surface heating and forcing along the gradient of a cold front and a weak upper-level trough allow for the removal of CIN and the CAPE halves from 1600 JKg^{-1} to 800 JKg^{-1}. Deep convection occurs from near the surface creating individual thunderstorms which begin to organise into one system.

- This case appears to be of the correct size and duration to satisfy the definition by Gray and Marshall (1998) indicating that it is an MCS. The MCS develops and is sustained between approximately 12 UTC 5 July 2012 and 21 UTC 5 July. Before and after these times the MCS is either developing or decaying. At 18 UTC 5 July 2012 is MCS is deemed most mature.

- After 03 UTC 6 July 2012, a developing frontal cyclone begins to impact the decaying MCS and causes an increase in convection associated with the PV tower.
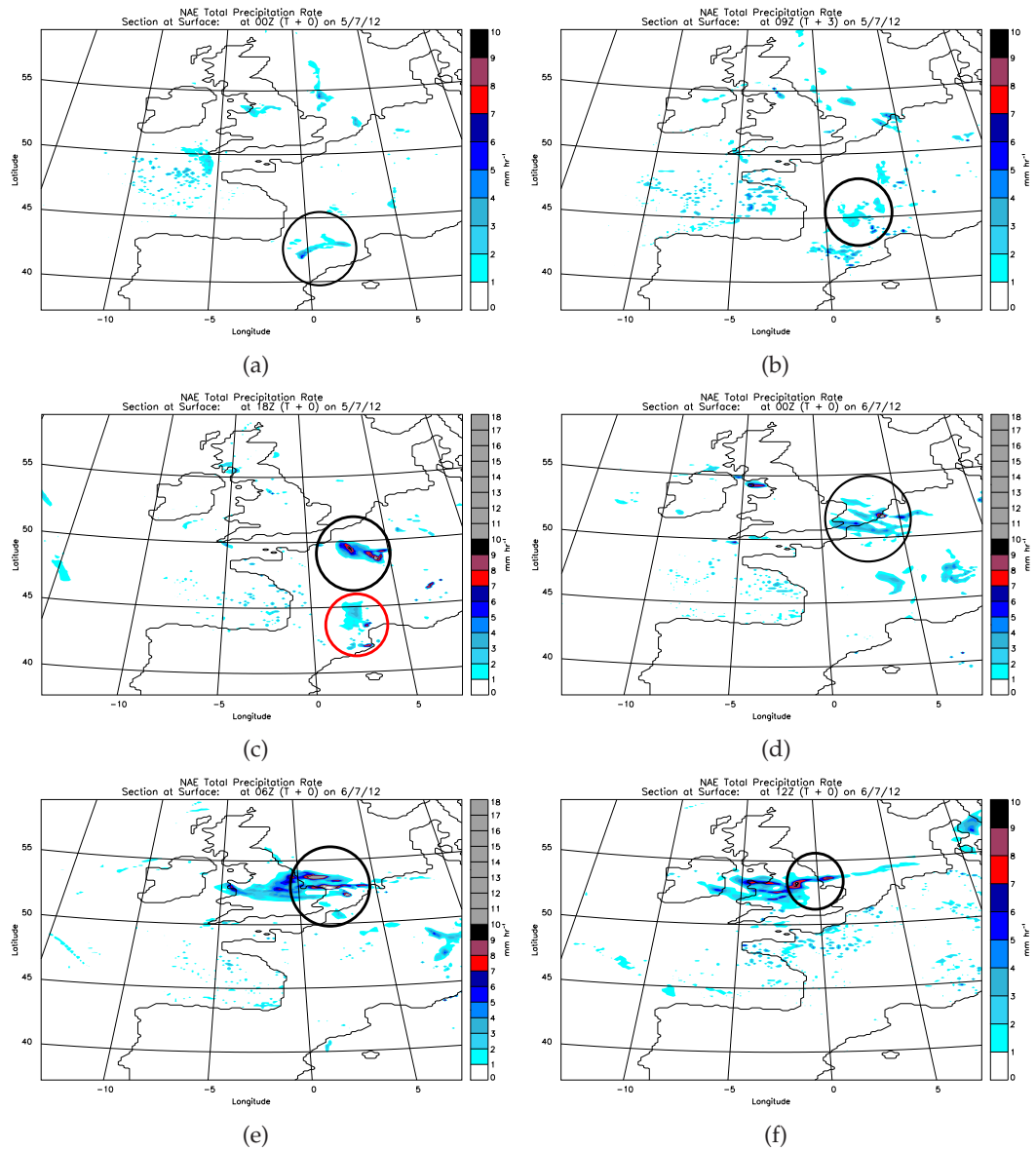
Figure 3.21: Total precipitation rates for (a) 00 UTC 5 July 2012, (b) 09 UTC 5 July 2012, (c) 18 UTC 5 July 2012, (d) 00 UTC 6 July 2012, (e) 06 UTC 6 July 2012 and (f) 12 UTC 6 July 2012. The black circles indicate the location of the northern France MCS. The red circle indicates the second MCS that developed over south France.
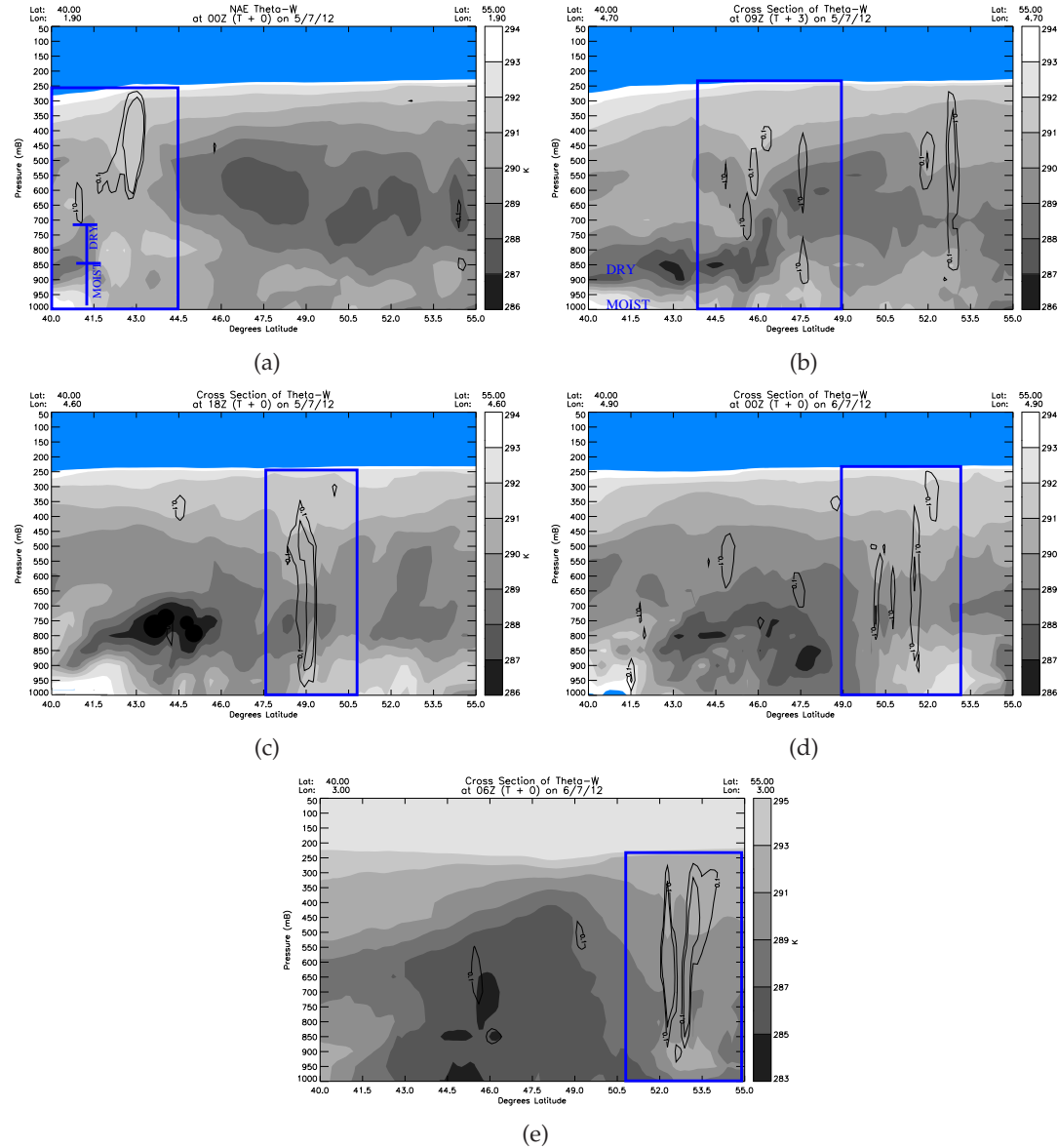
Figure 3.22: Vertical contours of θ_w (filled contours) with contours of ascent at 0.1 ms^{-1} and 0.2 ms^{-1} FOR (a) 00 UTC 5 July 2012, (b) 09 UTC 5 July 2012, (c) 18 UTC 5 July 2012, (d) 00 UTC 6 July 2012 and (e) 06 UTC 6 July 2012 (different contours were used for this plot due to a reduction in θ_w temperatures). The blue rectangle indicates the location of the MCS. Blue shading indicates θw temperatures exceeding 294 K.
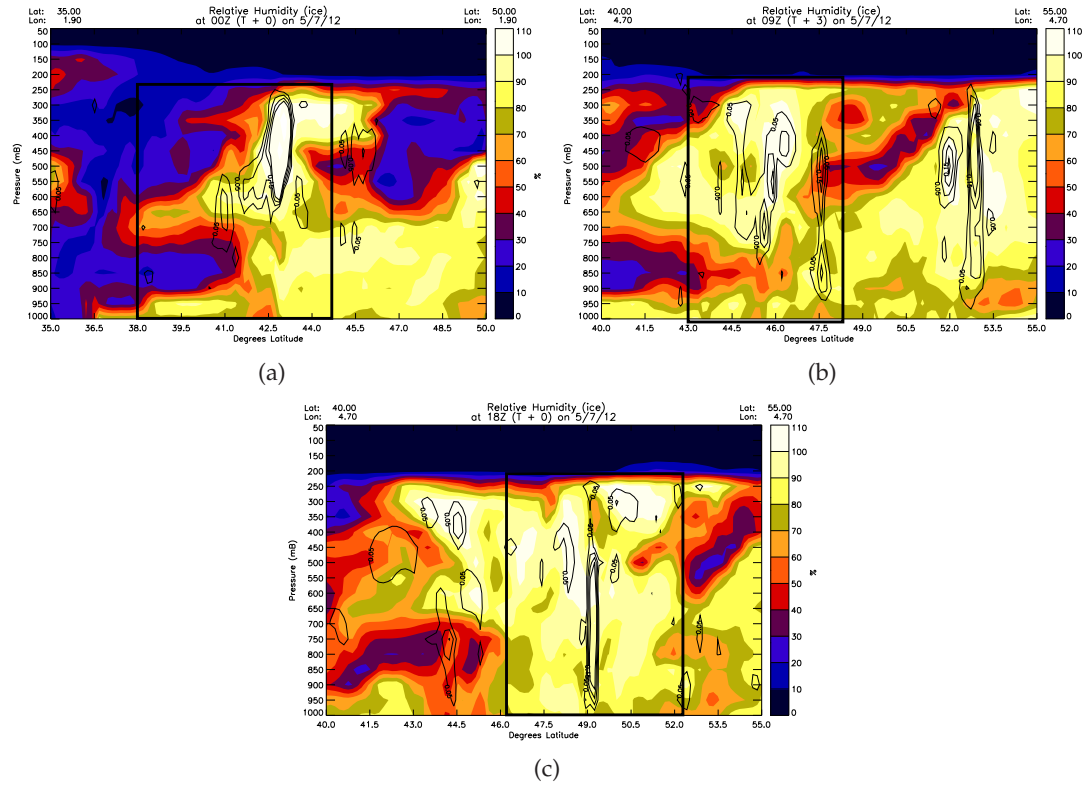
Figure 3.23: North-south cross sections of relative humidity for 5 July 2012 (a) 00 UTC (initial orographic convection), (b) 09 UTC (triggering of convection) and (c) (c) 18 UTC (MCS mature). The contours indicate ascent at 0.05, 0.1 and 0.2 ms^{-1}. The rectangle indicates the MCS location.
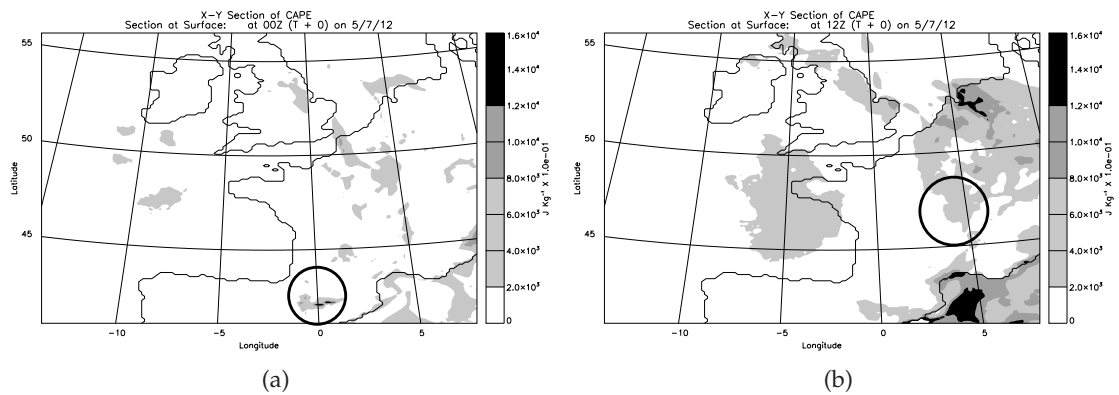

Figure 3.24: CAPE calculated from the NAE model, lifting from 1000 hPa for (a) 00 UTC 5 July 2012 and (b) 12 UTC 5 July 2012.
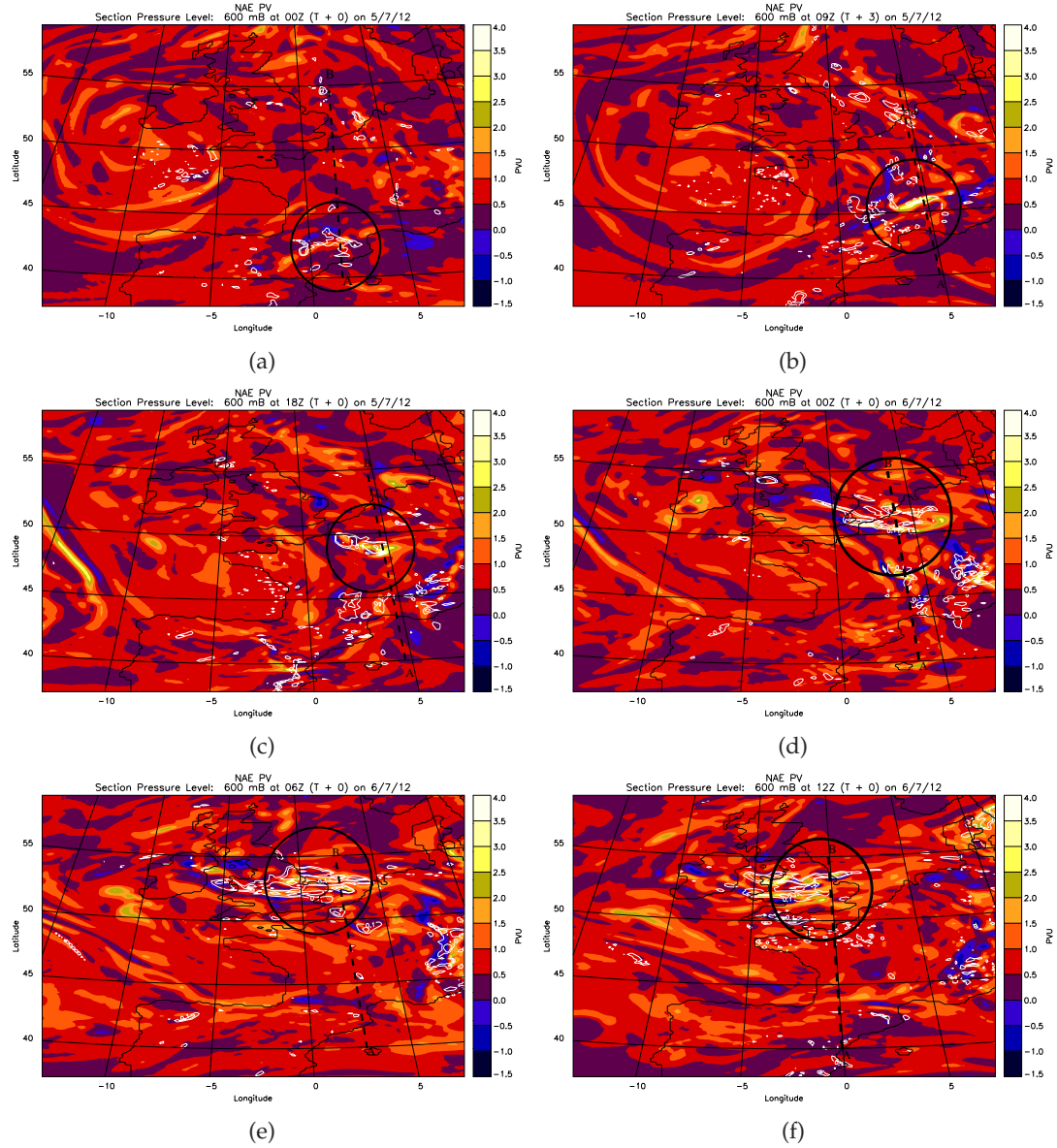
Figure 3.25: NAE model forecast plots for PV (units $Km^2Kg^{-1}s^{-1}$ is equivalent to PVU) at 600 hPa for times (a) 00 UTC 5 July 2012, (b) 09 UTC 5 July 2012, (c) 18 UTC 5 July 2012, (d) 00 UTC 6 July 2012, (e) 06 UTC 6 July 2012 and (f) 12 UTC 6 July 2012. Filled coloured contours show PV, white contours show ascent greater than 0.1 ms^{-1}. The black lines A-B show the cross-sections used for the corresponding time the vertical cross-sections of PV.
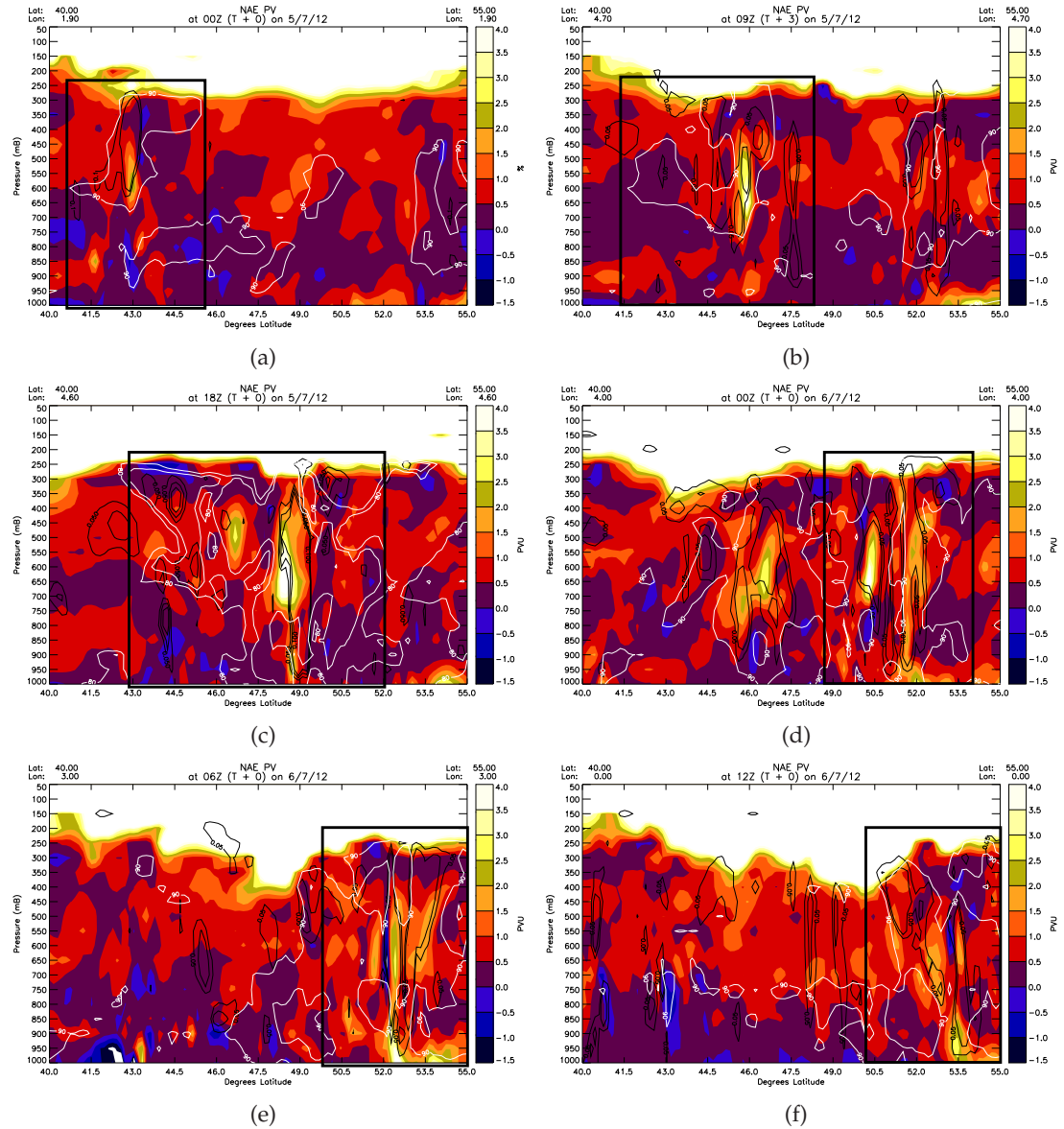
Figure 3.26: PV north-south cross sections taken through the MCS at each time for (a) 00 UTC 5 July 2012 (initiation of convection), (b) 09 UTC 5 July 2012 (this is given as this time will be used extensively throughout Chapter 4), (c) 18 UTC 5 July 2012 (MCS mature) and (d) 00 UTC 6 July 2012, (e) 06 UTC 6 July 2012 and (f) 12 UTC 6 July 2012. Black contours indicate areas of ascent >0.1 ms^{-1} and white contours indicate areas of relative humidity $>90\%$.

3.4 Comparison of MCS case studies

The following section compares and contrasts four MCS case studies, the two case studies studied in this Chapter (6 to 7 May 2011 and 5 to 6 July 2012) and the two case studies of MCSs analysed by Lewis and Gray (2010) (from 8 June 2007 and 19 to 20 June 2007). The four cases are labelled as 8 June 2007 (Case 1), 19–20 June 2007 (Case 2), 6–7 May 2011 (Case 3) and 5–6 July 2012 (Case 4). The aim is to analyse the synoptic and mesoscale conditions associated with each MCS case.

3.4.1 Occurrence - time and location

Cases 1, 2 and 4 all developed over central France whereas Case 3 developed north of Spain in the Atlantic Ocean. Cases 1 and 3 initiated in the late evening and became MCSs by late evening. In contrast, Case 2 initiated at midday (12 UTC) and was deemed an MCSs by 18 UTC. Case 4 initiated at midnight, but further convective triggering occurs at 09 UTC before being deemed an MCS around 12 UTC. MCSs in Cases 1, 2 and 4 all reach the UK around East Anglia after initiating over central France. Case 3, however developed further west over the Atlantic sea and tracked across the south coast of the UK near Southampton.

3.4.2 Synoptic environment and observations

Case 3 does not fit into any one particular category of a Spanish plume type; however, is similar to that of a European easterly plume in some aspects (as defined by Lewis and Gray (2010)), which was the type of Spanish plume that occurred in Case 1. When comparing the synoptic charts of these two cases, Figure 3.27(a), shows a low pressure northwest of the UK (low centre off picture) whereas in Case 3 the low pressure was further east and there was also a distinct low pressure in the area where the MCS developed, along with no blocking high pressure systems over Europe which is the atypical scenario for a European Easterly plume. Case 3, shows some similarities to a European easterly plume, but cannot be defined as any of the three Spanish plume types defined by Lewis and Gray (2010) (Figure 3.27(c)). In contrast, Cases 2 and 4 are examples of modified Spanish plumes, seen in Figures 3.27(b) and 3.27(d) (as defined by Lewis and Gray (2010)), signified by low-pressure systems close to the southwest of the UK. Since

the cases are of differing types of Spanish plume it is expected that the movement and mesoscale features of the MCSs will also differ.

Rainfall radar images show that Cases 3 and 4 were less intense than Cases 1 and 2 with a smaller area of rainfall of >10 mmhr^{-1} associated with the MCS occurring (not shown here).
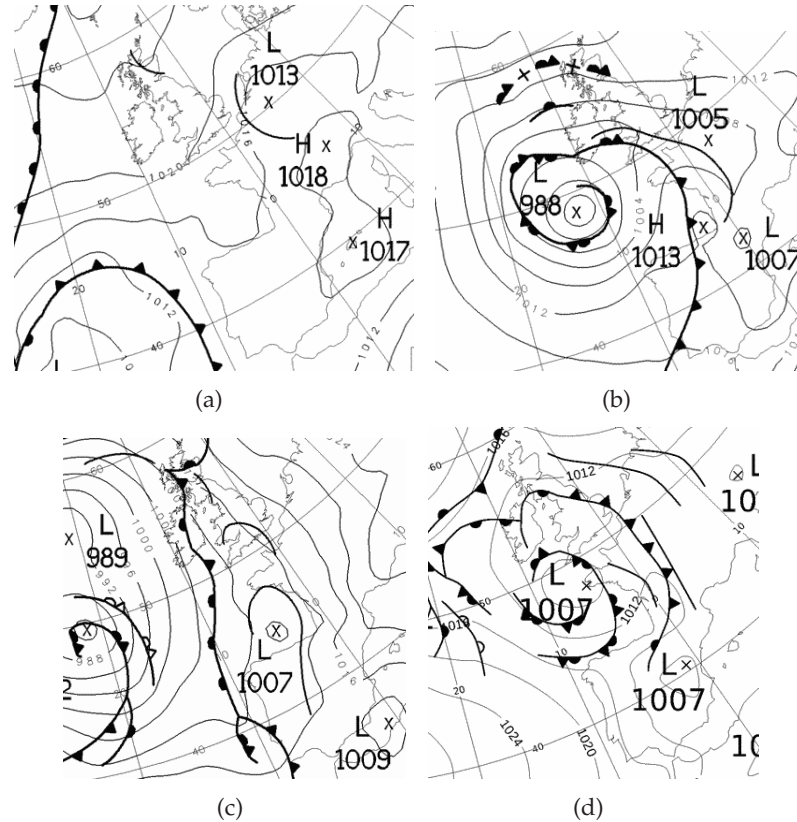

Figure 3.27: (a) Analysis chart for 00 UTC 8 June 2007. The MCS was marked by a weak low with an associated trough line to the southeast of the UK (Lewis and Gray (2010)), (b) Analysis chart for 18 UTC 19 June 2007, (c) Analysis chart for 00 UTC on 7th May 2011 and (d) Analysis chart for 12 UTC 5th July 2012. Each chart was chosen as the time deemed to be just after the initial development of the MCS before maximum intensity has been achieved (Archived by www.wetter.de).

3.4.3 Environmental stability

Cases 1 and 2 both have a convective cap (layer of moist air trapped beneath layer of dry air making it unstable below this level) at 900 hPa (Figures 3(a) and 3(b) of Lewis and Gray (2010)). Case 3 has a cap at 700 hPa and Case 4 had a cap around 900–850 hPa. Interestingly, in Cases 1 and 3 potential instability occurs from an elevated level above the 'cap' of 900 hPa (Figure 3.28(a)) and 800 hPa (Figure 3.28(c)), respectively. Con-

versely, Cases 2 and 4 experience potential instability from the surface (Figures 3.28(b) and 3.28(d)) indicating the possible connection between Spanish plume type and the level of potential instability.

Case 3 appears different to the other three cases (which have a warm, moist 'plume' of air visible in low levels travelling northwards (not shown here)) because the near surface air is cooled by the sea. In contrast, the air above is warmer and drier as it has come from the Spanish plateau which is elevated therefore convection is not possible from the lowest levels until it is triggered. Case 3 is also colder in general than the other cases as it is from May, whereas the others are from June and July. In Case 3 strong ascent occurs from 950 hPa to tropopause level (Figure 3.28(c)) as the air below 950 hPa is stable as it is dry and warm. In Case 4 peak values of CAPE (before convection initially triggers due to the effects of the Pyrenees) at 00 UTC 5 July are 1600 Jkg^{-1} (not shown), this is similar to the amount of CAPE seen in Case 1 before triggering (not shown). In Case 3 peak values of CAPE were 800 Jkg^{-1} which is considerably less than for the other cases. In comparison Case 2 had 2400 Jkg^{-1} of peak CAPE associated with it (in each Case peak values were found from parcel ascents from 1000 hPa; CAPE for Case 1 and 2 were taken from Lewis and Gray (2010)).

3.4.4   Mesoscale convective vortex (MCV)

This Section compares the potential vorticity structures found in the four European case studies to determine if there were any similarities. The PV structures of these European cases are then related to the MCV structure found in USA MCSs, by comparing these cases to the schematic from Fritsch *et al.* (1994). This schematic is based upon observations only and not model simulations.

The following details the similarities and differences between the four cases, along with a comparison to the schematic from Fritsch *et al.* (1994) (see Figure 1.15).

Similarities and differences in PV for each Case

- All Cases have a well defined PV 'tower' with the strongest positive PV anomalies at 500–700 hPa (Figures 3.29(a)–(d)).

- The vertical extent of the PV tower extends from the surface to tropopause level
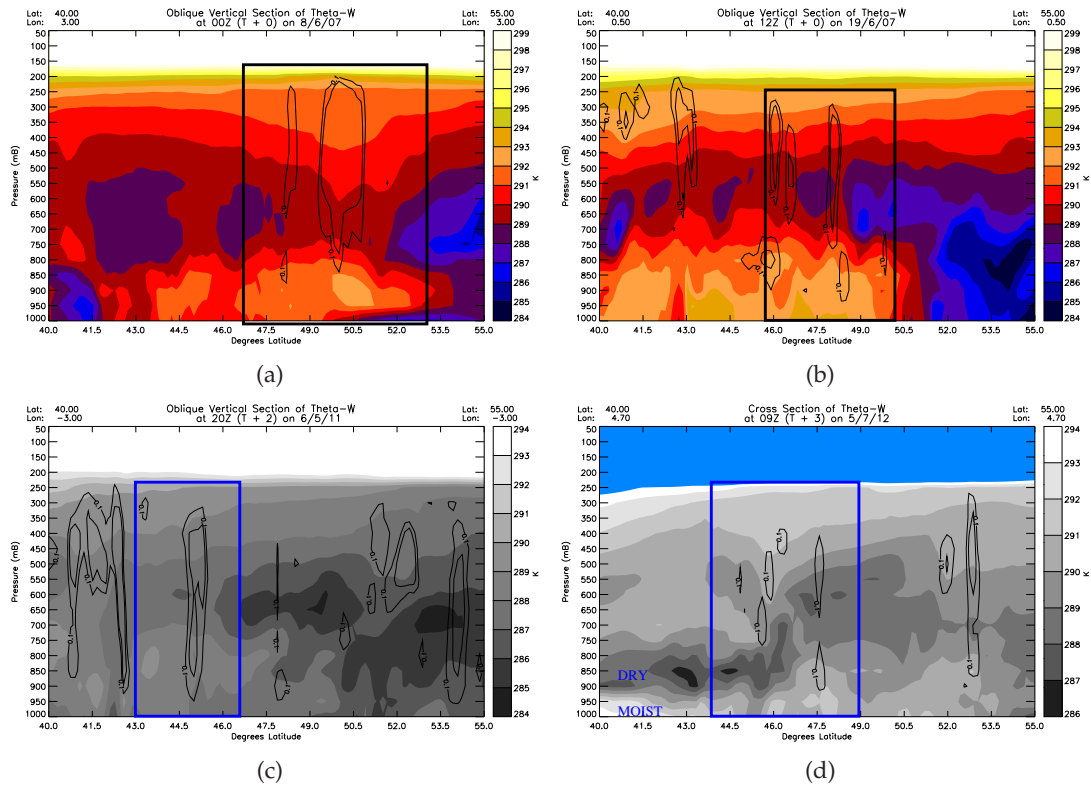
Figure 3.28: NAE operational forecast north-south vertical cross-sections of θ_w through the point of MCS triggering for (a) Case 1 00 UTC 8 June 2007, (b) Case 2 18 UTC 19 June 2007, (c) Case 3 20 UTC on 6 May 2011, and (d) Case 4 09 UTC 5 July 2012 . Contours of ascent at the 0.1 ms^{-1} and 0.2 ms^{-1} level are also plotted. Rectangle indicates the MCS in each Case.

except in Case 3 where it extends from 950 hPa.

- Each PV anomaly covers around 60 km in width. This is on the margin of whether the convection should be resolved or not in the NAE model with 12km grid spacing (Figures 3.29(a)–(d)).

- Case 3 initiates over sea, tilts with height and is less intense than the other cases in terms of PV anomalies (Figure 3.29(c)).

- All have negative PV above and to the sides of the positive PV tower (Figures 3.29(a)–(d)).

Comparison to Fritsch *et al.* (1994) (see Figure 1.15)

- All four Cases have a PV tower with maximum PV in middle-levels and minimum PV at upper-levels at similar heights to USA MCSs.
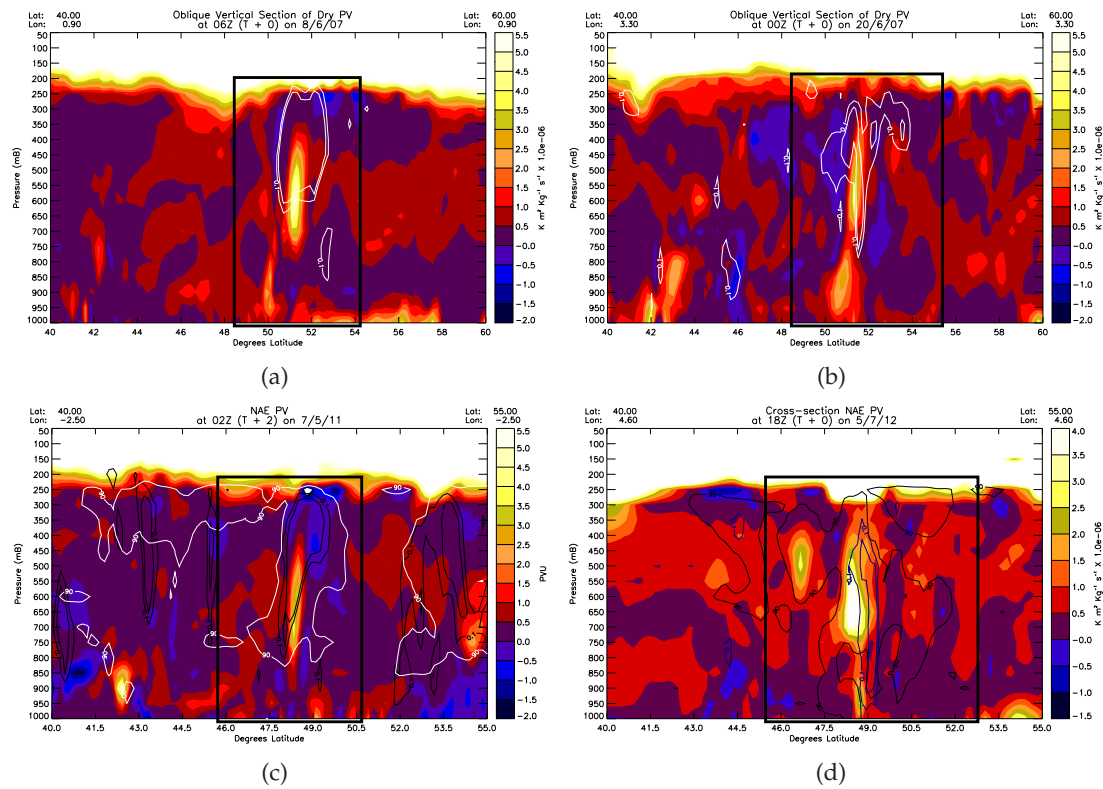
Figure 3.29: NAE forecast vertical north-south cross-sections of PV for (a) 06 UTC 8 June 2007, (b) 00 UTC 20 June 2007, (c) 02 UTC on 6 May 2011, and (d) 18 UTC 5 July 2012. Each forecast was chosen as the time deemed to be at the time the MCS was most mature and/or the MCV was most intense. White contours of ascent at 0.1 and 0.2 ms^{-1} are also plotted.

- Negative PV aloft occurs to the sides of the positive PV anomaly in these cases rather than just directly above it as suggested by the USA schematic. This may be due to the use of model data rather or that MCSs in Europe are usually less intense.

- Width of the PV tower spans 60 km in comparison to 250 km in USA.

- Cold pools and negative PV at low-levels did not occur in all cases as suggested should happen in the schematic of US MCSs.

3.4.5 Summary of the four cases

The table below provides a summary of the key information discovered for Cases (1)-(4).

	Case 1	Case 2	Case 3	Case 4
Initiation of convection	Late evening	12 UTC	20 UTC	09 UTC
Initiation location	Central France	Central France	North of Spain over sea	Central France
MCS identified	00 UTC	18 UTC	00 UTC	15 UTC
MCS location	N. France	N.France	NW. France	N. France
Type of Spanish plume	European Easterly	Modified	Not defined as any	Modified
Potential-instability level	900–650 hPa	1000–600 hPa	750–450 hPa	1000–600 hPa
Convective cap level	900 hPa	900 hPa	700 hPa	900–850 hPa
PV tower maximum value (PVU)	5.5	4.5	3.5/4	4.5
Level of PV maximum	700–500 hPa	700–500 hPa	700–500 hPa	700–500 hPa
MCV extent horizontal	60 km	60 km	60 km	60 km
MCV extent vertical	800–350 hPa	1000–350 hPa	800–400 hPa	1000–350 hPa
Ascent level in MCS	900 hPa	900 hPa	950 hPa	900 hPa

Table 3.1:: Comparison of the four MCS case studies

3.5   Conclusions

The aim of this Chapter was to investigate the question posed in Section 1.1: What are the mesoscale and synoptic-scale structures of PV anomalies generated by MCSs? To answer this a number of sub questions were posed in Section 3.1 to analyse during this Chapter. The conclusions are now discussed in relation to these questions.

1. **Are the synoptic conditions conducive to MCS formation?** Both cases developed an MCS in a Spanish plume environment with a movement of moist, warm air inland from the Atlantic Ocean towards the east. A low pressure system to the west of the UK in the Atlantic Ocean causes a movement of air northwards from Spain towards France and then the UK. Instability grew over time due to a dry layer of air capping a layer of moist warm air. This allowed CAPE to develop and for deep convection to occur once triggering of convection occurred.

2. **Do MCSs satisfying the criteria from Gray and Marshall (1998) form (see Section 1.2.1)?** Both cases satisfy the MCS criteria with a large area of rainfall (greater than $10\,\mathrm{mmhr}^{-1}$), lightning reports (greater than 100 km in any direction), warm surface temperatures and identification of a cold cloud anvil on satellite imagery.

3. **What led to the triggering of the MCSs?** The 6 May 2011 case, does not fit into any one particular Spanish plume category. The 6 May case triggers initially due to the orography of the Spanish plateau before further triggering occurs due to weak upper-level forcing. The 5 July 2012 case, however, is a modified Spanish plume case. The 5 July case initially triggers due to the orography of the Pyrenees before further triggering occurs in the warm air ahead of a cold front and due to forced ascent by the weak upper-level trough.

4. **What is the PV structure of the MCSs?** Both cases have a PV structure which develops and matures along with an increase in the rainfall and convection from the time of triggering. A positive PV anomaly (strongest at 600 hPa in both cases) is found at mid-levels and increases in magnitude and vertical extent as the MCS matures (by maturity the positive PV anomaly reaches from near surface to tropopause level). This positive PV anomaly at mid-levels tracks along with the MCS, northwards towards the UK. Negative PV anomalies occur above and to the

sides of the positive anomaly with a magnitude of -1.5 PVU.

To determine the answers to the above questions an analysis of whether the NAE model produced an MCS that compared well to reality was required and a number of things to analyse to determine this were described in Section 3.1. The results are now given below:

- **An MCS in the correct location in comparison to reality as determined from the location of rainfall**: the NAE model produces an MCS for both cases, but both MCSs occur further south than in reality when compared to rainfall radar and this is particularly apparent in 5 July 2012 case. The NAE model created too little rainfall in both cases compared to reality (particularly misses the weak stratiform rainfall).

- **An MCV structure typical of an MCS with related PV anomalies**: both cases create an MCV structure with a positive PV anomaly tower, with a maximum PV value at mid-levels around 600 hPa and a magnitude of approximately 4–5 PVU. The PV tower becomes more intense as the MCS matures and then the PV tower decays as the MCS decays. Both cases create negative PV to the sides and above the positive PV tower which was not expected as Fritsch *et al.* (1994) suggested negative PV occurs above the positive anomaly only. Negative PV anomalies above and to the side of this positive PV anomaly occur with a magnitude of -1.5 PVU from approximately 250 hPa to 500 hPa.

- **the expected conditions related to Spanish plume and instability**: In the NAE model both cases have a movement of air from Spain towards the UK with a layer of moist air capped by a layer of dry air. The NAE model for both cases show areas of high θ_w (up to 294 K in the lower troposphere) and high relative humidity (up to 90%) indicating a layer of warm, moist air and in both cases this layer is capped by a layer of lower θ_w (approximately 285 K) and low relative humidity (20–40%) indicating a layer of drier air which is stable. The 6 May case has a moist layer trapped between 950–700 hPa whereas the 7 July case has a moist layer trapped below 900 hPa.

- **CAPE/CIN in amounts necessary for an MCS**: both cases have a build up of CAPE before the MCS triggers but the 5 July 2012 case has a larger amount of CAPE

(around 1600 JKg^{-1} in comparison to approximately 800 Jkg^{-1} for 7 May 2011 case). The 5 July 2012 case has a typical CAPE value for MCS development (with a similar amount to that of case 1 from Lewis and Gray (2010) but less than the 2400 Jkg^{-1} from case 2 of Lewis and Gray (2010)).

- **a similar track of the system in comparison to reality**: both cases have a similar track in the NAE model to that which occurred in reality. Both cases move from Spain towards the UK in observations and in the NAE model. Both cases are just slightly delayed in reaching the UK (by approximately 1–2 hours) compared to reality due to them being further south in the NAE model (by approximately 50 km).

During this Chapter a number of other conclusions were formed:

- The PV structure created by the MCSs in each of the four case studies analysed using the NAE forecast model appears different to that of the MCV in Fritsch *et al.* (1994). The main difference is that while all cases have negative PV aloft, as in Fritsch *et al.* (1994), it tends to occur to the sides of the positive PV anomaly at upper-levels as well as above it instead of just diverging outwards (Figure 3.30). This could be due to the NAE model being used here to analyse the small-scale structures of the MCS whereas the Fritsch *et al.* (1994) figure was developed using observations only. The PV anomaly structure associated with MCSs may look very different depending on the grid-spacing of the model used. The negative PV anomalies diverging around the positive PV anomaly could also be caused by there being weaker convection in these European MCSs than occurs in MCSs that develop in the USA where Fritsch *et al.* (1994) looked at MCSs occurring. This structure could also be related to the resolution of the NAE model since it is convection-parametrizing so the convection is averaged over an entire grid box rather than being localised which could produce weaker convection and could lead to the lack of divergence of negative PV anomalies at tropopause level.

- Each of the four cases had a horizontal MCV extent of 60 km which is much less than the 250 km suggested by Fritsch *et al.* (1994). This is in line with the view that European MCSs are smaller than USA MCSs and could be related to there being less CAPE in European cases compared to that of USA MCS cases.

- It is hypothesised that the MCV structure created by the NAE model could be replicated by other grid spacing models too. If this is the case then this could have a significant effect on the forecast of the MCS itself. These negative PV anomalies produced at upper-levels could also impact on the circulation patterns in the forecast and consequently effect the downstream flow.
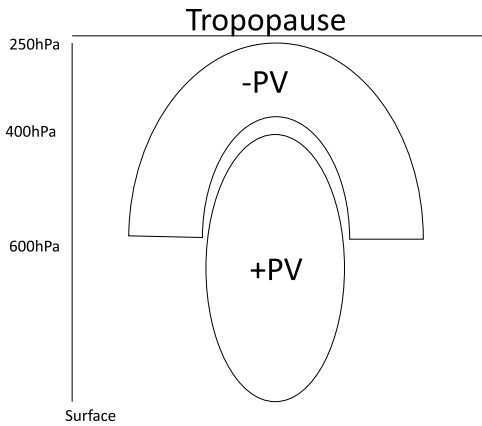

Figure 3.30: PV structure found to occur in UK and western European MCSs due to analysis of four case studies. For the NAE model the positive PV at mid-levels has a magnitude of 4–5 PVU, the negative aloft and to the sides has a magnitude of 1–1.5 PVU.

For the remainder of this thesis the MetUM is used to produce different grid spacing simulations of the MCS case study from 5 to 6 July 2012 to determine how the representation of convection and the associated PV anomalies varies depending on the grid spacing of the model. This case was chosen out of the two studied due to it being prolonged and gaining strength as it reached the UK. As the MCS reaches the UK it is impacted by a developing frontal cyclone. This interaction means that if the model failed to represent the MCS (or misrepresented it) then this could have a large impact on the subsequent forecast since the MCS wraps up with the cyclone causing large amounts of stratiform rainfall over the UK on 6 July 2012. ing at the synoptic charts? What is causing high PV/low PV which is not associated with the MCS

Chapter 4

Resolution dependence of modelled MCS case study

4.1 Introduction

The aim of this Chapter is to investigate the impact that using convection-permitting and convection-parametrising NWP models has on the forecast of the MCS case study from 5 July 2012 discussed in Chapter 3. The degree to which the representation of convection in the convection-permitting and convection-parametrizing models affects the forecast of potential vorticity, the associated windspeeds, potential temperature and the rainfall rates for the MCS is investigated. To investigate this, four different resolution models (Euro 4 km, Global, France 1.5 km and UKV models) will be compared and contrasted. The first 24 hours (00 UTC 5 July – 00 UTC 6 July) are investigated in this Chapter as it is thought that capturing the initiation stage of the MCS is a crucial aspect of an accurate forecast. If the MCS is not represented initially (or is poorly represented) then it is unlikely to be represented (or will be misrepresented) when mature and could have a large impact on the forecast of the MCS (and beyond this downstream in the days ahead).

Firstly, hypotheses are presented that form the motivation for the investigations conducted in this Chapter, before the methods utilised during the Chapter are discussed. Secondly, results are given for each of the four original model runs in terms of PV, rainfall and windspeeds. Thirdly, results are presented for the coarse grained models in terms of PV, rainfall and windspeeds. Finally, conclusions based on the hypotheses are presented.

4.2 Hypotheses

Four hypotheses will be examined during this Chapter to help answer the following question posed in Section 1.1: **How is the forecasting of MCSs affected by the representation of convection in NWP models (whether convection is parametrized or permitted by the model) and what are the associated PV structures produced?** These hypotheses are discussed below.

1. **Hypothesis: Convection and convective precipitation associated with the MCS will be represented better in the higher resolution models (when compared to reality), than in the Global model, since they represent convection explicitly.** It is expected that the track, timing, structure and intensity of convection and rainfall will be better represented by the Euro 4 km and UKV models (and the France 1.5 km model developed for this study), compared to coarser resolution models such as the NAE or Global models; however, the intensity may be too large in comparison to reality (Lean *et al.*, 2008) and the location may be slightly wrong in the convection-permitting models (Barrett *et al.*, 2016; Lean *et al.*, 2008). The higher resolution models which explicitly represent convection can have overactive updraughts as they cannot represent the turbulent mixing in clouds which in the atmosphere act to slow down updraughts. This can lead to updraughts which are too strong in the models compared to reality and thus too intense rainfall rates. The location of rainfall may be slightly wrong in the convection-permitting simulations as it is hard to predict all the small-scale features of the atmosphere initially due to insufficient observations or errors in the boundary conditions provided by the lower resolution convection-parametrizing model meaning that storms can develop in the wrong locations. The convection-permitting models are still expected to give a rainfall forecast that represents the MCS better than the convection-parametrizing model in terms of structure and intensity. The reasoning behind this hypothesis is detailed further in Section 1.4.1.

2. **Hypothesis: As the resolution increases the PV anomalies arising from diabatic heating due to convection will become better represented with a more detailed structure, have higher magnitude positive and negative PV anomalies and extend deeper in the vertical.** Since the typical width of the mesoscale convective

vortex (MCV) structure associated with the MCS is anywhere between 50–200 km (Bartels and Maddox, 1991, Brandes, 1990, Zhang and Fritsch, 1987) only the finer resolution model configurations will be able to resolve the main convective up-draught associated with the MCS without parametrizations; the MCV is the rotation around the PV anomaly, created in association with a MCS, therefore, the convective updraft is over an even smaller area. The forecast of the MCV should therefore, be better represented in the convection-permitting models. Convection-permitting simulations are able to simulate the local heating which occurs due to convection whereas convection-parametrization cannot represent this and simulates the average effect of an ensemble of cloud therefore the PV anomalies which form are likely to be stronger magnitude and deeper extending in the convection-permitting simulations. Chagnon and Gray (2009) found in a comparison between a 12 km and a 1 km model simulation that higher magnitude positive (and negative), and deeper PV anomalies occurred in the 1 km model. The 1 km model also showed more detailed PV anomaly structures. At coarser resolution (12 km grid spacing) where convection parametrization is used and the smallest resolved storms are larger than 50 km, the PV dipoles are orientated vertically and are of smaller magnitude, of the order 1 PVU (in the 1 km of the order 10 PVU) (Chagnon and Gray, 2009). These differences between the two models are due to convection being explicitly represented by the 1 km model, but parametrized by the 12 km model. The finer resolution, 1 km model, is able to represent the basic thunderstorm structure, since a typical thunderstorm cell is of the order 10 km in scale in all three dimensions (Bryan *et al.*, 2003), whereas the 12 km model cannot represent these mesoscale cells, as they are smaller than the grid-length of the model and therefore convective parametrization is required. It is therefore expected that in this Chapter stronger PV anomalies will be found in the convection-permitting models which will have a more detailed structure and be higher magnitude. Thus it is thought that once coarse grained onto a comparable grid-spacing similarly to the convection-parametrizing model the stronger negative and positive PV anomalies will persist, leading to associated impacts on the windspeeds and potential temperatures surrounding it. Differences between the impacts on the surrounding temperature and wind fields between the convection-permitting and convection-parametrizing models are hypothesised to occur since Chagnon and Gray (2009)

found that horizontal and vertical PV dipoles produce different impacts on the surrounding vorticity. Done *et al.* (2006) showed for a 12 km simulation when convection-parametrization is switched off, that the explicit representation of convection associated with an MCS leads to the development of a lens of negative PV at tropopause level which does not occur when simulated with convection parametrized. As grid-spacings become smaller than 1.5 km the effects of turbulence need to be accounted for in the NWP models and turbulence becomes a new grey-zone whereby large scale eddies can be explicitly represented by small-scale eddies require a parametrization scheme to represent them. Further horizontal PV dipoles are expected in these simulations.

3. **Hypothesis: Horizontal dipoles of PV may be produced in the Euro 4 km and UKV models (which have not been seen in the NAE model) as well as the vertical dipoles.** Chagnon and Gray (2009) state that since horizontal dipoles associated with convection are created on the cloud scale, they are only represented by high-resolution, convection-permitting simulations (e.g. Euro 4 km and UKV; they found horizontal dipoles in a 1 km model simulation). A coarser model (e.g. NAE model, Global model) using convective parametrization can simulate the vertical dipoles generated by MCSs, but are unable to represent horizontal dipoles generated by cumulus-scale systems. Horizontal dipoles of PV on the storm-scale represent a more 'primitive' evolutionary stage of the MCS than the vertical MCV structure which is typically associated with a mature MCS. This evolutionary stage is not well represented in coarse NWP models (because convection parametrization is required) and it is hypothesised that this will impact the forecast of the 'completely evolved' (mature) MCV stage of the MCS (Chagnon and Gray, 2009). This could ultimately produce both a different MCS forecast and an altered downstream forecast due to the impact the horizontal dipoles could have on the velocity surrounding it in comparison to the coarser models (since PV anomalies have associated circulation patterns) which are unable to represent these horizontal dipoles. It is expected that the PV anomalies will still be different between the models after coarse graining has been implemented since Chagnon and Gray (2009) found that the horizontal dipoles that occurred in the convection-permitting models were still apparent in comparison to the convection-parametrizing models which did not

represent the horizontal PV anomalies, even after coarse graining.

4. **Capturing the initial convection associated with the MCS using a 1.5 km grid-spacing will produce a better representation of the MCS than the UKV model** The domain of the UKV model does not cover France where the MCS initially develops and matures. Therefore, it is thought that extending the domain further south to cover France and northern Spain will allow for the triggering of convection to occur in the model and thus could lead to a better represented MCS once it reaches the UK in comparison to the UKV model.

4.3   Method

Forecasts for the case study 5–6 July 2012 are simulated using the convection-parametrizing Global (25 km grid spacing) model and the convection-permitting Euro 4 km (4.4 km grid spacing; convection-permitting one the MCS is mature but requires parametrization of convection for the initial storm development) , France 1.5 km (1.5 km grid-spacing developed for this study to capture the initial convection in the developing MCS; see Figure 2.3) and UKV (1.5 km grid spacing) models in this Chapter (see Figure 2.1 for the domains used for the convection-permitting models). For consistency, the Euro 4 km, UKV and France 1.5 km models were all set-up to use Global start dumps and boundary conditions (every hour).

All four of the model configurations were simulated for 24 hours with the Global model starting at 00 UTC 5 July 2012 and ending at 00 UTC 6 July 2012 (with the convection-permitting simulations being initialised at 03 UTC). Initially the Global model was ran for 24 hours and a dump was output at 03 UTC (T+3). Boundary conditions for the convection-permitting models were then produced using this Global 24 hours forecast. The Euro 4 km, France 1.5 km and UKV models were then ran from 03 UTC 5 July to 00 UTC 6 July 2012 from Global boundary conditions. Although the initial convection which eventually becomes the MCS occurs at 00 UTC 5 July, this initial convection was orographically induced. Triggering of convection that enables the organisation of the thunderstorms into an MCS occurs at 09 UTC 5 July (due to a weak upper-level trough). Therefore, although model spin-up will occur at the beginning of the model simulations (00 UTC) this time was deemed most appropriate to initialise, as

it gives enough time before the triggering at 09 UTC (6 hours) and the orographic convection at 00 UTC should still be captured by the model simulations. Additionally, no start dump was available for 18 UTC 4 July therefore the simulations would have needed to be initialised at 12 UTC 4 July which was deemed too early. Data was output every three hours for each model.

To test the hypotheses in Section 4.2, model output are analysed at times 09 UTC and 18 UTC. These times are used as they allow for an investigation into the conditions occurring at the development stage of the MCS (09 UTC) and the mature stage of the MCS (18 UTC). 09 UTC was deemed the best time (given the 3-hourly model output) as it avoids spin up issues and is a time when the MCS is developing (further deep convection is triggered and organisation into an MCS develops). This is especially important for the Euro 4 km model which has been found to take longer to spin up than the UKV model (Roberts, 2003). Lean *et al.* (2008) found that initially the convection permitting models (1 km and 4 km models) had too intense rainfall due to spin up issues from the lower resolution model providing the boundary conditions. They found, however, that rainfall rates produced by the 4 km and 1 km models became similar to radar rainfall rates after nine hours of the model run. They concluded that a forecasting system that produced information for times less than T+9 of the model run should include 'some method to allow high-resolution features to propagate from one forecast cycle to the next'. This means data assimilation (DA) is required, however, DA is not used during this study so 09 UTC will be used instead of times preceding it, due to the better comparison to rainfall radar at this time. Lean *et al.* (2008) found downscaling was useful for representing storms if the storm initiation was not too close to the start of the forecast. Nine hours into the run is deemed long enough for downscaling to be appropriate in this study.

For each of the times, PV, precipitation and windspeed are analysed in detail. These variables have been chosen as they provide a good summary of information about the convection representation and influence on the flow in the four models. Results are shown for two pressure levels (250 hPa and 500 hPa) as differences at middle and upper-levels in the three variables may occur because convection affects the atmosphere in differing ways at different heights. At 250 hPa, differences in the variables between the four models may impact on the downstream large-scale flow (due to PV having an action-at-a-distance impact), as this level corresponds to jet-stream level where the windspeed

and direction can have an effect on the atmospheric flow patterns. Additionally, differences in the variables at upper-levels (250 hPa) can have a large vertical feedback on the levels below, which could in turn affect the MCS itself, as well as the large-scale flow. At 500 hPa, differences may occur between models due to the convection representation which could create different PV structures in association with the MCS.

After the original model output from each of the four models is investigated an analysis of the coarse grained model data is conducted. Coarse graining requires that each of the four models is averaged onto the same 100 km grid spacing grid so that each model is on a comparable resolution and can be compared. The coarse graining technique used is described in Section 2.3. The following is conducted to investigate the MCSs produced:

- Hypothesis 1: Total rainfall figures are analysed for 09 UTC and 18 UTC on 5 July 2012. The total rainfall produced will be compared over a comparable resolution between the four models studying (Global, Euro 4 km, France 1.5 km and UKV) by using the coarse-graining technique. The total rainfall of each of the models will also be compared to observed rainfall totals to determine which compares best with reality (in terms of location, intensity, structure and timing).

- Hypothesis 2: Horizontal and vertical cross-sections through the convection are examined at 09 UTC and 18 UTC on 5 July 2012 for each of the models to determine the difference in PV intensity, location, timing and vertical extent after all are coarse-grained and thus associated impacts on temperature and windspeed patterns since PV is a relationship between vorticity and static stability.

- Hypothesis 3: Vertical cross-sections at 09 UTC and 18 UTC on 5 July 2012 are used to determine if horizontal PV dipoles are seen in the higher resolution models or not. An analysis of if convection-permitting models create stronger PV anomalies once coarse grained is performed.

- Hypothesis 4: The location and intensity of the rainfall from the France 1.5 km model is compared to the UKV model in comparison to what occurred in reality in the rainfall radar for the mature MCS at 18 UTC 5 July.

4.4 Comparison of different resolution MetUM simulations

4.4.1 Results: Analysis of the original model data

Initiation of the MCS occurs in the south of France thus at 09 UTC the storms (which are developing) are contained within France (see Figure 4.3(a)-(c)). The UKV model therefore, does not show the storm at this time. In all of the models (except the UKV model) the MCS initiates in the south of France before moving northwards towards the UK. Once the MCS reaches the UK it turns on a more north-westerly track. Since at 09 UTC the storm has not yet reached the domain of the UKV, Figures used at this time only include the Global, Euro 4 km and France 1.5 km models. The following fields are now compared: rainfall, PV and windspeeds.

Rainfall

The total rainfall rates (rainfall given by explicit and parametrized rainfall) show large differences between the models at both 09 UTC and 18 UTC (Figure 4.1(a)-4.1(c) and Figure 4.2(a)-(d)). When compared to the radar rainfall (see Figure 3.18(b)) the specific location of the most intense rainfall rates are different; however, both the Euro 4 km and France 1.5 km models manage to produce a similar overall rainfall pattern with small areas of high rainfall rates (although these rainfall rates are too strong with 30 mmhr^{-1} rainfall compared to 10 mmhr^{-1} in the radar) surrounded by an area of weaker rainfall (although the models fail to capture the true extent of this stratiform rainfall which covers a larger area in reality, this is a known issue with these models and is documented in Stein *et al.* (2015), Hanley *et al.* (2015), Clark *et al.* (2016) and Lean *et al.* (2008)). The France 1.5 km model produces many small-scale but heavy rainfall cells (Figure 4.1(c) and Figure 4.2(c)), whereas the Euro 4 km model produces a few larger-scale (than the France 1.5 km model) heavy rainfall cells which are larger-scale, more intense and more organised than in reality, similarly to Lean *et al.* (2008) (Figure 4.1(b) and Figure 4.2(b) compared to Figure 3.18(d)).

The Euro 4 km and France 1.5 km models seem to develop the second MCS (which develops in south France at 18 UTC) even more intensely than the MCS of interest, creating very large rainfall rates (up to 40 mmhr^{-1}) which did not occur in reality (Figure
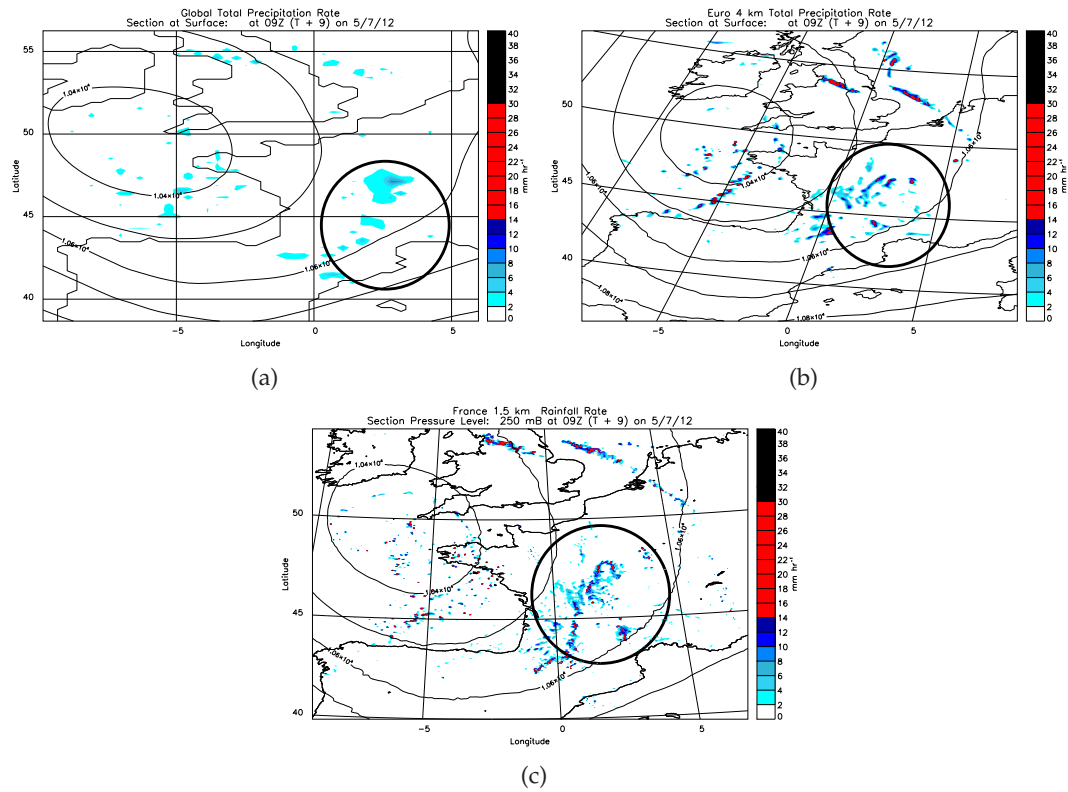
Figure 4.1: 09 UTC 5 July 2012: Total rainfall rates for (a) Global model, (b) Euro 4 km model and (c) France 1.5 km model . Each figure has contours of geopotential height (at 250 hPa) indicated at levels 10400 m to 10800 m, every 100 m.

4.2(b) and 4.2(c)) and Figure 3.18(d)). Similarly to in this case, Lean *et al.* (2008) previously found that a 4 km model creates overactive convection often leading to too organised and too intense cells of rainfall. The Euro 4 km was also found to be unable to represent the weak convection and thus sometimes does not create any (or creates little) stratiform rainfall, which was found for this case in both MCSs which developed. The lack of stratiform rainfall is largely due to the grey-zone in convection created through the use of the Euro 4 km model. A grey-zone develops as small-scale convection requires a parametrization scheme to represent it but once convection is large enough (approximately 16–20 km in scale) then it can be explicitly represented by the model. The Euro 4 km model thus has problems producing the weak stratiform rainfall.

The Global model at 09 UTC produces much weaker rainfall due to the rainfall being produced by the convection scheme (Figure 4.1(a)) thus it is unable to represent the intense rainfall cells created in the convection-permitting models (maximum of 8 mmhr^{-1} in comparison to 30 mmhr^{-1} for the convection-permitting models at 09 UTC). At 18 UTC the Global model does not represent the MCS at all so no rainfall is produced
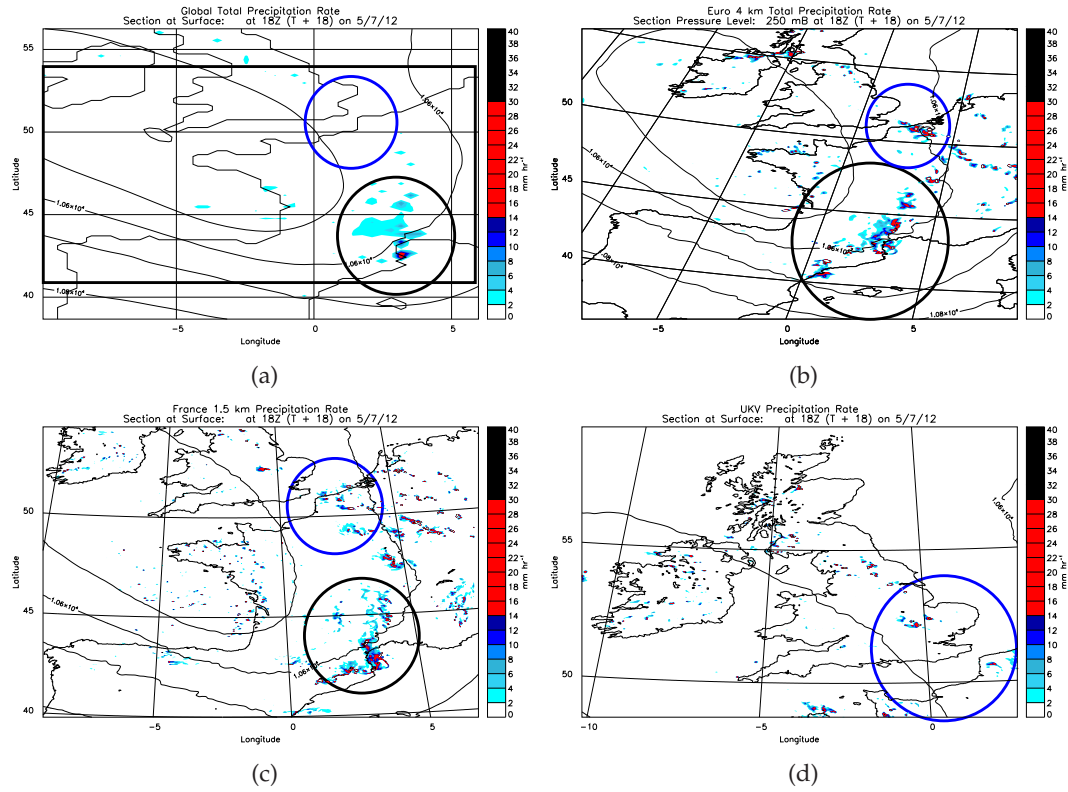
Figure 4.2: 18 UTC on 5 July 2012: Total rainfall rates for (a) Global model, (b) Euro 4 km model, (c) France 1.5 km model and (d) UKV model. Each figure has contours of geopotential height at 250hPa indicated at levels 10400 m to 10800 m, every 100 m. The black circles indicate the second MCS which developed and the blue circles indicate the location of the mature MCS being studied. The black rectangle on the Global model indicates the domain used to perform coarse graining in Section 4.6.

in association with it (Figure 4.2(a), at a smaller scale there is a small cell of rainfall with the magnitude 0.1 mmhr^1). Once the MCS is mature it should be large enough for the convection-permitting and convection-parametrizing models to both represent the storm. However, in this case, the Global model does not represent the initial storm well and the subsequent mature MCS is not represented at all in this model; however, a second MCS which developed over south France is represented well by the Global model when compared to rainfall radar (Figure 3.18(d)). It is thought that the Global model removes the instability associated with the MCS too quickly or does not create enough of it and thus, although the developing MCS was represented at 09 UTC, by 18 UTC the instability is gone from the model and no convection occurs (Lean *et al.* (2008) discusses how convection-parametrization can act to remove instability before showers are represented in the model, leading to an underestimation in the rainfall). This is similar to Clark *et al.* (2014) who found for an MCS case in the UK that the Global model failed to

represent the MCS so hardly any rainfall was produced in the model, whereas, the UKV model was able to represent the MCS well and produce a similar amount and structure of rainfall to what occurred in reality. However, in this case, the UKV model produces small, intense cells of rainfall (Figure 4.2(d)) but does not correspond to what occurred in reality (wrong location and covers a much smaller area, with hardly any stratiform rainfall). This is due to the MCS developing over the east of England in the UKV model (due to the MCS developing too early in the UKV model) producing rainfall too far northwest at 18 UTC (Figure 4.2(d)).

Since the Global model does not represent the mature MCS it means that there are no initial conditions present in the boundary conditions which would produce an MCS. Therefore, when the UKV model spins-up, instability grows and the model 'realises' there is an MCS that should be represented in the model when it reaches the boundary of the UKV domain (due to the improved resolution of the model). The UKV model therefore creates an MCS sooner (and thus its track is further advanced than the Euro 4 km and France 1.5 km models) than it occurs in the other convection-permitting models (as the convection 'blows' up when the high resolution comes in). This produces an MCS which is represented by the model, but is represented in the wrong location and is additionally more intense.

For this case both the Global model and UKV model did not represent the MCS well in comparison to reality (comparison of Figure 4.2(d) to Figure 3.18(d)). The France 1.5 km model developed to determine if capturing the initial convection of the MCS produced a more realistic forecast shows the MCS being represented better in terms of location and magnitude of rainfall than the UKV (Figure 4.2(c)). Extending the domain of the UKV model operationally could thus provide a means of improving the forecast of such systems that effect the UK however more case studies would be required first.

PV

Figure 4.3(a)-(d) show that at 09 UTC, there are already marked differences between the PV anomalies (in magnitude, location and amount) in all the model simulations, where the convection associated with the developing MCS takes place. These differences increase over time to 18 UTC (Figure 4.4(a)-(d)). The Global model, as expected due to

its larger grid spacing and parametrized convection, shows much less detailed structures (Figure 4.3(a) and 4.4(a)) and as the grid-spacing of the model simulations shortens the PV anomaly structure becomes more detailed (comparison of Figures 4.3(a)-(c) and 4.4(a)-(d)).

By 18 UTC the number of diabatically-generated PV anomalies has vastly increased (in comparison to at 09 UTC) within the Euro 4.4 km, France 1.5 km and UKV models (at the 250 hPa level) due to the MCS maturing and new cells forming (Figure 4.4(b)-4.4(d)). The Global model, has no PV anomalies at 250 hPa in association with the MCS over northern France (Figure 4.4(a), due to not representing the MCS at this time). It does, however, show a large negative PV anomaly in association with the MCS over south France at 18 UTC.
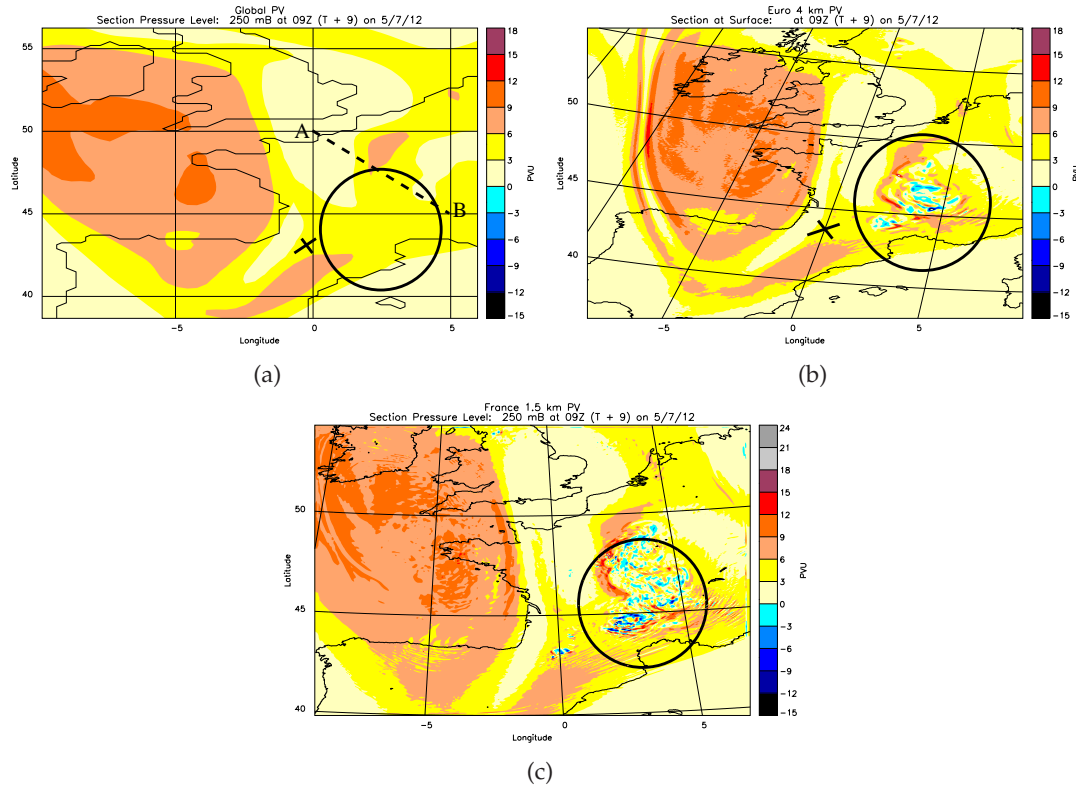

(a)

(b)

(c)

Figure 4.3: 09 UTC 5 July 2012: PVU at 250 hPa level for (a) Global model, (b) Euro 4 km model and (c) France 1.5 km model. On all figures the cross indicates the area of initiation of convection in reality. The circle indicates the location of the developing MCS in each of the models. The black line indicates the cross section A–B used for cross-section figures throughout this Section.

The PV anomalies occurring in the UKV model at 250 hPa (at 18 UTC) have a similar structure to the anomalies occurring in the Euro 4 km and France 1.5 km models in association with the mature MCS, however, they develop further west over the east of
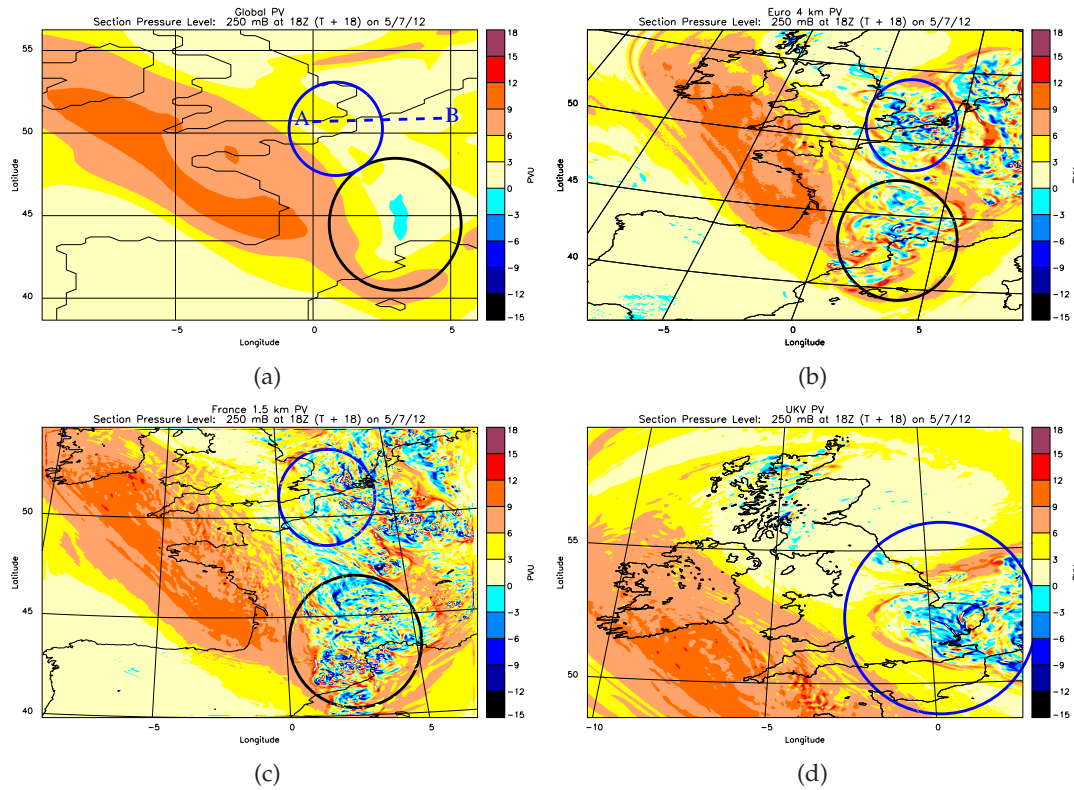
Figure 4.4: 18 UTC on 5 July 2012: PVU at 250hPa level for (a) Global model. The line A-B indicates the cross-section used in Figure 4.6(a)-(d), (b) Euro 4 km model, (c) France 1.5 km model and (d) UKV model. For each model the black circle indicates the second MCS which has developed (not on the UKV model as it is beyond the domain limits) and the blue circle indicates the area of the MCS being studied.

England in the UKV model (Figure 4.4(d)). It can clearly be seen when comparing Figures 4.4(b) and 4.4(c) to 4.4(d) that there is an area of both strong negative and positive PV anomalies occurring in this model over eastern England which does not appear in the other models. This is due to the previously mentioned earlier development of the MCS in the UKV model.

The detail in the PV anomaly structure over different pressure levels for the convection-permitting models (Euro 4 km and France 1.5 km) can be seen in Figure 4.5(b),(c), Figure 4.6(b) and 4.6(c)). These Figures show that the PV anomalies are more detailed in the France 1.5 km model due to the smaller grid-spacing and convection being explicitly formed by the model. Positive and negative PV anomalies occur in the Euro 4 km and France 1.5 km models at 09 UTC in association with the developing MCS. These positive PV anomalies can be seen at 250 hPa (highest magnitude 18 PVU and 24 PVU at 09 UTC and 18 UTC, respectively; for the France 1.5 km and Euro 4 km mod-
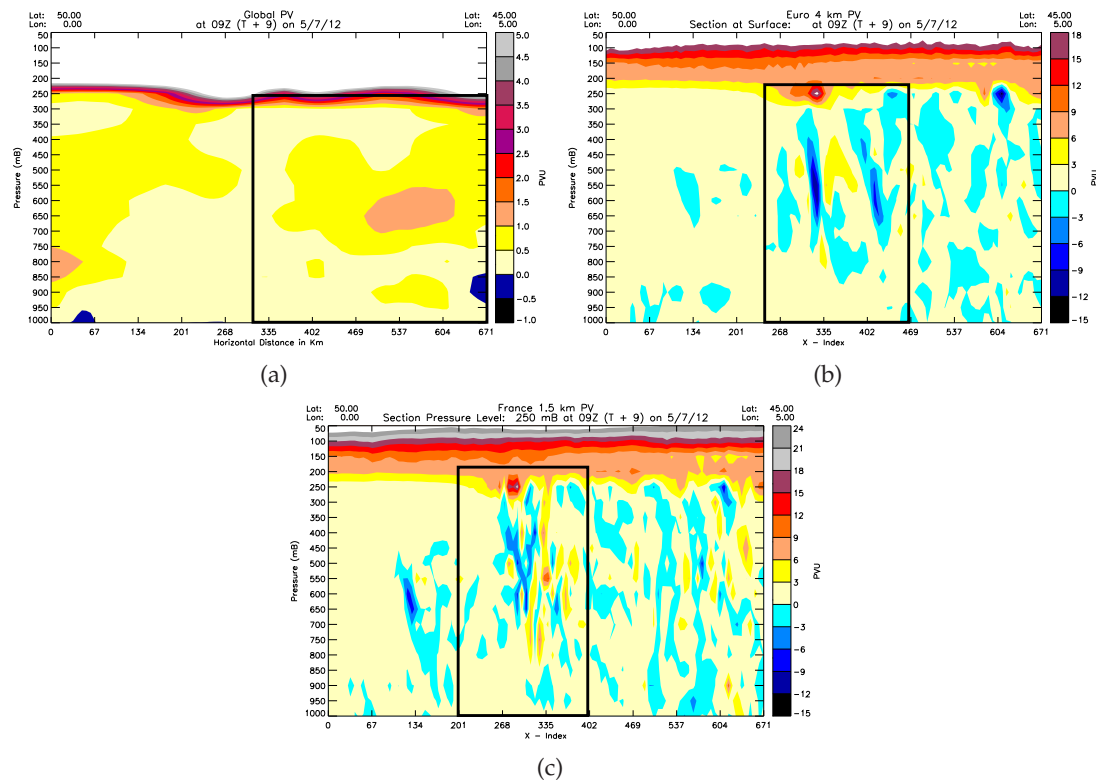
Figure 4.5: 09 UTC 5 July 2012: cross-section through the storm showing PVU for (a) Global model, (b) Euro 4 km model and (c) France 1.5 km model. The black cross indicates the centre of the MCS in the global model. The black rectangle indicates the MCS development region. Note: contours used for Global model differ to the other figures due to the much smaller magnitude PV anomalies.

els) and at mid level (500 hPa) the highest magnitude is 6 PVU for the Euro 4 km model (seen in Figure 4.5(b)) and 12 PVU for the France 1.5 km model (Figure 4.5(c)) at 09 UTC and at 18 UTC the Euro 4 km and France 1.5 km have a maximum magnitude of 18 PVU at this level (Figure 4.6(b) and (c)).

Negative PV anomalies can be seen at 250 hPa with a maximum magnitude of -6 PVU for the Euro 4 km and France 1.5 km models at 09 UTC. At 18 UTC the Euro 4 km model PV anomalies increases in magnitude to -12 PVU at 250 hPa in association with the MCS. These PV anomalies created in the Euro 4 km may be too strong as often this model is too overactive as turbulent mixing cannot be represented so updraughts are represented too strongly in comparison to what they would be in reality.

The convection-permitting simulations produce horizontal dipoles of PV similarly as shown in Figure 11 of Chagnon and Gray (2009) which are larger magnitude to the vertical PV dipoles produced in the convection-parametrizing simulation. Chagnon and

Gray (2009) stated that these horizontal dipoles appear to have a local effect to the storm themselves however an examination of the impact in the context of synoptic-scale error growth was required. It is likely though since the horizontal dipoles rapidly convert latent heating to relative vorticity on the time-scale of 10 minutes that the wind fields generated by the horizontal dipoles in the convection-permitting simulations will differ to those created by the vertical dipoles in the convection-parametrizing simulation (Chagnon and Gray, 2009). The horizontal dipoles of PV tend to be tilted in the direction of the environmental shear thus the associated vorticity is also tilted in comparison to that produced in the vertical dipoles which is likely to induce different flow patterns around the PV anomalies created between the convection-permitting and convection-parametrizing simulations.

At 500 hPa horizontal dipoles of negative PV occur with a maximum magnitude of -12 PVU at both 09 UTC and 18 UTC for both models and positive PV anomalies occur with a maximum magnitude of 12 PVU. These horizontal dipoles were similarly seen in Chagnon and Gray (2009) where they found that horizontal dipoles of PV occurred for the convection-permitting model simulation (1 km) but not the convection-parametrizing model (12 km).

The vertical extent of the positive PV anomaly is greater for the France 1.5 km model, with it extending from 800 hPa–250 hPa (at both 09 UTC and 18 UTC), indicating that the strong convection is occurring from the convective cap height of 800 hPa to tropopause level. Although the Euro 4 km model has a positive PV anomaly at mid levels, its vertical extent is minimal in comparison to the France 1.5 km model (approximately 650 hPa to 350 hPa). This could be due to the Euro 4 km model relying mostly on the convection scheme to produce convection in the model at this early stage in the development of the MCS.

The Global model has a positive PV anomaly (1–1.5 PVU; between 650 hPa to 500 hPa) at middle level occurring in the cross-section through the storm at 09 UTC (Figure 4.5(a)). This much smaller magnitude positive PV anomaly in this model is due to the convection scheme being required in the Global model meaning that the convection is an average effect over an ensemble of cloud so a PV tower type structure cannot be represented. Thus, the Global model does not produce the strong localised diabatic heating required for strong PV anomalies to be produced. Additionally, the convection-
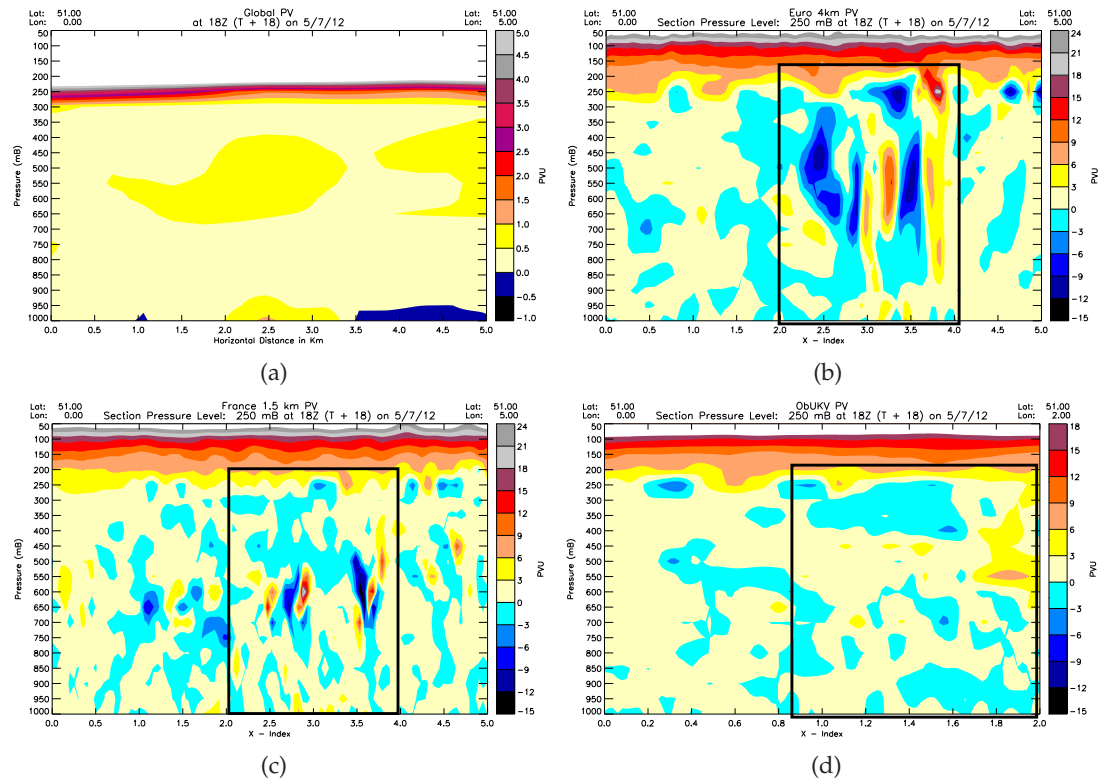
Figure 4.6: 18 UTC on 5 July 2012: cross-section of PV through the MCS for (a) Global model, (b) Euro 4 km model, (c) France 1.5 km model and (d) UKV model. On each figure the rectangle indicates the location of the MCS. Note: contours used for Global model differ to the other figures due to the much smaller magnitude PV anomalies.

parametrization scheme produces no storm lifecycle so it is hard to get the sustained heating produced in an MCS which creates the signature PV anomaly structure. This is particularly the case as the MCS is still developing so convection is not as strong as it would be when the MCS was mature. The MCS is also developing further to the north west in the convection-permitting models (Figure 4.5(a)-4.5(c)).

The Global model does not represent the MCS at 18 UTC thus the positive PV anomalies at 500–650 hPa is 0.5 PVU magnitude (Figure 4.6(a)). No negative PV anomalies occur at 09 UTC or 18 UTC in the Global model as the convection is too weak to develop the strong updraughts that lead to deposition of mass creating negative PV anomalies at upper-levels. Chagnon and Gray (2009) found convection-parametrizing models do not represent horizontal dipoles of PV similar to what has been found for this case (and was also found in Chapter 3 for the 12 km simulations). The deeper and more intense PV anomalies which occur in the convection-permitting models may have an impact on the wind circulation patterns surrounding it (which appears to already be occurring

due to the MCS being located further north west in the convection-permitting models). These differing environmental flow patterns between models could have an impact on the downstream forecast between the models and could even impact the synoptic-scale disturbances surrounding the MCS (Gray, 2001).

The large-scale synoptic pattern of PV in the four models is very similar though with the low-pressure system to the west of the UK being developed similarly for all models (Figure 4.3(a)-(d)). In the convection-permitting models the trough at 250 hPa is located further to the west than in the Global model. There is also a stronger gradient in PV at the boundary between the trough and the ridge. This not only has an impact on the PV between the convection-permitting and convection-parametrizing models but causes weaker potential temperatures (θ) at upper-levels in the convection-permitting models as the tropopause height is amplified higher (not shown).

At 18 UTC Figures 4.4(a)-(d) show that the large-scale cut off is similar for all the models. In Figures 4.5(b) and (c) at 200–250 hPa level where the MCS is developing a positive PV anomaly area occurs. This is related to a weak upper-level trough which occurred on this day and can be seen indicated by a trough line on the synoptic chart Figure 3.14(b).

Windspeed

The windspeeds of the Global, France 1.5 km and Euro 4 km models have similar large-scale patterns at all levels (250 hPa; Figures 4.8(a)–(d), other levels not shown here). However, in the location of the MCS the windspeeds and directions vary slightly between the models, specifically at 250 hPa level. It is particularly noticeable that the Global model (Figure 4.7(a)) shows more northerly airflow towards the UK where the France 1.5 km (Figure 4.7(c) and 4.8(c)), Euro 4 km models (Figure 4.7(b) and 4.8(b)) and the UKV model (Figure 4.8(d)) show a more north-westerly track (which was found to occur in reality). The higher the resolution the more the flow pattern veers towards the northwest (this is particularly apparent at 18 UTC; see Figure 4.8(a)–(d)). Figure 4.8(d) shows there are stronger windspeeds in relation to the MCS in the UKV model in comparison to the other models. Stensrud and Fritsch (1994) states that accurate representation of the MCS is known to be sensitive to mesoscale features present in the initial
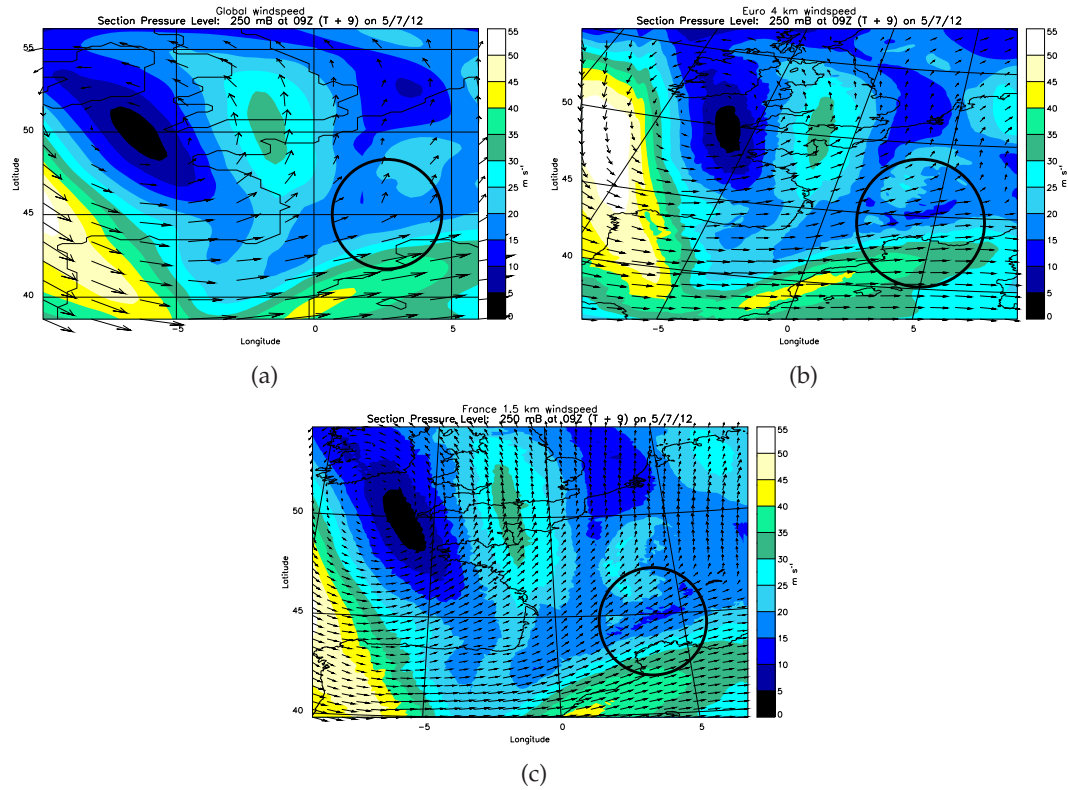
(a)

(b)

(c)

Figure 4.7: 09 UTC 5 July 2012: windspeed at 250 hPa level for (a) Global model, (b) Euro 4 km model and (c) France 1.5 km model. The black circles indicate the developing MCS location. Arrows indicate the direction of environmental flow.

conditions used in the model run and this is what happens in this instance.

Figures 4.7(a)–(c) and 4.8(a)–(d) show that the differences in PV anomalies, seen in Figures 4.3(a)–(d) and 4.4(a)-(d), produce associated differences in windspeed at the same level (250 hPa), with their being lower (10 ms^{-1}) and higher (35 ms^{-1}) windspeeds surrounding the PV anomalies created in association with the MCS for the convection-permitting models (in comparison to 15 ms^{-1} and 30 ms^{-1} for the Global model; Figures 4.7(a)–(c)).

The impact on windspeed associated with the PV anomalies is due to anticyclonic rotation being occurring around negative PV anomalies and cyclonic circulations developing around positive PV anomalies. Negative vorticity develops associated with negative PV anomalies with positive vorticity developing associated with positive PV anomalies. Therefore, in the convection-permitting simulations where negative PV is represented at upper-levels reduced windspeeds occur (due to associated negative vorticity) to the south east of the negative PV anomalies which do not develop in the convection-

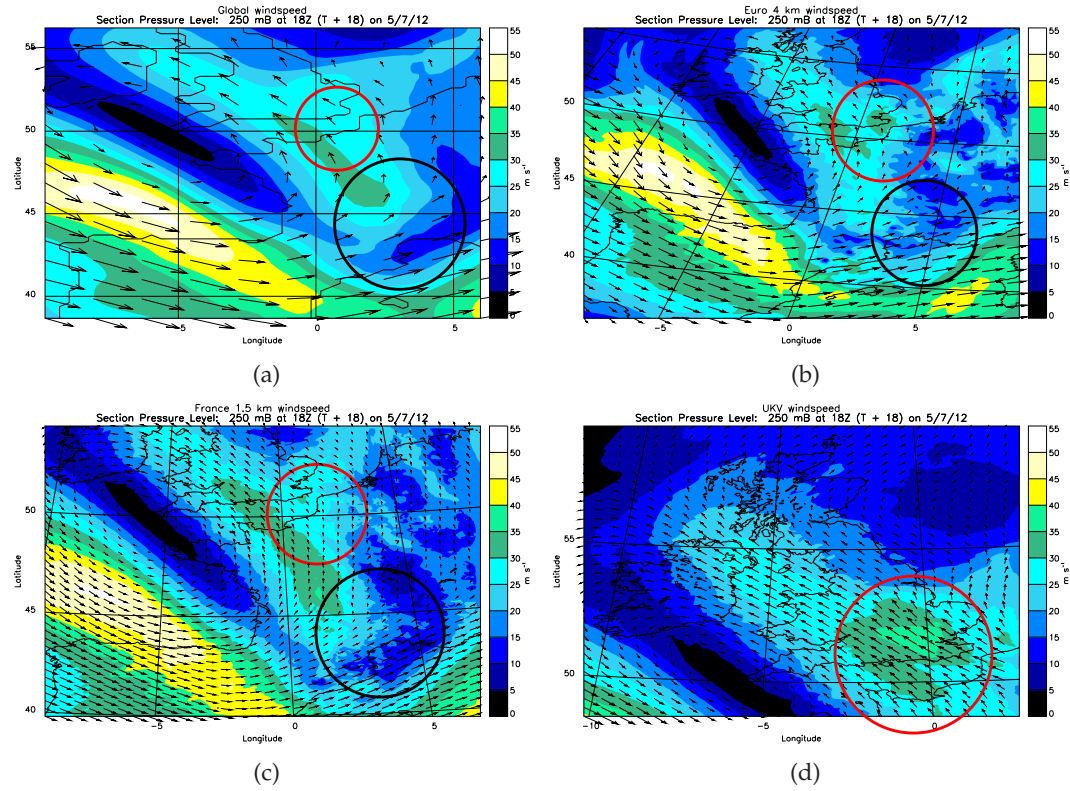parametrizing simulation. In both the France 1.5 km and Euro 4 km models (but not

Figure 4.8: 18 UTC on 5 July 2012: Windspeeds at 250 hPa for (a) Global model, (b) Euro 4 km model, (c) France 1.5 km model and (d) UKV model. For each of the models the blue circle indicates the location of the MCS being studied and the black circle is the second MCS which develops.

the Global model) there are areas of weaker wind speeds (see Figures 4.8(b) and (c)) in relation to the storm. These weaker windspeeds occur south-east of areas of negative PV at upper levels, since these negative PV anomalies have associated anti-cyclonic circulations. As a consequence stronger windspeeds occur to the west of the negative PV anomalies in the convection-permitting models that do not occur in the Global model. These differences in wind patterns at tropopause level could have an impact on the downstream flow. Wind speed below 250 hPa show that weaker wind speeds occur at these levels for the convection-permitting models but not the convection-parametrizing model (not shown here). This could be due to horizontal PV anomalies being formed in these models which are not formed in the Global model due to the representation of convection. Differences in wind speeds at lower levels will not have as great an impact as at tropopause level but are still important.

Despite the differences in PV, windspeed and rainfall rate at 09 UTC and 18 UTC, the

geopotential height at 250 hPa (and at all other levels; not shown) has minimal differences between the models and is not noticeable in the figures (see the black contours on Figures 4.1(a)-(c) and Figure 4.2(a)-(d)).

4.4.2 Results: Analysis of the coarse-grained data

In Section 4.4.1 differences have been shown in the windspeed, rainfall, temperature and PV of the four models depending on the grid-spacing of the model. In this Section coarse graining to 100 km grid spacing is implemented to test if these differences still exist due to the differences in the way convection is represented in the models and if the hypotheses from Section 4.2 are true once each model is averaged onto the same comparable grid. The coarse graining technique used is described in Section 2.3.

Coarse graining is implemented over a subsection of the Globe (which focused on the MCS region; seen in Figure 4.2(a)) due to it taking too much computer power to implement over the whole Globe. Unfortunately though, due to the France 1.5 km and UKV models not having much overlap, it meant that the subsection taken for the coarse graining only includes a small section of the UKV model. The coastline in the plots reflects the resolution of the coarse graining. Coarse graining the four models to the same comparable resolution allows for a comparison of each model to be conducted.

The following fields are compared for the four coarse grained models: rainfall, PV, potential temperature and windspeeds. The difference between the coarse-grained data originating from the convection-permitting Euro 4.4 km, France 1.5 km and UKV models and the coarse grained data from the convection-parametrizing Global model is also presented for the rainfall, PV and windspeed. To create the difference figures used in this Section the coarse-grained Global model data was taken away from the coarse-grained convection-permitting model data and then plotted. It must be noted that the location of the MCS differs slightly between the convection-permitting models and the Global model so could have an impact on these calculated differences, and is particularly important later on in the forecast when the MCS is not represented in the Global model but is in the other models.

Coarse-grained rainfall

Coarse grained rainfall at 09 UTC has a similar overall structure for all models; however, there are differences between the models related to the development of the MCS and two bands of rainfall (which form over the UK at this time) which are much weaker in the Global model which failed to capture the banded structure (Figure 4.9(a)–4.9(c)). The

strongest rainfall area in the Global model is further east than that in the France 1.5 km
and Euro 4 km models (Figure 4.9(a)). Both the Euro 4 km model (Figure 4.9(b) and
Figure 4.10(b)) and France 1.5 km model (Figure 4.9(c) and Figure 4.10(c)) show similar
locations and patterns in the rainfall at 09 UTC but the locations of the most intense
rainfall differs. The Euro 4 km model creates stronger rainfall rates in association with
the MCS being studied than in the other models due to larger cells of intense rainfall
forming in the original Euro 4 km model. The stronger rainfall can be seen in Figure
4.9(b) where there is a difference of around 2 mmhr^{-1} rainfall in the Euro 4 km model in
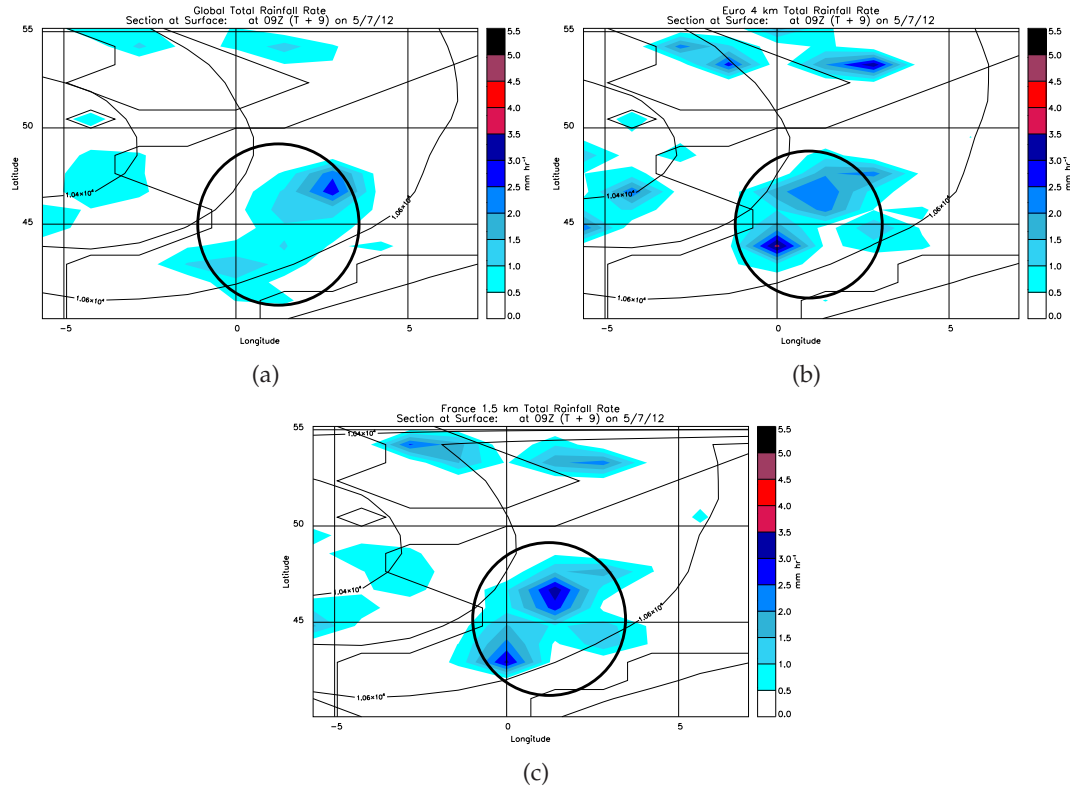comparison to the Global model.

(a)   (b)

(c)

Figure 4.9: 09 UTC 5 July 2012: Total rainfall rates coarse grained to 100 km for (a) Global model,
(b) Euro 4 km model, (c) France 1.5 km model. The black circles indicate the location of the MCS.
Contours of geopotential height at 250 hPa are plotted between 10400 m to 10800 m every 100 m.

The coarse grained total rainfall rates at 18 UTC are noticeably different for the four
models (Figure 4.10(a)–4.10(d)). Since the Global model only represents the second MCS
occurring over the South France and not the one over northern France at this time (only
represented 0.1 mmhr^{-1} rainfall), there is no rainfall in the coarse grained data in asso-
ciation with this MCS (Figure 4.10(a)). The Euro 4 km model (Figure 4.10(b)) continues
to show much more intense rainfall than the France 1.5 km (Figure 4.10(c)) due to the

over active convection in the model for this case. The UKV model (Figure 4.10(d)) shows more rain over south eastern England than the other models and this again is due to the storm being located over this area of England whereas in the other models the storm is further east. The storm in the UKV model is too far west even after coarse graining. It is likely that this could lead to serious issues with the rainfall forecast in the subsequent forecast, particularly since not only does the UKV model not produce enough rainfall but it develops rainfall in the incorrect location (too far west). The coarse-grained France 1.5 km and Euro 4 km models also produce much stronger rainfall over south France where the second MCS occurs in comparison to the rainfall created by the Global model (5–6 mmhr^{-1} compared to 3 mmhr^{-1} in the Global model; Figure 4.10(a)–4.10(d)). Each of the three models does, however, have the location of the rainfall from the second MCS in the same location (Figure 4.10(a)–4.10(c), not seen in the UKV model).
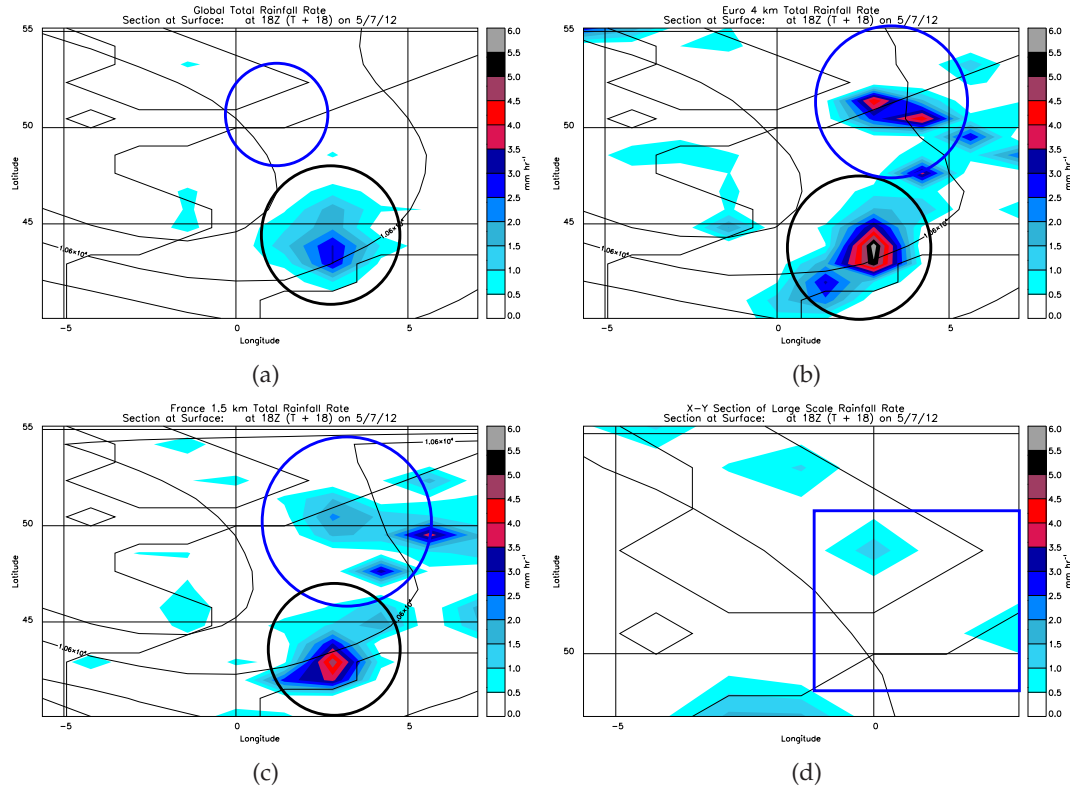

Figure 4.10: 18 UTC 5 July 2012: Total rainfall rates coarse grained to 100 km for (a) Global model, (b) Euro 4 km model, (c) France 1.5 km model and (d) UKV model. The black circle represented the second MCS that developed and the blue circles and rectangle represent the MCS being studied.

Coarse-grained PV

There are differences in the small-scale PV anomaly patterns after coarse graining at 09 UTC in the area of MCS development (Figure 4.11(a)–(c)). At 250 hPa in both the France 1.5 km (Figure 4.12(c)) and Euro 4 km (Figure 4.12(b)) models, lower-valued PV anomalies (of the order 1 to 3 PVU, in comparison to 6 PVU for the Global model; Figure 4.12(a)) occur locally in association with the developing MCS (at 09 UTC). This does not occur in the vicinity of the developing MCS for the Global model at the same height due to both the France 1.5 km and Euro 4 km models having negative PV at 250 hPa before coarse graining (Figures 4.3(b) and 4.12(c)) which the Global model does not (Figure 4.3(a)). This is important as if PV inversion was to be calculated it would show that these simulations have stronger associated anti-cyclonic rotation associated with them at 250 hPa, which could influence the subsequent environmental flow.
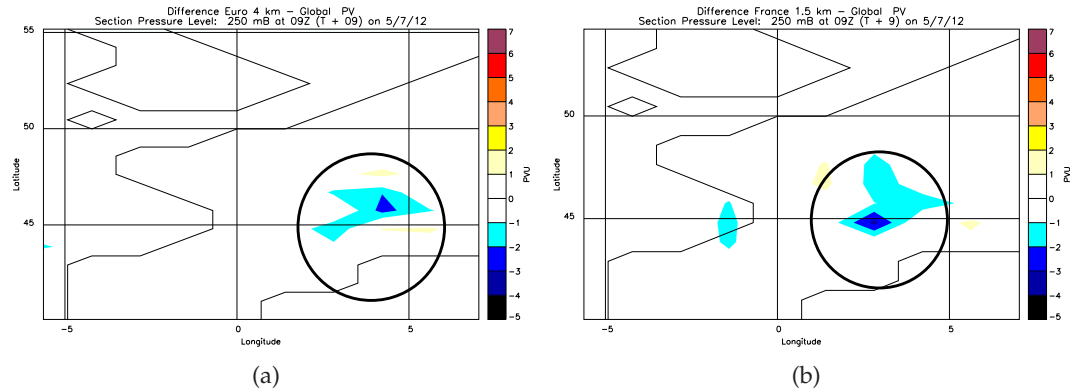

(a)   (b)

Figure 4.11: 09 UTC 5 July 2012: calculated difference between the PV at 250 hPa for the coarse grained (a) Euro 4 km model, (b) France 1.5 km model. The black circles indicate the MCS being studied.

At 18 UTC each of the four models show two areas of weaker PV values at 250 hPa in association with the two MCSs occurring (the MCS being studied and the MCS over south France; Figure 4.14(a)–4.14(d)). The magnitude of these weaker PV values differs between the four models though. The Euro 4 km model has an area of negative PV (-1 PVU) which is more negative than the 0 PVU occurring in the Global and France 1.5 km models in association with the MCS being studied. The Euro 4 km model shows a particularly large area of negative PV at tropopause level (Figure 4.14(b) and 4.18(b)) which could be the result of convection being overactive in this case for the Euro 4 km model.
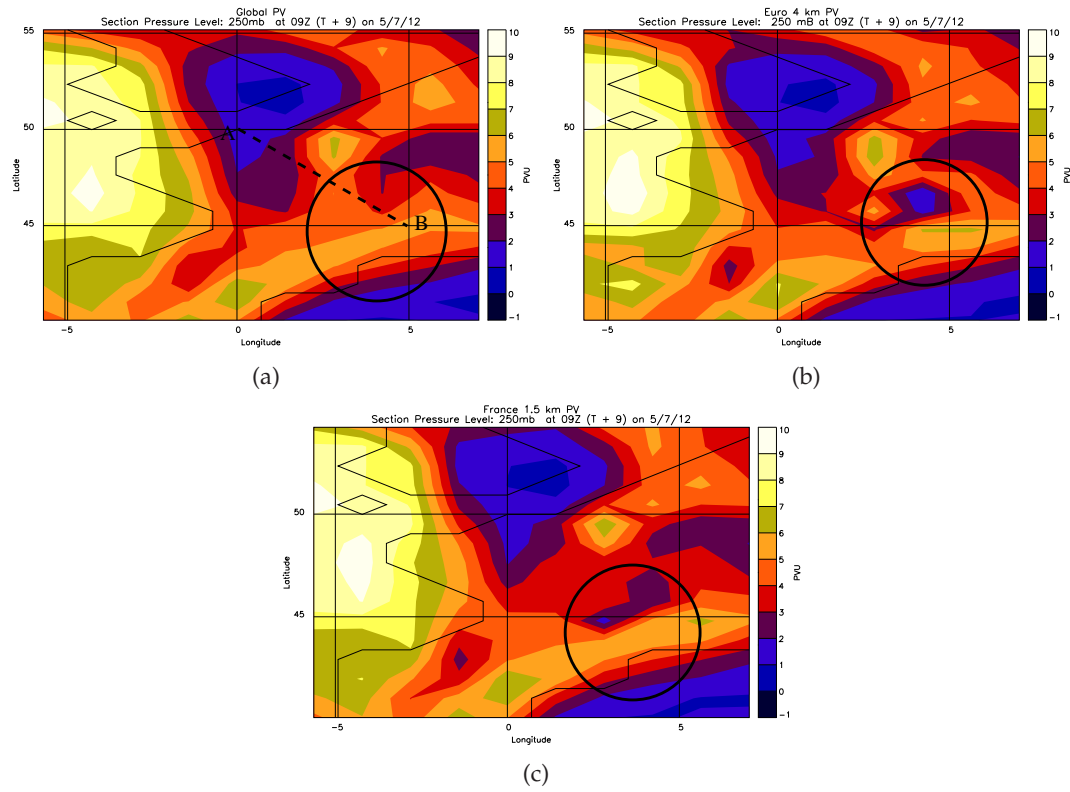
Figure 4.12: 09 UTC 5 July 2012: PV coarse grained to 100 km at 250 hPa for (a) Global model, (b) Euro 4 km model, (c) France 1.5 km model. The black circle on each figure indicates the location of the developing MCS. The line A-B indicates the cross-section used in Figures 4.17(a)-(c).

The UKV model shows an area of -1 PVU PV in association with the MCS. This negative PV covers a smaller area than in the Euro4 km model and is located further north-west than in the other three models (Figure 4.14(d)). This is due to the model creating convection explosively once the storm enters the domain of the model (Figure 4.14(d)), unlike the France 1.5 km model which will have developed the storm gradually. The coarse grained convection-permitting models show areas of weaker (negative) PV at 250hPa than the Global model suggesting their better representation of the convection impacting the PV anomalies produced still persists after coarse graining. The second MCS over the south of France can be seen at 18 UTC and the Global, Euro4 km and France 1.5 km models all show areas of weak or negative PV at tropopause level in association with this storm (the UKV doesn't cover this area; Figures 4.14(a)-4.14(c)). The France 1.5 km model gives the lowest PV values at tropopause level in association with this second MCS (-1 PVU; Figure 4.14(c)). The France 1.5 km and Euro 4 km models also have a greater amount of weak PV (-0.3 PVU to 0.3 PVU) in comparison to the Global model at 09 UTC at 250 hPa (lowest PV is 3 PVU).
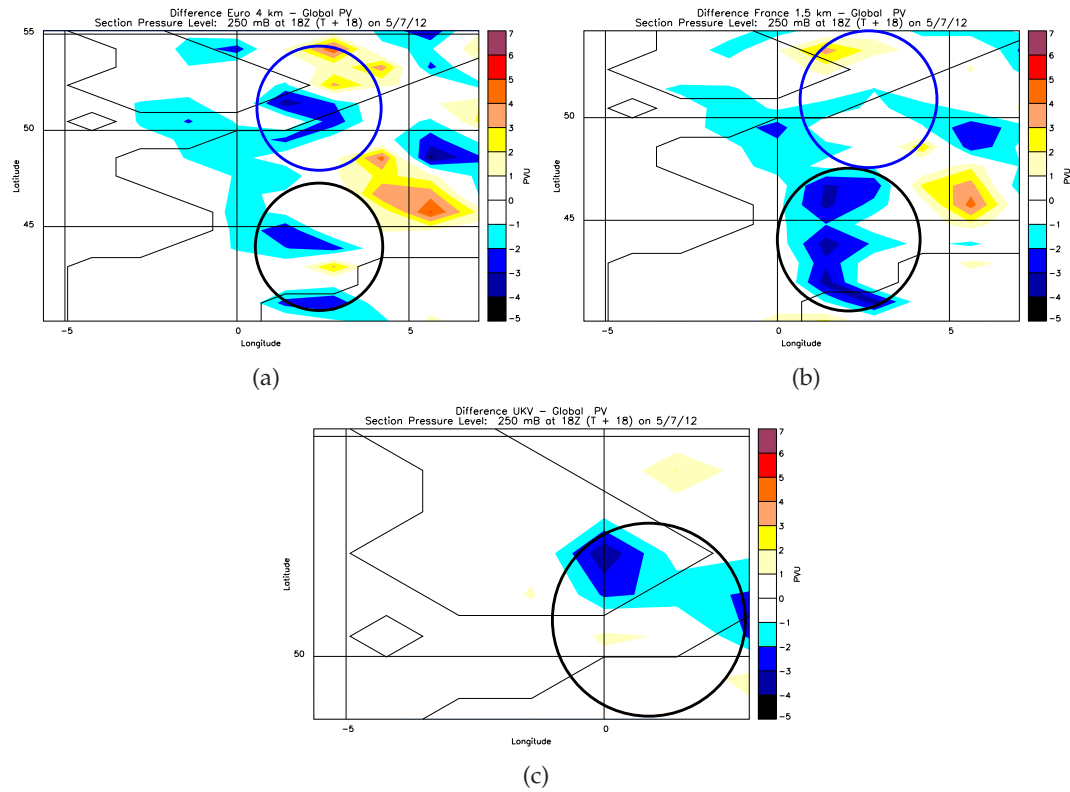
Figure 4.13: 18 UTC 5 July 2012: calculated difference between the PV at 250 hPa for the coarse grained (a) Euro 4 km model, (b) France 1.5 km model and (c) UKV model and the coarse grained Global model data. The black circles indicate the second MCS which developed and the blue circles indicates the MCS being studied.

At 09UTC for the 500 hPa level there are some distinct differences in the PV anomalies between the models (Figures 4.15(a)–(d)). These differences are associated with the location of the development of the MCS. Both the France 1.5 km and Euro 4 km models have areas of positive and negative PV anomalies from 900 hPa–250 hPa in association with the MCS (these can be seen in the cross-sections for each model Figure 4.5(b) and (c)). When coarse grained the Euro 4 km and France 1.5 km models still have positive and negative anomalies present but these are now weaker (maximum magnitude 1.25 PVU and -0.3 PVU, respectively) and spread over a larger area than before coarse graining (Figures 4.15(b) and (c)). The Global model does show a cut-off small area of slightly higher PV than the surrounding flow, with a magnitude of 0.9 PVU, but this is weaker than the positive PV anomalies in the France 1.5 km and Euro 4 km models and is also located further north (Figure 4.15(a)). Cross-sections through the MCS show a similar pattern for each model, however, the PV anomaly at middle levels associated with the MCS has a maximum magnitude of 0.5 PVU in the Global model whereas in the Euro
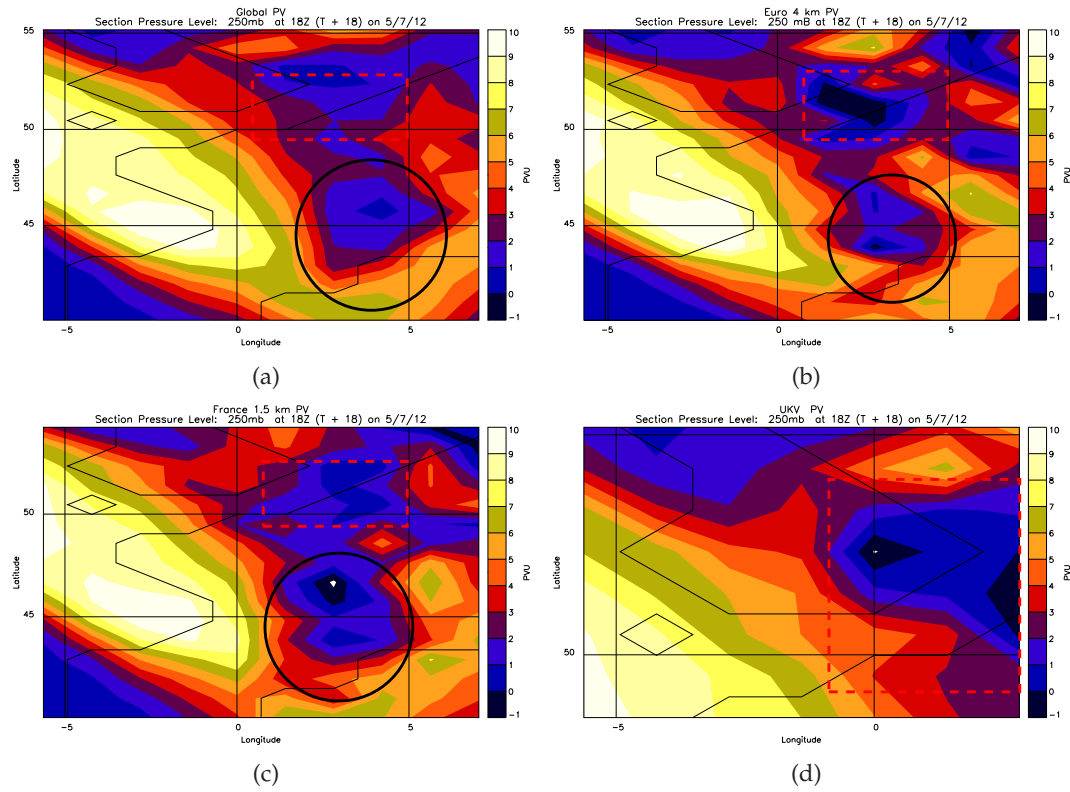
Figure 4.14: 18 UTC 5 July 2012: PV coarse grained to 100 km at 250 hPa for (a) Global model, (b) Euro 4 km model, (c) France 1.5 km model and (d) UKV model. The black circle represented the second MCS that developed and the red rectangles represent the MCS being studied.

4 km and France 1.5 km it is 1.25 PVU (Figure 4.17(a)–4.17(c)).

At 18 UTC, Figure 4.16(a))–(d), shows at 500 hPa just minor differences within the PV associated with the MCS, with the Euro 4 km model having a larger area of stronger PV than the other models (around 0.6 to 0.9 PVU compared to 0 to 0.3 PVU in the other models). Around mid-levels in the model at 09 UTC the Euro 4 km has an area of positive PV associated with the MCS covering a larger horizontal area than the other models (positive PV anomaly at 750 hPa to 400 hPa occurs in the Euro 4 km and France 1.5 km model; Figure 4.17(b) and 4.17(c)). At 18 UTC the positive PV anomalies cover an even wider area in the convection-permitting models (this is due to horizontal dipoles of PV being represented in these models and not the convection-parametrizing models; Figure 4.18(b) and (c)).

At 09 UTC and 18 UTC the large-scale pattern of PV is similar at all levels, for all the models (not shown), this is due to the low-pressure system affecting the large-scale being well represented by each model before they were coarse grained. At 250 hPa the low-
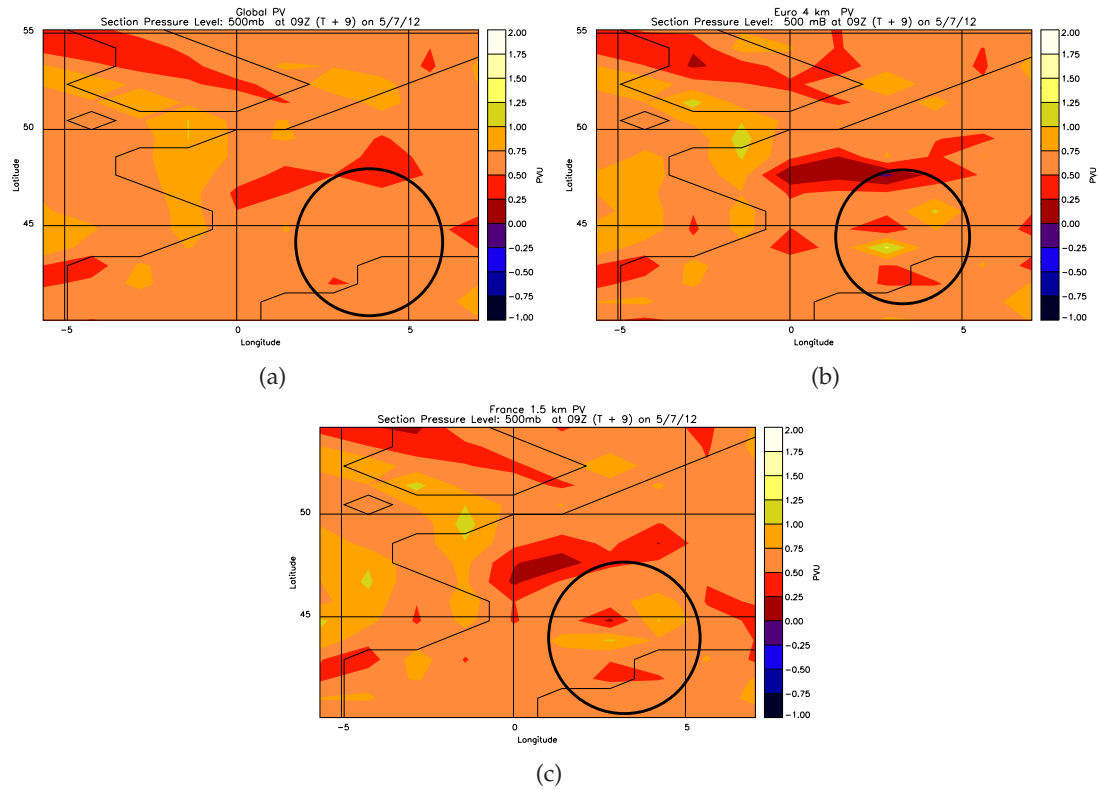
Figure 4.15: 09 UTC 5 July 2012: PV coarse grained to 100 km at 500hPa for (a) Global model, (b) Euro 4 km model, (c) France 1.5 km model. The black circle on each figure indicates the location of the developing MCS.

pressure system can be seen in the coarse-grained PV which shows all models having a similar region of high PV. The low-pressure centre causes stratospheric air (high PV-valued) down into the tropopause in a tropopause fold (Figure 4.12(a)–4.12(c) and Figure 4.14(a)–4.14(d)). In the convection-permitting models the ridge is located further west and is strengthened which causes negative PV differences to occur at upper-levels (up to 2 PVU negative differences; as the ridge is associated with negative PV; Figure 4.14(a)–4.3(b)–4.14(d)).

In the Euro 4 km model the negative PV anomaly (-1 PVU) at tropopause level can clearly be seen in the cross-sections (Figure 4.18(b), with the near zero PV anomaly at tropopause level occurring in the France 1.5 km model and UKV model which do not occur in the Global model (Figure 4.18(a)–4.18(d)).

Although the basis of PV dipoles is that both a negative and positive "charge" is produced which should essentially cancel out and therefore act locally to the storm, in an MCS it seems that the impact of the negative PV anomaly being generated at upper-
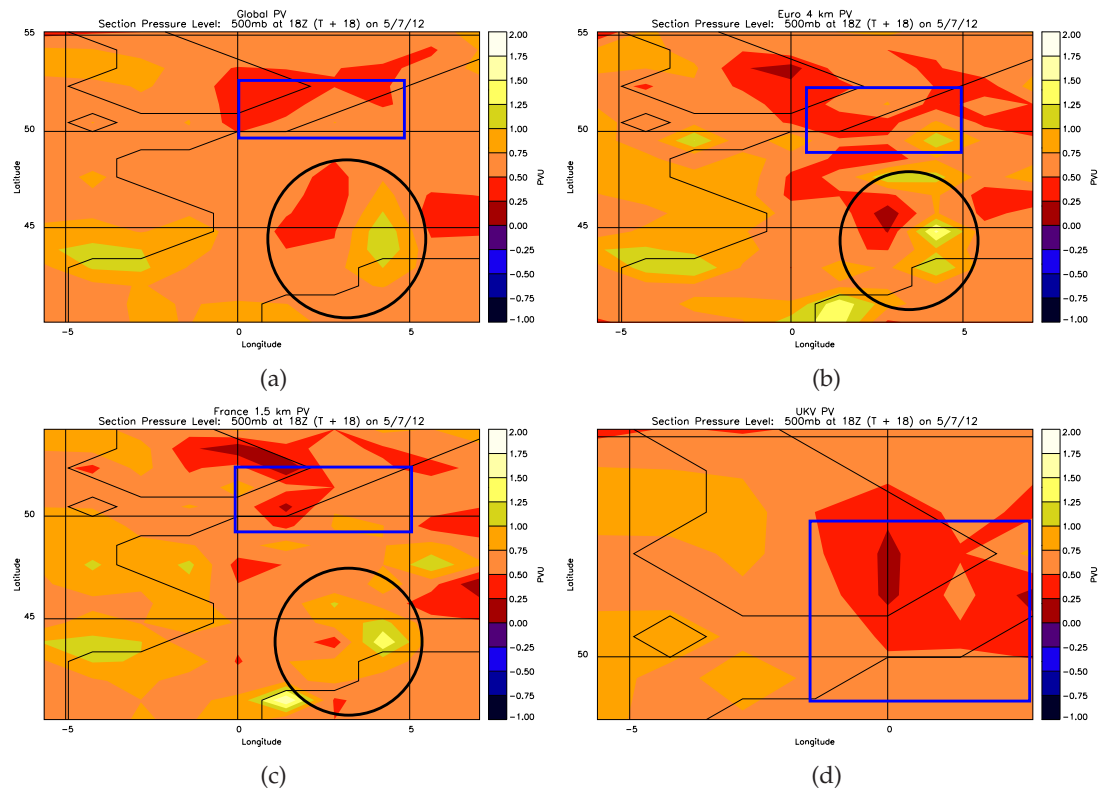
Figure 4.16: 18 UTC 5 July 2012: PV Coarse grained to 100 km at 500hPa for (a) Global model, (b) Euro 4 km model, (c) France 1.5 km model and (d) UKV model. The black circle represents the second MCS that developed and the blue circles represent the MCS being studied.

levels, where the background winds are stronger, is to create a larger impact on the flow than the positive PV anomaly at middle levels which produces larger magnitude differences at upper-levels than middle levels. It is likely however that the middle level positive PV anomaly acts to enhance the negative PV anomaly at upper-levels and thus a stronger magnitude positive PV anomaly will produce a stronger magnitude negative PV anomaly at upper-levels. Additionally, previous studies have found that negative PV anomalies at upper-levels induce larger perturbations than positive PV anomalies at middle levels (Pomroy and Thorpe, 2000) which provides a basis for the upper-level negative PV anomalies producing larger differences between the convection-permitting and convection-parametrizing simulations here, particularly since the upper-level negative PV anomalies are missing from the convection-parametrizing simulations.

Chagnon and Gray (2009) also suggested that horizontal dipoles of PV act only locally at the storm-scale however it appears in this study that many horizontal dipoles of PV are produced in an MCS simulated using convection-permitting simulations which act together to form a larger-scale PV structure, creating stronger magnitude and deeper
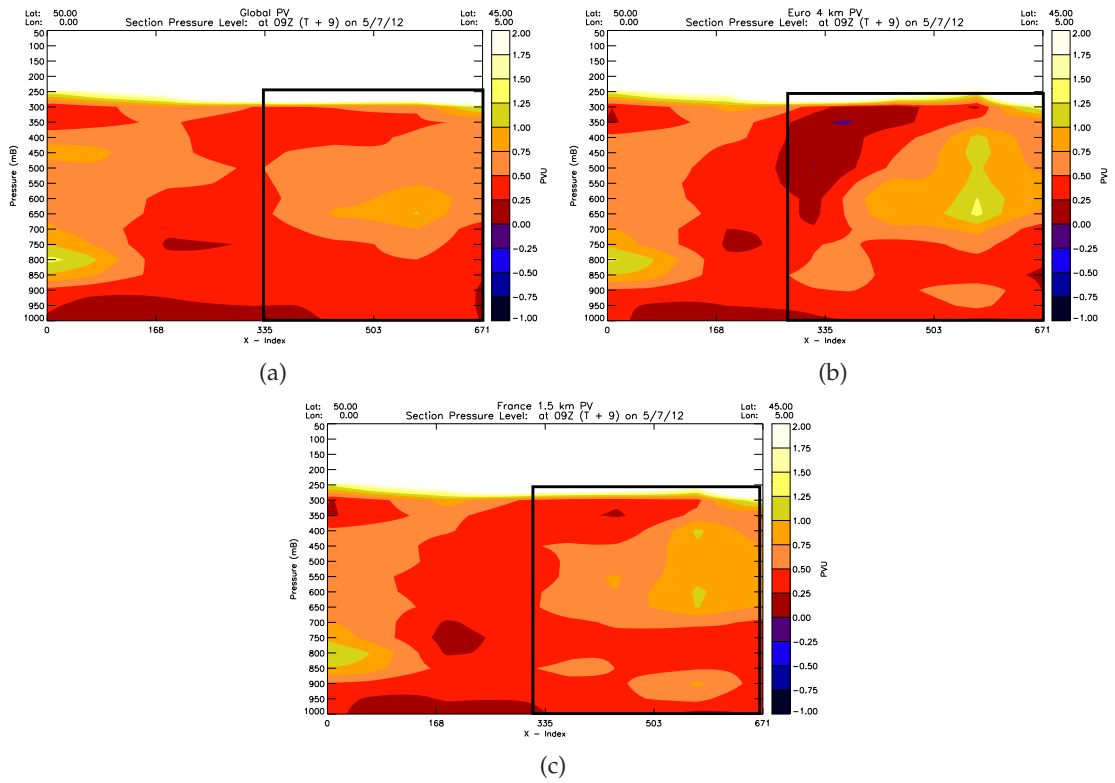
Figure 4.17: 09 UTC 5 July 2012: Cross-section of PV coarse grained to 100 km for (a) Global model, (b) Euro 4 km model, (c) France 1.5 km model. The black rectangle on each figure indicates the location of the developing MCS. Note: above 250 hPa the colour bar became saturated.

extending PV anomalies than in the convection-parametrizing case. In the convection-permitting cases the PV dipoles will also have different circulation and temperatures associated with them than in the PV anomalies produced in the convection-parametrizing case, (with larger penetration depth due to their greater magnitude) which will cause a variation in the gravity wave response from the PV anomalies leading to differences between the convection-permitting and convection-parametrizing simulations downstream from the PV anomalies produced by the MCS. The negative PV lens is missing in the convection-parametrizing case and thus the anticyclonic circulations will not be produced in upper-levels in this simulation as will occur in the convection-permitting simulations immediately producing different flow patterns at upper-levels between the models.
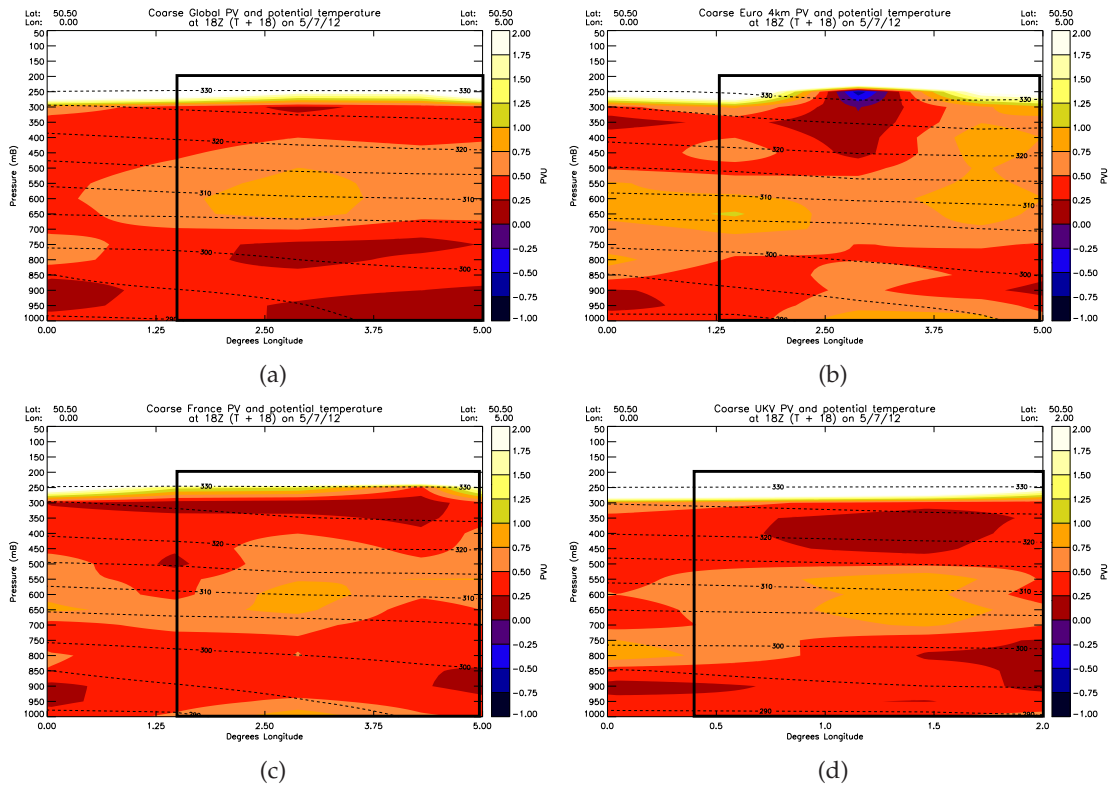
Figure 4.18: 18 UTC 5 July 2012: cross-section through the MCS for PV coarse grained to 100 km for (a) Global model, (b) Euro 4 km model, (c) France 1.5 km model, (d) UKV model. Rectangles indicate the area of impact from the MCS being studied. Above 250 hPa the colour became saturated. Black dashed lines indicate contours of θ from 290 K to 330 K every 5 K.

Coarse-grained Windspeed

At 09 UTC the coarse-grained windspeeds show very minor differences between the models at all levels (not shown), however slight variations do occur due to the differences in PV anomalies occurring between the coarse-grained models (can be seen for 250 hPa in Figure 4.19(a)-(d)). There are some small-scale higher magnitude windspeeds though (4 ms^{-1} faster than the Global model). Flow patterns vary in the models due to (anti) cyclonic flow anomalies related to the PV patterns created in each model. These flow anomalies act to enhance the winds in part of the domain and diminish them elsewhere depending on the background flow. This means that changes in the PV anomalies between models can have an impact on the windspeeds. Over time, differences in the windspeeds grow for the coarse grained Euro 4 km and France 1.5 km models with areas of weaker windspeeds created due to the anti-cyclonic flow produced in association with negative PV anomalies which do not occur in the Global model (Figures 4.21(a) and

4.21(b)). In the UKV model there are stronger windspeeds over the southeast of the UK due to the MCS being developed further west over the UK than in the other models (Figure 4.21(c)). The differences in windspeeds at levels below 350 hPa are small (around 0.5–1 ms^{-1}) but do grow over time (not shown).

Done *et al.* (2006) found that winds were impacted surrounding explicit convection at upper-levels associated with an MCS in a 12 km simulation as a negative PV lens developed here which did not occur in the convection-parametrization simulation therefore a feedback occurred on the wind surrounding the anomaly. This has similarly been found here whereby the PV anomalies has associated impacts on their surrounding windspeed patterns due to negative PV anomalies having associated anticyclonic circulations and positive PV anomalies having associated cyclonic circulations. It is shown that the feedback the PV anomalies have on the windspeeds grows over time from when the MCS is initiated to when it is mature with the spatial scale of the influence increasing along with the magnitude of the differences between the convection-permitting and convection-parametrizing model.

The large-scale wind pattern is similar for all models after coarse graining although at 18 UTC the convection-permitting models still have a more northwesterly track in comparison to a northerly track over the UK in the Global model. If PV inversion was implemented the rotation around the PV anomaly could be found however it was not clear how to invert these small-scale PV anomalies as no balance assumptions seemed relevant.

Coarse-grained potential temperature

Although PV inversion has not been implemented here it can be used to find the associated wind and temperature fields surrounding the PV anomalies and would show the temperatures surrounding the associated PV anomaly with warm temperatures above a positive PV anomaly (or collocated with it due to steady state heating in an MCS) with cold temperatures below it and warm temperatures below a negative anomaly and cold temperatures above it. Figure 4.18(a)–(d) show lines of θ and differences can be seen between the four models with the characteristic squeezing together of θ lines associated with a positive PV anomaly in the MCS as the static stability is increased associated
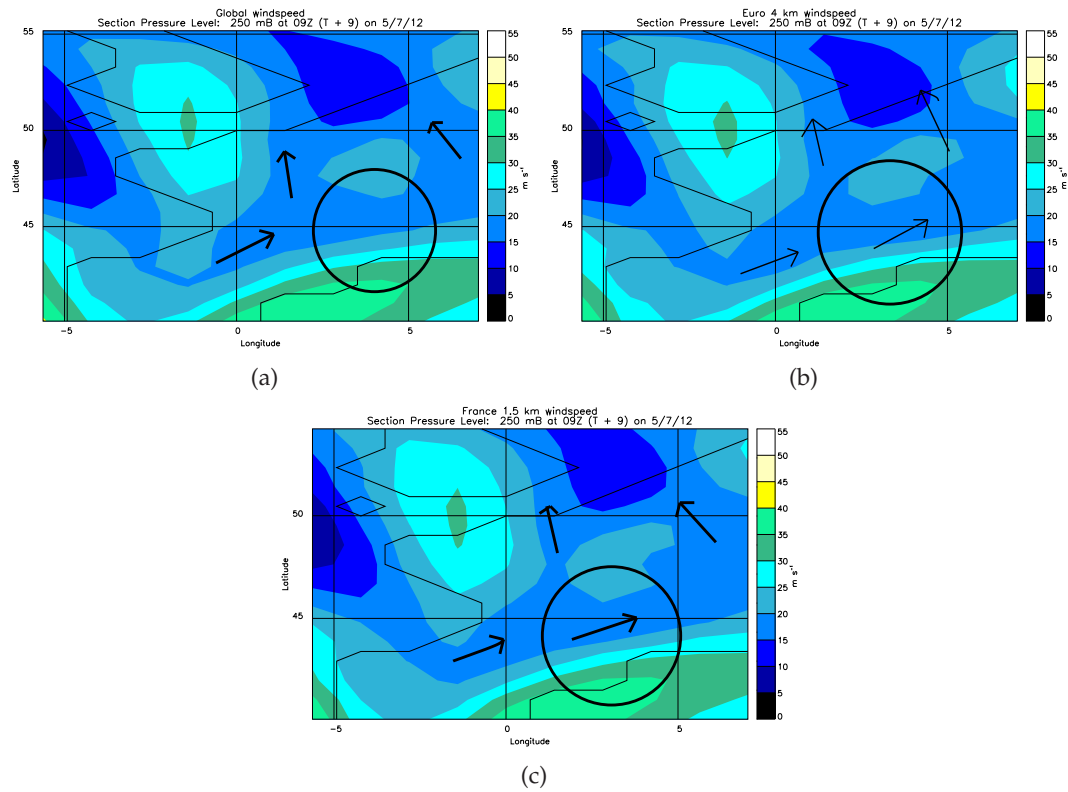
Figure 4.19: 09 UTC 5 July 2012: Windspeeds coarse grained to 100 km at 250h Pa for (a) Global model, (b) Euro 4 km model, (c) France 1.5 km model. The black circles indicate the location of the MCS. The arrows signify the direction of environmental wind flow.

with the positive PV anomaly at middle levels. The most noticeable difference is in the coarse grained Euro 4 km model which has negative PV at tropopause level (-1 PVU), this leads to the θ contour of 330 K being stretched lower down into the troposphere (Figure 4.18(b)) as the static stability is decreased surrounding the negative PV anomaly.

The negative PV anomaly at upper-levels associated with the MCS over western France in the coarse-grained Euro 4 km model causes a cooling in the θ up to 5.5 K in comparison to the coarse grained Global model at 18 UTC and 250 hPa (Figure 4.22(a)). The weaker magnitude PV anomaly at tropopause level in the coarse grained France 1.5 km and UKV than in the Global model causes θ differences of 1.5 K in association with the MCS being studied (Figure 4.22(b) and 4.22(c)). Similarly, for the MCS occurring in the southern France the negative and reduced PV at upper-levels in the convection-permitting models is consistent with the warm θ temperatures compared to the Global model (up to 3 K; Figure 4.22(a) and 4.22(b)). The warmer θ values in the convection-permitting models is due to the negative upper-level PV anomalies associated with the MCS (with the negative PV anomaly being associated with cooling above and warm-
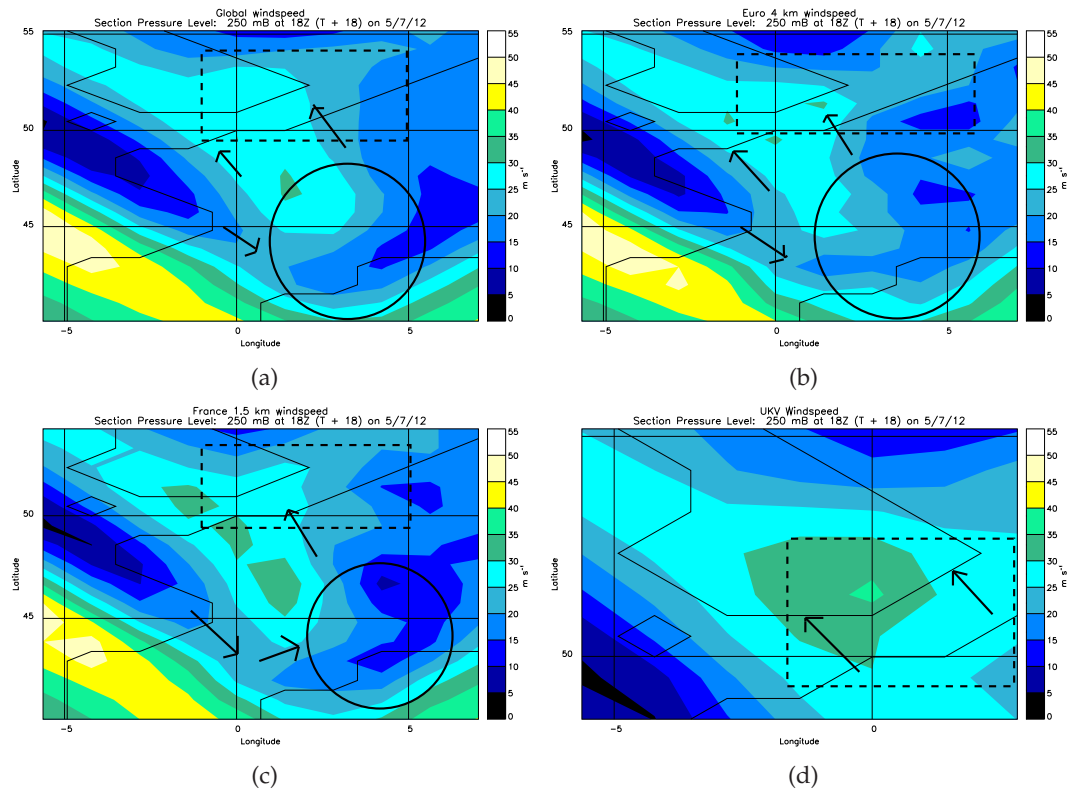
Figure 4.20: 18 UTC 5 July 2012: windspeeds coarse grained to 100 km at 250 hPa for (a) Global model, (b) Euro 4 km model, (c) France 1.5 km model and (d) UKV model. The black circle represents the second MCS that developed and the black rectangles represent the MCS being studied. The arrows signify the direction of environmental wind flow.

ing below thus a vertical divergence of the isentropes (see Figure 1.15 in this study and Figure 9.12 of Martin (2006)). The negative PV anomaly in the Euro 4 km is above the downward deflected isentrope which is consistent with this (Figure 4.18(b)).

The convection-permitting models, due to the reduction in PV above the MCS, cause the strong PV gradient boundary between the trough (associated with the low-pressure centre) and the ridge to strengthen which leads to differences in the PV here (negative PV differences of up to 4 PVU; Figure 4.14(a)-(d)). In an amplified ridge the tropopause height is raised which leads to lower θ values higher up. These lower θ values are also related to the ridge being located further west in the convection-permitting models meaning there are lower PV values at upper-levels in these models in comparison to the Global model (up to 2 K lower θ; Figure 4.22(a) and 4.22(b)). This displacement of the ridge can be explained by the PV erosion (seen in Figure 9.12 of Martin (2006)) or by the divergent outflow from the MCS inhibiting the progression of the trough.

The differences in θ created between the convection-permitting and convection-
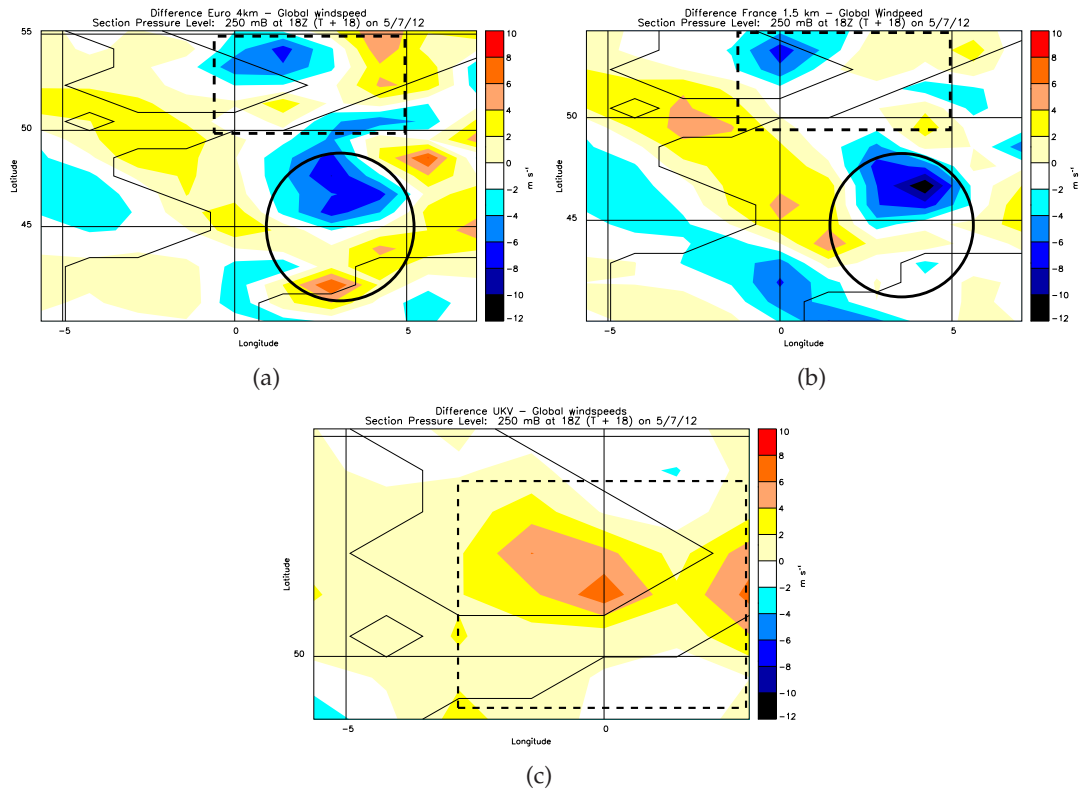
Figure 4.21: 18 UTC 5 July 2012: Calculated difference between the Windspeed at 250 hPa for the coarse grained (a) Euro 4 km model, (b) France 1.5 km model and (c) UKV model and the coarse grained Global model data. The black circles indicate the second MCS which developed and the black rectangles indicate the MCS being studied.

parametrizing model are related to the differences in PV associated with the MCS and consequently differences in the windspeed are seen surrounding these θ differences.

Coarse grained geopotential height

Due to all the differences found between the PV anomalies, windspeeds, temperature and rainfall rates it is unsurprising that the geopotential height patterns also appear to have small magnitude differences occurring (± 5 m, not shown here). These differences grow rapidly over time, in area and magnitude, going from a magnitude of 5 m differences at 09 UTC to in some areas having a 30 m magnitude difference at 18 UTC (not shown here). These differences are evidence of synoptic-scale impacts of MCS representation between the convection-permitting and convection-parametrizing models.

Upper-level negative PV anomalies create non-negligible perturbations to the geopotential height field which was similarly found by Pomroy and Thorpe (2000). Although
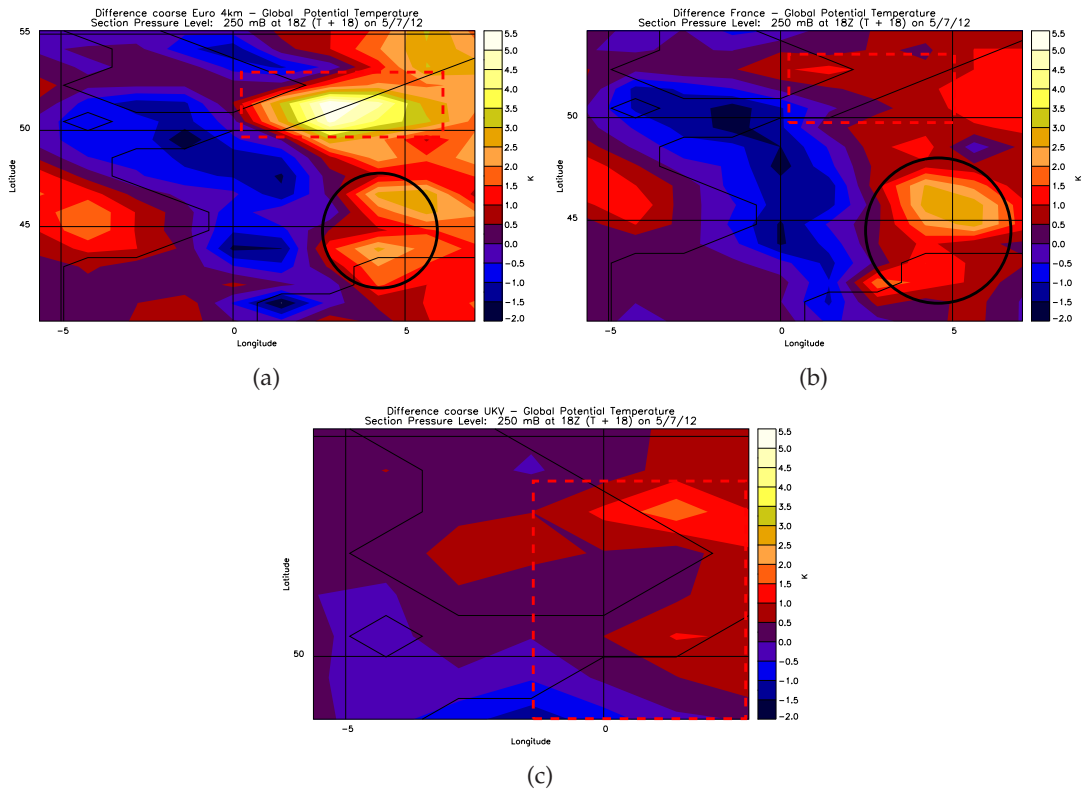
Figure 4.22: 18 UTC 5 July 2012: Calculated difference between θ at 250 hPa for the coarse grained (a) Euro 4 km model, (b) France 1.5 km model and (c) UKV model and the coarse grained Global model data. The black circles indicate the second MCS which developed and the red rectangles indicate the MCS being studied.

these differences are small in comparison to the values of typical geopotential heights at 250 hPa, they could grow very rapidly over time, so by five days into a forecast run they could create very important differences between the forecasts produced in the different resolution models. This upscale error growth at tropopause level has previously been studied by Zhang *et al.* (2007) and Selz and Craig (2015) related to extratropical cyclones and due to middle level mesoscale PV perturbations by Beare *et al.* (2003). Upscale error growth occurs due to the wind and temperature perturbations created by the PV anomalies associated with the MCS. Chagnon and Gray (2009) suggested the horizontal dipoles of PV produced in convection-permitting simulations have a local impact on the scale of the storm itself however in this Chapter it has been found that actually the upscale error growth onto the synoptic-scale is larger for the convection-permitting simulations particularly as they represent the negative PV anomaly produced at upper-levels related to the MCS.

The upscale error growth at middle levels is much smaller magnitude however does

become larger magnitude over time and covers a greater spatial extent. Pomroy and Thorpe (2000) found that the influence over time in their case study of PV anomalies from a cyclone was small but the maximum impact occurred upon the initial development of the low of the cyclone and thus can play a vital role in the long-term development of the cyclone. This finding was in direct contrast to the positive PV anomaly which had most influence in the later stages of the cyclone development.

Since it has already been found that the differences (in PV, wind and temperature) in this study grow over time at tropopause level in association with the MCS, it is expected that if this was continued for 5 days (or more) that the differences would grow onto the synoptic scale. Pomroy and Thorpe (2000) concluded that upper-level negative PV anomalies induce larger perturbations than lower-tropospheric positive PV anomalies. Therefore, since it has been found in this Chapter that the upper-level negative PV anomalies are not represented by the convection-parametrizing model it is likely that the perturbations in wind and temperature associated with the PV anomaly produced in the convection-permitting simulations but not the convection-parametrizing simulation will have a significant impact on the downstream flow impact. The impact on the downstream forecast is postulated to be particularly important on the development of the cyclone which develops over the UK since Pomroy and Thorpe (2000) found that negative PV anomalies at upper-levels had maximum impact on the initial development of the cyclone.

4.4.3 Statistical Analysis

The following section provides details of a statistical analysis of the coarse grained Global, Euro 4 km, and France 1.5 km model data. Statistics were not calculated for the UKV since the domain does not match that of the coarse grained Global model which would skew the statistics compared to the France 1.5 km and Euro 4 km data.

The mean PV at 250 hPa has only a small variation between the coarse-grained convection-permitting models and the coarse-grained Global model (0.5 PVU at 06 UTC) but this variation grows over time (up to 30% by 00 UTC 6 July; up to 1 PVU, see Table 4.1). The mean PV of the Global model at 250 hPa (Figure 4.23(a)) is higher than the France 1.5 km and Euro 4 km models (by 0.5 PVU at 00 UTC 6 July) providing evidence of the lack of negative/ low PV at this level in the convection-parametrizing model which occurs in the coarse-grained convection-permitting models (Figure 4.14(a)-4.14(c)). The mean PV at other levels is similar for all models at all times (not shown here) since the variation at levels below 250 hPa are much less. The coarse grained convection-permitting models have PV values of between 0 and -1 PVU at upper-levels where the MCS occurs whereas the Global model has PV values of 1 PVU which creates differences in the geopotential height and windspeeds due to the negative PV having anti-cyclonic circulations associated with it.

	09 UTC %	**18 UTC** %	**21 UTC** %	**00 UTC** %
Euro 4 km PV	-1.33	-9.19	-18.18	-29.41
France 1.5 km PV	-11.97	-16.55	-20.63	-30.45
Euro 4 km Windspeed	-1.31	-3.25	4.75	4.63
France 1.5 km Windspeed	-5.39	-3.60	0.33	-0.15
Euro 4 km Z	0.02	0.11	0.16	0.12
France 1.5 km Z	-0.01	0.07	0.11	0.08

Table 4.1:: Percentage difference in mean PV, windspeed and geopotential height (Z) between the France 1.5 km or Euro 4 km model and the Global model at 250 hPa for 09 UTC, 18 UTC and 21 UTC 5 July and 00 UTC 6 July 2012

The percentage differences in the PV at 250 hPa are continuing to grow over time

(Table 4.1) and could continue to grow at a rapid rate that could cause a large percentage difference in the mean PV after a few days of the forecast run. These percentage differences and the growth in them signifies the importance of convection representation in the NWP models. Since PV anomalies have associated cyclonic and anti-cyclonic rotations these percentage differences could be important on the direction of wind flow in the forecast of the MCS and downstream from the MCS. This impact is seen in the windspeed mean PV differences (Table 4.1). Although these differences are much smaller than for the PV it could still have an impact on the downstream flow (Table 4.1). Geopotential height percentage differences in mean PV are small (0.15% at 00 UTC 6 July) but they may grow over time and influence the large-scale environmental flow downstream (Table 4.1). These percentages are largely influenced by the fact the coarse grained convection-permitting models have lower PV at tropopause level than the coarse grained Global model which impacts the circulation patterns and consequently impacts the downstream pressure patterns.

An analysis of the standard deviation indicates that there is greater variation at the 250 hPa for all fields (PV, geopotential height and windspeed, not shown here). The convection-permitting models have larger standard deviations than the convection-parametrizing Global model at all levels (for PV, geopotential height and windspeed) showing that even after coarse graining, the variability that the convection-permitting models have still exists in comparison to the convection-parametrizing models due to the smoother fields.

When comparing the France 1.5 km and Euro 4 km models to the Global model at 250 hPa (for PV, geopotential height and windspeed) RMSD values grow considerably over time (from 06 UTC 5 July to 00 UTC 6 July for PV, windspeed and geopotential height; Figure 4.23(b) to 4.23(d)). The growth of RMSD values in PV, windspeed and geopotential height over time (06 UTC 5 July to 00 UTC 6 July) when comparing the coarse grained convection-permitting models to the coarse grained convection-parametrizing model shows evidence for the differences in the representation of convection between the models persisting after coarse graining to a comparable grid-spacing model. Although all of the models have been smoothed out to the same grid-spacing the stronger negative and positive PV anomalies in the convection-permitting models still persist after coarse graining and create differences in PV, windspeed and geopotential

height, when compared to the Global model which grow over time.

At all levels and for all fields (PV, windspeed and geopotential height) the Euro 4 km model has larger RMSD values when compared to the Global model than the France 1.5 km model (Figure 4.23(b) to 4.23(d)). The Euro 4 km model varies more than the France 1.5 km model when compared with the Global model due to the negative PV that occurs in association with the MCS being studied over northern France, as this impacts the windspeed and circulation patterns greater than in the France 1.5 km model which does not have the negative PV (but does for the second MCS which developed over south France). The greatest increase in the RMSD values occurs at 12 UTC as the MCS is identified as the triggering of deep convection at 09 UTC allows the organisation of individual thunderstorms into the MCS. The increase in RMSD values when the MCS is identified shows the importance of representing the convection associated with the MCS. The large increases in RMSD after 12 UTC is also related to the coarse grained Global simulation not representing the MCS that occurred over northern France. Therefore, once the MCS is identified in the convection-permitting simulations (at 12 UTC) the differences in PV, PMSL and windspeed grow rapidly when compared to the coarse grained Global model simulation showing that differences between the forecasts grow more rapidly upon moist processes occurring.

The RMSD below 250 hPa has less variability, as expected, however, there is a slight growth in RMSD PV at 500 hPa (by 0.1 PVU) which has associated variability in the windspeed and geopotential height at this level (Figure 4.23(b) to 4.23(d)). Geopotential height RMSD at 500 hPa grows from 1.8 to 5.8 between 06 UTC 5 July to 00 UTC 6 July indicating the shift in the pressure patterns due to the differences in the PV values, with the low/ negative PV at upper-levels changing the circulation patterns.

RMSD values at 250 hPa increase from 0.5 PVU–1.5 PVU for PV, 2.5–11 m for geopotential height and 0.7–4.0 ms^{-1} for windspeeds (for the Euro 4 km model) over the 18 hour period 06 UTC 5 July to 0 UTC 6 July 2012. The RMSD values have therefore at least tripled in value from 06 UTC 5 July to 00 UTC 6 July. This indicates that the differences in the representation of the MCS between the convection-permitting models and the convection-parametrizing model not only persist after coarse graining but have a profound impact on the PV, windspeeds and geopotential height surrounding the MCS. The differences in the PV, windspeed and geopotential height are growing rapidly in

magnitude and spatial area, indicating that large scale and large magnitude differences could occur downstream from the MCS which could lead to different forecasts.
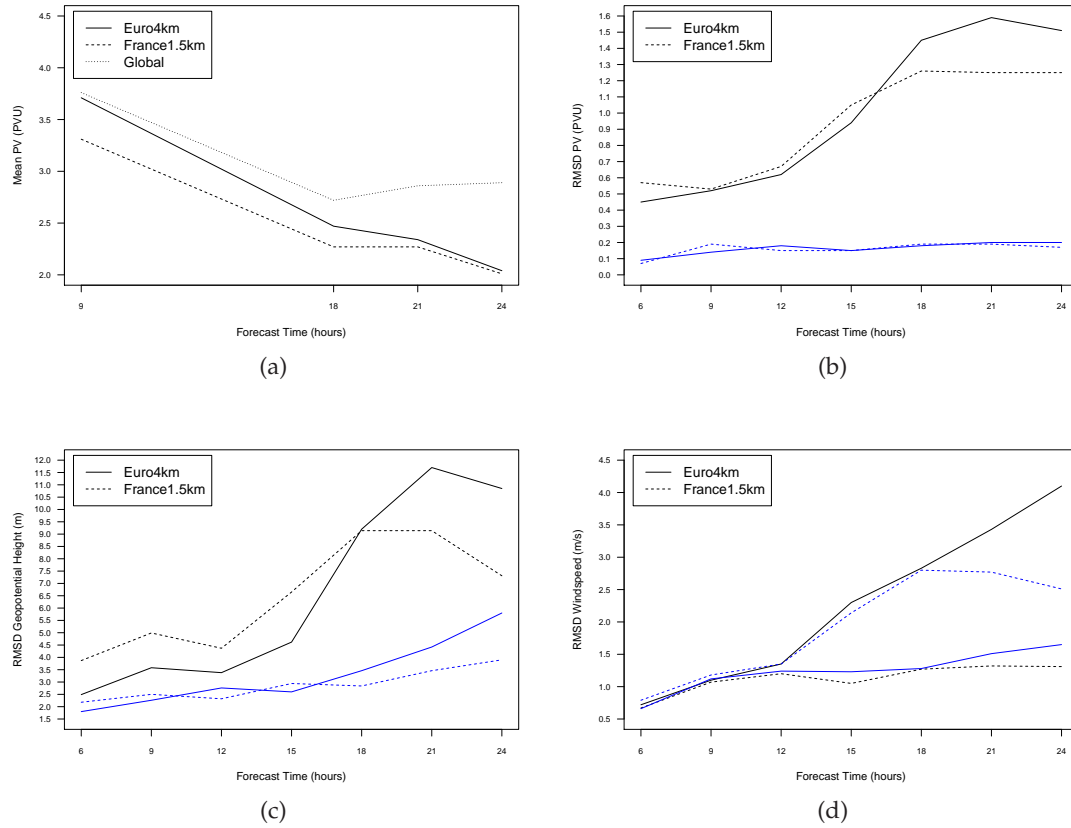

Figure 4.23: Coarse grained Euro 4 km and France 1.5 km compared to the coarse grained Global for (a) Mean PV at 250 hPa, (b) RMSD for PV, (c) RMSD for Geopotential height and (d) RMSD for windspeed. For figures (b), (c) and (d) black lines indicated 250 hPa and blue lines are 500 hPa. RMSD values are calculated over the sub-section used to coarse grain.

4.4.4   Summary of Coarse Graining

Although the forecasts are not expected to be identical between the four models (due to their grid-spacing), it is expected that once coarse-grained the four models could be similar which would suggest the extra detail the convection-permitting models provide would have little impact on the downstream forecast. Here, however, it has been shown that even after coarse graining, the PV, rainfall and windspeed of the four models are still different. These differences have also been shown to grow over time (comparing the differences between the models at 09 UTC to the differences at 18 UTC). The Global model, in particular, appears very different to the convection-permitting models. How-

ever, there are large differences between the convection-permitting models too (Euro 4 km, France 1.5 km and UKV models). Of these differences which occur in the coarse grained data, the most notable are:

- The explicit representation of convection in the convection-permitting models generates more localised and higher magnitude PV anomalies (both negative and positive) which still exist after coarse graining, causing growth in RMSD values for PV, windspeed and geopotential height over time (Figure 4.23(b)–4.23(d)). Differences below around 350 hPa after coarse graining are minor however any positive PV anomalies in the convection-permitting models cover a larger area due to horizontal dipoles of PV being represented in the original data which are not in the convection-parametrizing model.

- The convection-permitting models allow negative PV to be created at tropopause level (250 hPa), which does not occur in the convection-parametrizing Global model. In the Euro 4 km model this negative PV anomaly persists after coarse graining but in the France 1.5 km model it is smoothed out to near zero for the MCS being studied.

- Negative PV anomalies created at tropopause level in the convection-permitting models lead to differences in the windspeed and potential temperature at this level, when compared to the Global model, which persist after coarse graining. This impacts the environmental flow around it, creating divergent outflow and produces a north-westerly track over the UK instead of northerly track which occurs in the Global model.

- Rainfall rates are more intense and rainfall is more widespread in the Euro 4 km model than in the other models. However the location of the rainfall is similar between this model and the France 1.5 km model. The Global model shows no rainfall at 18 UTC due to not representing the MCS. The UKV model produces rainfall too far northwest.

4.5 Conclusions

The aim of this Chapter was to investigate the question posed in Section 1.1: How is the forecasting of MCSs affected by the representation of convection in NWP models (whether convection is parametrized or permitted by the model) and what are the associated PV structures produced? A number of hypotheses were posed in Section 4.2 to investigate this question. These hypotheses were investigated by performing an analysis of the comparison in PV, windspeed and rainfall between the Global, Euro 4 km, France 1.5 km and UKV models for the original model data and the coarse grained data. This section discusses the conclusions based on the hypotheses posed in Section 4.2 and whether these hypotheses are true once the model output is coarse grained.

Hypothesis: Convection and convective precipitation will be represented better in the higher resolution models (when compared to reality), than in the global model, since they represent convection explicitly

As anticipated, the convection-permitting models give a better representation of the convection (compared to rainfall radar; Figure 3.18(b) and 3.18(d))) associated with the MCS as it develops (at 09 UTC) and matures (18 UTC). The convection-permitting Euro 4 km and France 1.5 km models both represent the MCS in a similar location to reality and both create cells of intense rainfall surrounded by weaker stratiform rainfall which does not cover a large enough area (Figure 4.1(b),4.1(c),4.2(b) and 4.2(c)). At 09 UTC there were small cells of rainfall (>10 mmhr^{-1}) which did not occur in reality and at 18 UTC the Euro 4 km created too large cells of intense rainfall in comparison to reality. Both the Euro 4 km and France 1.5 km models did not produce the large area of stratiform rainfall that occurred in reality surrounding the cells of >10 mmhr^{-1} rainfall (Figure 3.18(b) and 3.18(d)).

The convection-parametrizing Global model represented the MCS initially (at 09 UTC; Figure 4.1(a)), but at MCS maturity (at 18 UTC; Figure 4.2(a)) the MCS was no longer represented (although the second MCS over the south France was) and thus no associated rainfall was produced in this model. Although the UKV model represented the MCS the rainfall produced was too light and occurred too far west in comparison to reality (Figure 4.2(d)). As the Global model provided the start dump and boundary conditions for the UKV model and did not represent the MCS, the UKV model produced the

MCS too early upon it reaching the boundary of the UKV model and thus the location, strength and track were misrepresented.

Upon coarse graining to comparable grid-spacing the more intense rainfall rates in the convection-permitting models still persist (up to 3 mmhr^{-1} stronger rainfall at 18 UTC for the second MCS which the Global model did represent). Stronger positive and negative PV anomalies also occur in the convection-permitting models after coarse graining (up to -5 PVU negative difference and 6 PVU positive difference at 18 UTC; Figure 4.13(a)–4.13(c)). These stronger negative PV anomalies at upper-levels (250 hPa) have an associated impact on the windspeeds causing there to be anticyclonic outflow (weaker windspeeds to the east and stronger windspeeds to the west; Figure 4.21(a)–4.21(c)). This impacts the circulation patterns causing the coarse grained convection-permitting models to have a more north westerly flow than the convection-parametrizing Global model which has a northerly flow. This leads to the ridge over western France being located further west in the convection-permitting models and a strengthened trough–ridge boundary also occurs.

The difference in positioning and amplitude of the ridge boundary leads to negative PV differences of up to 2 PVU with associated negative θ differences of up to 2 K and positive windspeed differences of up to 2ms^{-1}. Latent heat release in the convection-permitting simulations leads to negative or low-valued PV anomalies forming at upper-levels associated with the PV and these negative or low-valued PV anomalies persist after coarse graining. Negative PV advection by diabatically driven outflow at upper-levels has been found to amplify the tropopause height in previous studies related to tropical cyclones (Grams and Archambault, 2016) and has similarly been found in this study.

The largest differences (in PV, windspeed, potential temperature and geopotential height) between the convection-permitting and convection-parametrizing models after coarse graining occur at upper-levels (350–250 hPa) due to the persistent negative and low magnitude PV anomalies; this is important as it is at this level where the most influence on the downstream flow will occur. Below this level differences do develop over time but at a slower rate (Figure 4.23(b)–4.23(d)). The adjustment of the large-scale environment to the heating in an MCS is rapid as the gravity waves move away from the system at speeds of 50 ms^{-1} in response to the convective region heating profile (Mapes,

1993). This indicates that variations at the synoptic-scale are likely to happen eventually since there are small-scale (convection scale around the MCS) differences which have developed and have grown over time to 00 UTC 6 July. Davies and Didone (2013) found that errors in PV grow largest at upper-levels near the tropopause and generally grew along cutoffs and gradients of troughs and ridges which has found to be the area that differences between the convection-permitting and convection-parametrizing simulations occur in this study.

Previous studies have found that negative PV anomalies at upper-levels induce larger perturbations than positive PV anomalies at middle levels (Pomroy and Thorpe, 2000) which provides a basis for the upper-level negative PV anomalies producing larger differences between the convection-permitting and convection-parametrizing simulations here. Larger differences at upper-levels are particularly caused by the upper-level negative PV anomalies being missing from the convection-parametrizing simulations. In the convection-permitting cases the PV dipoles will also have different circulations and temperatures associated with them than in the PV anomalies produced in the convection-parametrizing case, (with larger penetration depth due to their greater magnitude) which will cause a variation in the gravity wave response from the PV anomalies. This difference in response leads to differences between the convection-permitting and convection-parametrizing simulations downstream from the PV anomalies produced by the MCS.

Hypothesis: As the resolution increases the PV anomalies arising from diabatic heating due to convection will become better represented with a more detailed structure, have higher values and extend deeper in the vertical

The convection-permitting models did represent the PV structures with more detail (due to the increased resolution) and they produced negative PV anomalies (up to -15 PVU at between 500 hPa and 250 hPa; Figure 4.5(b), 4.5(c) and 4.6(b)–4.6(d)) which did not occur in the Global PV structures (Figure 4.5(b) and 4.6(a), lowest PV approximately 0 PVU). Additionally, stronger positive PV anomalies were created in these convection-permitting models (up to 18 PVU, between 750 hPa to 250 hPa, whereas Global PV had a maximum of 3 PVU, at 500 hPa, where the MCS occurred). The PV anomalies produced by the MCS extend from around 800 hPa to 250 hPa in the convection-permitting models, but in the Global model they only extend from 700 hPa to 400 hPa, showing the impact

of the stronger convection created by the convection-permitting models due to localised heating in these models which the convection-parametrizing simulations cannot represent.

The negative PV anomalies at upper-levels in the convection-permitting models cause the wind direction to be in a more northwesterly direction in the these models compared to the more northerly flow in the Global model. Previous studies have shown that negative PV anomalies at upper-levels can cause the retardation of eastward progression of weather systems due to the anti-cyclonic circulations associated with them (Grams and Archambault, 2016; Quinting and Jones, 2016; Riemer *et al.*, 2008). Although the magnitude of the negative and positive PV anomalies found in association with the MCS are much larger magnitude in the convection-permitting models than was found in the previous Chapter for the NAE model and for the Global model in this Chapter, the same coherent structure was also seen in this Chapter. The negative PV anomaly aloft at tropopause level along with a positive PV anomaly at middle levels with negative PV either side of it was seen in the convection-permitting simulations. Therefore, the strength of the PV anomalies created is dependant on the resolution of the model however, the same coherent structure develops (except for in the Global model where negative PV anomalies do not develop as the convection is too weak).

After coarse graining was implemented the convection-permitting simulations were smoothed out so they no longer had the detailed structure but covered a larger horizontal area. The magnitude of the PV anomalies remained stronger in the convection-permitting simulations than in the Global model simulation after coarse graining however, the vertical extent was similar between all models after coarse graining. The convection-permitting models did retain the negative or low-valued PV at 250 hPa after coarse graining that does not occur in the Global model.

Hypothesis: Horizontal dipoles of PV may be produced in the Euro 4 km, France 1.5 km and UKV models as well as vertical dipoles

As expected from Chagnon and Gray (2009) the Euro 4 km, France 1.5 km and UKV models all create horizontal dipoles of PV associated with the MCS whereas the Global model does not. These horizontal PV anomalies covered a larger horizontal area over time due to the MCS developing and maturing. The horizontal PV anomalies help to amplify the magnitude of the PV anomalies in the coarse grained convection-permitting

models since they create a stronger PV anomalies that occur over a wider area than in the Global model.

Chagnon and Gray (2009) found that these horizontal dipoles of PV have different impacts on the vorticity than vertical dipoles with horizontal dipoles rapidly converting latent vorticity to relative vorticity. Therefore, it is expected that the downstream impact of these different dipoles produced in the convection-permitting and convection-parametrizing simulations will cause differences to develop between the forecasts. These horizontal dipoles of PV do not impact just the local scale though and appear to act to produce a larger scale PV structure which has a downstream impact on the flow.

Hypothesis: Capturing the initial convection associated with the MCS using a 1.5 km grid-spacing will produce a better representation of the MCS than the UKV model

For the purposes of this Chapter a so-called France 1.5 km simulation of the 5 July 2012 case was produced which encompasses the area over which the MCS initially develops as well as where it matures. The purpose of this France 1.5 km model was to investigate if including the area over which the MCS develops improves the forecast of the MCS, in comparison to the UKV model, which is the same resolution but misses the initial triggering of convection associated with the MCS as it does not extend into France.

For 5 July 2012 case the Global model fails to represent the MCS at its mature stage (18 UTC) even though it produces rainfall at the triggering stage (09 UTC). This has an impact on the UKV forecast of the MCS as the UKV model produces an MCS too early so the location of the MCS is too far west by 18 UTC which also caused the wind direction to be in a more westerly direction than in the other simulations. Negative PV anomalies also occurred at 250 hPa level over the east coast of the UK at 18 UTC which did not occur in the other simulations as they were further east still. This meant that the rainfall produced in the UKV model was too far west in comparison to reality. The France 1.5 km model had a better representation of the rainfall produced by the MCS in terms of location and magnitude suggesting that including the area where the MCS triggers may be favourable to the forecasting of MCSs. Extending the domain of the UKV model operationally could thus provide a means of improving the forecast of such systems that effect the UK. This was only for one case study though so further cases should be examined first to determine the robustness of the result. None of the simulations

managed to capture the full spatial extent of the stratiform rainfall associated with the MCS.

The mean PV of the coarse grained Global model at 250 hPa was found to be between 0.5–1 PVU larger than the mean PV for the convection-permitting simulations after the MCS matured (at 18 UTC; Figure 4.23(a)). The mean PV is lower for the convection-permitting simulations as the better representation of convection in these models leads to larger numbers of negative PV anomalies along with stronger magnitude negative PV anomalies at upper-levels that persist when coarse grained. As a consequence, after 18 hours (from 06 UTC 5 July–00 UTC 6 July) the RMSD differences between the coarse-grained convection-permitting models and convection-parametrizing model (in terms of PV, windspeed and geopotential height) have at least tripled in value (Figure 4.23(b)–4.23(d)), with the largest increase at upper-levels (250 hPa level). These differences increase over time, particularly after the MCS is identified (at 12 UTC), indicating that if the models were to be run for 5 days (or an extended period of time such as in an ensemble run) the differences could increase rapidly creating forecasts which will be very different to each other and could have a significant impact on the large-scale downstream forecast.

Adding idealised PV structures into model simulations has been found to improve forecasts of cyclones (Fehlmann and Davies, 1997) and MCSs (Gray, 2001) in some cases, compared to simulations that misrepresented the PV structures at middle and tropopause levels. In this Chapter convection-permitting models have been found to have persistent stronger negative and positive PV anomalies associated with the MCS from the 5 July case study even after coarse graining that cause differences in the windspeed, potential temperature and pressure patterns that grow over time. Therefore, this raises the question of whether it may be beneficial to add these convection-permitting coarse-grained PV structures associated with the mature MCS into the convection-parametrizing simulations to give a better representation of the PV structures associated with MCSs and a better representation of the subsequent downstream forecast.

It is important to investigate the impact of the persistent differences in PV, windspeed, potential temperature and geopotential height created between the convection-permitting and convection-parametrizing models on the large-scale environmental flow, specifically on the weather systems and downstream development in the days after an

MCS. The next Chapter will investigate the impact that the differences in PV structures associated with the mature MCS has on the downstream forecast.

Chapter 5

Downstream influence of MCS convection: deterministic simulations

5.1 Introduction

In Chapter 4 the differences in PV, windspeeds, temperature and rainfall between the convection-permitting and convection-parametrizing model configurations related to the MCS, were shown to persist after coarse graining was implemented. These differences were found to be initially of a small magnitude and small scale; however, it became apparent that these localised differences increased to cover a wider area and have a much larger magnitude when the MCS is mature as upscale transfer occurs(18 UTC 5 July). After 18 UTC 5 July when the MCS is mature the differences in PV, windspeeds and rainfall were shown to continue to grow up to 00 UTC 6 July. As a consequence, it is hypothesised that if the forecast were to be simulated for 5 days then these differences would increase markedly and lead to large-scale differences in the downstream forecasts.

Representation of the convection associated with the MCS being studied has been shown to be important, particularly due to the convection-parametrizing Global model not representing the MCS at all at its maturity. The convection-parametrizing model consequently did not represent the typical PV structure expected in an MCS which led to RMSD values increasing over time between the convection-permitting and convection-parametrizing models. The convection-permitting models also produced much higher magnitude negative and positive PV anomalies due to these models creating more localised convection than the convection-parametrizing model. Localised convection leads to associated impacts on the temperature and circulation patterns causing differences between the forecasts produced by the convection-permitting and convection-parametrizing models.

Differences in the PV anomalies (between the convection-permitting and convection-parametrizing models) associated with the MCS have been shown to persist after coarse graining, and the PV anomalies created by MCSs are known to be an important factor in producing an accurate forecast downstream (Gray, 2001). Therefore, the aim of this Chapter is to investigate the downstream impact of the differences found in the PV anomalies formed between the convection-permitting and convection-parametrizing models associated with the mature MCS because of the MCS only being explicitly represented in the convection-permitting model.

The following Section describes the hypothesis that is investigated in this Chapter along with a discussion of previous related studies. Next, the method used to investigate the hypothesis is discussed. This is followed by the results. Finally, the conclusions are presented.

5.1.1 Hypothesis

This Section discusses a hypothesis based on the question posed in Section 1.1: How does the representation of an MCS effect forecast evolution and forecast skill (compared to analysis) for the synoptic-scale forecast downstream from the MCS?

Hypothesis: Circulations associated with PV anomalies produced by the MCS may influence the downstream flow. Since the PV anomalies produced by the convection-permitting and convection-parametrizing models after coarse graining are different (because the convection-parametrizing models do not explicitly represent convection) this could lead to variations in the downstream forecast between models.

Rodwell *et al.* (2013) found that a 6 day forecast for western Europe was influenced by the first 12 hours of the simulation and the initial conditions that went into the model (especially related to deep convection over the USA). Therefore, it is likely that large-scale differences in the flow will be produced in this experiment since there are already differences after 12 hours.

The largest differences between the convection-permitting and -parametrizing models in this study occur at upper levels (350–250 hPa) at jet-stream level. The differences at this level are associated with a region of negative PV (in association with the MCS) developing in the convection-permitting models at this level. This negative PV at upper-levels was similarly found by Done *et al.* (2006) for a 12 km convection-permitting simulation

and did not occur for the same simulation with convection parametrization. This is important as it is at this level where the most influence on the downstream ridge–trough pattern will occur and hence influences the development areas for weather systems. Fehlmann and Davies (1997) found that the pattern and structure of PV distributions at tropopause elevations can be key to achieving a successful forecast in some cases.

The impact of the differences between the model simulations on the large-scale environmental flow, specifically on the low-pressure systems and downstream flow in the days after an MCS is investigated. Differences in the representation of PV anomalies in convection-permitting and convection-parametrizing models may impact the associated circulation patterns leading to downstream influences on the forecast due to their influence on the static stability and the large-scale circulation patterns (Gray, 2001). Gray (2001) found in global model simulations (at a grid spacing of $0.833° \times 0.555°$) that MCS PV anomalies can have a significant impact on the subsequent evolution of synoptic-scale disturbances. Specifically they found that, in one instance, the PV anomalies associated with an MCS acted to deepen the low-pressure centre by 3 hPa at least 48 hours ahead. Both papers emphasised the importance of accurately representing the intensity, timing and location of mesoscale areas of convection in the NWP model.

Gray (2001) found that the mid-level MCV associated with MCSs had the biggest impact on the NWP forecast due to the circulations associated with the positive PV, creating ascent and decent around the MCV. This study used a NWP model with the resolution $0.833° \times 0.55°$. This may have impacted their conclusion since it has been found in Chapter 4 that the convection-permitting models can develop a negative PV anomaly at tropopause level that the Global model fails to produce. This indicates that whether convection is explicitly represented or is parametrized has an important influence on if the negative PV at upper-levels is represented and was similarly found by Done *et al.* (2006).

It is likely that these negative PV anomalies could have a large impact on the downstream flow that Gray (2001) were unable to detect because of insufficient resolution to explicitly represent the MCS. Convection-parametrizing models also average the effect of convection over a grid-box so PV destruction at upper-levels does not occur to the same extent meaning negative PV tends to not develop in these models at upper-levels associated with MCSs. Additionally, the PV anomalies introduced at tropopause level

were idealized from satellite imagery and were added as near zero rather than being negative at tropopause level. Gray (2001) did however find that the mid-level PV anomalies could persist after the PV anomalies at tropopause level had dissipated so it is still possible that the MCS produced PV anomalies at mid-level can have more of an impact in MCS forecasts.

Since Gray (2001) found an improvement in the forecasts when MCS PV anomalies are simulated in a Global convection-parametrizing model, convection permitting models may also produce downstream forecast improvements if the PV anomalies are accurately represented and positioned. Selz and Craig (2015) and Zhang *et al.* (2007) found that errors (related to the addition of initial condition perturbations) on the convective scale grow most quickly at the location of convection with errors growing much slower on the synoptic scale. Three stages of error growth were found. Firstly, small-scale errors grow quickly driven by convective instability and moist processes. Secondly, errors at the convective-scale start to spin up balanced motions, and these continue to grow at a slower rate in stage 3 through baroclinic instability. The impact of MCS convection on the downstream flow is investigated to determine how differences grow and what impact they cause on the downstream development. The method is now discussed that is implemented throughout the Chapter.

5.2 Deterministic forecast

To investigate the hypothesis we first investigate the impact on the evolution of a single forecast before performing ensemble simulations in Chapter 6. A deterministic control Global model forecast is performed along with a deterministic forecast with MCS perturbations added. The following section describes the methodology used to produce the MetUM simulations used during this Chapter using the case study 5 July 2012. Five-day forecasts are simulated between the period 18 UTC 5 July 2012 to 18 UTC 10 July 2012 (initialised from 00 UTC 5 July 2012 using Global IC and BCs). The simulations are Global 25 km grid spacing.

5.2.1 Method

A Global MetUM simulation is produced that starts at 00 UTC 5 July 2012 and runs for 18 hours. Using this run, a start dump is created at 03 UTC (T+3) and 18 UTC (T+18) 5 July 2012 (3 hours and 18 hours into the forecast). The 3 hour dump at 03 UTC is used to produce a Euro 4 km MetUM simulation that is run for 15 hours (initialised using Global IC and BCs at 00 UTC; run for 3 hours first to allow for model spin-up). From the Euro 4 km simulation output is produced at 18 UTC 5 July 2012. This output of winds and temperatures is reconfigured to Global model vertical levels (lid at 80 km instead of 40 km) and is then coarse grained to the Global model horizontal resolution (25 km grid spacing). The difference between the coarse grained Euro 4 km dump and the Global dump at 18 UTC is computed. The differences are calculated over the western European area that both of the MCSs covered and can be seen in Figure 5.6(b). It encloses the area over which the representation of both MCSs in the convection-permitting model produces differences in the Global model forecast.

The MCS over northern France was not represented by the Global model whereas the MCS over south France was represented by the Global model, although the PV structure was represented differently than in the convection-permitting models (see Chapter 4). The differences between the Euro 4 km coarse-grained to the Global model grid and the Global model forecast form the perturbations, termed MCS perturbations, which are added into the Global model at 18 UTC (18 hours into the forecast). These MCS perturbations are added using incremental analysis update (IAU) capability of the MetUM (see Section 2.4). This allows for an investigation into how the wind and temperature differences that persist after coarse graining related to the PV structures associated with the MCSs impact the downstream forecast. The methodology can be seen in Figure 5.1.

The various Global model simulations are then run for five days starting at 18 UTC 5 July 2012 (when the MCS perturbations are included T+18; initialised at 00 UTC 5 July using Global IC and BCs) and ending at 18 UTC 10 July 2012. One simulations is the control (the original forecast without any changes). The other simulations have the MCS perturbations added over different vertical model levels at 18 UTC 5 July 2012. The differences between the simulations are then analysed and the results of this are given in Section 5.3. Four different MCS perturbation files are added (at different vertical levels) in to the Global model simulations and these are now described.
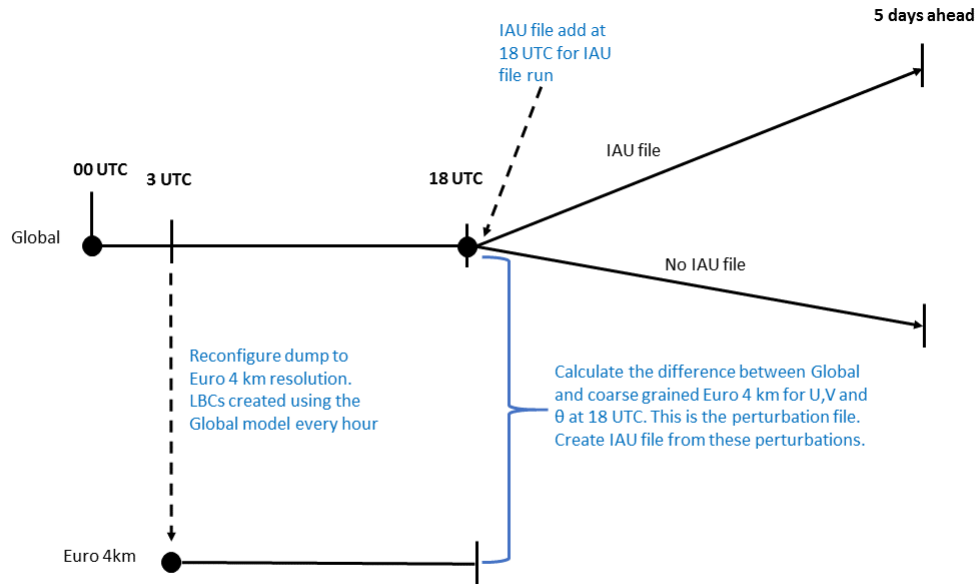
Figure 5.1: Ensemble run plan. Time starts at 00 UTC 5 July 2012 on the left of the figure. 5 days ahead indicates 18 UTC 10 July 2012. IAU file is the MCS perturbations added.

5.2.2 MCS Perturbations

For the purposes of this study, MCS perturbations are added at 18 UTC 5 July 2012 (T+18) and are added uniformly with equal weighting over a 60 minute period (added at every timestep which is every 10 minutes). The perturbation files used are calculated as the difference between the coarse-grained Euro 4 km model simulation and the Global model simulation at 18 UTC on 5 July 2012 when the MCS is mature. The MCS perturbations are created using 18 UTC 5 July fields as this is the time that the MCS was found to be most mature. Inputting the PV structures associated with the mature MCS will allow for a determination into how the downstream forecast is influenced by these MCS PV structures.

The fields zonal wind (u), meridional wind (v) and potential temperature (θ) are used to provide the perturbations. These fields were chosen due to the previous Chapter showing the influence of the PV structures associated with the MCS resulting in an impact on the circulation patterns and the temperature (since PV anomalies are associated with changes in the temperature and circulation patterns), since we cannot feed PV into the model as it is not a diagnostic variable in the MetUM this acts as a surrogate. In this case the fields in the IAU perturbations are found using start dumps generated by the MetUM. These fields were similarly used in the study by Gray (2001); however, PV

inversion was used to find the U, V and θ fields in that case. It is not clear how PV inversion could be utilised in this study though due to the scale of the PV anomalies and the fact they are very noisy meaning that it is unlikely any of the balance conditions required for PV inversion would hold in this case. As PV inversion was not used in this study the u, v and θ fields input as MCS perturbations are unbalanced therefore the model will react to them upon them being included in the simulation. Four IAU perturbation files are introduced and are described as follows:

1. Perturbations added at upper levels (levels 33–40) in the model equivalent to approximately 250 hPa–350 hPa. These levels were chosen because they showed the largest differences between the convection-permitting and -parametrizing models (Figure 4.13(a)). These perturbations will be known as UPERTS. An example of these perturbations is shown in Figure 5.2(a).

2. Perturbations added over all model levels (levels 1-70) equivalent to 1000 hPa–50 hPa. These perturbations will be known as ALLPERTS. It must be noted that although the Euro 4 km model has 70 levels the lid of the model is at 40 km whereas the Global model is at 80 km. Above 40 km is the stratosphere so will not impact on the MCS structures in the troposphere. The Euro 4 km simulations are also reconfigured to Global model vertical levels before coarse graining is performed to produce the MCS perturbations. An example of these perturbations is shown in Figure 5.2(a) and 5.2(b).

3. Perturbations added at middle levels (levels 18–30) in the model equivalent to 450 hPa–750 hPa. These levels are where the positive PV tower related to the MCS is visible in the Euro 4 km model (Figure 4.6(b)). These perturbations will be known as MPERTS. An example of these perturbations is shown in Figure 5.2(b).

4. Perturbations described in 1 above, multiplied by a factor of three. These perturbations are used to see if larger perturbations at the jet-stream level have a greater impact on the downstream forecast since the differences at this level seem to be larger. These perturbations will be known as X3PERTS. An example of these perturbations is shown in Figure 5.2(c).

Figure 5.2(a)–5.2(c) show that the magnitude of the perturbations of θ added at upper-levels is up to 6 K whereas at middle levels the magnitude is up to 2.5 K. When
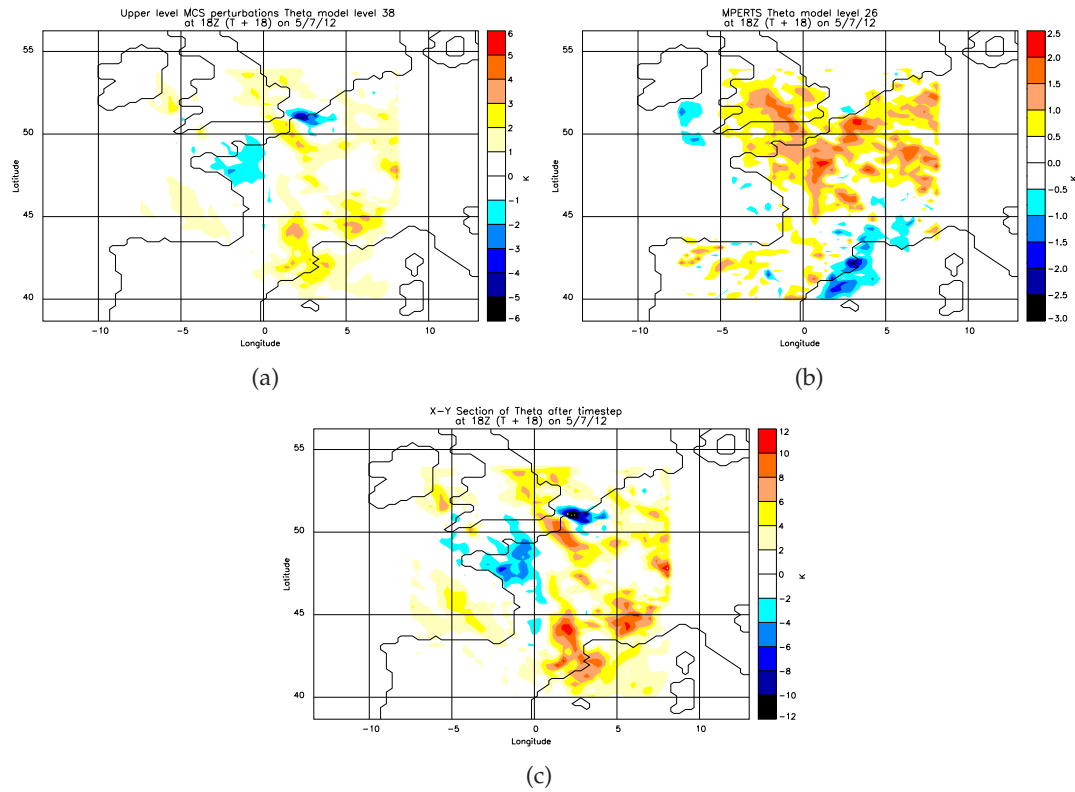
Figure 5.2: 18 UTC 5 July 2012: MCS perturbations of θ for (a) model level 38 (approximately 250 hPa) for ALLPERTS and UPERTS, (b) model level 26 for ALLPERTS and MPERTS (approximately 500 hPa), (c) model level 38 for X3PERTS. Perturbations are calculated as the difference between the coarse grained to 25 km grid spacing Euro 4 km and the 25 km grid spacing Global model.

the MCS perturbations are added to the simulations the u, v and θ fields are perturbed.

The model then follows these modified fields to the next timestep. The results of adding

these four MCS perturbation files to the Global model configuration are now discussed.

5.3   Deterministic results

The following section presents the results from the deterministic model simulations. For each simulation the PV and geopotential height fields are analysed at 250 hPa. This level is used as it is here that the most differences occur and where the largest influence occurs on the downstream flow.

The Global simulation with no MCS perturbations added is compared to the four simulations that have MCS perturbations added. Firstly, an analysis of the differences produced between all the simulations one hour after the perturbations have been added (at 19 UTC) is given. Secondly, the impact that the perturbations have on the developing UK cyclone on 6 July 2012 is discussed. Thirdly, the PV and geopotential heights at 250 hPa for 06 July 2012 to 10 July 2012 is analysed for the original Global model simulation and the Global model simulation with MCS perturbations added at all model levels. Lastly, root mean square difference (RMSD) plots are discussed for PV and mean sea-level pressure (PMSL).

5.3.1   Immediate impact of MCS perturbations on 5 July

The MCS perturbations are added in equal weights over an hour period from 18 UTC to 19 UTC 5 July 2012. The differences in the geopotential height and PV are analysed at 19 UTC. The differences in PV are minimal below 350 hPa hence are not shown. The largest differences are seen at 250 hPa.

Regardless of the levels MCS perturbations are added they lead to a reduction of the geopotential height (up to a maximum of 40 m when the perturbations are added over all levels, Figure 5.4(d)). Deepening occurs along the axis of the upper-level trough over the UK at this time. The magnitude of the deepening is largest for the X3PERTS but for ALLPERTS the geopotential height is reduced further than in the MPERTS and UPERTS simulations (Figure 5.4(b)-(e)). The MPERTS still have a detectable impact and cause a reduction in geopotential height by 10 m at 250 hPa (Figure 5.4(e)).

The short-term impact of adding the MCS perturbations to the Global model (immediately after the MCS perturbations have stopped being added) is to deepen the upper-level trough over the UK by sharpening the gradient in geopotential height at 250 hPa on the western edge of the tip of the trough which is associated with an enhanced upper-
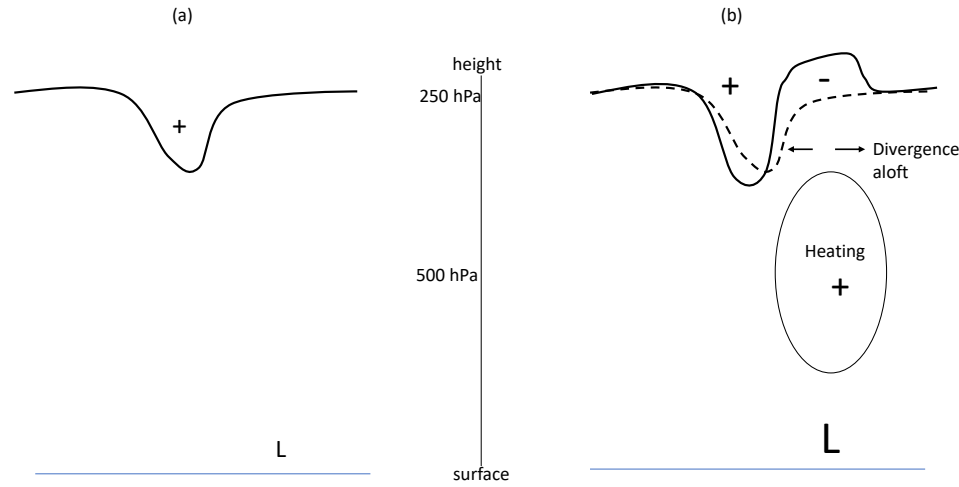
Figure 5.3: Schematic to show how the PV anomalies associated with the MCS impact the upper-level trough. (a) indicates an upper-level trough where there is no MCS present. A positive PV anomaly exists associated with the upper-level trough and a low-pressure system develops at the surface. (b) indicates an upper-level trough which is impacted by the presence of an MCS and its associated positive PV anomaly at middle levels and negative PV anomaly at upper-levels due to divergent outflow. The negative PV at upper-levels causes an erosion of the upper-level trough and causes the tropopause height to be heighten. The upper-level trough is also pushed backwards towards the west in comparison to (a) where no MCS is present. The low pressure at the surface is also deepened and the positive PV anomaly associated with the upper-level trough is magnified along with an enhancement of the jet out of the upper-level trough. The impact of upper-level negative PV anomalies associated with MCS can also manifest in increasing the PV gradient at the trough-ridge boundary. This figure was modified from Figure 9.12 in Martin (2006). The $+$ symbol indicates positive PV anomaly and the $-$ symbol indicates a negative PV anomaly. L indicates a low-pressure system and height is indicated in pressure levels (hPa).

level jet in the MCS perturbation simulations. The upper-level trough is also shifted to the west in the simulations with the MCS perturbations included and this impact is shown in the schematic in Figure 5.3.

At the 500 hPa level at this time the perturbations added cause a deepening but of a smaller magnitude: around ± 12 m for the UPERTS (Figure 5.5(b)), showing the influence that the upper-level perturbations already have on the atmosphere below. For ALLPERTS the geopotential height is up to 16 m lower (Figure 5.5(d)) which is larger than the difference created in UPERTS, MPERTS and X3PERTS (Figure 5.5(c)). The UPERTS leads to a greater impact on the geopotential height at 500 hPa as MPERTS only deepened the geopotential height by -4 m (Figure 5.5(e)). Figure 5.5(e) shows a difference of approximately 10–15 m which is equivalent to about 1 hPa after 1 hour of the simulation. Beare *et al.* (2003) found that middle level perturbations of PV caused a 5 hPa difference in pressure after 48 hours. Figures 5.5(b)–(e) also show a striking resemblance to that of Figure 3, 4 and 5 of Beare *et al.* (2003) which shows the vertical velocity response

to PV perturbations being added in the simulation of extratropical cyclones.

PV differences at this time show similar patterns for all four MCS perturbation simulations but different magnitude PV differences are found (Figure 5.6(b)-(d)). At 250 hPa there are no differences at this time for the model simulation with perturbations added at middle-levels. Differences in PV occur in relation to the upper-level jet. The MCS perturbations lead to a reduction in the magnitude of the negative PV (-4 PVU difference) related to the reduction in geopotential height, although the reduction in PV is noisier than the reduction in geopotential height (as it is an inherently noisier field; Figure 5.6(a)-(d)). This reduction in PV is due to the location of the high PV (associated with the tropopause fold of the frontal cyclone which pulls high PV air down from the stratosphere) differing between the perturbed and the unperturbed models (further west) along with the gradient at the ridge-trough boundary being stronger in the perturbed simulations (see schematic in Figure 5.3 for how this occurs due to the addition of the MCS). This location difference changes the amplitudes and patterns of PV between the model simulations and leads to associated differences in the circulation patterns and is related to more negative PV occurring in the simulations with the MCS perturbations included (Figure 5.6(a)-(d)).

5.3.2 Impact of MCS perturbations on the developing UK cyclone of 6 July

A cyclone developed over the UK on 6 July 2012 (Figure 3.14(g)). The influence on the development of the cyclone by adding the MCS perturbations to the convection-parametrizing model simulation is now investigated by examining rainfall, PMSL (00 UTC and 12 UTC 6 July) and geopotential height and PV (18 UTC 6 July) (Figure 5.7(a)-(d) and Figure 5.8(a)-(d)). In this case both the Global and Euro 4 km model simulations failed to capture the area of stratiform rain occurring over the UK on this day. Heavy rainfall up to 10 mmhr^{-1} was represented in the Euro 4 km model simulation (not shown here) though as it represented the MCS whereas the Global model simulation failed to represent the MCS at all at 18 UTC.

The Global model simulations with MCS perturbations added does have an impact on the rainfall especially over south France, although still fails to capture most of the stratiform rainfall that was occurring over southeast UK (Figure 5.7(b)-(e); colour bars differ between model simulations and rainfall radar, however, the model simulations

represent very little rainfall <1 mmhr^{-1}). Heavier rainfall occurs in ALLPERTS (Figure 5.7(c)) than in the deterministic Global simulation (Figure 5.7(a)), with ALLPERTS being more similar to rainfall radar in terms of positioning (Figure 5.7(f)). At 00 UTC 6 July differences in the PMSL can also be seen to occur in the area where the MCS perturbations are added (see black rectangle in Figure 5.7(c)), with the 1010 hPa pressure contour being shifted further north in Figure 5.7(c) in comparison to Figure 5.7(a) where the MCS over the English channel is occurring. Differences in PMSL are apparent at the location of the MCS over south France along with the rainfall associated with the MCS being better represented in location in ALLPERTS (Figure 5.7(c)). The representation of the MCS over south France varies considerably between each of UPERTS, MPERTS, ALLPERTS, X3PERTS and the control.

At 12 UTC 6 July 2012, when the UK cyclone has fully developed, the simulations with the MCS perturbations added create heavier rainfall, over a larger area than in the unperturbed deterministic Global simulation (Figure 5.8(a)–(e)). All the simulations still fail to capture the true extent of the stratiform rainfall produced by the UK cyclone in reality though (even when plotting values of rainfall <1 mmhr^{-1}, Figure 5.8(f)). The ALLPERTS simulation gives a better representation of the spatial extent of the rainfall and the location of the heavier rainfall than the deterministic simulation (Figure 5.8(c)). It also seems to have twisted the rainband further, which is more in line with reality. The error in the cyclone development is due to errors in the assimilation of the upper level structure therefore adding MCS perturbations improves the cyclone forecast but only for the simulation where perturbations are added at all levels. 12 UTC 6 July is 18 hours after the MCS perturbations are added to the Global simulation and already there are marked differences in the intensity and area of the rainfall produced along with differences in the PMSL. Geopotential height in the low-pressure region is reduced by 15 m in the ALLPERTS simulations at 250 hPa where the UK cyclone is located (not shown here).

Differences in PV are created surrounding the cyclone due to the upper-level trough being shifted to the south west when the perturbations are added and the ridge being amplified to the north west along with the gradient in PV at the boundary of the ridge being increased when the perturbations are added (Figure 5.3). A -1 PVU PV anomaly occurs at the boundary of the trough where the cyclone is impacting the UK that does not occur in the deterministic simulation (not shown here). These negative PV anomalies

at upper levels in the perturbed simulations immediately hinder the eastward progression of the trough and ridge by changing the upper-level wind patterns and push the tropopause higher in the perturbed runs, which amplifies the ridge consequently slowing it down.

Previous studies have shown that perturbations added to model simulations tend to grow fastest due to the influence of moist processes and tend to grow on the convective scale at first (Zhang *et al.*, 2007). In this case differences grow on the convective scale at first related to the cyclone over the UK. The magnitude of the differences decreases somewhat over the first day as the simulations dampen the initial perturbations (compare the amplitude of the differences in Figure 5.6(b)-(e) to Figure 5.9(b)-(e)). The spatial area of the differences increases rapidly over the first 24 hours though as it grows around the cyclone and begins to spread eastward as the perturbations begin to influence the downstream flow (Figure 5.9(a)-(e) and Figure 5.10(a)-(e)). The growth of the differences follows this same pattern regardless of the level at which the MCS perturbations were added and occurs for both PV and geopotential height. The slowest growth in the differences occurs for the simulation in which MCS perturbations are just added at middle levels (Figure 5.9(e)). Adding perturbations over all model levels and the associated mutual amplification of PV anomalies through action-at-a-distance may explain why the cyclone and MCS are represented better in this case.

On the first day of the forecast the differences that develop are related to the cyclone affecting the UK on this day with a larger amount of rainfall developing in the perturbed models and the high amplitude PV differences being spatially related to the frontal cyclone pattern. This could be related to errors growing on the convective scale growing in areas of convection (Zhang *et al.*, 2007). Zhang *et al.* (2003) also found that errors grow faster in higher resolution convection-permitting simulations therefore adding perturbations from a convection-permitting model may cause errors to grow more quickly. Both Zhang *et al.* (2007) and Selz and Craig (2015) found a three stage growth in errors. In the first stage convective scale errors grow and saturate quickly. The second stage occurs when convective-scale errors spin up to create balanced motions on the large-scale and they continue to grow into a third stage where growth slows due to baroclinic instability. Saturation of the errors occurs at this stage (Zhu and Thorpe, 2006).

Over the first 24 hours the first stage of the error growth has been seen in this study

by the differences growing on the convective scale related to the cyclone and the second stage is beginning with the differences spinning up eastwards onto the larger scale. Beare *et al.* (2003) also gives the balanced response to PV perturbations and found that there is a nonlinear response to the addition of localised finite amplitude PV anomaly perturbations in extratropical cyclones. The regions of sensitivity to these localised PV perturbations are situated at the minimum steering level and in the baroclinic region. Beare *et al.* (2003) also found that latent heating enhances the energy growth of the PV perturbations but they concluded that the maximum amplitude of the analysed PV is not necessarily the same as the location of maximum sensitivity to PV perturbations.
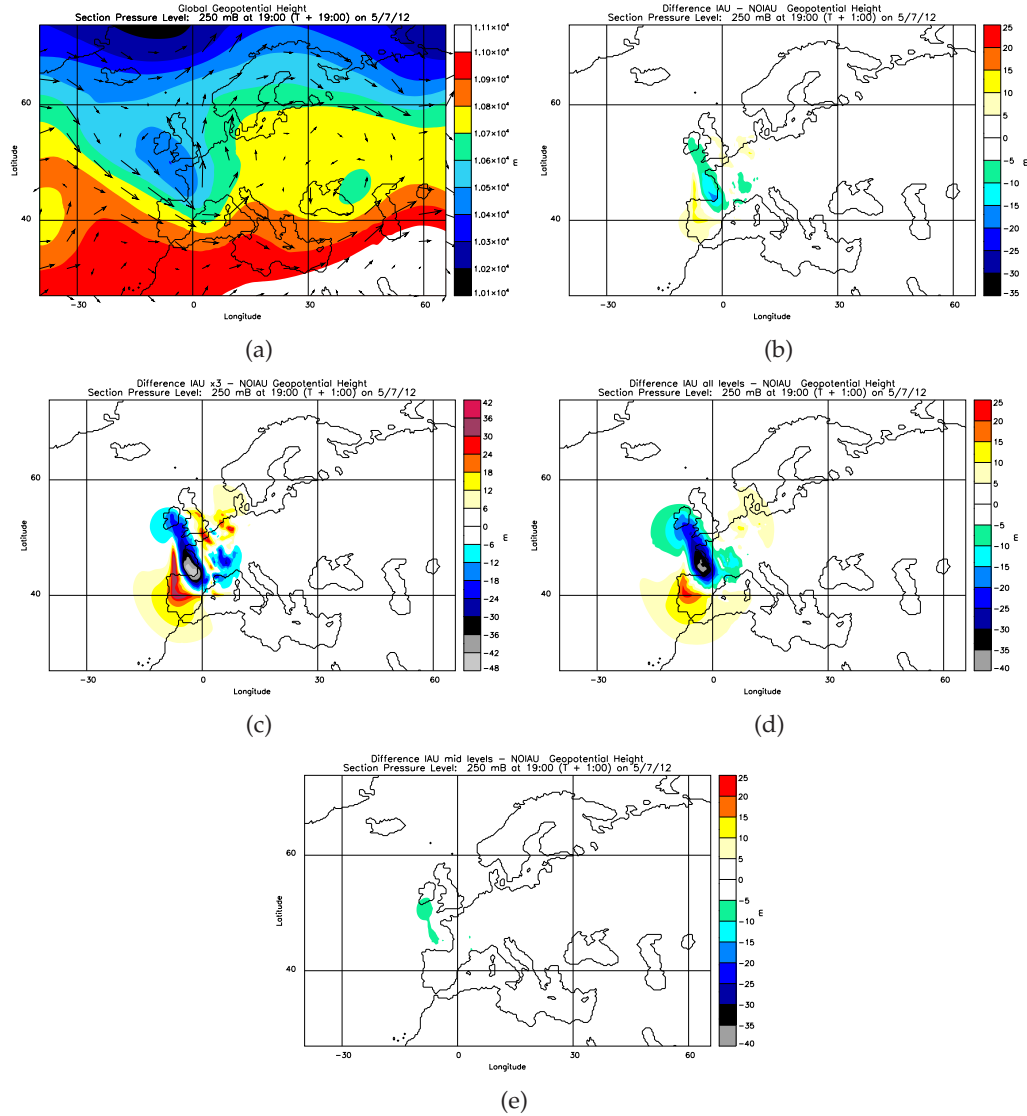
(a)

(b)

(c)

(d)

(e)

Figure 5.4: 19 UTC 5 July 2012: Geopotential heights at 250 hPa for (a) Global model, and the differences between the Global model simulation with and without the MCS perturbations added for (b) UPERTS, (c) X3PERTS, (d) ALLPERTS And (e) MPERTS.
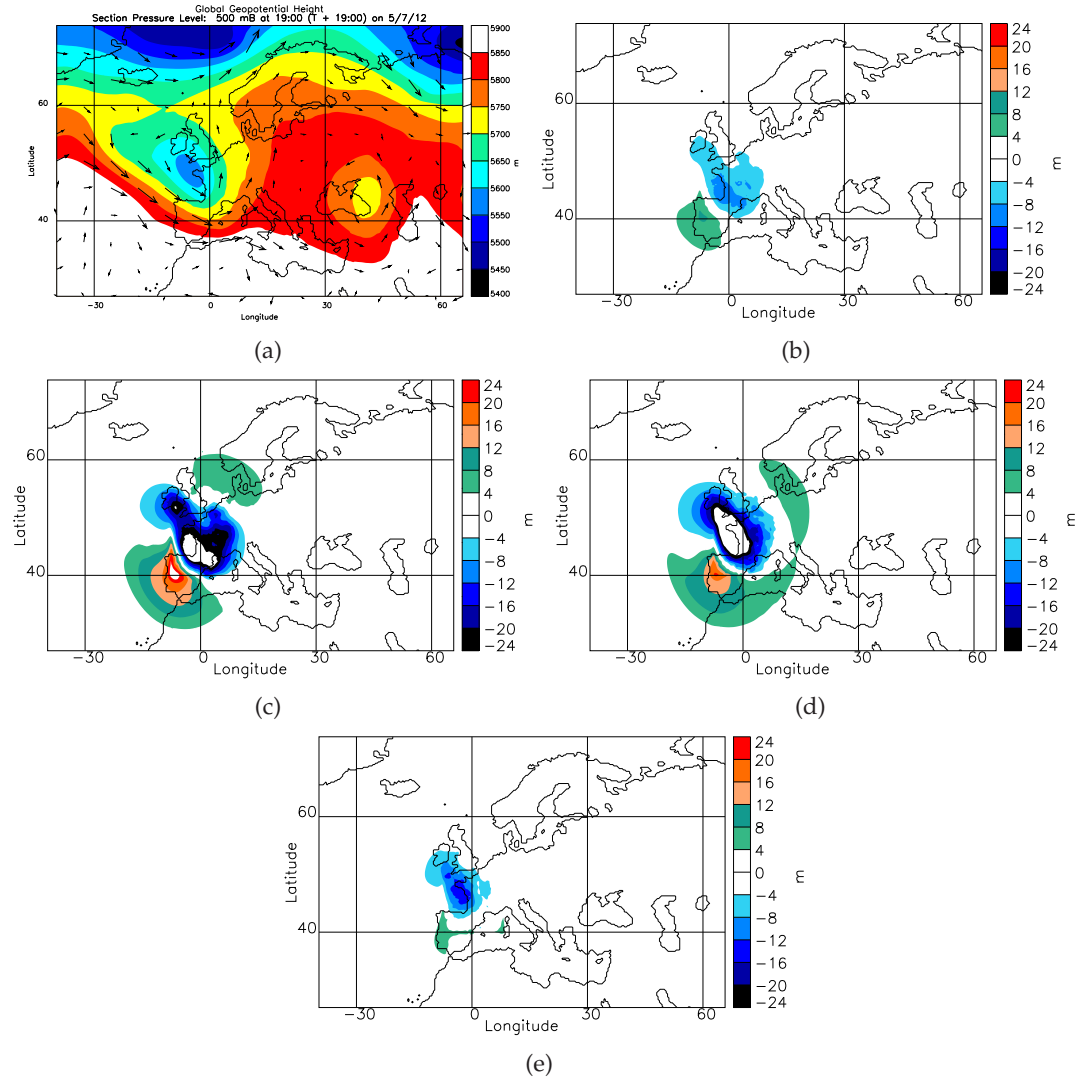
(a)

(b)

(c)

(d)

(e)

Figure 5.5: 19 UTC 5 July 2012: Geopotential heights at 500 hPa for (a) Global model, and the differences between the Global model simulations with and without MCS perturbations added for (b) UPERTS, (c) X3PERTS, (d) ALLPERTS and (e) MPERTS. Note that in figures (c) and (d) the colour bar saturates with the maximum value in (c) being 30 m and -30 m and (d) -40 m.
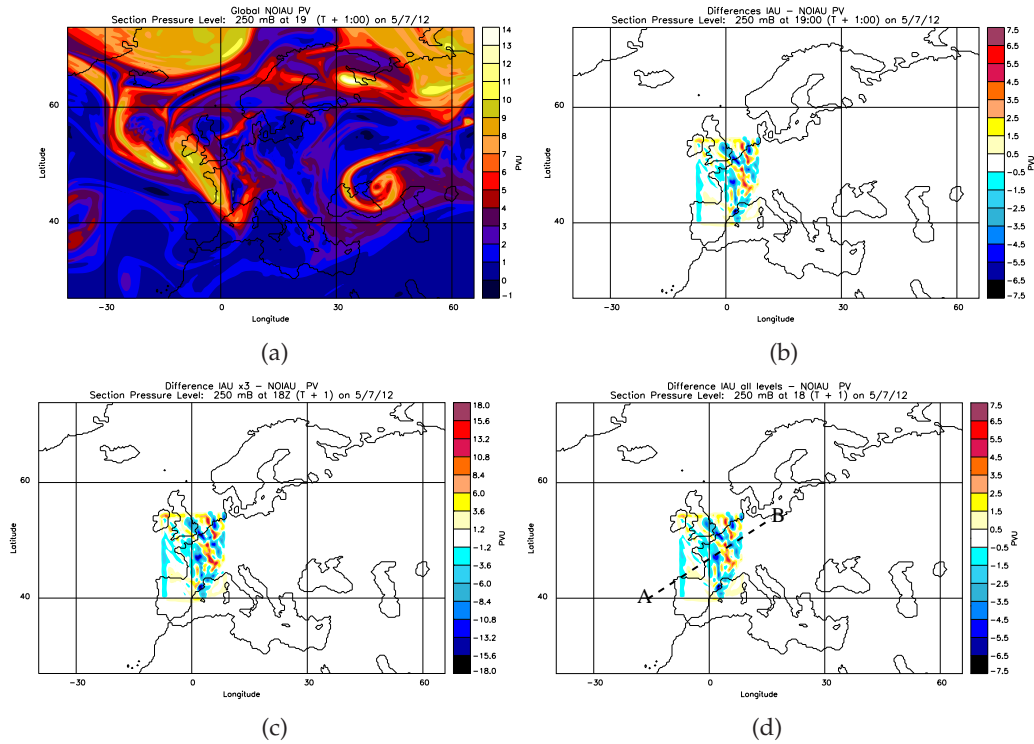
(a)

(b)

(c)

(d)

Figure 5.6: 19 UTC 5 July 2012: PV at 250 hPa for (a) Global model, and the differences be-tween the Global model simulations with and without MCS perturbations added for (b) UPERTS, (c) X3PERTS (contours are larger in this plot due to larger magnitude of perturbations) and (d) ALLPERTS. Cross-section A–B is used in Figure 5.16(a).
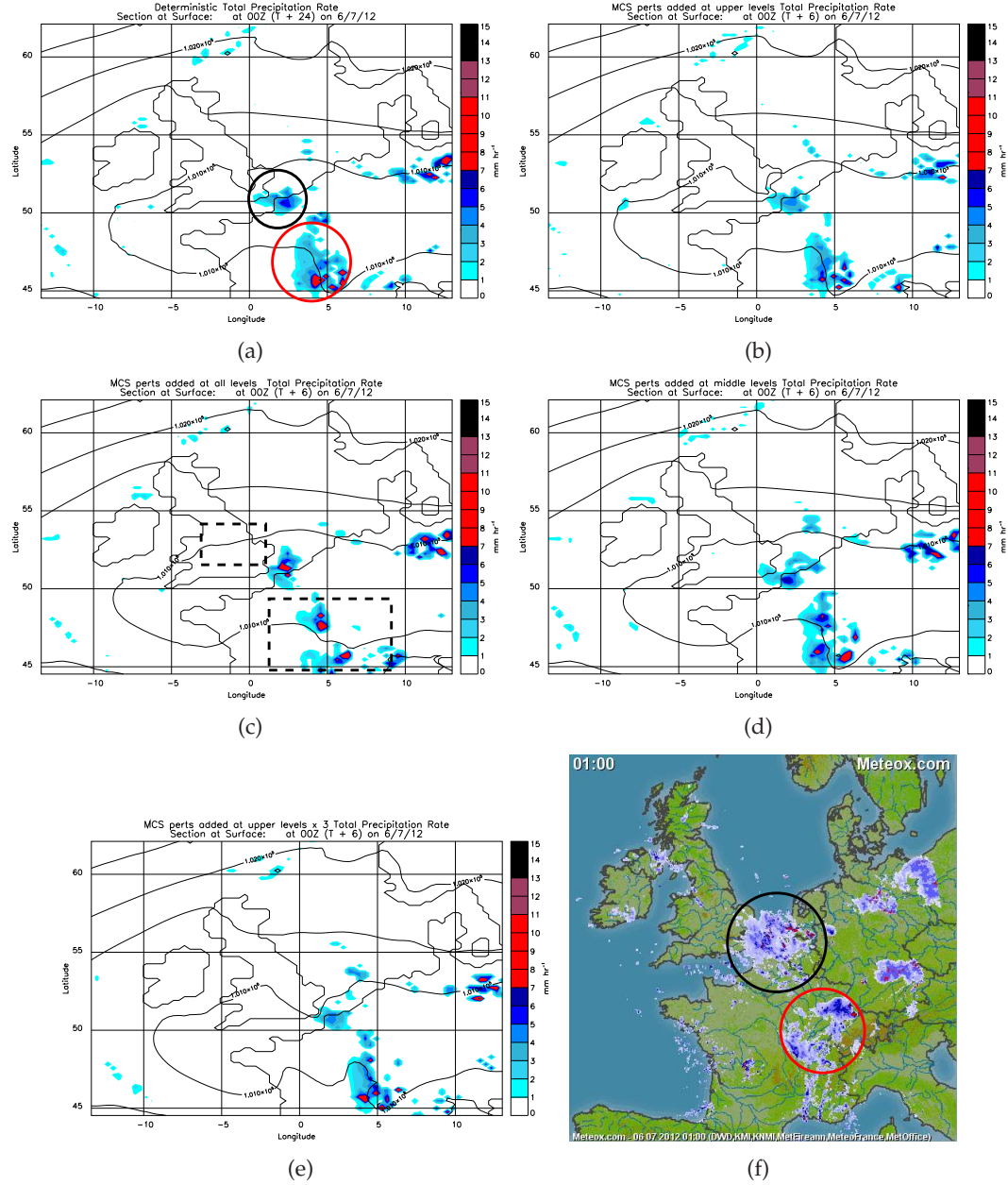
Figure 5.7: 00 UTC 6 July 2012: Total precipitation rates with black contours of PMSL (at 5 hPa intervals) for (a) Deterministic simulation and Global model simulation with MCS perturbations added at (b) UPERTS, (c) ALLPERTS, (d) MPERTS, (e) X3PERTS and (f) Rainfall radar taken from meteox website, blue colours signify <10 mmhr^{-1} rain and red signifies >10 mmhr^{-1}. Black circle signifies the MCS over northern France/ UK and the red circle indicates the MCS over south France. Colour bars differ between model simulations and radar however simulations represent very little rainfall <1 mmhr^{-1} so was not shown. Black dashed rectangle indicates areas where the PMSL differ between the simulations due to the MCS perturbations added.
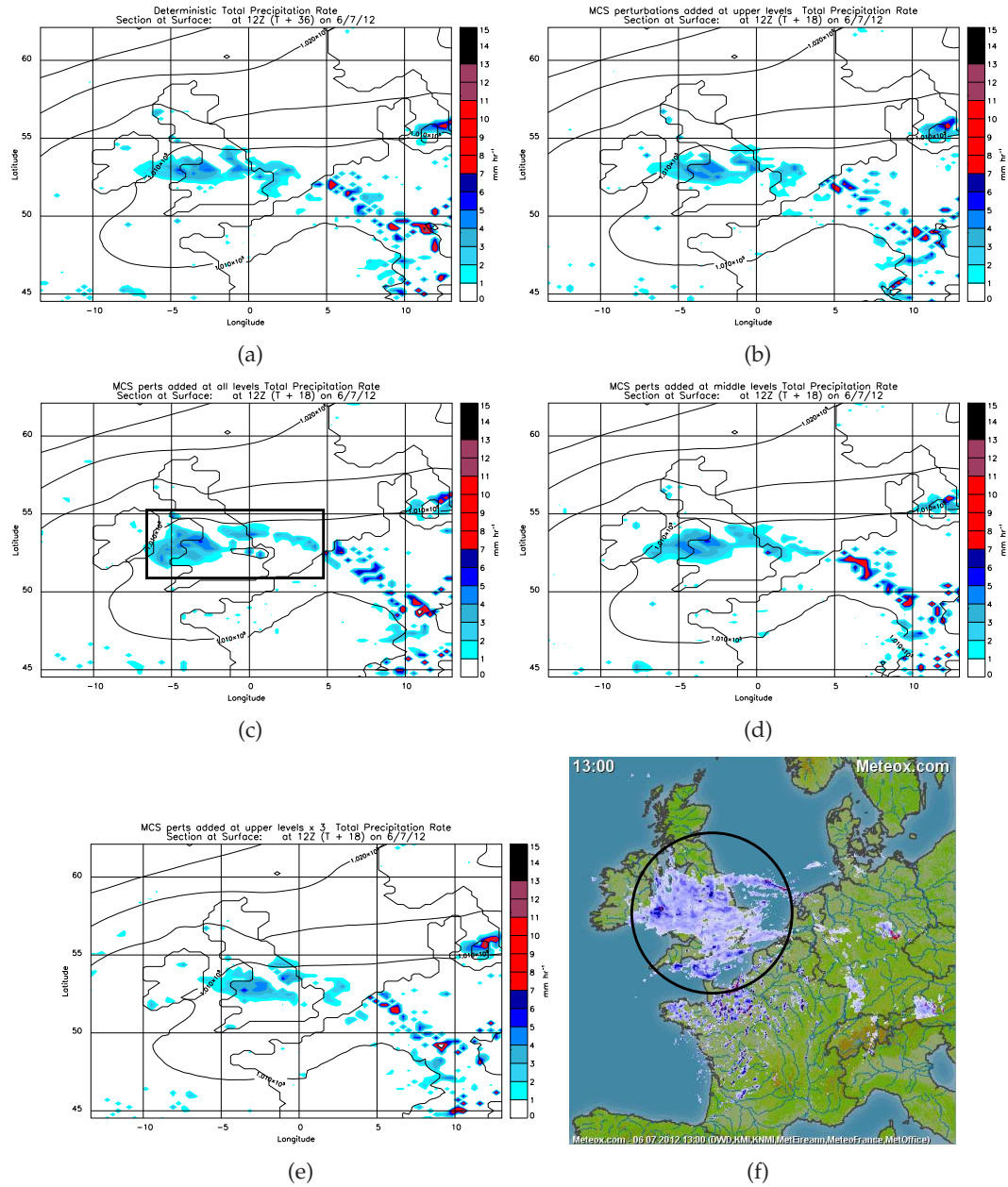
Figure 5.8: 12 UTC 6 July 2012: Total precipitation rates with black contours of PMSL (at 5 hPa intervals) for (a) Deterministic simulation and Global model simulation with MCS perturbations added at (b) UPERTS, (c) ALLPERTS, (d) MPERTS, (e) X3PERTS and (f) Rainfall radar taken from meteox website, blue colours signify <10 mmhr^{-1} rain and red signifies >10 mmhr^{-1}. Black circle and rectangle indicates the cyclone over the UK. Colour bars differ between model simulations and radar however simulations represent very little rainfall <1 mmhr^{-1} so was not shown.
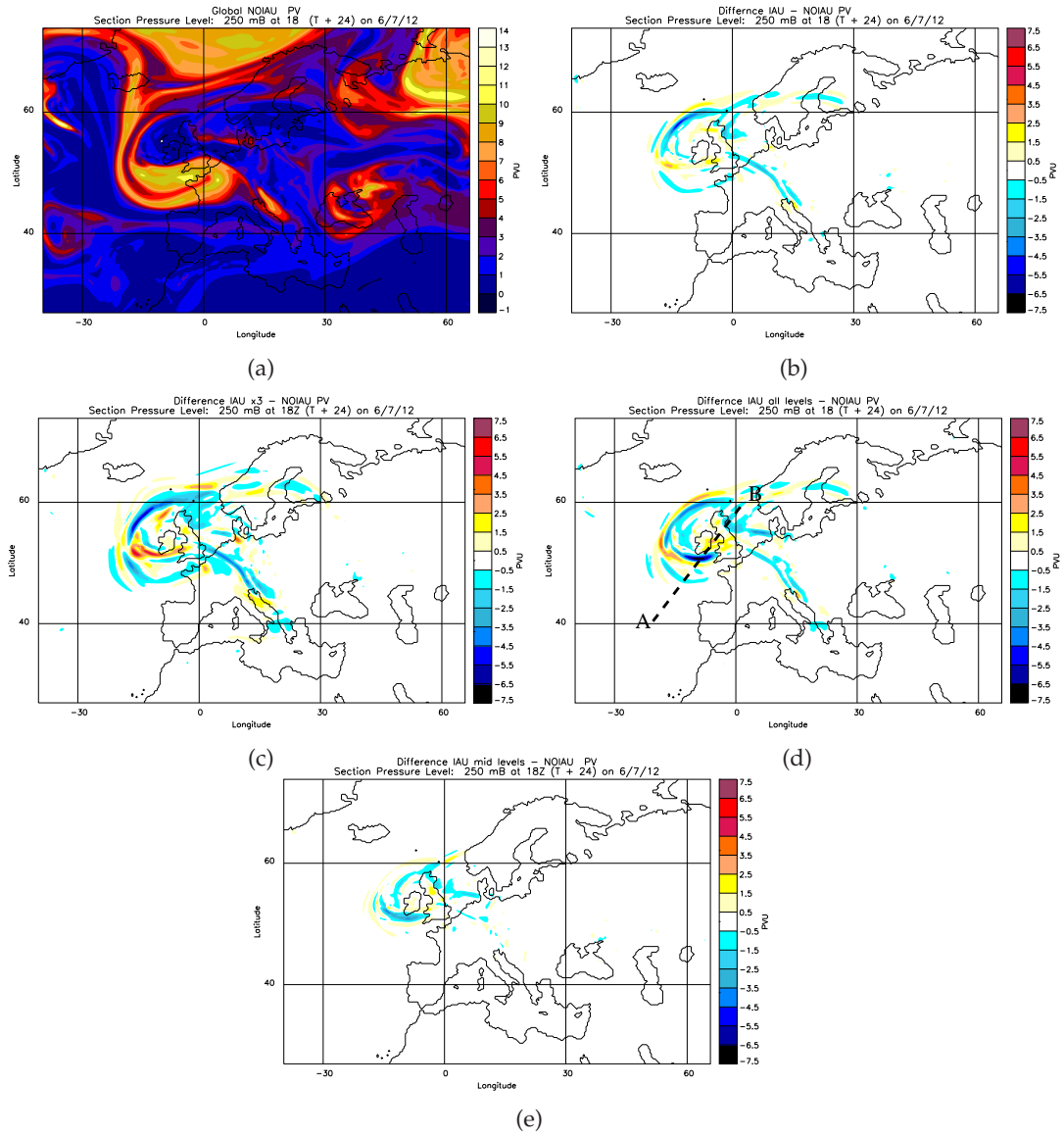
(a)

(b)

(c)

(d)

(e)

Figure 5.9: 18 UTC 6 July 2012: PV at 250 hPa for (a) Global model, and the differences between the Global model simulation with and without MCS perturbations added for (b) UPERTS, (c) X3PERTS, (d) ALLPERTS and (e) MPERTS.

Figure 5.10: 18 UTC 6 July 2012: Geopotential height at 250 hPa for (a) Global model, and the differences between the Global model simulation with and without MCS perturbations added for (b) UPERT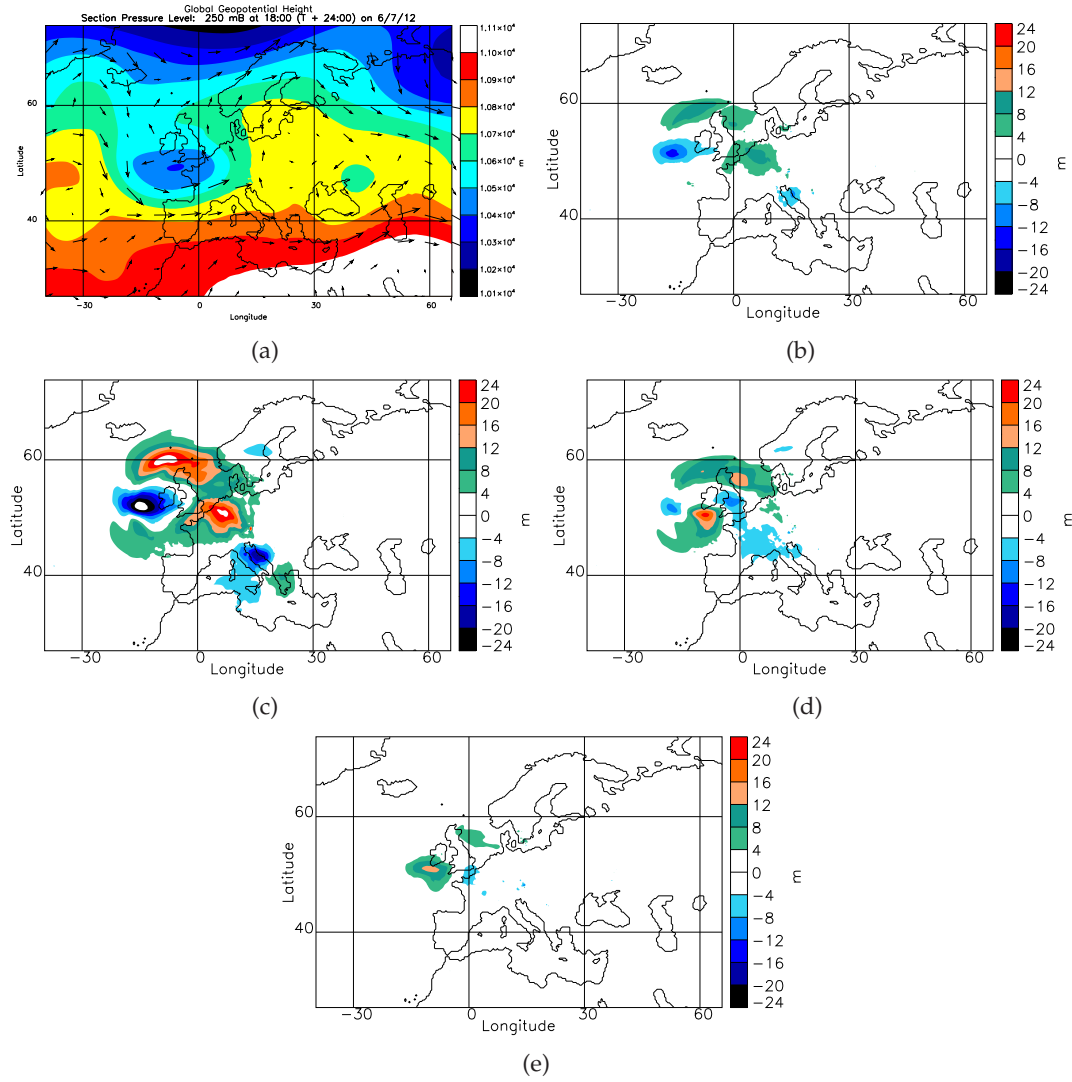S, (c) X3PERTS, (d) ALLPERTS and (e) MPERTS. Note that in figure (c) the colour bar saturates with the maximum value reaching 35 m and -35 m.

5.3.3 Medium-range impact of the MCS perturbations out to 10 July

The impact on the downstream forecast (out to 18 UTC 10 July 2012, 5 days after the MCS perturbations are added) due to the addition of the MCS perturbations is now investigated. An analysis of geopotential height, PV and root-mean squared differences (RMSD) in PV and PMSL is conducted. The RMSD will be discussed followed by an analysis of the impact that the perturbations have on the ridge-trough patterns. The Section closes by discussing the effect that the MCS perturbations have on the downstream pressure systems.

RMSD calculations over the northern hemisphere

Each of the simulations (except for MPERTS) decreases in RMSD values (calculated over the whole northern hemisphere) for the first 24–30 hours for both PMSL and PV (Figure 5.11(a) and 5.11(b)) as the simulations react to the perturbations being added by dampening them out due to adding unbalanced fields, therefore, the magnitude of the differences decreases while the spatial area increases. At levels below 350 hPa the differences increase in spatial area over time, but the magnitude of the differences are much smaller than at upper levels (not shown). As expected X3PERTS has the largest RMSD values for both PMSL and PV. It appears that the perturbations were too large to begin with though when giving them a factor of 3 increase as the RMSD values of PV almost halves (from 0.55 to 0.28 PVU; see Figure 5.11(a)) over the first 24 hours and the PMSL is reduced by a third (from 28 Pa to 9 Pa; see Figure 5.11(b)) over the first 30 hours of the model simulation as the model considerably dampens the perturbations. After approximately 30 hours into the model run the differences in PV and PMSL between the unperturbed and perturbed simulations increase in amplitude and spatial area with no sign of saturating after 120 hours (Figure 5.11(a) and 5.11(b)).

RMSD values provide further evidence for the perturbations added at all levels causing differences to grow further than when perturbations are just added at upper-levels with the RMSD values of PV and PMSL being larger at 120 hours into the forecast for ALLPERTS (RMSD of 46 m for PMSL for ALLPERTS compared to 25 m for MPERTS and 32 m for UPERTS). Perturbations added over middle levels as expected have less of an impact on the RMSD values but nonetheless they do have an impact on PV at 250 hPa

showing the influence that the PV anomalies created in MCSs have not only at middle levels where the atypical positive PV tower develops but this impacts upper levels over time (Figure 5.11(a)). Upper level MCS perturbations have been found to have a greater influence on the development of downstream differences than the middle level MCS perturbations but together they have a larger influence on the downstream flow than they do individually. This larger range of influence by upper-level perturbations may be related to the background winds being stronger at upper-levels and the magnitude of the perturbations being larger. Perturbations added over all levels have larger RMSD values though suggesting that the action-at-a-distance principle of the wind and temperatures associated with PV and the mutual amplification created by lower and upper-level PV anomalies has a greater influence on the downstream flow than when considered separately.

After 120 hours the growth in RMSD values does not appear to be slowing down or saturating as the impact of the perturbations is still affecting a larger area at every timestep (Figure 5.11(a) and 5.11(b)). Although the PV RMSD values are increasing steadily until 120 hours, the PMSL RMSD values are beginning to level off in growth.

PV, and geopotential height

Analysis of the difference growth (for PV and geopotential height) over the 5-day forecast shows that small-scale convective-scale differences develop initially in association with the MCS and developing UK cyclone (Figure 5.14(a) and (b) and Figure 5.15(a) and (b)). The magnitude of the differences then grows with each day of the forecast, as well as growing to cover the synoptic scale, to cover the whole northern hemisphere after 5 days. The magnitude of the differences are smallest for MPERTS, however, the spatial extent of the differences is similar for all MCS perturbation simulations. This is important as it means that any MCS perturbations added to a model simulation will have a downstream influence on the forecast, but the magnitude of the impact will be dependant on the perturbations initially added. The amplitude of the perturbations was found to be the main determinant of perturbation growth in Leoncini *et al.* (2010) and has similarly been found in this study with the X3PERTS having the greater impact on

the growth of differences downstream (this does not mean that these perturbations give a better forecast though compared to the other perturbations).

The differences in PV and geopotential height seem to propagate along a Rossby wave guide with PV differences occurring along the ridge boundary. This has an impact on the circulation patterns at jet stream level. By 120 hours into the forecast the majority of the differences are related to the ridge being impacted by the addition of the MCS perturbations causing PV and geopotential height differences to be produced along the boundary.

Negative PV differences at 250 hPa show that the addition of MCS perturbations leads to ridge strengthening and amplification to the north with PV differences up to a maximum amplitude of -7.5 PVU by 120 hours (Figure 5.14(j)). The amplification of the ridge leads to associated differences in windspeeds at the ridge boundaries and causes the tropopause height to be higher in the simulation with the MCS perturbations included. This ridge amplification was also found in Grams and Archambault (2016) when comparing simulations with a tropical cyclone included to simulations without the tropical cyclone. The effect is of a similar magnitude of PV differences (-7 PVU at 108 hours) and covers a similar spatial area growing over time (see Figure 6 Grams and Archambault (2016)). This suggests the importance of the latent heating and moisture caused by the addition of the MCS perturbations. Analysis of the geopotential height differences indicates that the ALLPERTS simulations have a slight retardation in eastward progression due to the negative PV at jet stream level causing anticyclonic outflow (Figure 5.15(a)-(j), Figure 5.3).

Cross-sections through the ridge show the 2 PVU tropopause being amplified upwards approximately by up to 50 hPa in the simulation with the MCS perturbations added at all levels (marked by black solid circles on Figure 5.16(a), 5.16(b) and 5.16(c)). On 6 July 2012 the amplifying of the ridge can be seen at the boundary between the ridge and the trough over the UK at this time (marked by black circle on Figure 5.16(b)). This amplifies the tropopause height upwards from 300 hPa to 225 hPa as low PV air (between 0-2 PVU) outflow occurs and the ridge amplifies.

By 10 July 2012 the troughs in the perturbed compared to the unperturbed models have been shifted due to the slower eastward movement of the perturbed simulations created due to the amplification of the ridge (Figure 5.16(c); marked by dashed black cir-

cles). Colder temperatures ($\theta = 270$ K) are seen at the surface in the perturbed simulation due to the trough being slightly wider and deeper but also occurring further west than in the deterministic simulation (Figure 5.16(c)).

Precipitation and PMSL

Previous studies have noted that errors develop in association with moist processes (Zhang *et al.*, 2003) with little error growth occurring without the effects of moist processes (Tan *et al.*, 2004). Moist processes enhance underlying dry growth of errors Beare *et al.* (2003) since error do grow when moist processes are not acting but error growth is much slower. An analysis of the rainfall rates over the 5 day forecast (not shown) shows that where rainfall occurs in the models is related to where differences in the perturbed and unperturbed forecasts develop. This can be seen on the first day where differences in PV and geopotential height occur where there is rainfall in the model at this time (Figure 5.9(a)-(e) and Figure 5.10(a)-(e) and Figure 5.8(a)-(b)). For example, on day 5 of the forecast rainfall occurs on the east coast of north America around Florida and Georgia and a large area of rainfall develops in north Korea. Both of these areas have associated large amplitude differences in the PV. Although both the perturbed and unperturbed forecasts develop rainfall in these areas, the amplitude of rainfall created is larger in the perturbed model as an amplified ridge means more ascent through positive vorticity advection. Therefore, differences in the rainfall between the perturbed and unperturbed models are related to the differences created at the ridge boundaries as an amplified ridge leads to heavier rainfall.

Figure 5.17 shows that the deterministic run has a low pressure centre over northern Russia which is located further east than the simulations with the MCS perturbations. The ALLPERTS simulations have the least eastward progression (apart from in X3PERTS) showing the greater impact of adding the perturbations over all levels compared to just at upper or middle levels. However, the upper-level perturbations seem to cause a slower eastward progression than when perturbations are just added at middle levels. There is a deepening of the low pressure centre over northern Russia in X3PERTS and ALLPERTS (990 hPa in XPERTS and 991 hPa in ALLPERTS compared to 992 hPa in non perturbed simulation) suggesting again there is a connection between the strength

of the MCS perturbations and the impact on the downstream forecast.

The deepening of the low-pressure centre downstream in ALLPERTS again provides evidence for MCS perturbations added over all levels having a greater impact on the downstream development. The MCS perturbations in these simulations do not impact on the strength of the low centre in MPERTS and UPERTS with each having a low pressure centre of 992 hPa similarly to the deterministic forecast (X3PERTS has a low pressure centre of 990 hPa and ALLPERTS 991 hPa). This slower eastward progression in the simulation with the MCS perturbations was also seen in Grams and Archambault (2016) in their simulations with tropical cyclones having a slower eastward progression than in the simulation without the tropical cyclone. This is due to diabatically enhanced upper-level divergent outflow from the non-linear interaction between the tropical cyclone and the midlatitude flow and impedes the eastward propagation (Riemer *et al.*, 2008; Quinting and Jones, 2016) . Grams and Archambault (2016) concluded that this was due to the latent heating associated with the tropical cyclone causing low PV air to be transported into the upper-troposphere leading to a higher tropopause height and ridge building and amplification of the midlatitude upper-level Rossby wave pattern due to the irrotational wind associated with the diabatically driven outflow and has similarly been found to occur in this study.
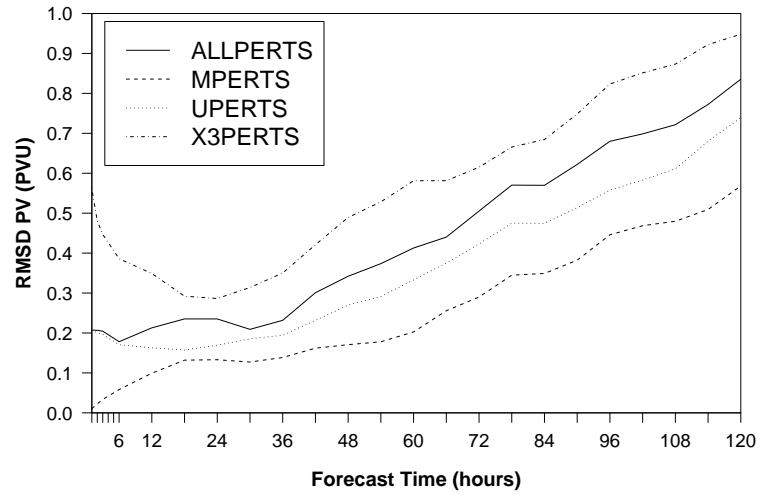
(a)
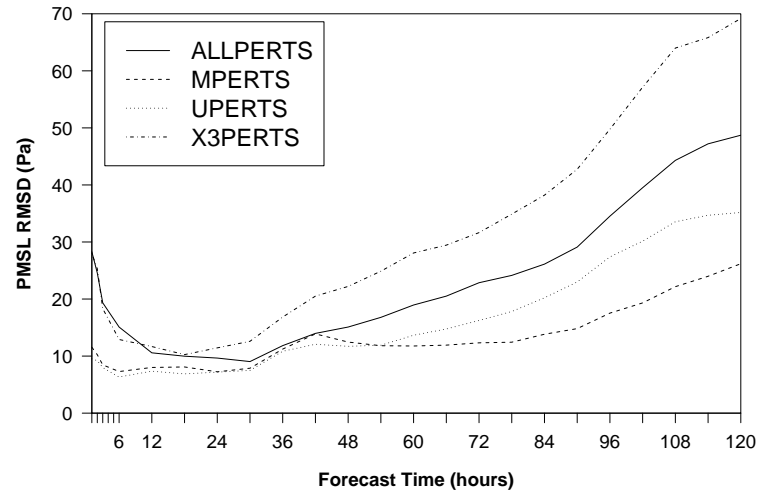
(b)

Figure 5.11: Root mean square difference (RMSD) for differences between the Global model simulations with and without MCS perturbations for (a) PV at 250 hPa and (b) Mean sea-level pressure.
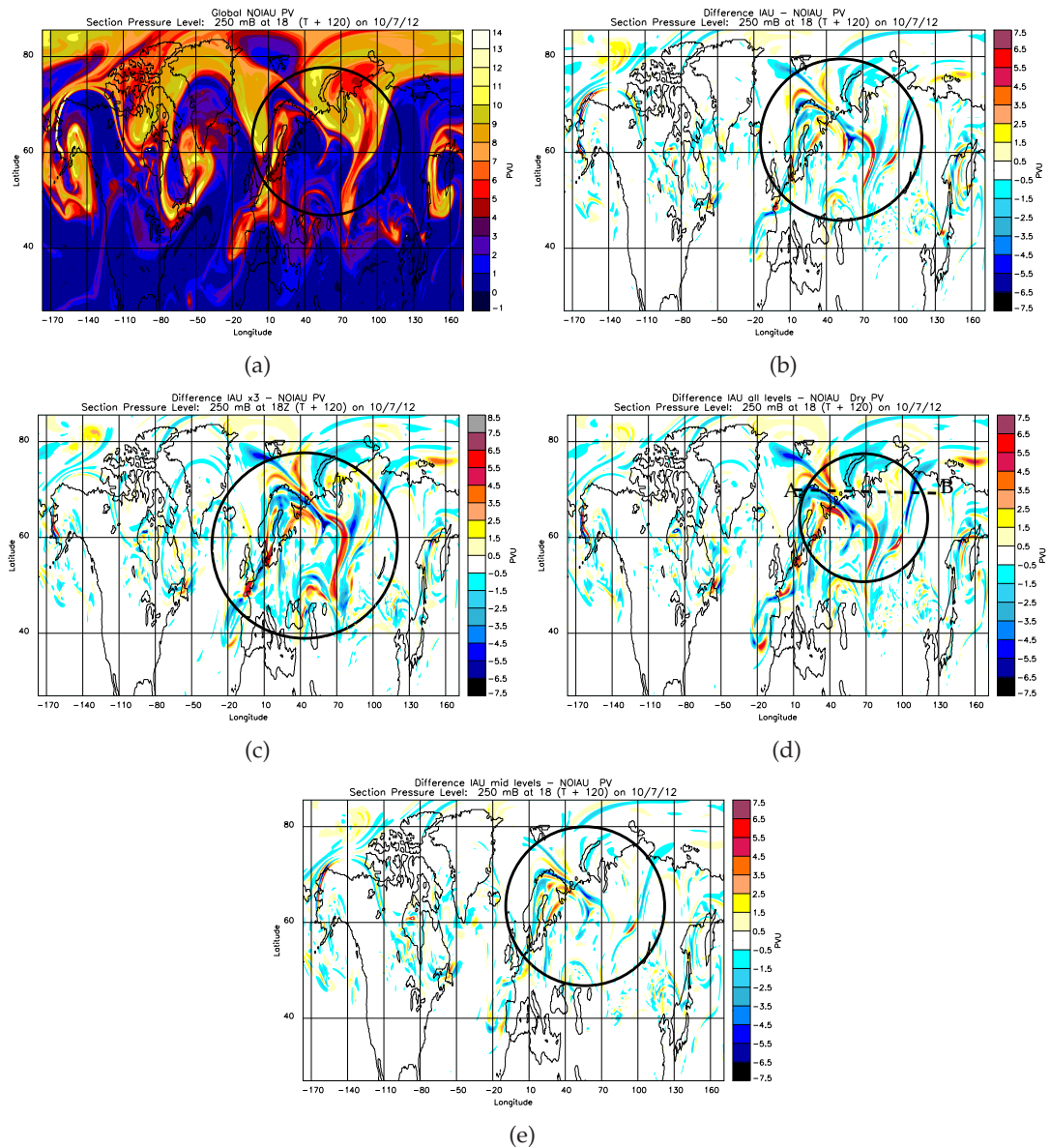
(a)

(b)

(c)

(d)

(e)

Figure 5.12: 18 UTC 10 July 2012: PV at 250 hPa for (a) Global model, and the differences between the Global model simulation with and without MCS perturbations added for (b) UPERTS, (c) X3PERTS, (d) ALLPERTS and (e) MPERTS. Cross-section A–B used in Figure 5.16(c). Black circles indicate PV differences that occur at the boundary of the Rossby wave ridge downstream of where the MCS perturbations were added.
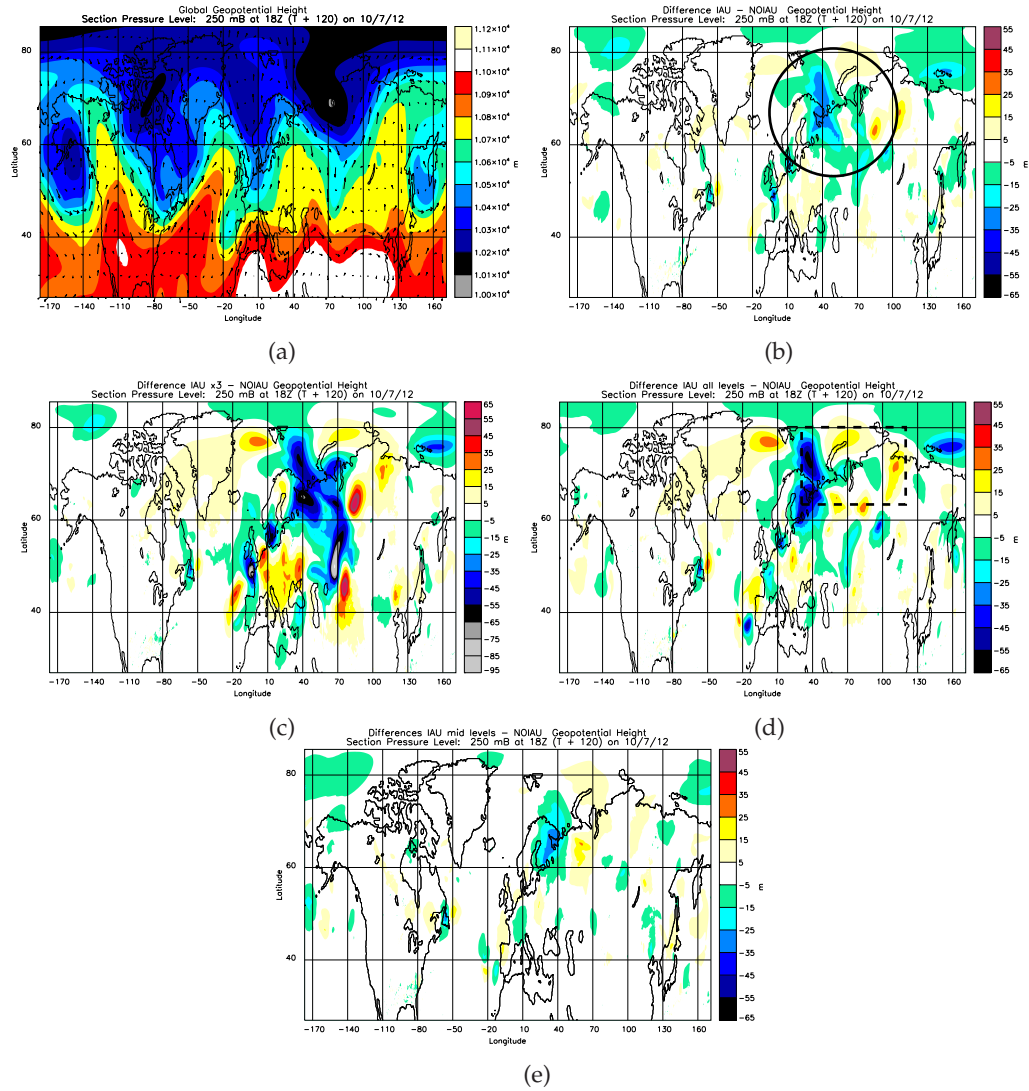
(a)

(b)

(c)

(d)

(e)

Figure 5.13: 18 UTC 10 July 2012: Geopotential height at 250 hPa for (a) Global model, and the differences between the Global model simulation with and without MCS perturbations added for (b) UPERTS, (c) X3PERTS, (d) ALLPERTS and (e) MPERTS. Black circle indicates the differences in geopotential height that develop downstream related to the ridge–trough pattern. The black rectangle is the sub-section used for Figure 5.17.
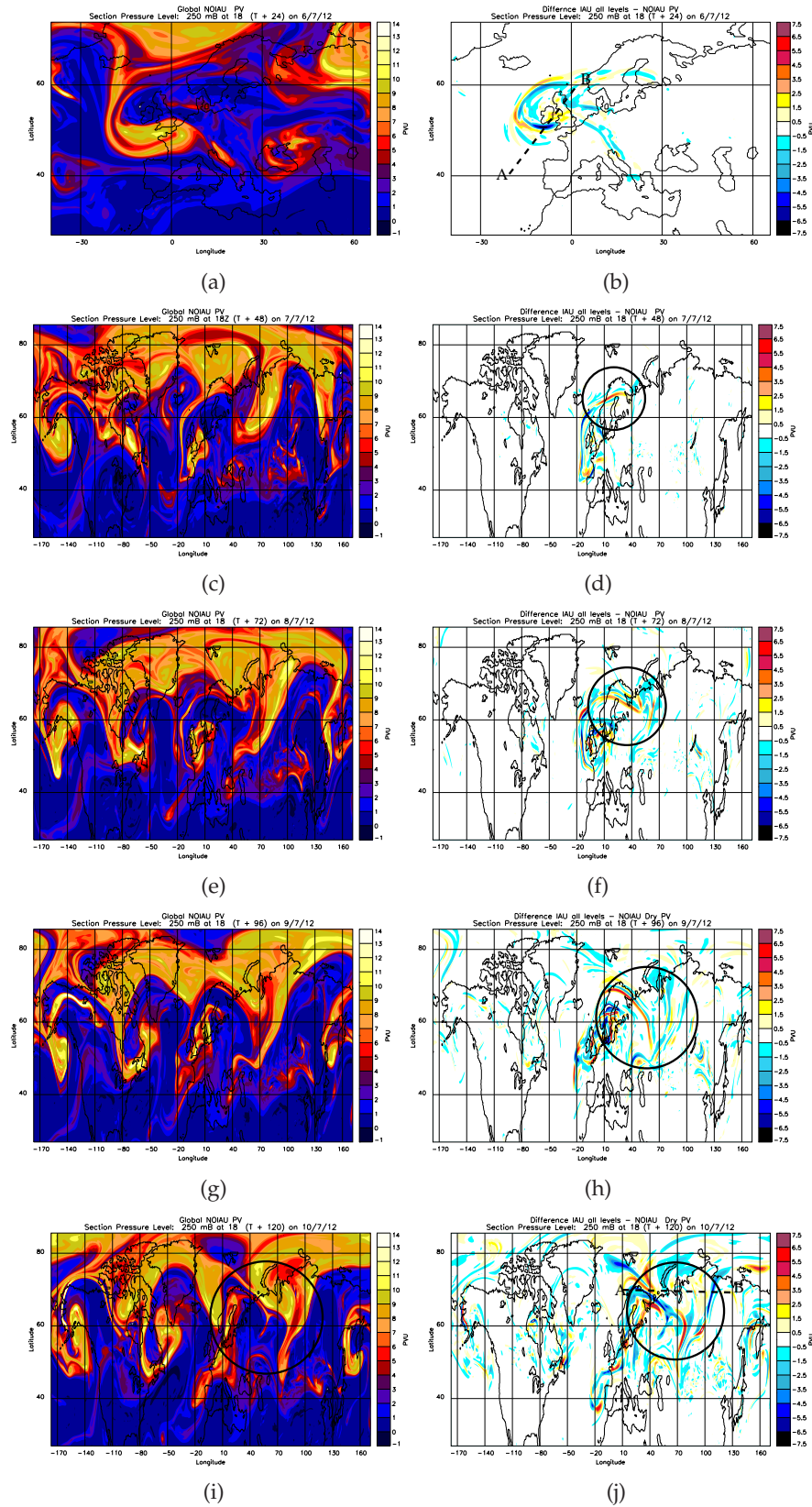
Figure 5.14: 18 UTC 6 July 2017 to 10 July 2012: PV at 250 hPa for (a), (c), (e), (g), (i) Global PV and (b), (d), (f), (h) and (j) The difference between the Global model and the Global model with perturbations added at all levels (ALLPERTS). Black circles indicate PV differences created following a Rossby wave ridge. Cross-section A–B is used in (b) for Figure 5.16(b) and (j) for Figure 5.16(c).
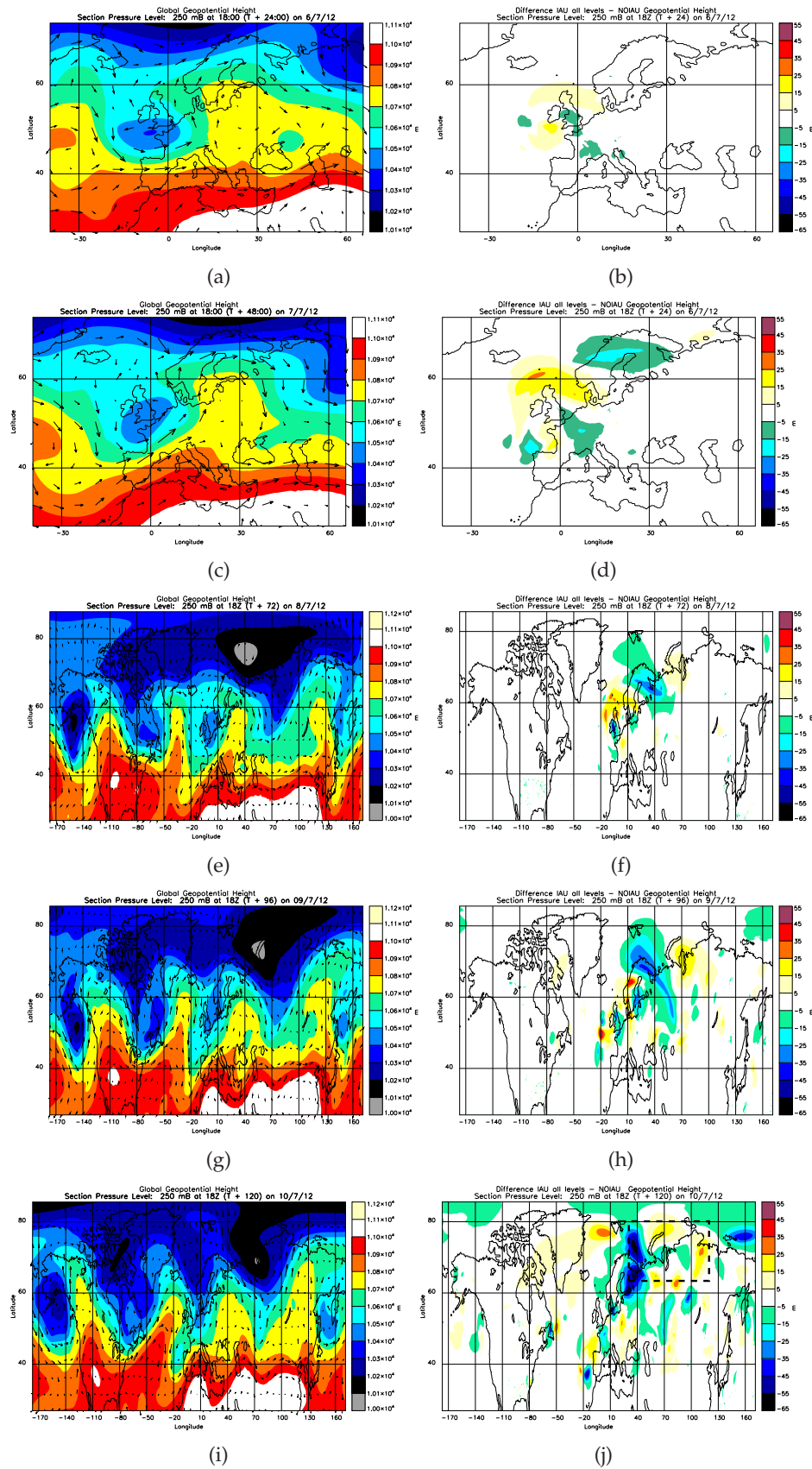
Figure 5.15: 18 UTC 6th to 10th July 2012: Geopotential heights at 250hPa for (a), (c), (e), (g), (i) Global model and (b), (d), (f), (h), (j) Differences between the Global model and the Global model with perturbations added at all levels (ALLPERTS).Black rectangle indicates the subsection used for Figure 5.17.
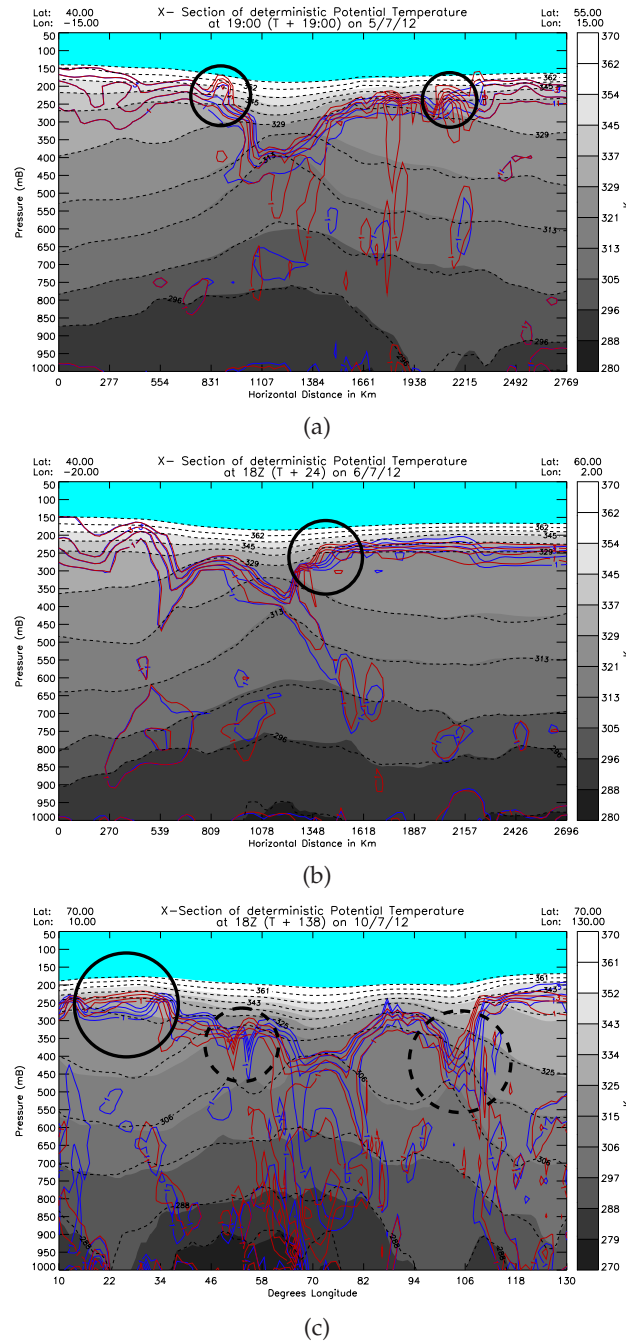
Figure 5.16: Cross-sections of deterministic potential temperature with contours of PV (-1 PVU to 4 PVU) plotted in blue for deterministic simulation and red for the simulation with MCS perturbations added at all levels. Contours of potential temperature are also plotted for the ALLPERTS simulation in black dotted lines. Each cross-section is taken to pass through the ridge/trough. (a) 19 UTC 5 July 2012, (b) 18 UTC 6 July 2012 and (c) 18 UTC 10 July 2012. Each cross-section has black circles marked to indicate areas of marked differences in PV with the dashed black circles indicating where specifically the upper-level trough is shifted between the forecasts.

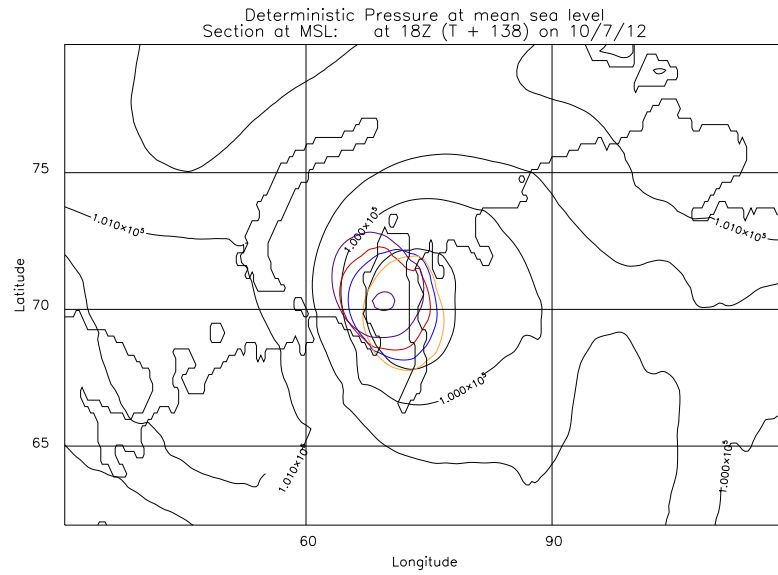**Figure 5.17:** PMSL 18 UTC 10 July 2012. Black contours are the deterministic simulation. The centre of the low-pressure system is marked for each simulation with the MCS perturbations added at different levels. The contour level marked is for 995 hPa and 990 hPa. Blue contour is UPERTS, red contours is MCS perturbations ALLPERTS, orange contours is MPERTS and purple contour is X3PERTS. Sub-section used is marked on Figure 5.15(j).

5.4   Conclusions

The aim of this Chapter was to investigate the downstream impact of the PV anomalies associated with the MCS to answer the following question posed in Section 1.1: How does the representation of an MCS affect forecast evolution for the synoptic-scale forecast downstream from the MCS? To help answer this question a hypothesis was posed in Section 5.1.1 and the conclusions are now presented related to this hypothesis.

Hypothesis: Circulations associated with PV anomalies produced by the MCS may influence the downstream flow. Since the PV anomalies produced by the convection-permitting and convection-parametrizing models after coarse graining are different (because the convection-parametrizing models do not explicitly represent convection) this could lead to variations in the downstream forecast between models.

MCS perturbations added over all levels of the model (compared to upper-level or middle levels only) have the largest impact on the differences created but the upper-level perturbations cause larger differences than the middle-level perturbations. Gray (2001) found that perturbations of PV added at middle levels of MCSs had the largest effect on the model. This contrast in results is due to the model resolution used in Gray (2001) being 80 km; therefore, the negative PV anomalies associated with the MCS at upper-levels (where the biggest differences developed) were not represented in that study whereas in this study they are (they were also not input as perturbations as PV anomalies were near zero at upper levels). Pomroy and Thorpe (2000) found that upper-level negative PV anomalies induce larger perturbations in wind and temperature than lower-tropospheric positive PV anomalies. These larger induced perturbations in wind and temperature (anticyclonic circulations and cold anomaly) associated with the negative PV anomaly is thus the likely reason why upper-level negative PV anomalies associated with the MCS produce larger difference growth downstream than the positive PV anomalies at middle-levels produce. In addition to this the background winds at upper-levels are stronger than at middle-levels due to the jet stream and this will cause differences at this level to grow more quickly away from the initial perturbations.

The MCS and cyclone created in the simulation with MCS perturbations added at all-levels were better represented in terms of magnitude of rainfall and the location it occurred, when compared to rainfall radar, showing that representing the PV structure

at all levels of the MCS is important to represent the MCS and cyclone well.

The magnitude of the MCS perturbations added at upper-levels has an impact on the magnitude of the differences that occur downstream. Figure 5.2(a) and 5.2(b) show that the magnitude of θ perturbations at upper-levels was a maximum of 6 K whereas at middle levels the magnitude was 2.5 K. The fact that the upper-level perturbations are stronger magnitude may have an impact on the results since Leoncini *et al.* (2010) found that the amplitude of perturbations was important, rather than the perturbations that were used. Therefore, it may be the amplitude of the perturbations rather than the altitude that they are added that has the largest impact on the downstream forecast; however it is hard to determine this since the middle level perturbations are smaller amplitude. The important point here is that it is the magnitude of the upper-level MCS perturbations that have had the largest influence on the downstream differences in this study. Therefore, the MCS perturbations used are important as it is the upper-level PV structures in the MCS which have been found to have the greatest impact on the downstream forecast. This impact is largely due to negative PV anomalies associated with the MCS not being represented by the convection-parametrizing simulations. These negative PV anomalies at upper-levels caused by divergent outflow lead to erosion of the upper-level trough and cause a shift to the west of the upper-level trough. The ridge is also amplified as the negative PV aloft leads to the tropopause being amplified (see Figure 5.3). Due to the amplified ridge the jet streak is also accelerated in the MCS perturbation cases. It has been found that the stronger the amplitude of the upper-level perturbations added, the slower the eastward progression of the weather systems and the magnitude of differences in PV and geopotential height (due to the magnitude of the negative PV at upper levels being increased). When MCS perturbations are added over all model levels this gave the best forecast of the late stage MCS and the UK cyclone though.

The spatial extent of the differences in PV and geopotential height is the same for all simulations regardless of where the MCS perturbations are added; however, the magnitude of the differences does vary between simulations. The growth of differences downstream in geopotential height perturbations has a resemblance to Figure 5 of Beare *et al.* (2003) with negative and positive differences developing around the area where perturbations are added which grow in spatial scale and magnitude away from the initial input

area. Zhang *et al.* (2007) found that perturbations (random noise added at tropopause level in a baroclinically unstable jet) added begin by influencing the small-scale before growing onto the synoptic-scale. This finding was supported by Selz and Craig (2015) and has also been found to be the case in this study, with differences covering the whole northern hemisphere after 5 days initially developing associated with the MCS.

Regardless of at what level the MCS perturbations are added to the simulation, the RMSD values (for PV and PMSL) grow slowly for the first 30 hours as differences between the MCS perturbed simulations and the deterministic control simulation grow on the convective scale and are initially damped due to adding unbalanced fields. After this time differences (in PV and PMSL) grow rapidly as they start to impact the synoptic scale.

The MCS perturbations cause a slower eastward movement of the low-pressure centre which develops downstream over northern Russia by 120 hours, with the perturbations added at middle levels having the least difference in positioning of the centre of the low in comparison to the deterministic forecast (Figure 5.17). The MCS perturbations added at all levels caused a deepening of the low-pressure centre by 1 hPa compared to the deterministic forecast which did not occur when the perturbations are added at just middle or upper levels. The MCS perturbations added at upper-levels multiplied by a factor of 3 caused a deepening of the low-pressure centre by 2 hPa compared to the deterministic forecast, again showing that the magnitude of the perturbations added at upper levels is important. Figure 5.3 indicates how the MCS perturbations may have led to this deepening of the low pressure centre downstream and the slower eastward movement. Figure 2 of Plant *et al.* (2003) also suggests a mechanism by which the negative PV anomalies at upper-levels erode the upper-level trough and an associated positive PV anomaly at low-levels leads to a deepened low-pressure system.

MCS perturbations have been shown to have a downstream impact on the forecast creating large-scale differences from the deterministic forecast by 120 hours. Therefore, the following Chapter will investigate the robustness of the impact of adding MCS perturbations (to determine if a similar impact occurs each time) to model simulations along with the downstream predictability by using an ensemble approach.

Chapter 6

Downstream influence of MCS convection: ensemble simulations

6.1 Introduction

In Chapter 5 differences were found in PV, geopotential height and PMSL downstream (after 5 days on 10 July 2012) from the MCS (on 5 July 2012) due to the addition of the MCS perturbations. These differences grew from convective scale surrounding the MCS (on 5 July) and UK cyclone (on 6 July) to synoptic-scale covering almost the entire northern hemisphere by 5 days of the simulations. The biggest influence on the downstream forecast occurred due to the addition of the MCS perturbations at upper-levels as opposed to at middle levels . However, a better representation of both the MCS and UK cyclone occurred in the simulation with MCS perturbations added over all model levels. Therefore, the aim of this Chapter is to investigate how the MCS perturbations (added at all model levels) impact the realisations of the downstream forecast produced using an ensemble approach, to determine if these MCS perturbations have a similar impact for each forecast. To test this two ensembles are created; one with MCS and initial condition perturbations and one with just initial condition perturbations. These ensemble forecasts are simulated for a 5 day forecast from 18 UTC 5 July to 18 UTC 10 July 2012.

This Chapter investigates the question posed in Section 1.1: How does the representation of an MCS effect forecast evolution and forecast skill (compared to analysis) for the synoptic-scale forecast downstream from the MCS? To answer this question the hypothesis posed in Section 5.1.1 is investigated further to determine the robustness of the results found in Chapter 5 by using an ensemble approach. The results of Chapter 5 produce two further hypotheses to be investigated during this Chapter:

1. the MCS perturbations have a consistent impact on the forecast evolution (in an ensemble)

2. the MCS perturbations lead to enhanced ensemble spread compared to the corresponding initial condition perturbation ensemble and/or new forecast evolutions.

These hypotheses are posed as downstream differences in PV, PMSL and geopotential height were found resulting from the addition of MCS perturbations to the simulation in Chapter 5. Therefore, it is hypothesised that these differences will occur downstream for every simulation in an ensemble. It is thought that a consistent impact on the downstream forecast will occur due to the effect that was found to occur in Chapter 5 as a consequence of the negative PV anomalies at upper-levels associated with the MCS that occurs in the coarse grained convection-permitting simulation but not in the Global model simulation. It is expected that the negative PV anomalies will slow the eastward progression downstream in the simulations with the MCS perturbations included which will create associated differences in the PV, windspeed and PMSL. These differences in PV, PMSL and windspeed are expected to create an enhanced ensemble spread when compared to the spread in the ensemble with just initial condition perturbations, along with different forecast evolutions.

The following Section describes the method used throughout the Chapter then the results of the model simulations are given. Finally, the conclusions are discussed.

6.2   Method

To investigate predictability of MCSs, five operational MOGREPS-G ensemble initial condition (IC) perturbations (chosen randomly from the 24 members used operationally at 00 UTC 5 July 2012; members 1, 5, 12, 15 and 21 are used) and the operational MOGREPS-G start dump for 00 UTC 5 July 2012 are used. This study is of a case from 2012 and at this time the Met Office used a grid spacing of 60 km for the MOGREPS-G operational simulations. Therefore, six 60 km MetUM MOGREPS-G simulations are produced using the five different IC perturbation files and one control run, initialised at 00 UTC 5 July using MOGREPS-G IC and BCs. These 60 km simulations are run for 3 hours (T+3) and then reconfigured to Global resolution (25 km grid spacing). The experimental design can be seen in Figure 6.1.

This allows six MetUM Global model simulations to be produced (with one of the six members being the control member which has no IC perturbations added at the start

of the simulation). These six Global model simulations are run from 03 UTC 5 July for 15 hours (T+18) and output is produced at 18 UTC 5 July. Global model simulations are produced which are 25 km grid spacing rather than just simulating MOGREPS-G for the 18 hours as it is deemed more suitable to go from 25 km to 4 km grid spacing (Euro 4 km) than to go from 60 km grid spacing to 4 km grid spacing as less information is lost upon interpolation. A start dump at 06 UTC (T+6) 5 July 2012 is output for each of the six Global model simulations to initialise six Euro 4 km model simulations which run from 06 UTC to 18 UTC 5 July 2012.

An MCS perturbation file is then calculated for each of the six ensemble members using the same method as in Section 5.2.1 (using the difference between each Global model simulation and the corresponding coarse grained Euro 4 km simulation from the same start dump); however, this time the MCS perturbations are calculated over all model levels only (this is possible since the Euro 4 km output is reconfigured to Global vertical levels before being coarse grained). The IC perturbations added to the run have a similar magnitude to the MCS perturbations added but are added across the whole Globe (up to 15 ms^{-1} for the U wind component and 4 K for θ).

Examples of the MCS perturbations for model level 38 (approximately 250 hPa) are shown in Figure 6.2(a)–6.2(f). The MCS perturbations that are calculated have a similar magnitude for all five members when looking over all model levels. The positioning of the MCS and the strength of the MCS varies in each member which has an impact on the perturbations produced. Negative θ perturbations of up to 6 K occur in association with the ridge over western France in 4 of the members. These negative θ perturbations could indicate that the ridge is amplified more in the coarse grained Euro 4 km simulations in comparison to the Global model in some of the members which could influence the downstream flow. These negative θ differences were found in Chapter 4 at the ridge boundary when comparing the convection-permitting and convection-parametrizing simulations together indicating that the ridge is strengthened in the convection-permitting simulation.

Six Global model simulations are performed that start from 18 UTC 5 July 2012 (that were initialised as a 60 km model with the IC perturbations added). A further six Global model simulations are then formed which are the same except that MCS perturbations are introduced at the start of the simulation (18 UTC 5 July 2012; added with equal
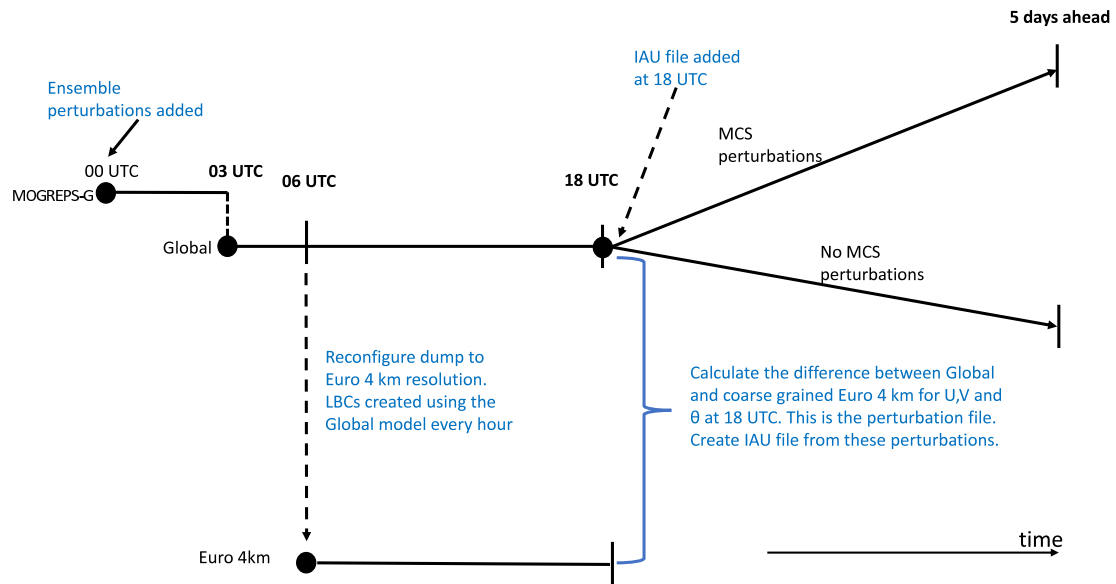
Figure 6.1: Ensemble run plan

weighting every 10 minutes over a 60 minute period).

This research allows a determination of the impact of the MCS (and the associated PV anomalies) on the downstream flow and how this varies depending on the MCS produced (if one is produced at all). The two ensembles are used to investigate whether the MCS perturbations cause an impact on the downstream forecast which occurs similarly for all members of the ensemble along with determining if the MCS perturbations cause differing realisations to that of the members where just IC perturbations are added. This requires an analysis of the differences between corresponding members of the two ensembles in terms of PV, precipitation and PMSL, a determination of the variability between the forecasts (using RMSD) and an anlysis of the spread produced between the ensembles with and without the MCS perturbations added (through correspondence ratio calculations).
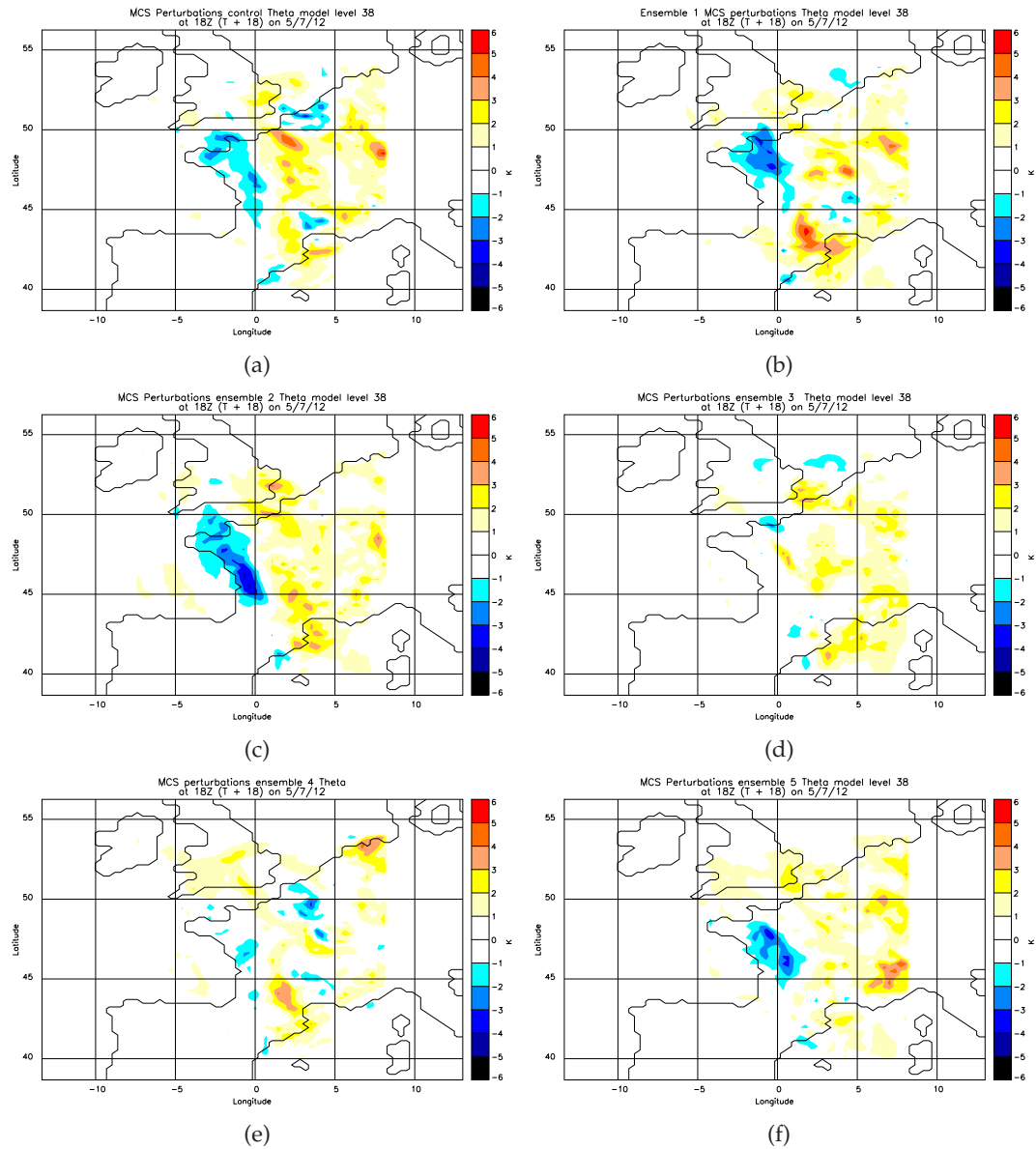
Figure 6.2: 18 UTC 5 July 2012: MCS perturbations of θ at model level 38 (approximately 250 hPa) for (a) Control member, (b) Ensemble member 1, (c) Ensemble member 2, (d) Ensemble member 3, (e) Ensemble member 4 and (f) Ensemble member 5. Perturbations are calculated as the difference between the coarse grained to 25 km grid spacing Euro 4 km and the 25 km grid spacing Global model.

6.3 Ensemble simulations results

The following Section contains an analysis of the results from the two ensemble simulations each with five members that were initialised with IC perturbations and a control which has no IC perturbations. The ensemble with IC perturbations and MCS perturbations added will be referred to as EN-MCS (including the control member which just has MCS perturbations added) and the ensemble with just the IC perturbations added will be referred to as EN-NOMCS (including the control member which has neither MCS nor IC perturbations). The MCS occurring over northern France and the southeast of the UK will be referred to as the northern MCS (black circle on Figure 6.3(a)) and the MCS occurring over southeast France will be referred to as the southern MCS (blue circle on Figure 6.3(a)).

The objectives:

1. To determine the initial impact of adding the MCS perturbations (on 5 July) in terms of PV structures represented by each of the ensemble members.

2. To analyse the impact of the MCS perturbations on the MCSs produced (both the northern and southern MCS; 5 July) and the UK cyclone (6 July).

3. To analyse the downstream influence (5 days into the simulation) focusing on PV, precipitation and PMSL differences between the EN-MCS and EN-NOMCS members.

The Section closes through an investigation of the variability between the two ensembles using root mean square difference calculations for PMSL and PV and fraction of common points calculations for PV and precipitation. This is followed by an analysis of the spread between the two ensembles through the correspondence ratio for PV and precipitation before the conclusions are discussed.

6.3.1 Immediate impact of MCS perturbations on 5 July

One hour after the MCS perturbations have been added to each of the ensemble members in EN-MCS clear differences in PV are seen between the members of EN-NOMCS and EN-MCS (Figure 6.3(a)-(f) shows the PV fields for the EN-NOMCS and Figure 6.4(a)-(f) shows the differences between the two ensembles). The magnitude of the PV anomalies

added in each of the members of EN-MCS does not markedly differ, but the location of the anomalies varies greatly depending on where the MCS is created in the Euro 4 km simulations (for all levels). In ensemble member 5 though the MCS perturbations added are too weak to produce the MCS (this member is either too stable or convection is too weak) therefore it is not simulated in the model (no rainfall is produced in either EN-NOMCS or EN-MCS).

At 250 hPa, without the addition of the MCS perturbations none of the members of EN-NOMCS produce a negative PV anomaly for the northern MCS; however, all members do show an area of near zero PV (Figure 6.3(a)–(f)). In contrast, each ensemble member of EN-MCS has a negative PV anomaly produced in association with the MCS at 250 hPa (which creates negative differences in Figure 6.4(a)-(f)). However, the magnitude of the PV anomaly depends on the ensemble member, with ensemble members 3 and 4 having the strongest negative PV anomaly for the northern MCS at approximately -6 PVU (see negative differences in Figure 6.4(a)–(f)). Each of the ensemble members also have larger magnitude negative PV (maximum of -8 PVU) produced in association with the southern MCS (in comparison to the strength in the ensemble without the MCS perturbations at a maximum of -2 PVU).

Positive PV anomalies are also amplified in EN-MCS members in association with both MCSs. These differences are related to the fact that the Global model fails to produce the northern MCS in any of the 6 ensemble members of EN-NOMCS, but when the MCS perturbations are added all members of EN-MCS represent the MCS (in terms of PV structures at 500 hPa and 250 hPa). The differences in the PV at 250 hPa between EN-NOMCS and EN-MCS are shown in Figure 6.4(a)-(f) with large amplitude PV differences between the two ensembles for all members (-10 PVU to 8 PVU differences). The fact that such large differences in PV are produced by the MCS perturbations suggests that the circulation patterns will be influenced (particularly at upper levels) resulting in forecast differences between EN-MCS members and EN-NOMCS members at longer lead times downstream.

When analysing the 500 hPa level PV it is apparent that the members of EN-MCS have more localised PV anomalies associated with the MCS perturbations in comparison to the members of EN-NOMCS (Figure 6.5(a)–(f) compared to Figure 6.6(a)–(f)). Each member of EN-MCS, has a positive and negative anomaly at 500 hPa in association with

the two MCSs but the magnitude of the anomalies differ depending on the ensemble member. The largest positive PV anomaly at 500 hPa has a magnitude of 3 PVU for the northern MCS and occurs in EN-MCS member 3 whereas in EN-NOMCS the positive PV anomaly has a magnitude of 0.5 PVU. Each member of EN-MCS shows the negative PV anomalies at middle levels in association with both MCSs again showing evidence for these negative PV anomalies occurring either side of the positive anomaly in European MCSs (Figure 3.30).

Again, the southern MCS is amplified by the MCS perturbations (in terms of larger magnitude positive PV anomalies occurring). Figure 6.5(a)–(f) shows that only a very weak positive PV anomaly (<1.5 PVU) is produced by member 3 and 5 of EN-NOMCS at 500 hPa suggesting that the southern MCS produced in each of the members of EN-NOMCS differs in magnitude over south France (control, member 1 and member 4 have 2.5 PVU).

In summary, the MCS perturbations added to each member of EN-MCS can be seen to add a MCS signature (negative PV anomaly at upper-levels and a negative and positive anomaly at middle levels) to the simulations which is otherwise missing in the members of EN-NOMCS (particularly the negative PV at upper-levels). None of the members of EN-NOMCS produce the northern MCS (in terms of PV structures), but they do all produce a typical PV structure associated with the southern MCS (with weaker magnitude PV anomalies than in the EN-MCS members) . The magnitude of the negative anomalies at 250 hPa and the positive anomalies at 500 hPa differ between the members of EN-NOMCS for the southern MCS although the Global model and Euro 4 km model both simulate the southern MCS for each member. These differences in PV are expected since in Chapter 4 it was found that the Euro 4 km model produces larger magnitude negative and positive PV anomalies associated with the MCS that are diluted by coarse graining but still persist, producing more localised PV anomalies than in the Global model.

Therefore, the IC perturbations cause differing forecasts of both MCSs (particularly due to the members of EN-NOMCS not developing the northern MCS) in terms of the PV structures, as well as, the MCS perturbations causing differing forecasts of both MCSs (when the members of EN-MCS are compared to each other and to the members of EN-NOMCS).

In Chapter 5 it was shown that differences created by the MCS perturbations grow

over time to cover a synoptic-scale and here the differences in PV after one hour into the simulation have been found to vary considerably between the members of EN-NOMCS and EN-MCS. The impact of these differing structures on the ensemble forecast downstream is analysed in the next Section to determine if these initial differences caused by the MCS perturbations still persist between the members of EN-MCS and EN-NOMCS. The aim is to determine if these differences in PV structures create differing forecasts of the UK cyclone at 12 UTC 6 July and whether they cause differences to develop downstream after five days of the simulations.
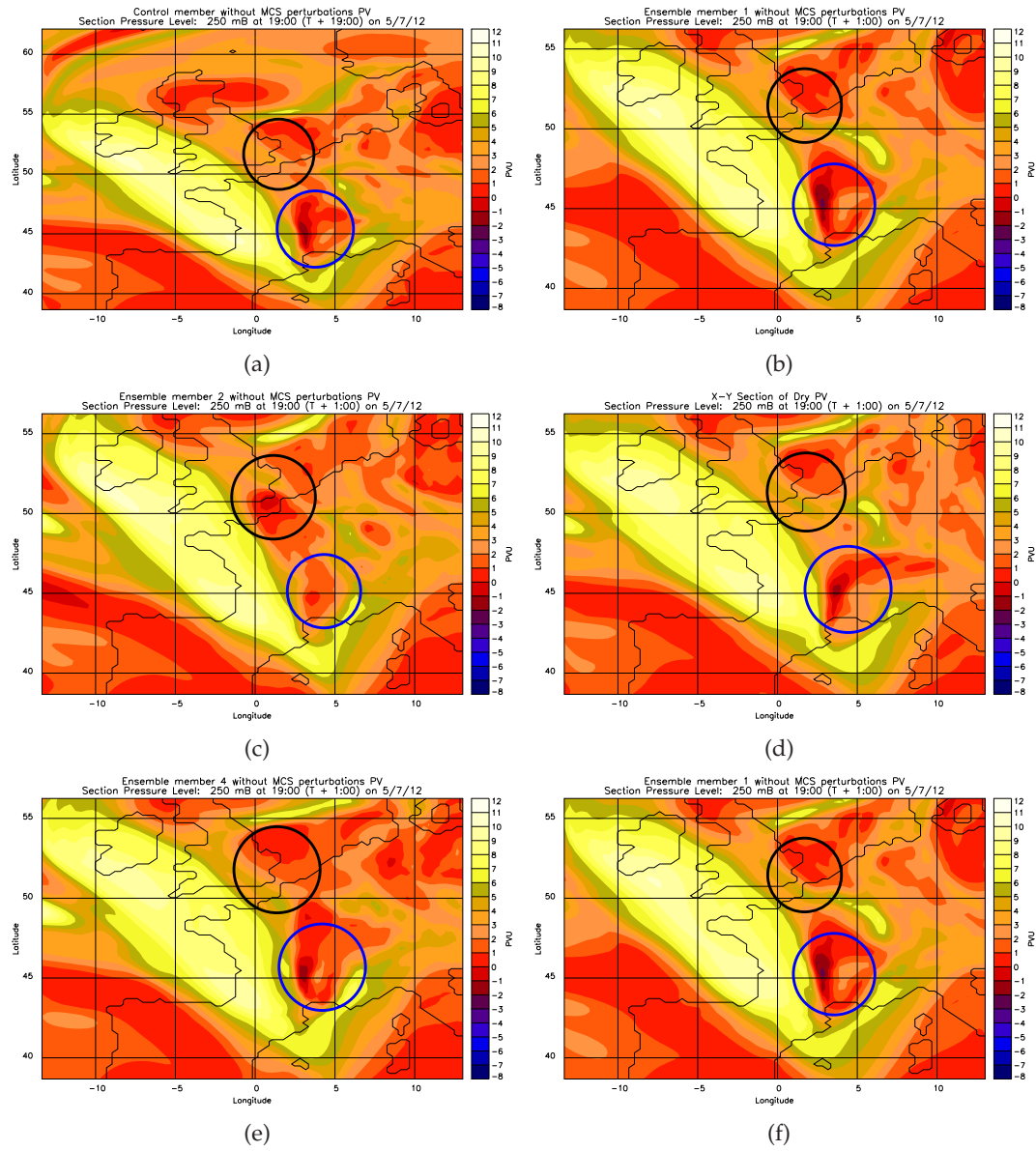
Figure 6.3: PV at 250 hPa 19 UTC 5 July 2012 for each member of EN-NOMCS for (a) Control, (b) ensemble member 1, (c) ensemble member 2, (d) ensemble member 3, (e) ensemble member 4 and (f) ensemble member 5. The black circles indicate the location of the northern MCS and the blue circles indicate the location of the southern MCS.

Figure 6.4: Difference in PV at 19 UTC 5 July 2012 250 hPa between each corresponding ensemble member of EN-MCS minus EN-NOMCS (EN-MCS–EN-NOMCS) for (a) Control, (b) ensemble member 1, (c) ensemble member 2, (d) ensemble member 3, (e) ensemble member 4 and (f) ensemble member 5. The black circles indicate the location of the northern MCS and the blue circles indicate the location of the southern MCS.
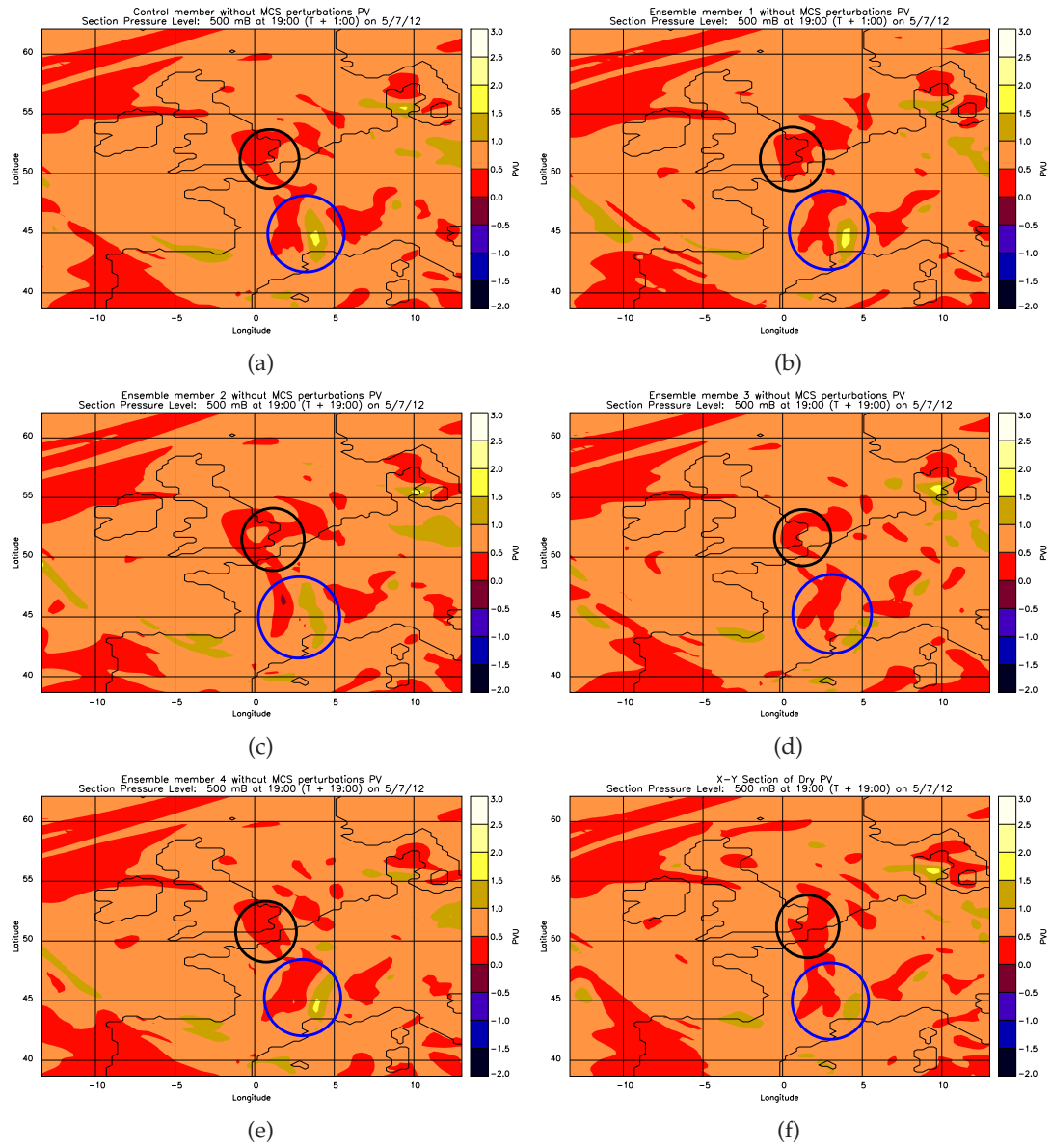
Figure 6.5: PV at 500 hPa 19 UTC 5 July 2012 for each member of EN-NOMCS for (a) Control, (b) ensemble member 1, (c) ensemble member 2, (d) ensemble member 3, (e) ensemble member 4 and (f) ensemble member 5. The black circles indicate the location of the northern MCS and the blue circles indicate the location of the southern MCS.
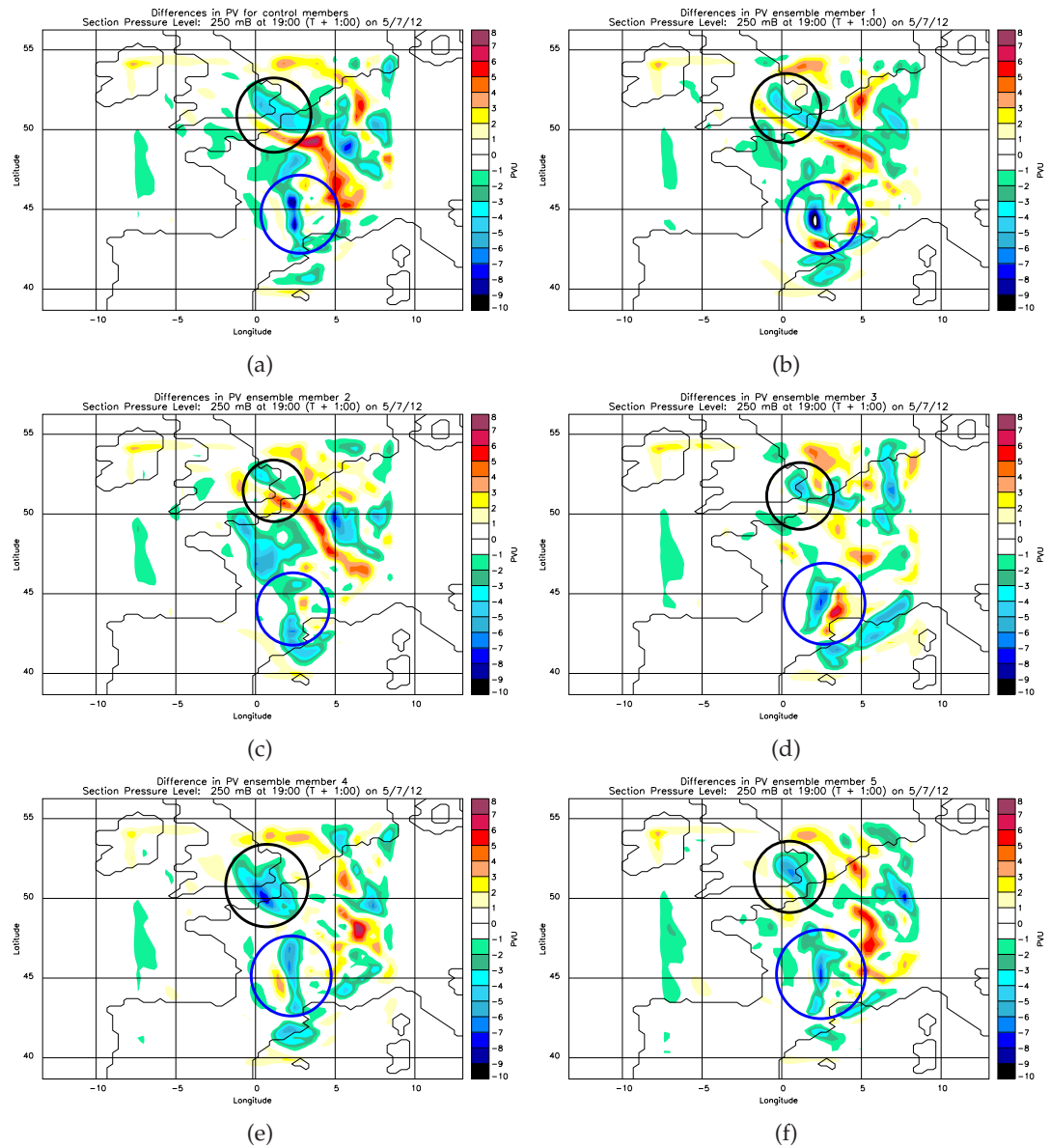
Figure 6.6: Difference in PV at 19 UTC 5 July 2012 500 hPa between each corresponding ensemble member of EN-MCS taken away from EN-NOMCS for (a) Control, (b) ensemble member 1, (c) ensemble member 2, (d) ensemble member 3, (e) ensemble member 4 and (f) ensemble member 5. The black circles indicate the location of the northern MCS and the blue circles indicate the location of the southern MCS.
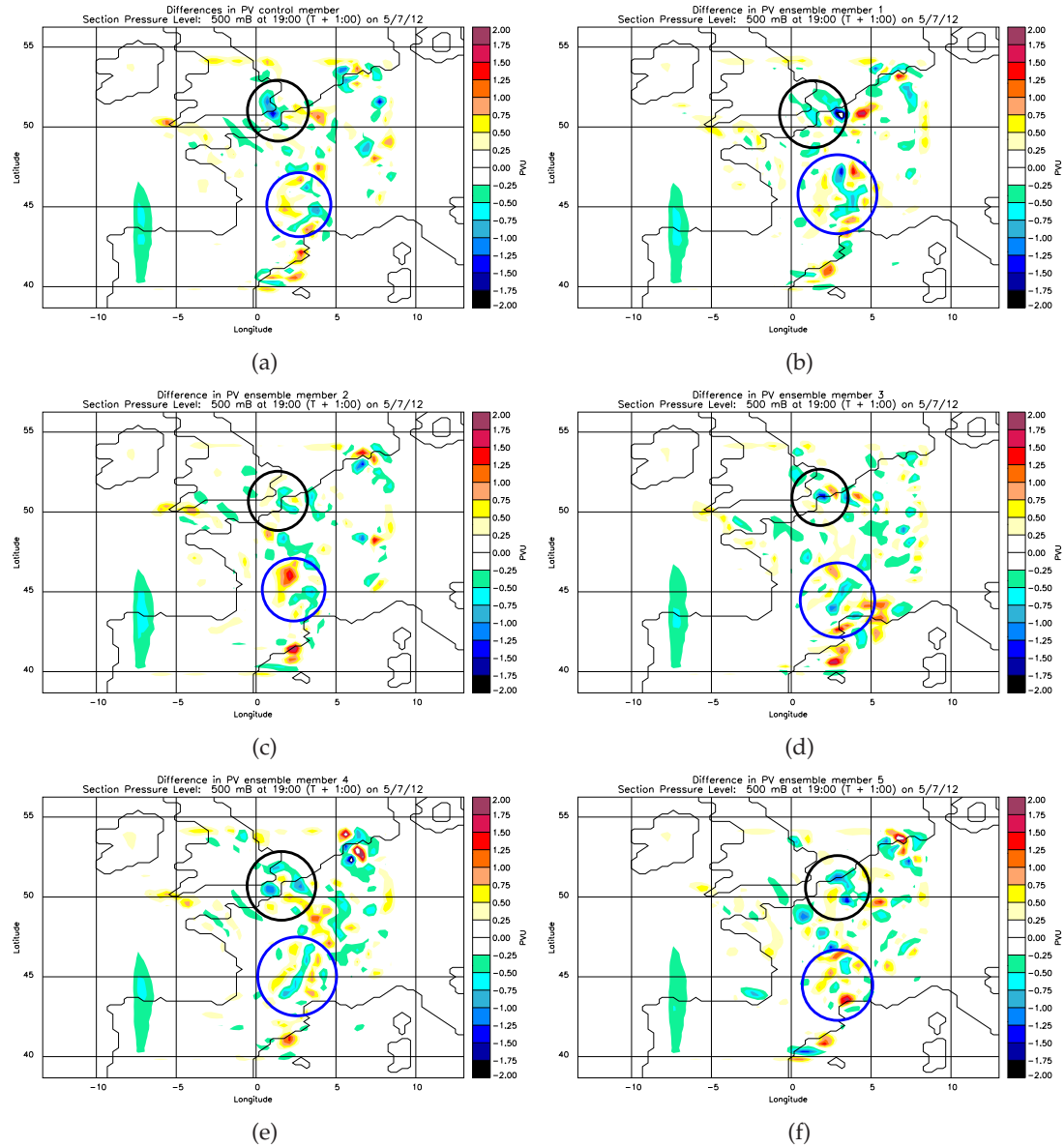
6.3.2 Impact of the MCS perturbations on the UK cyclone 6 July

In Section 5.3.2 it was found that adding MCS perturbations at all levels to the Global model simulation produced a better representation of the rainfall created by the northern MCS (00 UTC 5 July) and UK cyclone (12 UTC 6 July) in terms of magnitude and location compared to the deterministic simulation. In this Section the robustness of this result will be investigated to see if this happens for all of the members of EN-MCS.

An analysis of the rainfall six hours after the MCS perturbations are added is now discussed (to allow for model spin-up and some initial damping of MCS perturbations added). The magnitude of the precipitation varies depending on the ensemble member with ensemble member 5 producing no rainfall in association with the northern MCS for EN-NOMCS or EN-MCS. None of the EN-NOMCS members produce the northern MCS at 18 UTC 5 July, although some convection is triggered in the models by 00 UTC 6 July (Figure 6.8(f)–(f)). The associated rainfall produced is much weaker than the rainfall created in the members of EN-MCS though (Figure 6.7(f)–(f)). The location and magnitude of the rainfall (associated with both MCSs) in the members of EN-MCS is therefore better than in EN-NOMCS when compared to rainfall radar at this time (Figure 5.7(f)).

Each member of EN-MCS creates more intense rainfall associated with both MCSs than in the members of EN-NOMCS. When comparing with the rainfall radar (Figure 5.7(f), 6.8(f)–(f) and 6.7(f)–(f)) it seems that the most comparable to reality is the control member from EN-MCS (Figure 6.7(a)), with the location being represented well and the strongest rainfall occurring in the correct location at the correct magnitude. Thus, representation of the mature MCS was important on the subsequent rainfall development in the cyclone that impacted the UK.

This case study was an example of a non-equilibrium case, where the CAPE steadily increases before triggering of convection occurs and the CAPE values drop. The conclusions from these results are similar to that of Done *et al.* (2012) . That study concluded that in a non-equilibrium case the predictability of the location and patterns of the rainfall were similar, however the magnitude varied considerably between members. EN-MCS has greater variability in the location of individual storms due to the MCS perturbations interacting with the large-scale flow creating convection in some of the models, but not others where the triggering may still not have been strong enough due to strength of the perturbations added. Ensemble member 5 in both EN-NOMCS

and EN-MCS did not produce an MCS as the model was too stable even with the addition of the MCS perturbations. The rainfall produced in member 5 in association with the southern MCS on 5 July is also shifted to the north in comparison to all the other members (Figure 6.7(f)).

None of the members of EN-NOMCS and EN-MCS capture the true spatial extent of the rainfall that occurred in reality for the UK cyclone (as the Global model simulations failed to represent the true extent of the very weak stratiform rainfall; Figure 6.9(a)-(f) and Figure 6.10(a)-(f) compared to Figure 5.8(f)). The members of EN-MCS have a better representation of the stratiform rainfall though than the members of EN-NOMCS, with a greater spatial extent of the lighter rainfall. The control, and members 1,3 and 4 of EN-MCS all produce heavier rainfall than in the corresponding members of EN-NOMCS.

All members of EN-MCS except for member 5 have the rainfall shifted south west in comparison to the EN-NOMCS members due to the trough being further south west in these simulations (not shown). Rainfall seems more zonal across the UK in the members of EN-MCS compared to the northwest–southeast tilt in the EN-NOMCS simulations. This makes the location of the rainfall better in the members of EN-MCS when compared to rainfall radar (Figure 6.9(a)–(f) and 6.10(a)–(f) compared to Figure 5.8(f)).

The ridge over the UK at 12 UTC 6 July has a stronger gradient in PV for the members of EN-MCS (shown for control; see PV contours on Figure 6.11(a)). The ridge is also shifted to the south west in the the members of EN-MCS. The members of EN-MCS also have negative PV (-2 PVU) over the UK at 250 hPa which does not occur in the members of EN-NOMCS. This accounts for the shift in the ridge as the negative PV at upper-levels inside the ridge has an impact on the circulation patterns, by slowing down the eastward progression of the ridge. The more southerly location of the ridge in EN-MCS members can be seen in Figure 6.11(b) which shows a cross-section through the ridge. The UK cyclone has an associated tropopause fold that is further south in the EN-MCS members (50 km further south). This accounts for the better location of the rainfall produced by the cyclone in EN-MCS members. The ridge is also elevated in the members of EN-MCS compared to EN-NOMCS members (indicated by circle in Figure 6.11(b)). Although this is only shown for the control member this also occurs for all other members of the ensembles.

The 5th members of both EN-MCS and EN-NOMCS have rainfall produced further

east than in the other members due to a different pressure pattern with the UK cyclone developing too far east in comparison to the other members and to reality. Despite this, member 5 of EN-MCS does produce some weak rainfall over the west coast of the UK (where the other members produced the strongest rainfall in association with the cyclone) which the corresponding member of EN-NOMCS does not produce (Figure 6.10(f)). The fact that the location of the rainfall is so different in member 5 to the other members could be related to the MCS not being produced in this member in either EN-NOMCS or EN-MCS; triggering of convection may have occurred later thus rainfall was produced further east.

The rainfall location shift in member 5 could also be related to no convection being produced earlier in the simulation so ridge amplification was delayed. Although the stronger gradient and the shift in the ridge is seen in all members of EN-MCS, member 5 of both EN-MCS and EN-NOMCS has an upper-level high PV jet which extends further north east than in any of the other members of EN-MCS and EN-NOMCS which accounts for the rainfall in the cyclone occurring further eastward in this member (not shown here).

The above discussions provide evidence for the importance of moist processes (Zhang *et al.*, 2003; Tan *et al.*, 2004) on the subsequent forecast as in the only member which did not create the northern MCS (or any convection at all in EN-NOMCS and a small amount in EN-MCS at the location of the MCS) the subsequent forecast of the UK cyclone is very different to that of the UK cyclone forecast in the other members.

In all members of EN-MCS the PV gradient at the boundary of the ridge is increased and the ridge is elevated by the addition of negative PV anomalies at upper-levels. This is important as it is this ridge of the Rossby wave that moves downstream over the 5 day forecast and will impact the circulation patterns. The MCS perturbations also cause a displacement in the tropopause fold and positive PV at mid-levels (to the southwest) associated with the UK cyclone. Thus, the IC perturbations have a bigger impact on the forecast (between members) than the MCS perturbations (an MCS was not produced in member 5), however the MCS perturbations do influence the location and magnitude of the rainfall produced by the UK cyclone due to the displacement and amplification of the ridge. The next Section investigates the downstream impact of this ridge amplification and displacement on the subsequent downstream development of the simulations.

Figure 6.7: Total precipitation rates 00 UTC 6 July 2012 for each member of EN-MCS for (a) Control, (b) ensemble member 1, (c) ensemble member 2, (d) ensemble member 3, (e) ensemble member 4 and (f) ensemble member 5. The black circles indicate the location of the northern MCS and the blue circles indicate the location of the southern MCS.

Figure 6.8: Total precipitation rates 00 UTC 6 July 2012 for each member of EN-NOMCS for (a) Control, (b) ensemble member 1, (c) ensemble member 2, (d) ensemble member 3, (e) ensemble member 4 and (f) ensemble member 5. The black circles indicate the location of the northern MCS and the blue circles indicate the location of the southern MCS.
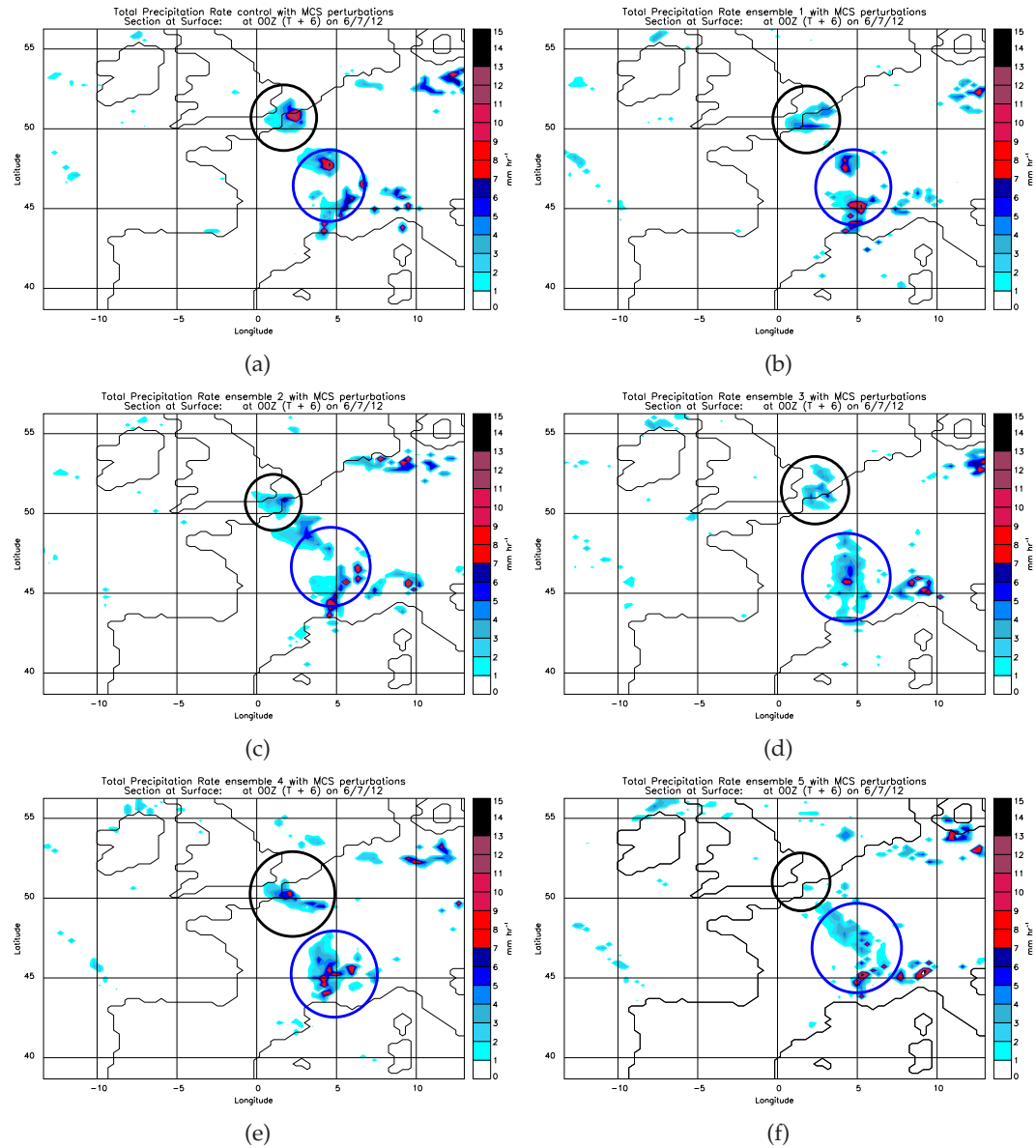
Figure 6.9: Total precipitation rates 12 UTC 6 July 2012 for each member of EN-NOMCS for (a) Control, (b) ensemble member 1, (c) ensemble member 2, (d) ensemble member 3, (e) ensemble member 4 and (f) ensemble member 5. Contours of PMSL are plotted 980 hPa to 1030 hPa contour interval is 5 hPa.
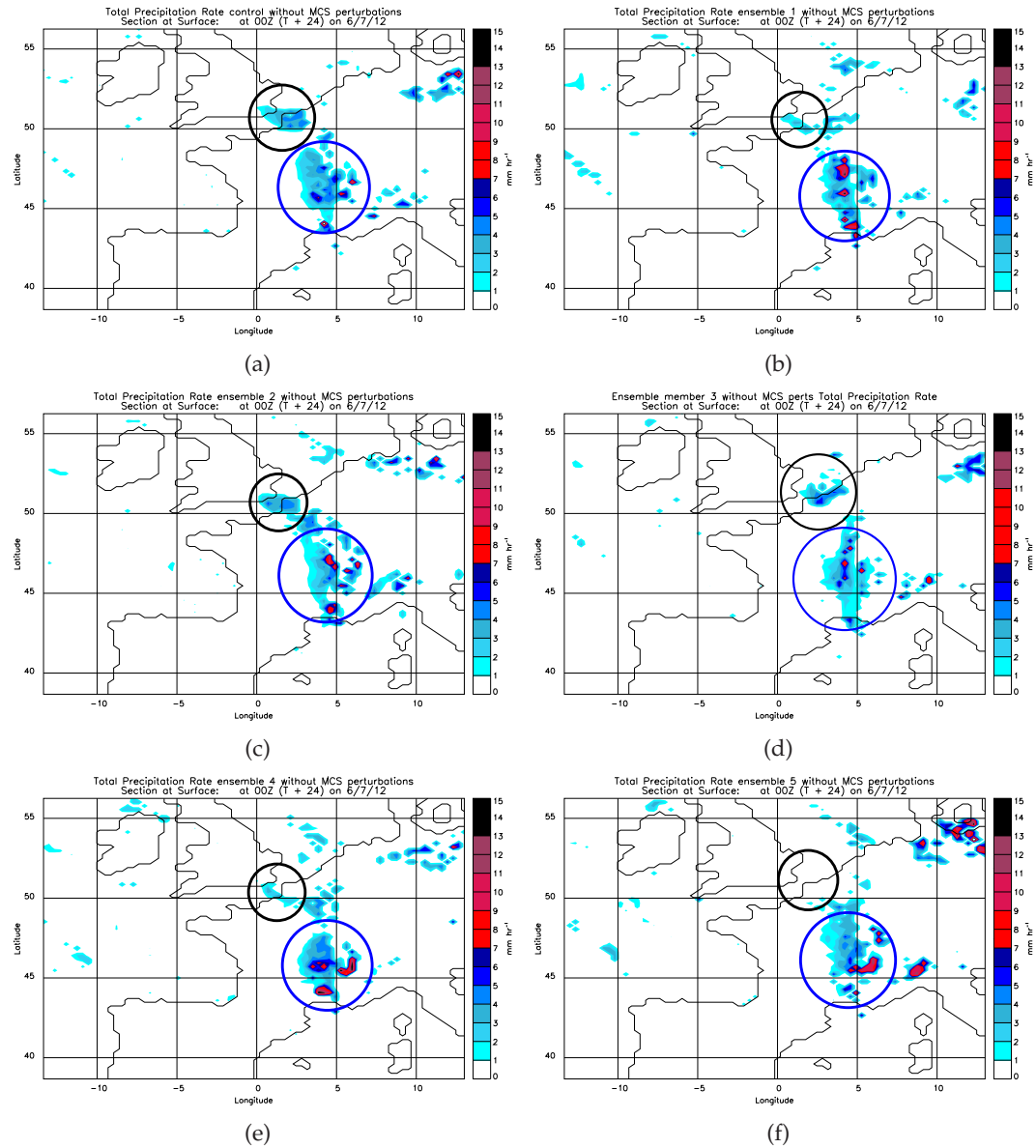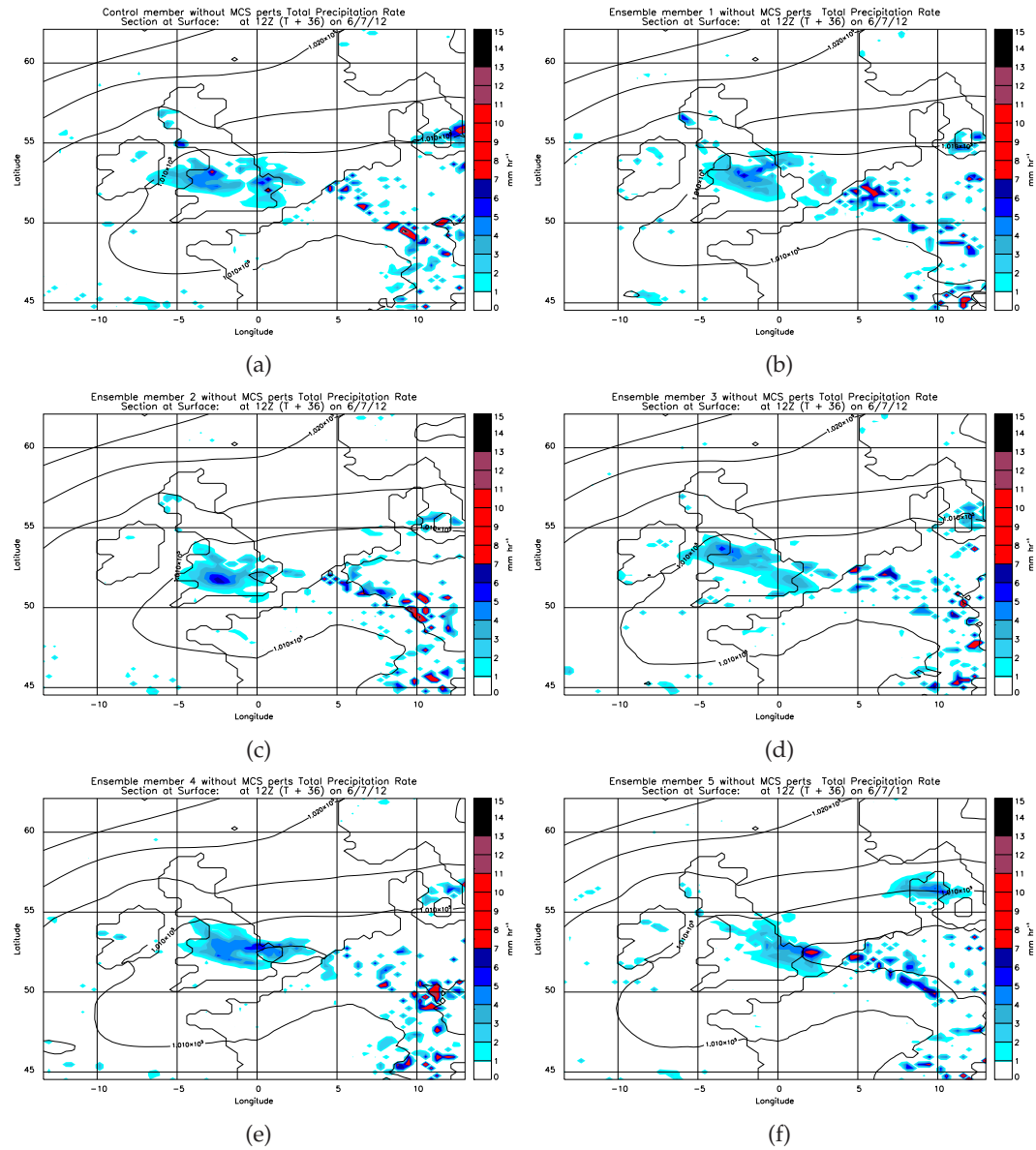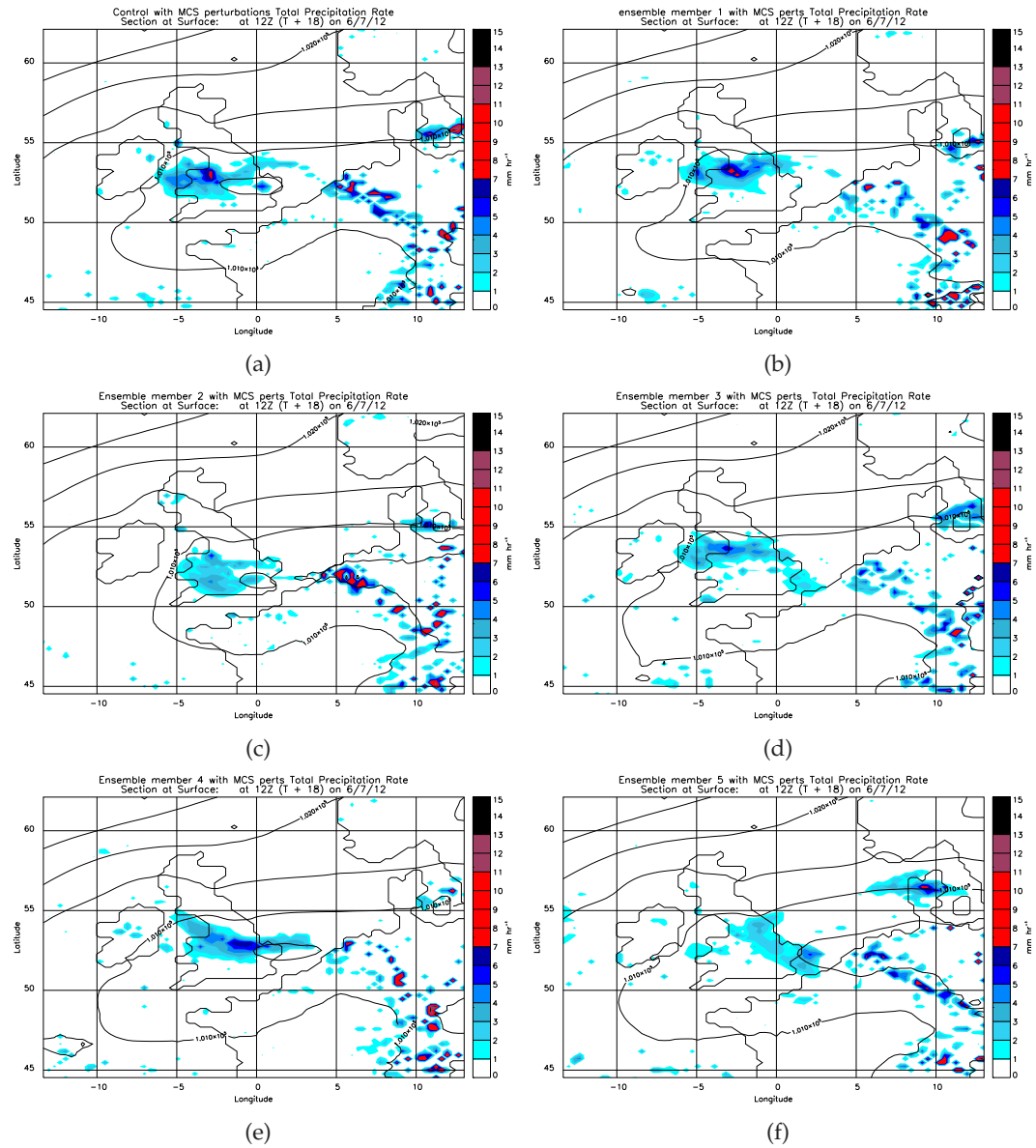
Figure 6.10: Total precipitation rates 12 UTC 6 July 2012 for each member of EN-MCS for (a) Control, (b) ensemble member 1, (c) ensemble member 2, (d) ensemble member 3, (e) ensemble member 4 and (f) ensemble member 5. Contours of PMSL are plotted 980 hPa to 1030 hPa contour interval is 5 hPa.

(a)

(b)
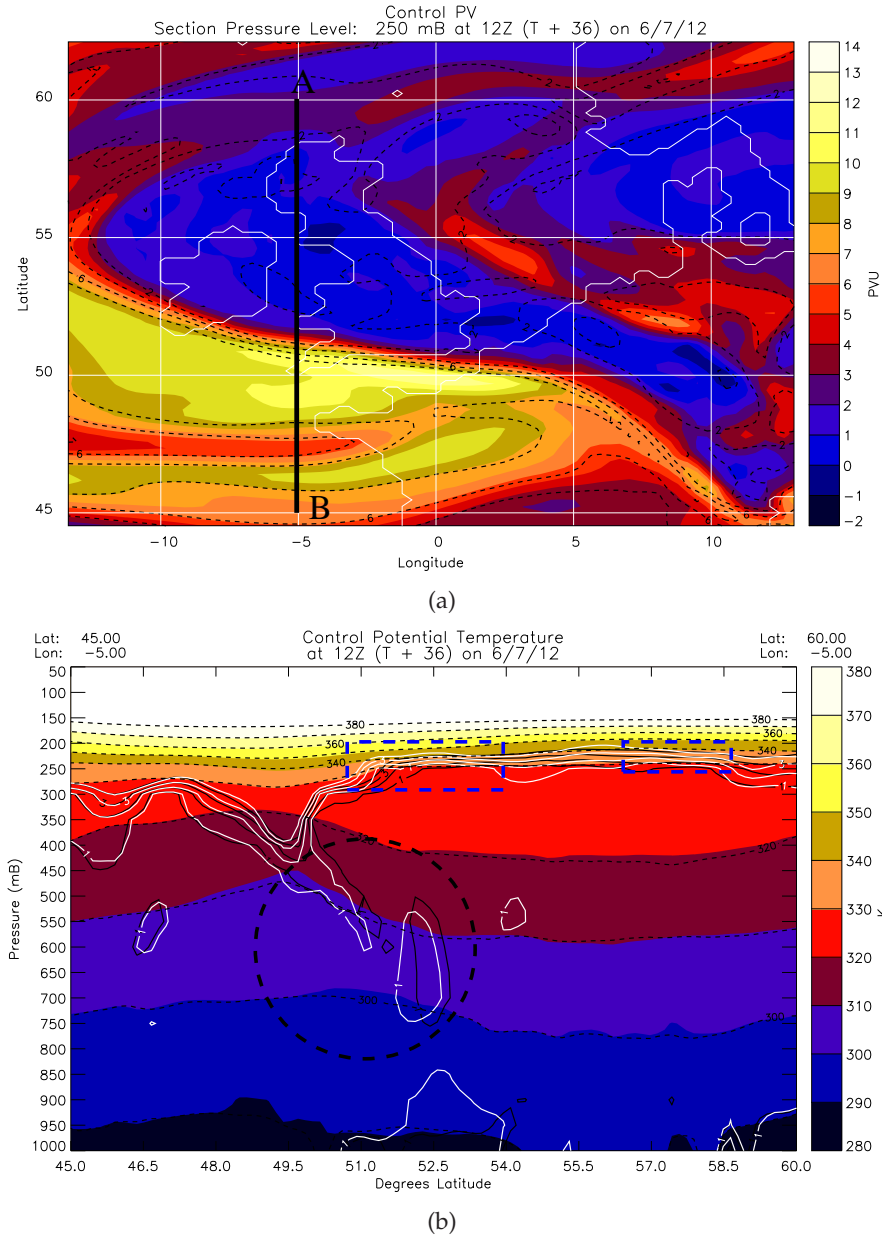
Figure 6.11: (a) PV at 250 hPa 12 UTC 6 July 2012 for EN-NOMCS for (a) control with black dashed contours of PV -2 PVU–8 PVU for the corresponding member of EN-MCS. Cross-section A–B used for Figure (b). (b) Cross-section of potential temperature for EN-NOMCS with contours of PV at 1–3 PVU in black for EN-NOMCS plotted for the corresponding member of EN-MCS as white contours and dashed black lines of potential temperature. The blue dashed rectangles indicate areas where the EN-MCS member has a higher tropopause height and stronger PV gradient. The black dashed circle indicates where the trough is shifted to the south in the EN-MCS case.

6.3.3 Medium-range impact of the MCS perturbations out to 10 July 2012

In Section 6.3.1 it was shown that the MCS perturbations added to the simulations create a differing forecast of PV for the EN-MCS members in comparison to the members of EN-NOMCS at 19 UTC 5 July. In Section 6.3.2 these differences in the PV structures between the members of each ensemble were shown to have a consequential impact on the forecast of the UK cyclone at 12 UTC 6 July. The rainfall produced in association with the UK cyclone in the members of EN-MCS was heavier and located further southwest than in the corresponding members of EN-NOMCS (member 5 of EN-MCS had weaker rainfall but a better location). The objective of this Section is to determine how the forecasts from EN-MCS and EN-NOMCS diverge from each other downstream (after 5 days) from the MCS and UK cyclone. To investigate the downstream impact, the differences between the members of EN-MCS and EN-NOMCS in PV, PMSL and precipitation are analysed.

PV

The magnitude of the differences in PV at 250 hPa between each corresponding ensemble member of EN-NOMCS and EN-MCS differs between each member after 5 days (Figure 6.12(a)–(f) and Figure 6.13(a)–(f)). The smallest differences in PV at 250 hPa occur in member 5 though related to this member not developing an MCS in either EN-MCS or EN-NOMCS and poorly representing the positioning and magnitude of rainfall associated with the UK cyclone on 6 July.

The larger differences in PV which occur in the other members (in comparison to member 5) are not related to the strength of the MCS perturbations added since each member had similar magnitude perturbations. It is speculated that the larger differences in the other members are due to the heavier rainfall created (in association with the two MCS and the UK cyclone) in these members of EN-MCS, due to the addition of the MCS perturbations. Many previous studies have found that latent heat release is an important factor in the growth of errors in the model (Selz and Craig, 2015; Hohenegger and Schlar, 2007; Zhang *et al.*, 2007) causing errors to grow rapidly, particularly in areas of precipitation. Therefore, since these members of EN-MCS have heavier rainfall in association with both MCSs than in the corresponding member of EN-NOMCS the downstream dif-

ferences in PV are larger than in member 5 which does not develop the northern MCS and poorly represents the UK cyclone (in terms of positioning and magnitude of precipitation).

Differences in the PV patterns at 250 hPa are created along the strong PV gradient at the edges of the ridges in the Rossby wave and track downstream throughout the 5 day forecast, from the initial ridge which was strengthened and amplified to the west, by the addition of the MCS perturbations (Figure 6.11(a)). Since the PV gradient at the ridge boundary is strengthened by the MCS perturbations there are negative PV differences at upper-levels (up to a maximum of -10 PVU) created downstream at the ridge boundaries after 5 days. This is caused by a combination of the PV gradient being strengthened at the boundary and a westerly shift in the ridge of the EN-MCS members (Figure 6.12(a)-(f) and Figure 6.13(a)).

At 500 hPa differences in PV seen in Figures 6.14(a)-(f) and Figures 6.15(a)-(f) are due to variations in the location of the frontal zones and regions of moist ascent of the corresponding members of EN-MCS and EN-NOMCS. The members of EN-MCS have a slower eastward movement due to enhancement of divergent outflow and amplification of the ridges. Since the members of EN-MCS have a slower eastward movement the low-pressure centres are further west in this ensemble leading to differences in PV at the 500 hPa level (due to the location of the tropopause fold differing between EN-MCS and EN-NOMCS).

The members of EN-MCS have a slower eastward progression than the members of EN-NOMCS; this can be seen in Figure 6.16(a) which shows that the troughs and ridges are shifted to the west in EN-MCS (also found in Grams and Archambault (2016)). Again, there are areas in the cross-sections (Figure 6.16(a) and (b)) that show the tropopause height is raised (in the ridge) in the EN-MCS members showing evidence for the negative PV differences in Figure 6.13(a). These negative PV differences are related to a strengthening in the PV gradient at upper-levels in EN-MCS members since the PV dipole at the edge of the ridge reduces the PV in the troposphere and increases it in the stratosphere. Therefore, since the PV is reduced further in the members of EN-MCS (larger magnitude negative PV) the PV gradient at the tropopause is increased. This has an impact on the windspeed patterns at 250 hPa, with windspeed differences up to 28 ms^{-1} occurring at the boundary of the ridge, as the gradient in PV values at the boundary is amplified

in the EN-MCS members and the jet streak is accelerated due to the amplified ridge in these members. The circulation patterns are altered between the members of EN-MCS and EN-NOMCS (Figure 6.17(a)-(f)) as the lower PV (at upper-levels) in the EN-MCS members enhances the divergent outflow aloft, amplifying the ridge which slows down the eastward progression. These negative PV differences created at the boundary of the ridges was also found in Grams and Archambault (2016) with a similar magnitude (7 PVU) related to extratropical cyclones.

Figure 6.16(a) shows a cross-section taken through the low-pressure centre downstream after 5 days (north of Russia; discussed later) of the control members of EN-MCS and EN-NOMCS and a similar pattern was seen in other members as well (not shown). The position of the centre of the low is further west in the members of EN-MCS and this is shown by the tropopause (taken as being the 2 PVU contour) being at its lowest height (500 hPa) further east than in the control of EN-NOMCS, with there being approximately 10 km difference between them (Figure 6.16(a)). This slower eastward progression is due to stronger divergent outflow at tropopause level due to the negative PV in the EN-MCS members which causes larger amplitude ridges which have an associated slower progression.

When analysing figures of PV at both 250 hPa (Figure 6.12(a)–(f) and Figure 6.13(a)–(f)) and 500 hPa (Figure 6.14(a)–(f) and Figure 6.15(a)–(f)) it can be seen that the differences between the ensemble members within each individual ensemble are greater than the differences between corresponding ensemble members from the two ensembles. The IC perturbations have a greater impact on the forecast than the MCS perturbations. Differences in PV at 250 hPa downstream are related to the ridge and trough patterns and differences in PV at 500 hPa are related to the weather systems which developed downstream (low-pressure centre of a cyclone with associated fronts and moist convection). These findings are related to previous studies that found negative PV at tropopause level causes increased divergent outflow and a slower eastward progression (Grams and Archambault, 2016; Quinting and Jones, 2016; Riemer *et al.*, 2008), along with a strengthening of the PV gradient at the boundary of ridges leading to variations in the position and strength of the low-pressure centres of cyclones (due to the associated impact on the upper-level jets; a stronger PV gradient causes a faster jet with associated larger temperature differences).
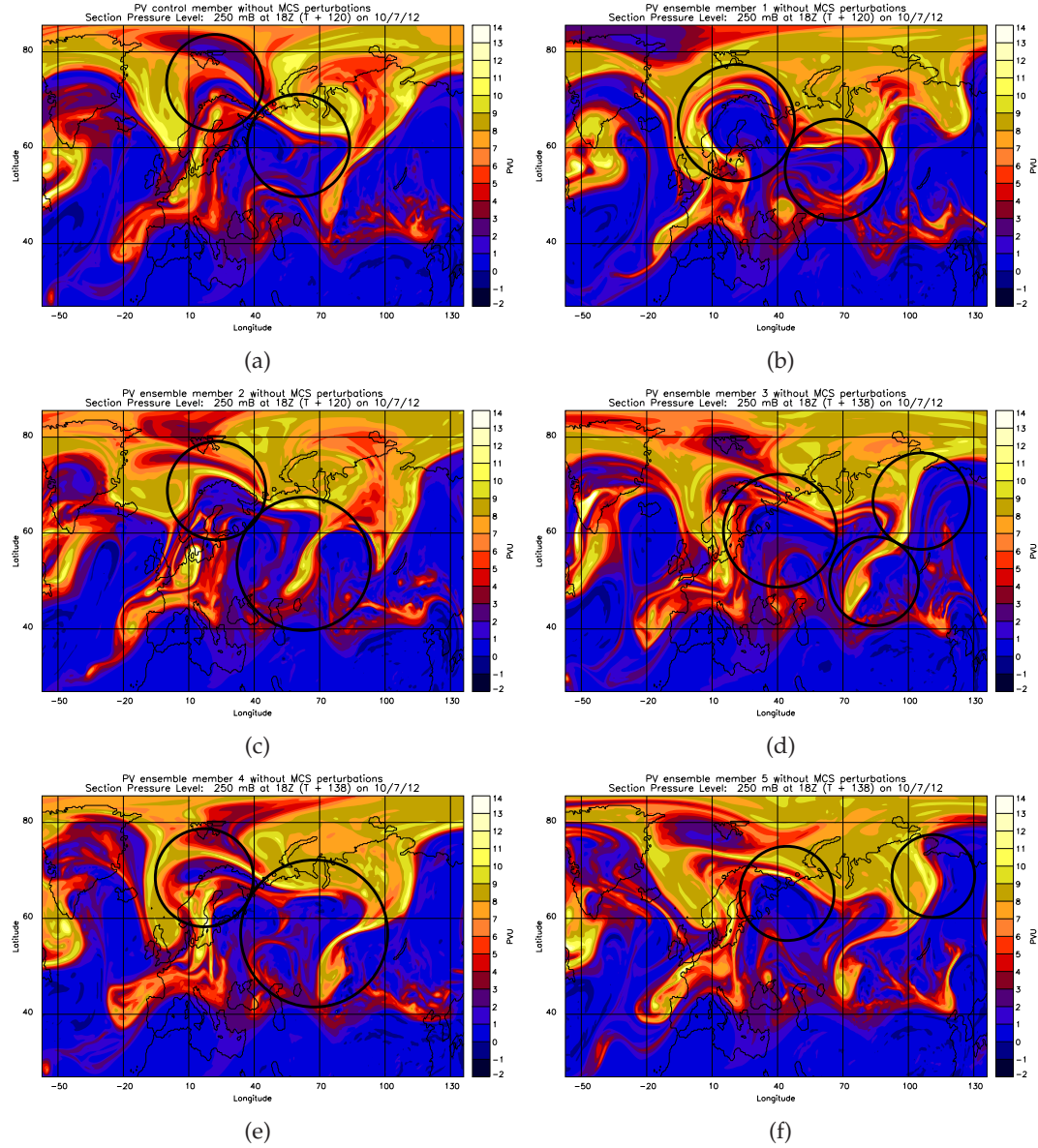
Figure 6.12: PV at 250 hPa 18 UTC 10 July 2012 for each member of EN-NOMCS for (a) Control with cross-section A–B being used in Figure 6.16(b), (b) ensemble member 1, (c) ensemble member 2, (d) ensemble member 3, (e) ensemble member 4 and (f) ensemble member 5. Black circles indicate areas where differences in PV are shown to occur at the boundary of the ridges in Figure 6.13(a)-(f).
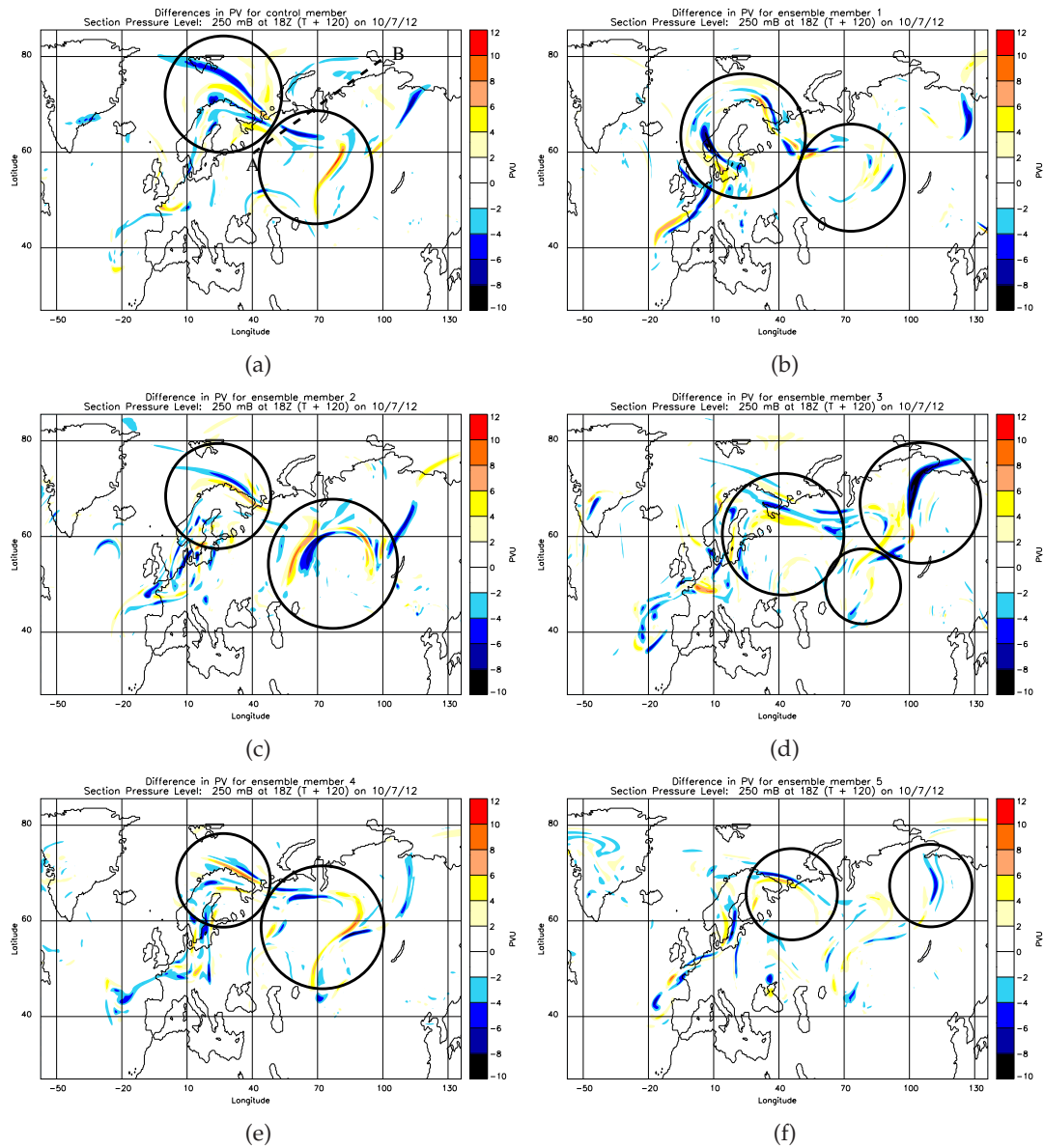
Figure 6.13: Differences in PV at 250 hPa 18 UTC 10 July 2012 EN-MCS−EN-NOMCS for (a) Control, (b) ensemble member 1, (c) ensemble member 2, (d) ensemble member 3, (e) ensemble member 4 and (f) ensemble member 5. Black circles indicate areas where differences in PV are shown to occur at the boundary of the ridges seen in Figure 6.12(a)-(f). Cross-section A–B is used in Figure 6.16(b).
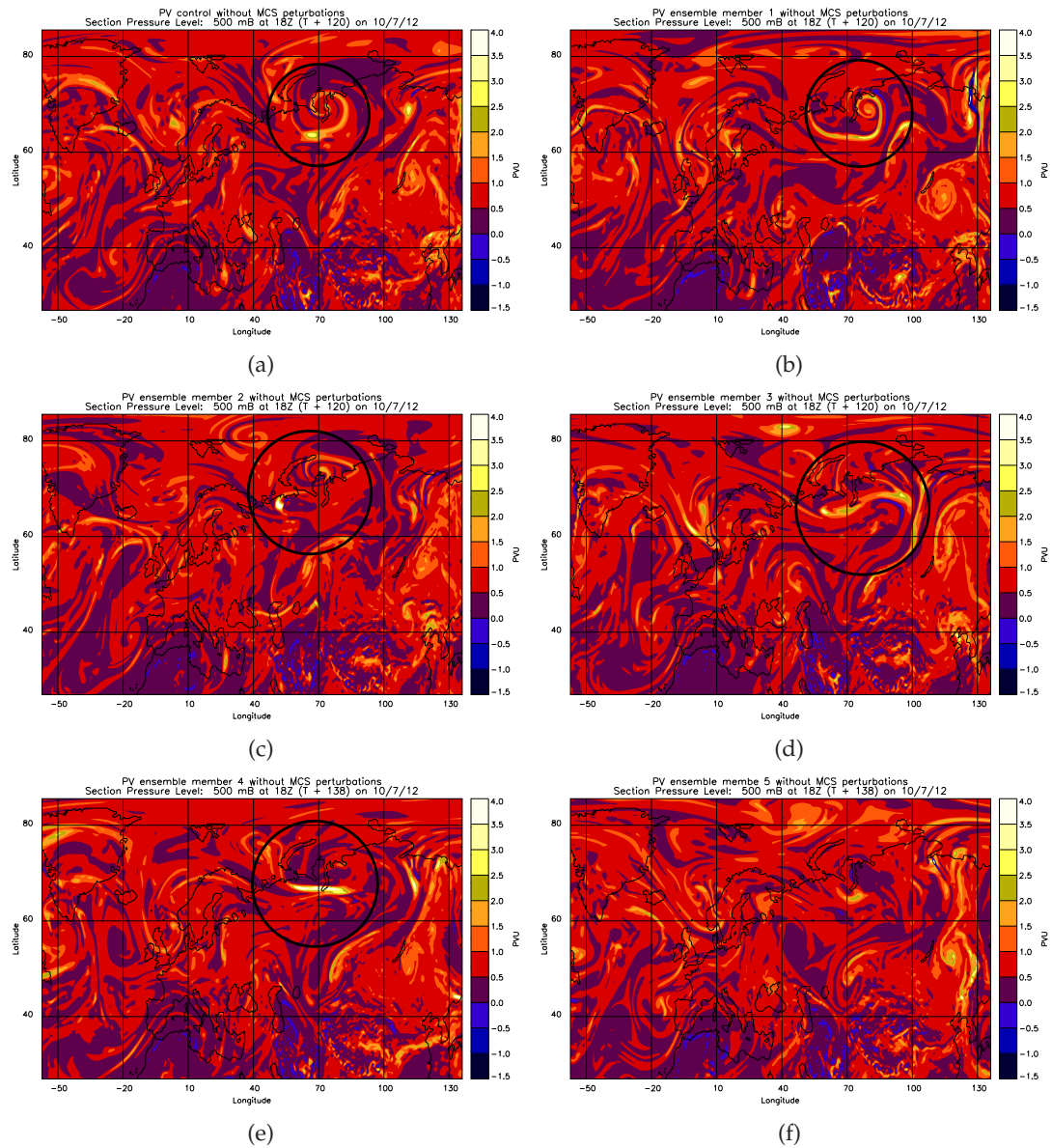
Figure 6.14: PV at 500 hPa 18 UTC 10 July 2012 for each member of EN-NOMCS for (a) Control, (b) ensemble member 1, (c) ensemble member 2, (d) ensemble member 3, (e) ensemble member 4 and (f) ensemble member 5. Black circles indicate the area where differences between corresponding EN-NOMCS and EN-MCS members occurs in the PV at 500 hPa due to the low pressure centre which develops downstream over northern Russia.
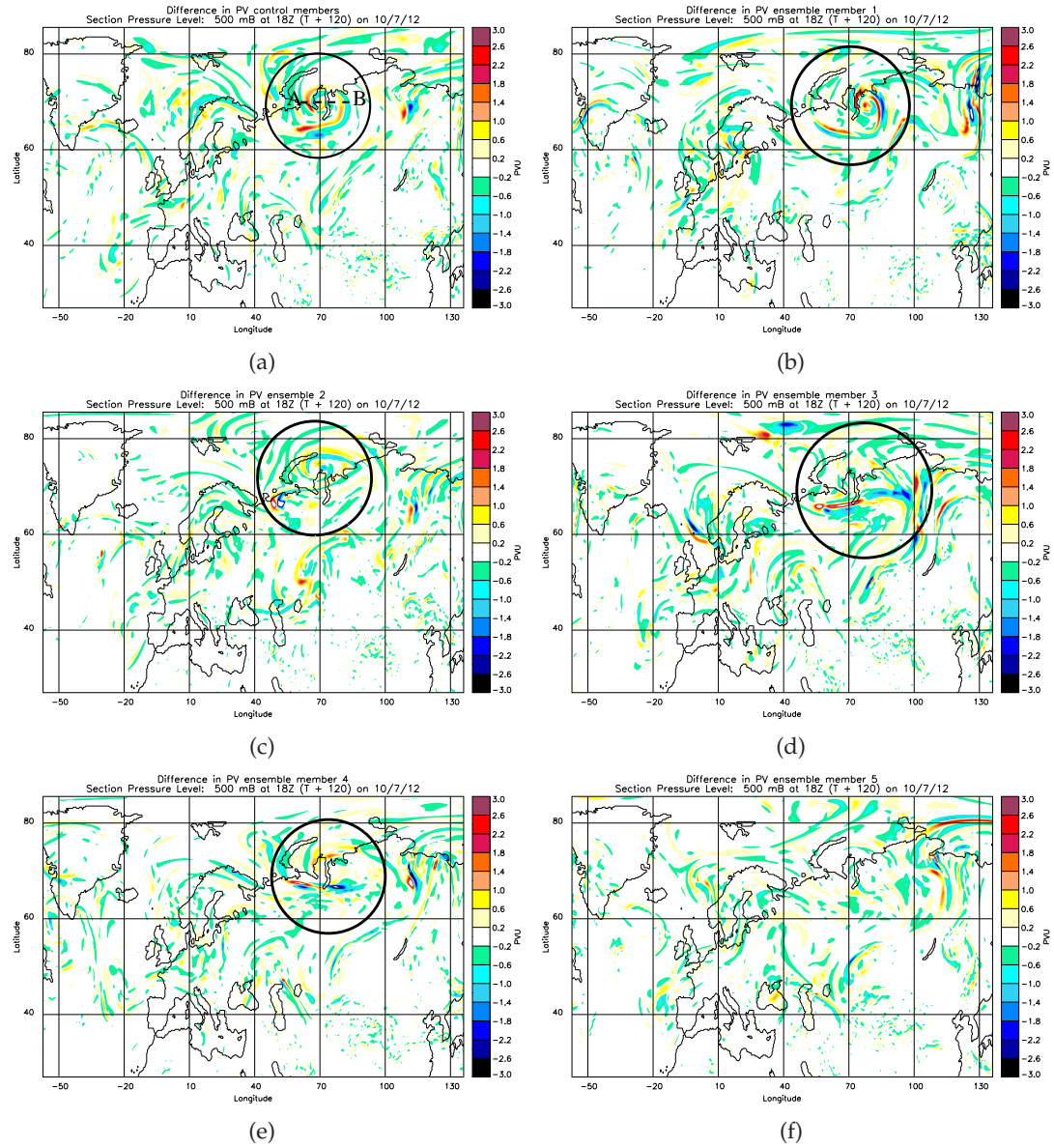
**Figure 6.15:** Differences in PV between each of the corresponding ensemble members from each of the two sets of ensembles at 500 hPa 18 UTC 10 July 2012 for EN-MCS minus EN-NOMCS for (a) Control, (b) ensemble member 1, (c) ensemble member 2, (d) ensemble member 3, (e) ensemble member 4 and (f) ensemble member 5. In some areas the colour bar became saturated but the contours were chosen to best represent the differences. Black circles represent the area of PV differences related to the low-pressure centres shown in Figure 6.31(a)-(f). Cross-section A–B is used for Figure 6.16(a).

(a)

(b)
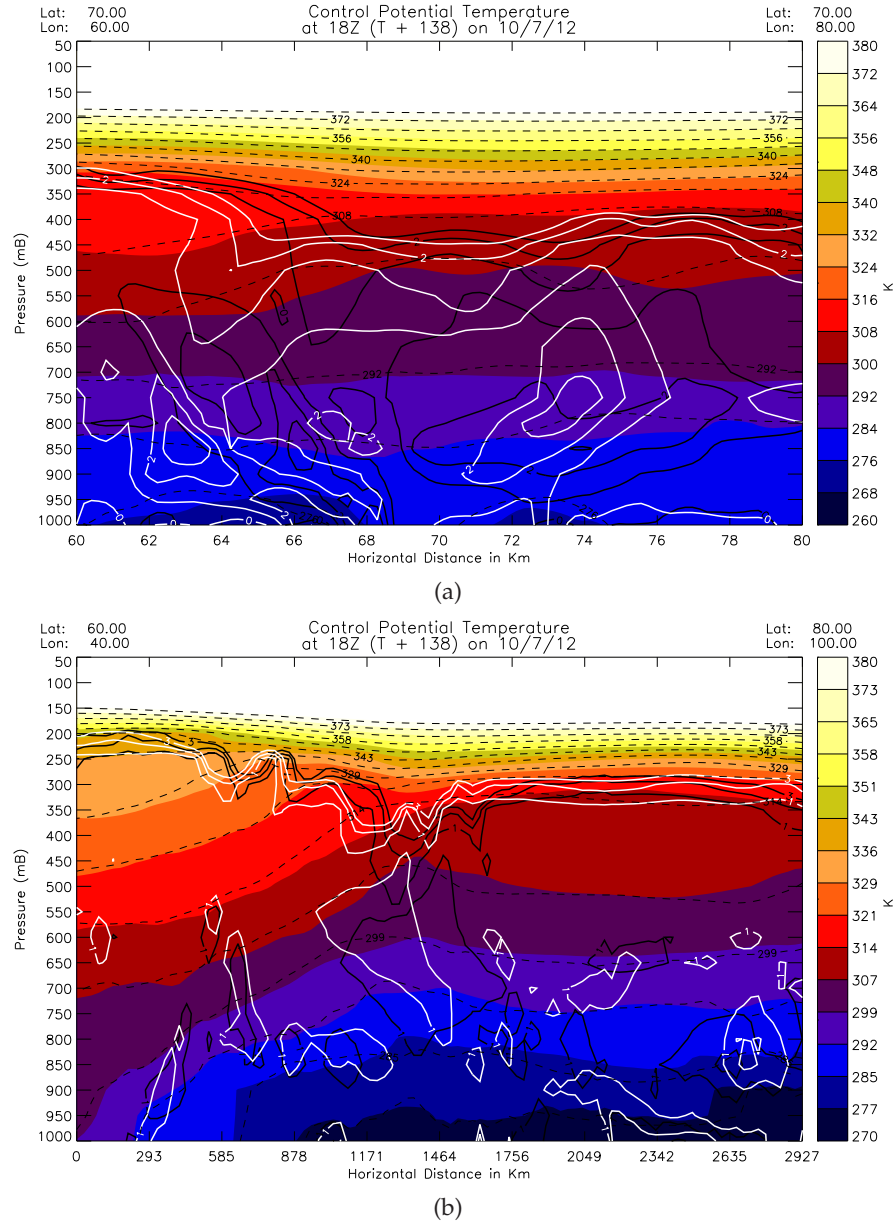
Figure 6.16: Cross-section of potential temperature through the low-pressure centre 18 UTC 10 July 2012 for the control member of EN-NOMCS with contours of PV at 0–3 PVU (black EN-NOMCS and white control member of EN-MCS) with dashed black lines of potential temperature for control EN-MCS. (a) is taken through the trough to cross through the centre of the low pressure marked on Figure 6.15(a) and (b) is taken to pass through the ridge and the trough marked on Figure 6.13(a).

(a)　　　　　　　　　　　　　　　(b)

(c)　　　　　　　　　　　　　　　(d)

(e)　　　　　　　　　　　　　　　(f)
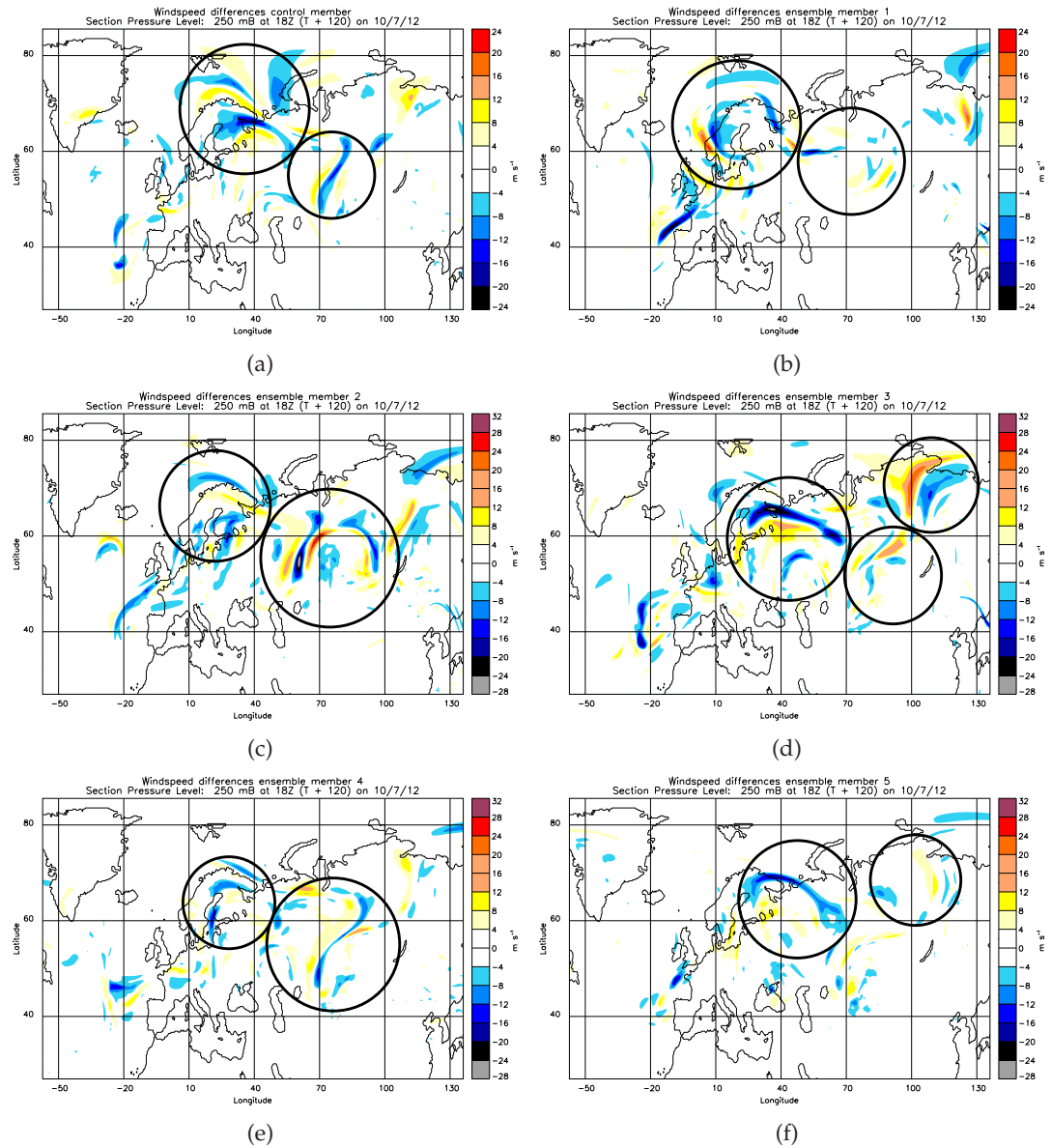
Figure 6.17: Differences in windspeeds at 250 hPa 18 UTC 10 July 2012 between corresponding members of EN-MCS minus EN-NOMCS for (a) Control, (b) ensemble member 1, (c) ensemble member 2, (d) ensemble member 3, (e) ensemble member 4 and (f) ensemble member 5. Black circles indicate areas of windspeed differences that correlate to areas of PV and PMSL differences.

Precipitation and PMSL

A comparison of the total precipitation produced in each ensemble shows that the overall pattern of precipitation after 5 days is very similar in EN-MCS and EN-NOMCS (Figure 6.18(a)–(f) and Figure 6.19(a)–(f)). Precipitation develops at the boundary of ridges and troughs and in some areas where the ridges are amplified by the MCS perturbations the precipitation is stronger in the members of EN-MCS. The stronger precipitation in the EN-MCS members is a consequence of a deeper low pressure leading to stronger ascent leading to larger amounts of rainfall.

The MCS perturbations lead to a deepening of the low pressure system downstream (cyclone to the north of Russia in the Kara sea, marked by circles on Figure 6.19(a), Figure 6.19(c) and Figure 6.19(e). The differences in PMSL can be seen in Figure 6.20(a)–(f)) from the MCS after 5 days, but only in the control member and member 2 and 4, and varies in magnitude with the strongest differences in PMSL being around -6 hPa (due to the deepening of the cyclone in 3 members, by a maximum of 3 hPa and the slower eastward progression in the EN-MCS members) . This deepening of the low-pressure centre develops after 3 days of the forecast as the low-pressure begins to develop downstream (not shown here). The control and member 2 of EN-MCS have a central low pressure of 989 hPa whereas the corresponding member of EN-NOMCS has a central pressure of 992 hPa. In members 1 and 3 the low-pressure centre is not deepened, but it is shifted to the east in the EN-MCS members so large differences in PMSL are still seen in Figure 6.20(b) and 6.20(d) at around ±6 hPa. In member 5 of EN-NOMCS and EN-MCS the differences in PMSL are small as the low-pressure centre is similar in both ensembles due to the lack of representation of the MCS (on 5 July) in either simulation. Also the eastward movement in member 5 of EN-MCS is not as slow as the other members of EN-MCS, so differences in PMSL are smaller (maximum of -3 hPa). Member 5 of EN-NOMCS and EN-MCS both have the weakest low-pressure centre in comparison to the other members at a minimum of 995 hPa whereas the other members had a minimum of 988 hPa.

Analysis of PMSL and precipitation rates shows that the areas of rainfall produced by each ensemble member is related to the trough patterns which differ between the members. The large-scale variability in the PMSL seems more related to the IC perturbations added to the ensembles rather than the MCS perturbations added (since there is larger variability between each of the members of the ensemble than between the cor-

responding member of the ensemble with the MCS perturbations added). The addition of the MCS perturbations causes differences in PMSL downstream related to variations in the location of the low-pressure centre downstream and the slower eastward progression due to the amplification of the ridges by negative PV in the EN-MCS members at tropopause level.

The MCS perturbations do lead to areas of heavier rainfall in the EN-MCS members than in the EN-NOMCS members in some areas where the PMSL patterns have either been deepened or the trough has been extended or shifted by the MCS perturbations. This heavier rainfall in the EN-MCS members are also related to the PV anomaly patterns varying between ensemble members. The PV patterns are also varied between the members of EN-NOMCS and EN-MCS as the patterns, particularly at tropopause level are strongly influenced by the pressure patterns. Differences in the PV at tropopause level are associated with differences in the PMSL patterns. The ridges and trough patterns are shifted due to the MCS perturbations along with the tropopause height. Most of the rainfall produced in both EN-NOMCS and EN-MCS occurs at the boundary of the ridges (where the PV gradient is strengthened in the EN-MCS members) of the Rossby waves in the model (the transition between high PV and low PV air). Outflow from cyclones in the EN-MCS simulations may reach higher into the troposphere if they are deeper (more intense). This will amplify the ridge and the feedback on the upper and lower levels will amplify the trough.

A comparison of Figures 6.13(c),(d),(e), Figures 6.20(c),(d),(e) and Figures 6.19(c),(d),(e) and Figures 6.18(c),(d),(e) show that the MCS perturbations cause a deepening or a shift in the PMSL which corresponds to an area of negative and positive PV anomaly differences at 250 hPa and 500 hPa, respectively, at 18 UTC 10 July 2012. The magnitude of the PV differences varies between the ensemble members, but in member 2, 3 and 4 the differences in PMSL are largest at up to 6 hPa (due to both the deepening of the low-pressure centre, by up to 3 hPa and the slower eastward progession) corresponding to PV differences of ± 3 PVU at 500 hPa. These differences in PMSL and PV also correspond to areas of stronger rainfall in members 2, 3 and 4 of EN-MCS by up to 4 mmhr^{-1} at ridge boundaries, where differences in PV occur at 250 hPa (Figure 6.13(a)). As a consequence of the low pressure centre north of Russia being further west there are also colder temperatures (lower θ) further west as well in EN-MCS along with colder

surface temperatures in 3 of the members of EN-MCS compared to EN-NOMCS due to the low pressure centre being depeer in these members of EN-MCS. In member 5 the eastward progression is not slowed as much as in the other members of EN-MCS.

In summary, the MCS perturbations seem to deepen the low-pressure centre downstream after 5 days (north of Russia) from where the MCS perturbations are added in 3 out of the 6 members (the control and member 2 are deepened by 3 hPa; member 4 deepened by 2 hPa), Gray (2001) also found in one case that idealised PV added to a model simulation associated with an MCSs led to a deepening of the low-pressure system downstream. The MCS perturbations led to a slower eastward progression of the weather systems in the members of EN-MCS due to ridge strengthening and amplification from stronger negative PV anomalies in these members (which has also been found in previous studies related to tropical cyclones and extratropical cyclones).
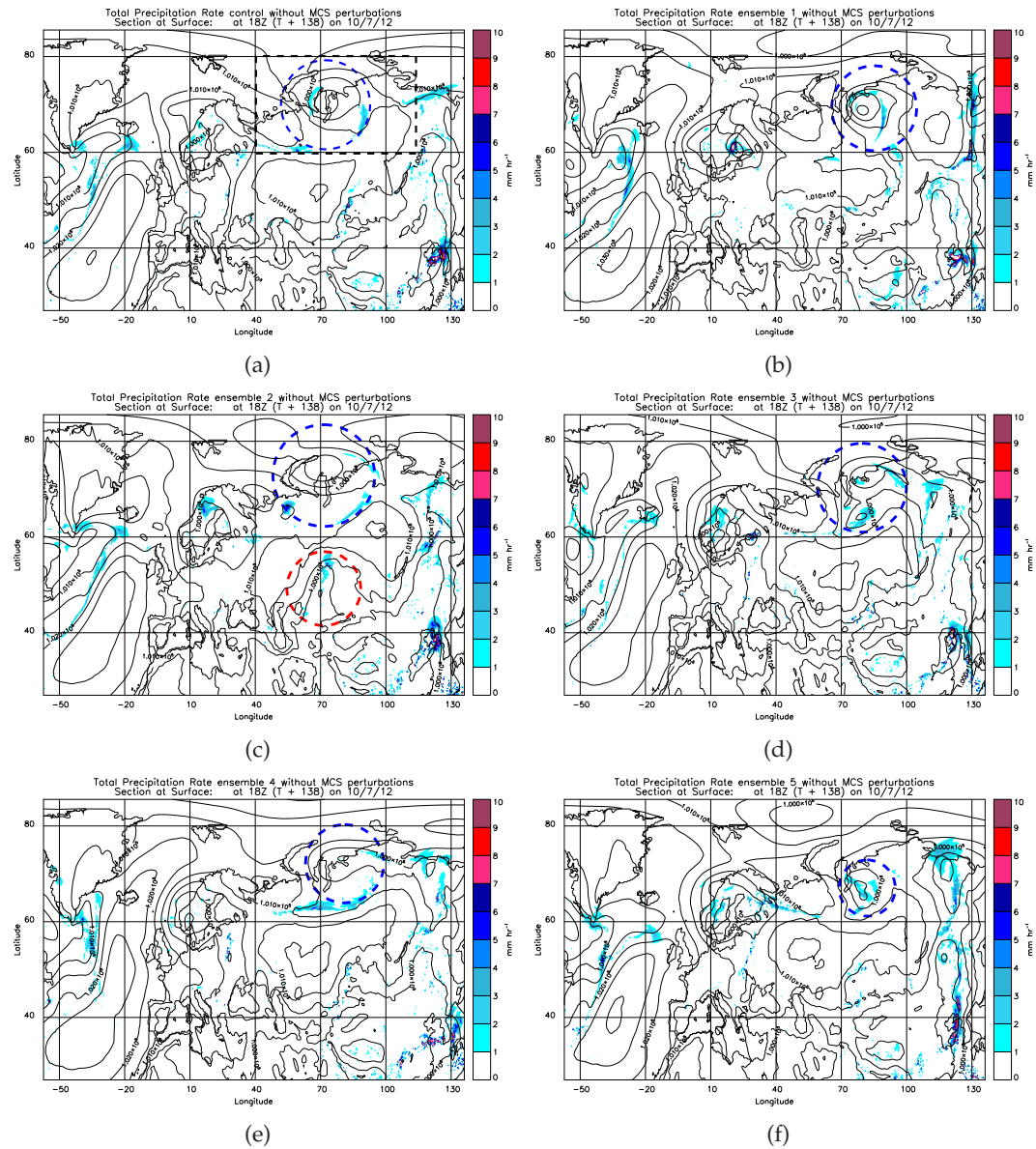
Figure 6.18: Total rainfall rates for each member of EN-NOMCS at 18 UTC 10 July 2012 for (a) Control, (b) ensemble member 1, (c) ensemble member 2, (d) ensemble member 3, (e) ensemble member 4 and (f) ensemble member 5. Each figure has contours of PMSL at 980 hPa to 1030 hPa every 5 hPa. The dashed line square marked on (a) indicates the sub-section used for Figures 6.31(a)-(f). Blue dashed circles indicate the location of the low-pressure centre.
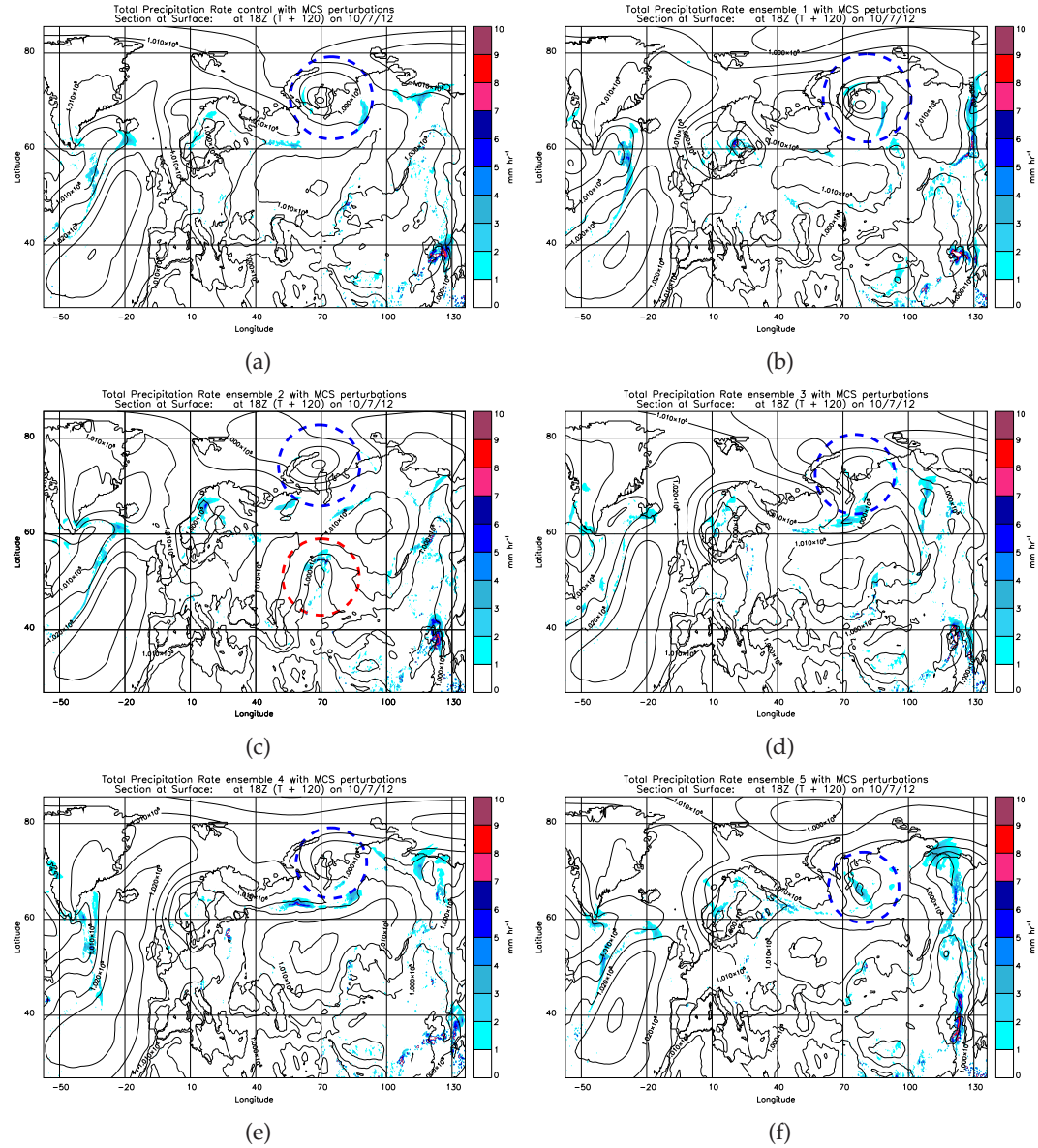
Figure 6.19: Total rainfall rates for each member of EN-MCS at 18 UTC 10 July 2012 for (a) Control, (b) ensemble member 1, (c) ensemble member 2 with the red dashed circle indicating the second low-pressure centre which forms in this member but in none of the other members of EN-MCS or EN-NOMCS, (d) ensemble member 3, (e) ensemble member 4 and (f) ensemble member 5. Each figure has contours of PMSL at 980 hPa to 1030 hPa every 5 hPa. Blue dashed circles indicate the location of the low-pressure centre.
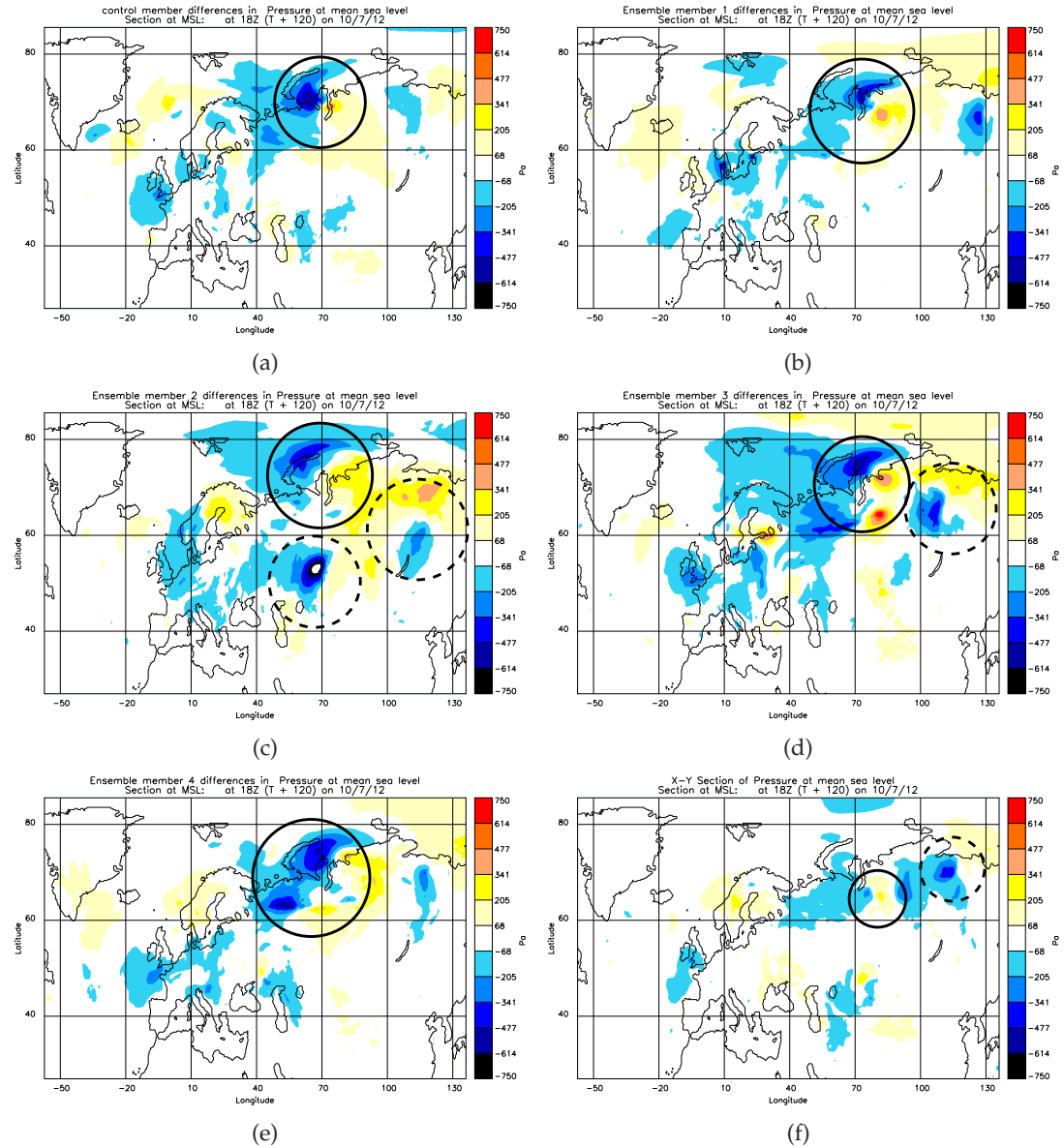
Figure 6.20: Differences in PMSL between corresponding members EN-MCS – EN-NOMCS at 18 UTC 10 July 2012 250 hPa for (a) Control, (b) ensemble member 1, (c) ensemble member 2, (d) ensemble member 3, (e) ensemble member 4 and (f) ensemble member 5. Black circles indicates areas of differences in PMSL related to the different strengths and locations of the low-pressure centre between the members of EN-NOMCS and EN-MCS. Dashed black lines shown differences in PMSL related to differences in the PV in these areas due to the strengthening of the ridge in EN-MCS members.

6.4 Analysis of ensemble diagnostics

In the following Section root mean squared differences (RMSD) are calculated for PV and PMSL. Firstly, RMSD is calculated over the entire northern hemisphere and secondly, over a European sub-section, to determine how the MCS perturbations impact the growth of RMSD values and the variability of the ensemble forecasts (see Section 2.5.3).

- Variability of an ensemble is given by the range of RMSD values when comparing ensemble members to the control or the ensemble mean (calculated as member−control or member−ensemble mean).

- The ensemble difference due to the addition of the MCS perturbations is given by the difference between the RMSD values of the corresponding members of EN-MCS and EN-NOMCS (calculated as EN-MCS−EN-NOMCS).

This Section closes with a discussion of the correspondence ratio and fraction of common points (2.5.3) for PV and precipitation of the ensembles.

6.4.1 RMSD for the northern hemisphere

As time progresses in the forecasts the PV differences between each corresponding member of EN-NOMCS and EN-MCS increase (Figure 6.21(a)); however, the variability in the RMSD values for each of the ensembles is similar regardless of if it is EN-NOMCS or EN-MCS (with a maximum RMSD value of 2.4 PVU and a minimum of 2.2 PVU). All members diverge from the control in a similar way and this is the same for both ensembles. A comparison of the RMSD between each corresponding member from EN-NOMCS and EN-MCS reveals that over time RMSD values increases for each member (calculated over the whole northern hemisphere; Figure 6.21(b)), indicating that although the variability of each ensemble is not increased by adding the MCS perturbations, the forecasts themselves are nevertheless altered. The MCS perturbations cause associated variations in the circulation and heating patterns which lead to the growth in RMSD values (indicating differing forecasts) over the 5 day forecast between corresponding members of EN-MCS and EN-NOMCS.

The MCS perturbations cause differences in PV to develop between equivalent EN-

NOMCS and EN-MCS members. These differences are shown through a slow growth of RMSD values for PV over the first 30–36 hours of the forecast as they grow on the convective scale (and could be largely due to the perturbations damping over this time due to the MCS perturbations being unbalanced), before rapidly growing thereafter, as they impact a much larger area after this time (Figure 6.21(b)). Similarly, this occurs for the PMSL and windspeed RMSD between members (not shown here). The RMSD for PMSL reaches up to 350 Pa after 120 hours and grows steadily over time (not shown here).

Hohenegger and Schlar (2007) did a comparison between a Global ensemble at 80 km grid spacing and a limited area model with 2.2 km grid spacing and found that for both configurations the initial perturbations (calculated from singular vectors) amplified, but in the Global configuration large finite-amplitude perturbations developed, with peak values of ±125 m geopotential height after 30 hours into the forecast. RMSD values of geopotential height here were found to be a maximum of 40 m after 120 hours (not shown) and 8 m after 30 hours. Saturation of perturbation growth was found to occur after 6 to 10 days into the forecast for the Global ensemble (Hohenegger and Schlar, 2007) suggesting evidence for why at 120 hours into the forecast in this study the RMSD values of geopotential height have not saturated yet and are still growing (not shown) this also occurs for PV though (Figure 6.21(a) and 6.21(b)).

6.4.2 RMSD calculated for European sub-section

The previous RMSD calculations were performed for the entire northern hemisphere because of the interest in the effect over the whole hemisphere. Since the MCS perturbations seem to mostly impact the subsection of the northern hemisphere encompassing Greenland through to eastern Russia that has been plotted in Figure 6.17(a) , further RMSD calculations were performed to determine the impact over this smaller area.

The RMSD for PV calculated against the ensemble mean over this area shows that there is an increase in the range of RMSD values in comparison to when calculated over the entire northern hemisphere (Figure 6.21(a)) by the end of the 5 day forecast; however, the variability in the RMSD values still remains similar between both ensembles (compared against the mean of the ensemble members Figure 6.22(a)). The increased range of RMSD values over the smaller sub-section is largely due to the control member

being included which is much more similar to the ensemble mean than the other members. As PV is a noisy field calculating the RMSD over the smaller sub-section where the largest differences in PV occur due to the addition of the MCS perturbations creates more variability in the RMSD values and leads to saturation quicker.

When comparing each member to the control over the European sub-section the RMSD values for PV show a similar trend as to when compared to the ensemble mean, with increased variability in the range of RMSD values compared to when calculated over the whole northern hemisphere (Figure 6.22(b) and Figure 6.21(a)). Figure 6.22(a) and 6.22(b) show that the ensemble members of both EN-MCS and EN-NOMCS are more similar to the ensemble mean than to the control (which is as expected) with larger RMSD values occurring when the members are compared to the control (maximum of 2.3 PVU compared to 1.75 PVU when the members are compared to the ensemble mean).

When calculating the member–member differences over the European sub-section there is a greater variation in the RMSD values after 5 days (larger range) between the members (Figure 6.23 compared to Figure 6.21(b)). This suggests that the corresponding members of EN-MCS and EN-NOMCS differ from each other more when analysed over the sub-sections rather than when the whole northern hemisphere is taken into consideration; this is expected since the largest differences in PV occur over this sub-section due to the spatial influence of the MCS perturbations. The RMSD values for PV at 250 hPa member–member differences seem to follow 3 phases. Between 0–30 hours the RMSD values stay at a consistent level (approximately 0.3 PVU). In phase 2 between 30–96 hours the RMSD values rapidly grow until phase 3 occurs and the RMSD values saturate by 120 hours (Figure 6.23).

Analysis of the RMSD for PMSL (when the members of EN-MCS and EN-NOMCS are compared with the control of their ensemble) shows that the range of RMSD values between the two ensembles appears to be minimally affected by the addition of the MCS perturbations, whether calculated over the entire northern hemisphere (not shown here or for the smaller European subsection; Figure 6.24(a)). Similarly, this occurs for the geopotential height at 500 hPa and 850 hPa and the windspeed at 250 hPa (not shown here). The range of RMSD again increases over time for PMSL with a maximum of 350 Pa and a minimum of 210 Pa, showing a slight increase in variation when MCS perturbations are included.

The RMSD values for member–member comparisons of PMSL show for the first 30 hours the RMSD values reduce. This reduction in RMSD values suggests that the model reacts to the MCS perturbations being added for the first 30 hours, with the model smoothing out the perturbations, due to adding unbalanced fields over a 25 km grid spacing scale, thereby reducing their magnitude and causing there to be little growth in the area of influence of the differences before this time (impacting just the convective scale). After 30 hours the MCS perturbations cause forecast differences in PMSL to grow on the synoptic-scale which also grow in magnitude. Unlike with the PV RMSD values, the PMSL RMSD does not saturate and is still growing after 5 days into the simulation. The PV saturates because it is a more noisy field than PMSL therefore once the PV patterns have been shifted between the EN-NOMCS and EN-MCS members a larger shift does not cause the RMSD values to be larger because the features are so small scale and have no overlap. PMSL is a large scale field though with lots of overlap between the members of EN-MCS and EN-NOMCS therefore differences grow rapidly if any shifts between the members occurs.

There are minimal differences within the range of RMSD values (for PV and PMSL) between EN-NOMCS and EN-MCS, suggesting that the MCS perturbations have little to no impact on the robustness of the ensemble. Leoncini *et al.* (2010) found that root-mean-square-error values for precipitation between ensemble members and the control forecast were similar regardless of the amplitude of the perturbation added to the simulation (the perturbations were in potential temperature) and they concluded that this is due to perturbation growth being relatively independent from the perturbation amplitude used due to nonlinearities of the atmosphere.

In this study the spatial extent of the impact of the MCS perturbations does not seem to vary between members however the magnitude of the differences does differ (for example, see the differences in PV between the members in Figure 6.15(a)–(f)). Ensemble member 5 has the smallest differences when looking at RMSD values (Figure 6.24(b)) and differences in PV, windspeed and PMSL (Figure 6.13(f), Figure 6.17(f) and Figure 6.20(f)) and it is this member which has the worst representation of the location of the MCS and cyclone (member 5 does not produce an MCS at all) again providing evidence for the importance of representing MCSs well to help avoid forecast busts (Rodwell *et al.*, 2013). Each ensemble had similar magnitude initial condition and MCS perturbations

added at the start of the simulations therefore the MCS and associated latent heating and convection produced in the simulations seems more important than the actual MCS perturbations added to the simulations.

Previous studies found that in the presence of moist convection errors grow more rapidly and at smaller scales than in a dry version of the model (Zhang *et al.*, 2003; Tan *et al.*, 2004). Both Tan *et al.* (2004) and Zhang *et al.* (2003) found that moist convection is responsible for the rapid growth of differences in the simulations (when comparing per-turbed simulations against non-perturbed; where convective parametrization is active) and it is thought that this is why member 5 has the smallest difference growth by 120 hours as it does not produce an MCS at the start of the simulation. The largest RMSD member-member differences occur in member 2, 3 and the control (Figure 6.23 and Fig-ure 6.24(b)). It can be argued that this could be due to these members producing a better forecast of the MCS in EN-MCS (in terms of location and magnitude of rainfall) than in the corresponding members of EN-MCS (Figure 6.8(a),(c),(d) and Figure 6.7(a),(c),(d)) which lead to a better representation of the cyclone that occurred on 6 July in terms of the location of the rainfall (Figure 6.9(a),(c),(d) and Figure 6.10(a),(c) and (d)).

Comparing all of the members of EN-MCS and EN-NOMCS to the ensemble mean (Figure 6.25, so that a comparison to Figure 6.22(a) can be made) for PV shows that the control members of both EN-MCS and EN-NOMCS are more similar to the ensemble mean than the other members of each ensemble. It is speculated that this is a conse-quence of the initial condition perturbations. The standard deviations of the control members are also slightly lower (by 10% when looking at PV and PMSL; not shown here) which may contribute to the control being closer to the ensemble mean. Compar-ing all 12 members to the ensemble mean extends the range of the RMSD values by a small amount by day 5 (Figure 6.25, 0.05 PVU) but there are no noticeable differences in the variability of the members of EN-MCS compared to EN-NOMCS again.

The PMSL RMSD values when all members are compared to the control of EN-NOMCS (Figure 6.26) shows that there is an increased range of RMSD values compared to Figure 6.24(a). The largest variation in RMSD value for PMSL between correspond-ing members of EN-MCS and EN-NOMCS when both are compared to the control of EN-NOMCS occurs for member 2 (differing by 0.4 hPa). Member 2 has the largest dif-ference in PMSL created downstream due to the deepening of the low-pressure centre

downstream over northern Russia (deepened by 3 hPa; creating PMSL differences up to 6 hPa). Member 2 of EN-MCS also had large negative PMSL differences at the ridge boundary due to low-pressure related to the trough of the Rossby wave being deepened by the MCS perturbations (deepened by 2 hPa; creating PMSL differences of up to 10 hPa due to the slower eastward movement in the EN-MCS member) which do not occur in any of the other members (Figure 6.20(c)). Therefore, in member 2 the low-pressure centre is deepened in two places downstream (in comparison to the corresponding member of EN-NOMCS), where the second low-pressure centre does not develop in any of the other members of EN-MCS or EN-NOMCS (Figure 6.19(c)). This low-pressure centre causes the high pressure over eastern Europe on 10 July to be displaced to the east in comparison to the other members.
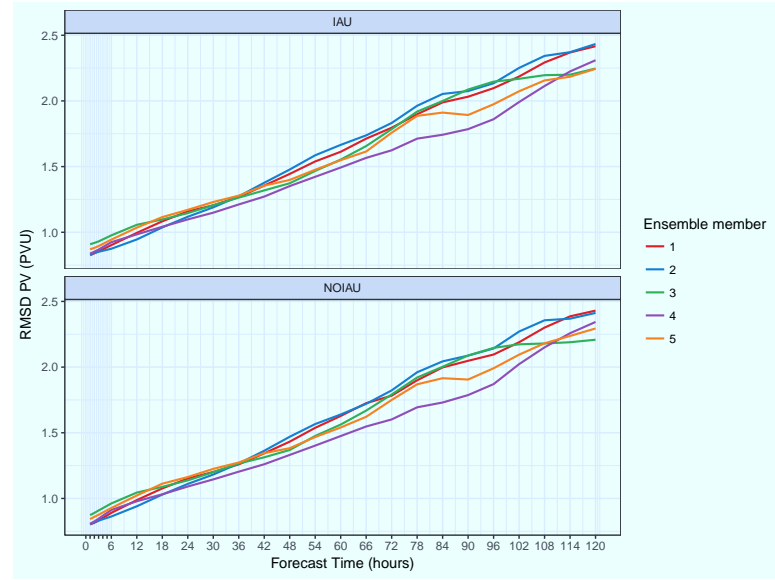
(a)
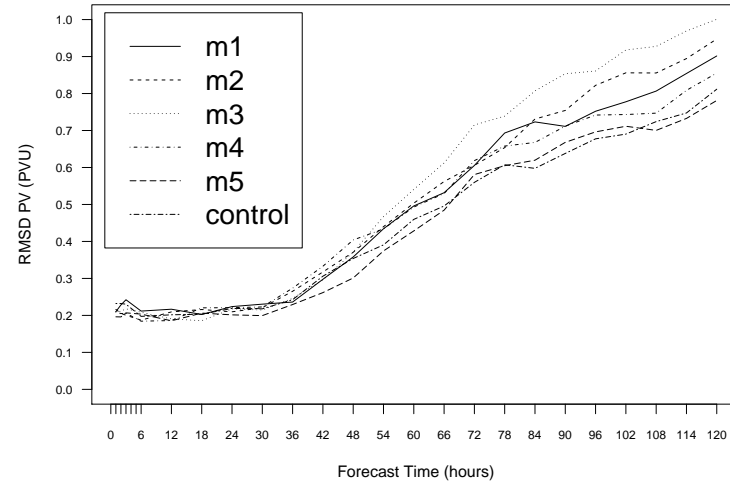
(b)

Figure 6.21: Root mean square difference (RMSD) starting at 19 UTC 5 July 2012 to 18 UTC 10 July 2012 calculated over the entire northern hemisphere for (a) PV between the ensemble members and the control at 250hPa, NOIAU signifies EN-NOMCS and IAU is EN-MCS and for (b) PV between the corresponding members of EN-MCS and EN-NOMCS. EN-MCS minus EN-NOMCS.
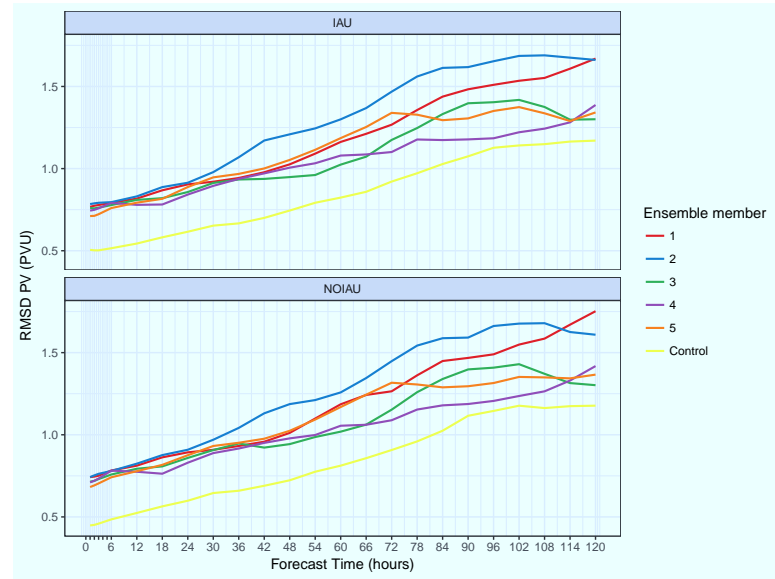
(a)
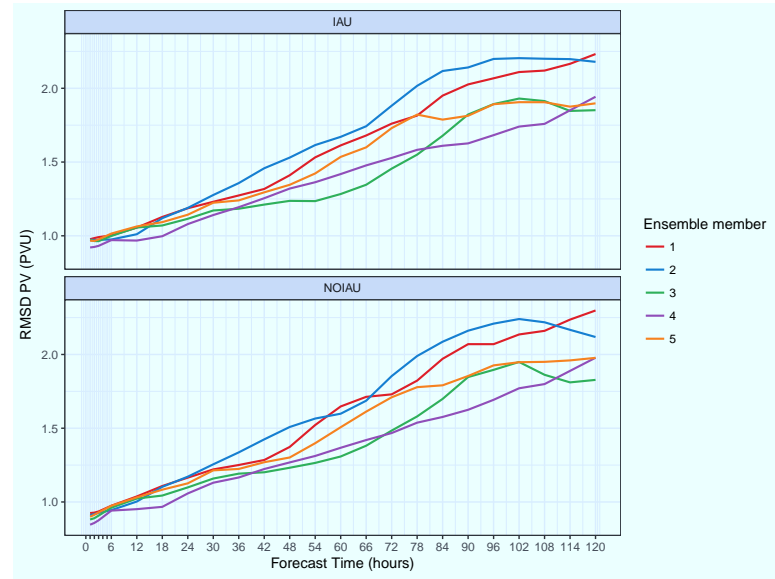
(b)

Figure 6.22: Root mean square difference (RMSD) from 19 UTC 5 July 2012 to 18 UTC 10 July 2012 for (a) PV between the ensemble members and mean of the ensemble at 250 hPa for a subsection over Europe and (b) PV between the ensemble members and the control at 250hPa. NOIAU signifies EN-NOMCS and IAU is EN-MCS.
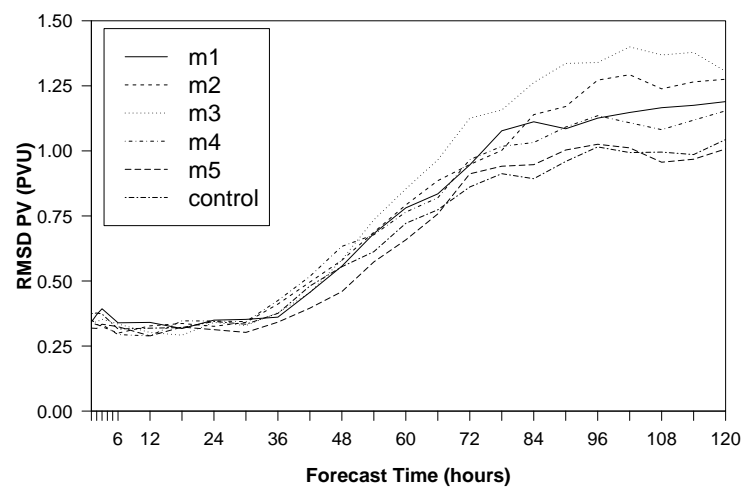
Figure 6.23: RMSD from 19 UTC 5 July 2012 to 18 UTC 10 July 2012 for PV at 250 hPa over the European subsection for member-member comparison EN-MCS–EN-NOMCS.
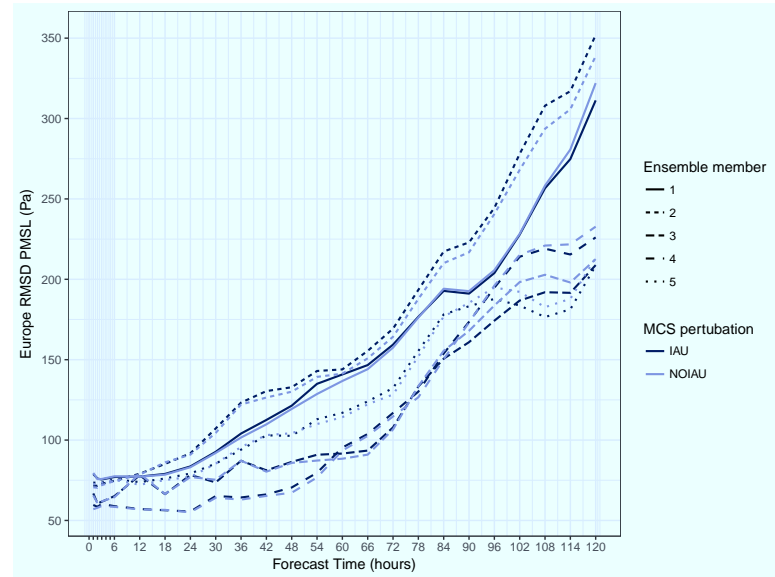
(a)
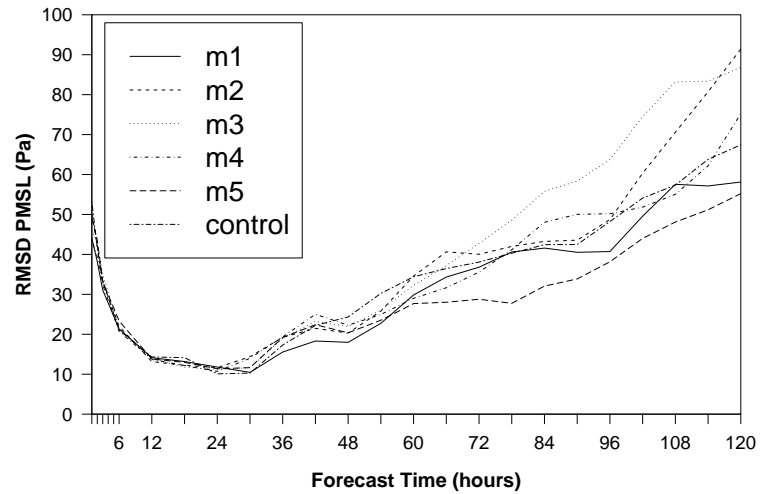
(b)

Figure 6.24: Root mean square difference (RMSD) for differences for (a) PMSL between the members of EN-MCS and EN-NOMCS and the control of each ensemble and (b) The PMSL differences between each of the corresponding members of EN-MCS–EN-NOMCS for the European subsection.
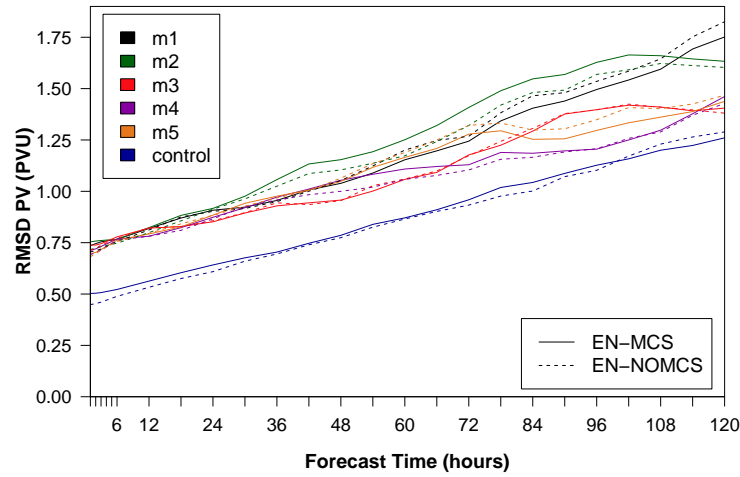
Figure 6.25: Root mean square difference (RMSD) for PV for all 12 members between 00 UTC 6 July 2012 to 18 UTC 10 July 2012 compared to the mean of all ensemble members of both EN-MCS and EN-NOMCS.
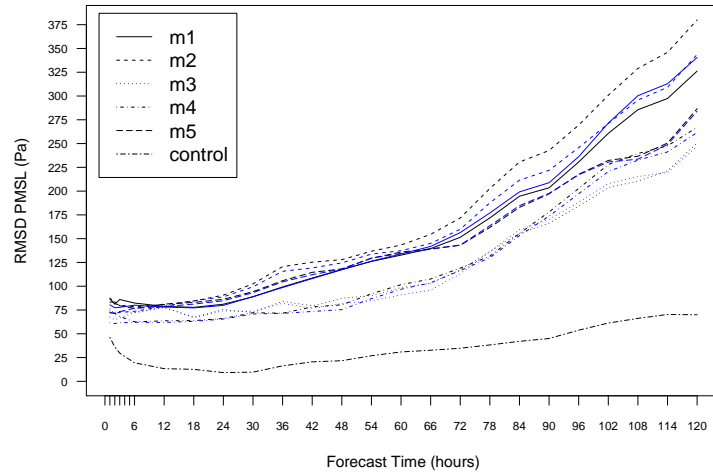
Figure 6.26: Root mean square difference (RMSD) 00 UTC 6 July 2012 to 18 UTC 10 July 2012 PMSL for each member from both EN-NOMCS and EN-MCS compared to the control of EN-NOMCS. Black lines are the EN-MCS members and blue lines are the EN-NOMCS members.

6.4.3 Correspondence ratio

The correspondence ratio (CR) compares all members to each other and is used to measure the spread within an ensemble. CR is discussed in Section 2.5.3. The CR calculations are conducted over the European sub-section used for the RMSD calculations in the previous Section. CR is calculated for PV and precipitation in this Section.

The precipitation CR shows a ratio of approximately 0.05 (at 120 hours; 18 UTC 10 July) for a threshold of 0.1 mmhr^{-1} (Figure 6.27(a) and 6.27(b)) which was the same threshold used by Gebhardt *et al.* (2011) where their CR after 24 hours reached this level. They used a 2.8 km grid spacing model though which is convection permitting and errors have been found to grow ten times quicker in these models than in convection parametrizing models such as the Global model used in this study (Hohenegger and Schlar, 2007) suggesting why it takes until 120 hours into the forecast for the CR to reach this level here. The CR starts off at a low level of approximately 0.2 though due to the grid-spacing of the Global model with lighter rainfall rates that cover a larger area than in the convection-permitting models.

The CR for total precipitation rates of the members of EN-NOMCS (Figure 6.27(a)) and EN-MCS (Figure 6.27(b)) are very similar. Both EN-MCS and EN-NOMCS have peaks and troughs that can be attributed to the diurnal cycle in the CR for precipitation (highest value 0.175 at 00 UTC 6 July; lowest value 0.025 at 18 UTC 10 July 2012 for 0.1mmhr^{-1} threshold). The lowest CR values are found at 18 UTC on each day of the run. The diurnal cycle suggests that the convection scheme is influencing the results by producing more rainfall during the middle of the day (when the effects of surface heating cause the convection scheme to be most active in the model). Despite this diurnal pattern the peaks and troughs the CR do decrease every 24 hours. The similarity between the two ensembles suggests that the spread is not effected by the addition of the MCS perturbations. It is possible that the lack of precipitation in the Global model simulations could limit the usefulness of CR measurements for precipitation during the 120 hour forecast.

The CR for PV greater than 2 PVU at 250 hPa has a value of 0.6 at the start of the simulations, but by 120 hours into the forecast it drops to 0.35 in both EN-MCS and EN-NOMCS (Figure 6.27(c) and 6.27(d)). Again since both EN-MCS and EN-NOMCS have similar CR values for PV it provides further evidence that the overall spread (using this
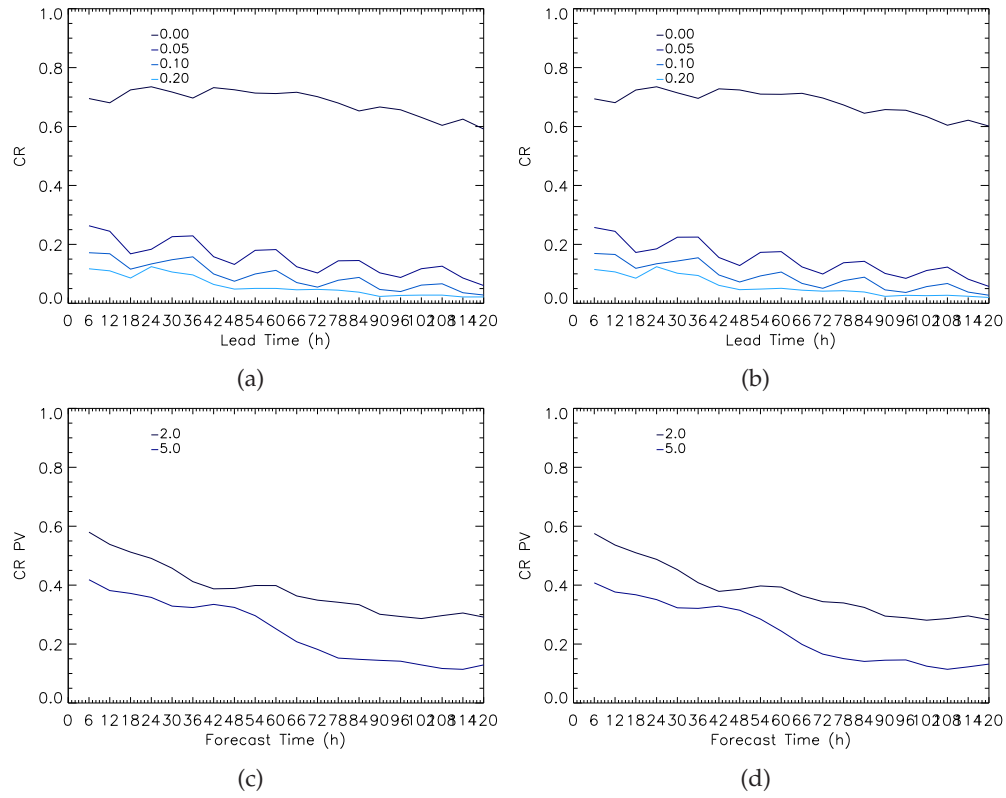
Figure 6.27: Correspondence ratio (CR) for (a),(b) Precipitation rates at thresholds greater than 0 mmhr^{-1}, 0.05 mmhr^{-1}, 0.1 mmhr^{-1} and 0.2 mmhr^{-1} for (a) EN-NOMCS, (b) EN-MCS, (c),(d) PV at 250 hPa using threshold greater than 2 PVU and 5 PVU for (c) EN-NOMCS and (d) EN-MCS. Calculated for the European sub-section.

measure) of the forecasts is not being impacted by the addition of the MCS perturbations. A CR of 0.35 for the 2 PVU threshold by 120 hours suggests that the pattern of PV varies greatly at this level because of differences in the ridge–trough patterns (which can be seen when comparing the members in Figure 6.12(a)–(f)).

Since the CR values are found to not vary between EN-MCS and EN-NOMCS an investigation into the impact on the CR when all 12 members are compared is conducted. A comparison of the CR for EN-MCS (Figure 6.27(b) and 6.27(d)) and EN-NOMCS (Figure 6.27(a) and 6.27(c)) to the 12 member CR (Figure 6.28(a) and 6.28(b)) shows that the CR values for the 12 member comparisons are less at all times in the forecast (showing an increased spread when all members are compared to each other). For the precipitation the CR value for the 0.05 mmhr^{-1} threshold is 0.025 smaller in the 12 member comparison by 120 hours. All thresholds start and end at a value that is approximately 0.025 lower than the corresponding CR for the individual ensembles.

The 12 member PV comparisons show that the 2 PVU threshold has a CR of 0.09

compared to 0.14 in the individual ensemble CR calculations. The conclusion is that the MCS perturbations cause the member–member forecasts to differ but these differences do not impact the spread when EN-MCS and EN-NOMCS are analysed individually. When comparing all 12 members together though these differences between the members have a slight impact on the spread with a CR which is 0.05 less by 5 days into the simulations. The increased spread is due to the MCS perturbations having a systematic effect on the simulations in EN-MCS creating differences in the thermodynamic and dynamical structures in these simulations compared to the members of EN-NOMCS, however, these impacts are far less than the effect that the IC perturbations have on the simulations (similarly found in the RMSD calculations). Therefore, when comparing all 12 members the spread is slightly increased (with CR values reduced by 0.05 after 120 hours) but when comparing the ensembles separately the impact on the spread is minimal since the IC perturbations have more of an impact on the spread than the MCS perturbations.

(a)   (b)
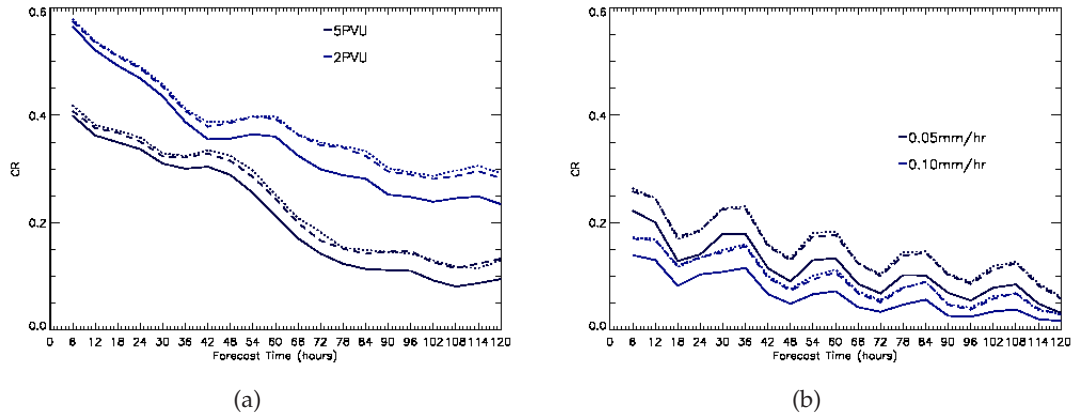
Figure 6.28: Correspondence ratio between all 12 members from both EN-MCS and EN-NOMCS over the European subsection for (a) PV at 250 hPa at threshold greater than 5 PVU and 2 PVU and (b) Total precipitation rates at thresholds greater than 0.05 mmhr^{-1} and 0.1 mmhr^{-1}. Calculated for the European sub-section. Solid lines indicate the CR for all 12 members. Dashed lines are the CR values calculated for EN-MCS and dotted lines indicated CR values for EN-NOMCS.

6.4.4 Fraction of common points

The fraction of common points (FCP) compares one member to another member to determine how well two members of the ensemble compare to each other. FCP is discussed in Section 2.5.3. The FCP calculations are conducted over the European sub-section used for the RMSD calculations in the previous Section. FCP calculations are performed for

precipitation and PV in this Section.

The FCPs values for PV decrease over time, slowly over the first 30 hours and then more rapidly as the variability between members increases (Figure 6.29(a)–(c)). The variability between the member–member comparisons (red lines) is smaller than the variability in the member–control comparisons (blue lines), which was similarly seen in the RMSD calculations. After 72 hours the variability between member–member increases which is important as it is after this time that the low pressure system begins to develop downstream. At the start of the simulations the FCP for the member–member comparisons at 2 PVU is 0.95 and after 120 hours the FCP is 0.8–0.85 (Figure 6.29(b)). This shows that the downstream PV patterns are altered (compared to the corresponding member) by the addition of the MCS perturbations.

The FCP value drops from 0.9 to approximately 0.3 for the member–member comparisons at 500 hPa (1 PVU threshold) suggesting that the MCS perturbations impact the forecasts at this level considerably downstream. At 500 hPa the FCP values for PV drop much more rapidly but this could also be related to the threshold used as at 500 hPa there are not many 1 PVU anomalies to compare (Figure 6.29(c)), after 84 hours the FCP values for some of the the member–control comparisons lines drop below that of the chance line indicating that at this threshold the forecast could have been made by chance with somewhat more accuracy.

The member–member FCP values has a steeper drop than the member–control comparisons however the member–control FCP saturates after 84 hours at 500 hPa. At 500 hPa PV has small-scale features so agreement between members is lost quickly and there are also fewer PV anomalies at this level (hence the chance line also has lower FCP values). The drop in FCP at 500 hPa is also related to the differences in the positioning and depth of the low-pressure centres between members as this impacts the PV anomalies produced at middle levels.

Similar to the RMSD calculation of PV the FCPs suggests that the corresponding members from EN-NOMCS and EN-MCS although different are less different than when comparing each member to the control member of their ensemble (as the F common values are larger for the member–member comparisons; Figure 6.29(a)–(c)). This again provides evidence for the IC perturbations added at the start of the simulation having a greater impact on the forecast spread than the MCS perturbations.

The FCPs for the total precipitation rates suggest there is a diurnal cycle in the rainfall with the lowest FCP correlating to 18 UTC everyday of the forecast and this cycle is repeating every day but has less correspondence at the following days forecast (Figure 6.30(a) and 6.30(b)). The FCP value is lowest when the convection scheme is most active in the Global model (at 18 UTC). Again the FCPs is lower when comparing the members to the control than the member-member comparisons. Unlike for the PV there does not seem to be a slow decrease in FCP value over the first 36 hour due to the diurnal cycle found for the precipitation FCP. The member–control and member–member comparison have larger FCP values than the red chance line indicating that these forecasts are better than what could be made by pure chance related to the number of precipitating points in the forecast.

(a)
(b)

(c)
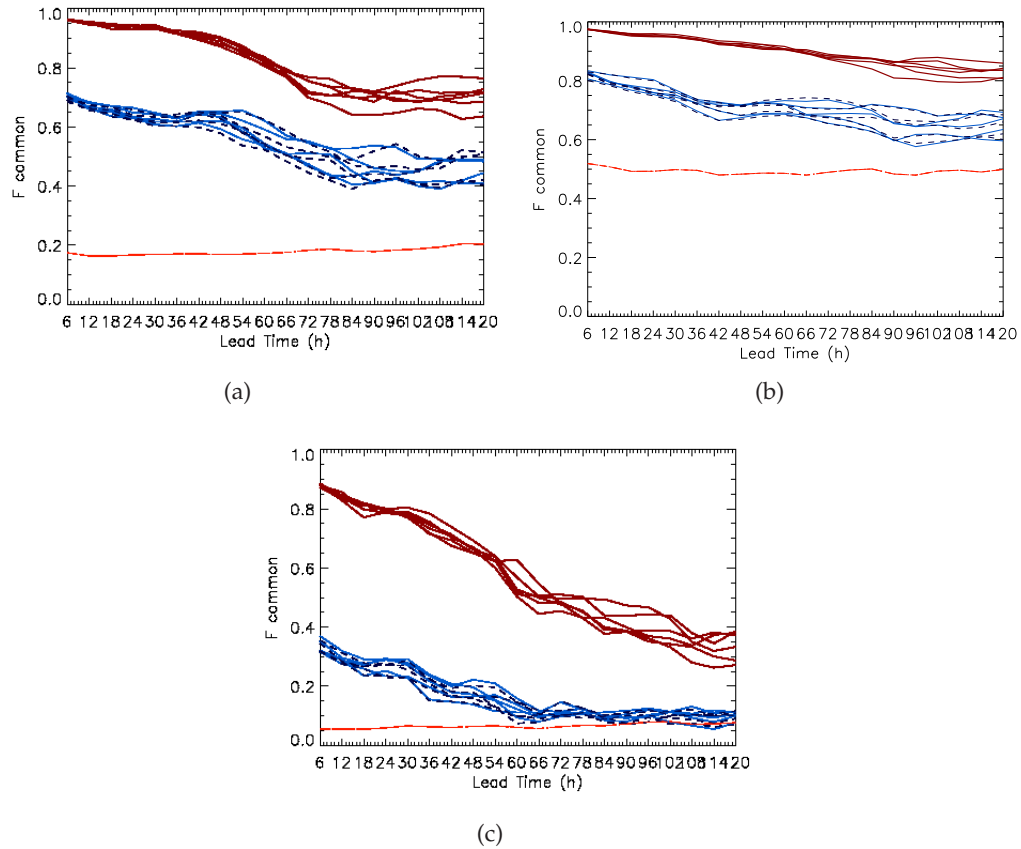
Figure 6.29: Fraction of common points for PV over the European subsection at thresholds (a) greater than 5 PVU for 250 hPa, (b) greater than 2 PVU for 250 hPa and (c) greater than 1 PVU for 500 hPa.The red line is each member from EN-NOMCS compared to the corresponding member of EN-MCS. The blue dashed lines are each ensemble member from EN-NOMCS compared to the control member of EN-NOMCS and the blue solid lines are each ensemble member of EN-MCS compared to the control of EN-MCS. The red line on all panels represents the fraction of points that would be the same in both forecasts through chance based on the number of PV points with that particularly threshold in the control forecast. Calculated for the European sub-section.

(a)

(b)
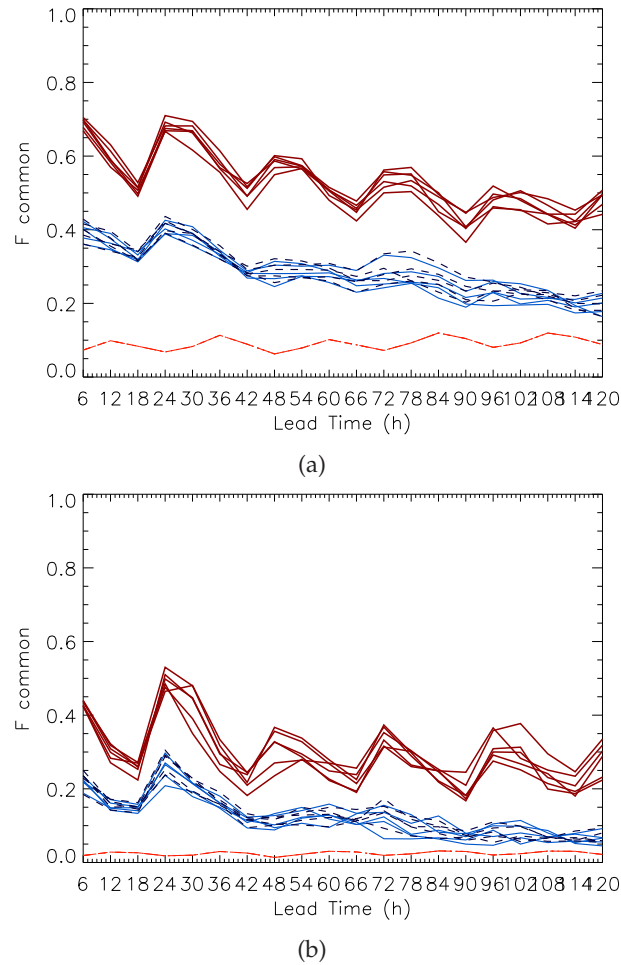
Figure 6.30: Fraction of common points for total rainfall rates over the European subsection for thresholds (a) 0.1 mmhr^{-1} and (b) 1 mmhr^{-1}. The red line is each member from EN-NOMCS compared to the corresponding member of EN-MCS. The blue dashed lines are each ensemble member from EN-NOMCS compared to the control member of EN-NOMCS and the blue solid lines are each ensemble member of EN-MCS compared to the control of EN-MCS. The red line on all panels represents the fraction of points that would be the same in both forecasts through chance based on the number of precipitating points in the control forecast. Calculated for the European sub-section.

6.4.5   Ensemble diagnostics summary

The RMSD, CR and FCP calculations have determined that the control–member comparisons show greater differences than the member–member comparisons showing that the IC perturbations have more of an impact on the forecast than the MCS perturbations. When analysing the members of EN-MCS and EN-NOMCS separately the spread of the ensembles is the same. However, when comparing all 12 members to each other the spread is increased (through a reduction in CR values for PV and precipitation).

Although the IC perturbations have a greater impact on the forecast the MCS perturbations do create noticeable differences between the corresponding members of EN-MCS and EN-NOMCS. These differences (in PV and PMSL; found using RMSD and FCPS) between corresponding members grow slowly over the first 30 hours while growing on the convective scale before a rapid increase occurs when they grow onto the synoptic scale. This suggests including the MCS perturbations leads to further realisations of the downstream forecast that may not be produced without the MCS perturbations included.

6.5   Comparison to forecast analysis

It has been shown in the previous Sections that the perturbations can change the forecasts. The next question is whether this can improve the predictability compared to reality. The predictability of the downstream forecast in Europe has previously been found to be sensitive to any MCSs forecast over the USA (Rodwell *et al.*, 2013). Therefore, it is hypothesised that producing a better representation of an MCS over the UK and France could tend an ensemble towards a better spread of forecasts downstream. To test this a comparison of the PMSL is conducted between the Global analysis from 18 UTC 6 July 2012 to 18 UTC 10 July 2012 and the PMSL of each of the members of EN-MCS and EN-NOMCS. The main focus of the investigation is on the low-pressure centre which developed downstream over northern Russia.

None of the members capture the true extent of how deep the low-pressure centre was (980 hPa) with the lowest centre being 988 hPa in member 1 (Figure 6.31(b)). All of the members of EN-MCS have a low-pressure centre further west than the corresponding member of EN-NOMCS. As a result the members of EN-NOMCS were closer in location (some more so than others) to the centre of the low-pressure from the analysis (and are well positioned in Figure 6.31(d) and (e) but are too weak; hence the MCS perturbations did not improve positioning).

Figure 6.31(a)–(f) shows a comparison of the low-pressure centre (after 120 hours, north of Russia) for the analysis with contours of the low-pressure centre from the corresponding member of EN-MCS (blue contours) and EN-NOMCS (red contours) plotted over the top. The addition of the MCS perturbations deepens the low-pressure centre of the control and members 2 and 4 (member 4 is deepened by 2 hPa; central pressure 994 hPa compared to the EN-NOMCS member with 996 hPa). Member 2 and the control of EN-MCS has a low pressure of 989 hPa in comparison to a central pressure of 992 hPa in the corresponding member of EN-NOMCS. Therefore, the control and member 2 of EN-MCS have a better correspondence to the analysis in terms of the depth of the low (980 hPa). In terms of location, member 1 and 3, of EN-MCS are shifted to the north east in comparison to the members of EN-NOMCS however, the central low-pressure in both of these members is 988 hPa and 992 hPa, respectively in both ensembles, so the depth of the low is unaffected in these members. Both EN-MCS and EN-NOMCS member 5s had low-pressure centres that were too weak (994 hPa in EN-NOMCS and 995 hPa in

EN-MCS) and the positioning was far too south by approximately 1000 km. None of the members of either EN-MCS or EN-NOMCS produce a low-pressure centre which is deep enough or in the correct location compared to the analysis.

In summary, the addition of the MCS perturbations does cause three of the members of EN-MCS to have a deeper low pressure centre (by up to 3 hPa) over northern Russia and the centre is shifted to the west in all members. The low-pressure centres which are deepened in the control, member 2 and member 4 of EN-MCS correspond to the members which created the heaviest rainfall in association with the MCS (Figure 6.7(a),(c) and (e)). The weakest and worst positioned low-pressure system occurs in member 5 which does not represent the northern MCS in either EN-MCS or EN-NOMCS which provides further evidence for the importance of representing the MCS for producing a more successful downstream forecast in this situation. If used operationally these MCS perturbations could have allowed forecasters to determine that the low-pressure centre might plausibly be deeper than the IC perturbation members determined or that the low might have a more varied location.

6.5.1   RMSD calculated against analysis

The low-pressure centre over northern Russia has been shown to differ between the members of EN-MCS and EN-NOMCS but also to the analysis forecast. Therefore, the RMS error values for PMSL for 18 UTC 6 July – 18 UTC 10 July are calculated against the PMSL of the analysis for the European sub-domain (Table 6.1). RMS error calculations are performed to determine whether there is a tendency for forecasts to get closer to the analysis or not through the addition of the MCS perturbations.

Hours	Control member	Member 1	Member 2	Member 3	Member 4	Member 5
24	0.00	-1.29	-1.95	-1.15	-0.74	-1.97
48	0.00	-3.48	-1.91	-2.59	0.00	-0.51
72	-5.79	0.00	-4.07	-1.60	-0.87	-1.23
96	3.49	1.79	-2.86	2.30	1.23	1.23
120	2.27	1.25	-4.62	1.10	0.24	0.22

Table 6.1:: Percentage difference in the RMS error values for PMSL between the members of EN-NOMCS and EN-MCS (calculated by (EN-NOMCS-EN-MCS)÷ EN-NOMCS) for 18 UTC 6 July 2012 to 10 July 2012.

Table 6.1 shows that for all of the members there is a decrease in the RMS error for day 1–3, meaning that the members of EN-MCS gave a worse comparison to the analysis compared to EN-NOMCS members. However, there is an improvement (i.e. reduction) in the RMS error values with the MCS perturbations for day 4 and 5 (giving positive % differences in Table 6.1) into the run (before this time the RMS error is increased). The improvement in the RMS error values in the EN-MCS members on day four and five of the forecast are interesting as it shows that the forecasts all tend to be closer to analysis in the longer range due to the MCS perturbations. The improvement in forecast errors in the EN-MCS members after day 3 is also important as it is after this time that the low pressure system begins to develop downstream. On each of the five days the percentage differences between the members of EN-MCS and EN-NOMCS compared to the analysis are small (maximum of 5.79%) therefore these results although interesting, may not be significant. Table 6.1 shows that there could be a slight beneficial impact on the downstream forecast errors (reduced them after 3 days) by adding MCS perturbations, but further case studies are required.

As discussed earlier, member 2 developed a second low-pressure system (over Kazakhstan, red dashed circle in Figure 6.19(c) and Figure 6.18(c)) that does not form in any of the other members nor the analysis, thus the PMSL varied more in comparison to the other members. Thus, member 2 has the highest RMS error values compared to the other members (Table 6.1). Member 2 of EN-MCS has a worst RMS error value than member 2 of EN-NOMCS (Figure 6.32) and this is due to the low-pressure over Kazakhstan that

is not present in the analysis being deepened further by the addition of the MCS pertur-
bations.

As expected the smallest percentage difference (in RMS error values) between mem-
bers occurs for member 5 due to the lack of representation of the MCS in either members
at the start of the simulation causing less difference growth downstream (Figure 6.32).
The control and member 4 have the smallest RMS errors compared to the analysis (Figure
6.32) with there being a beneficial impact (2.27% and 0.24%, respectively) when including
the MCS perturbations. This is important as these two members have a deepening of the
low-pressure centre downstream over northern Russia due to the inclusion of the MCS
perturbations which made the low more representative of the analysis. However, this
also demonstrates that these ensemble members gave a better representation of analysis
PMSL than the other members regardless of the MCS perturbations being included or
not since there is little difference in the RMS error values of EN-MCS and EN-NOMCS
when compared to the analysis (Figure 6.32). The IC perturbations are therefore very
important on the downstream forecast created, with the MCS perturbations leading to
systematic differences which help to produce further realisations of the forecast.

RMS error values for all 12 members compared to the analysis forecast show that
there is a steady increase in RMS error values and after 5 days there is a maximum
value of 480 hPa (Figure 6.32). This is in line with Bowler *et al.* (2008) that found an
RMS error of 575 Pa after 120 hours (for a 60 km ensemble run with initial condition
perturbations only when comparing forecast to observations). The improved RMS errors
in the MCS perturbed cases indicates that the slower eastward movement created by the
MCS perturbations could reduce the forecast errors and thus increase the predictability
downstream from the MCS.
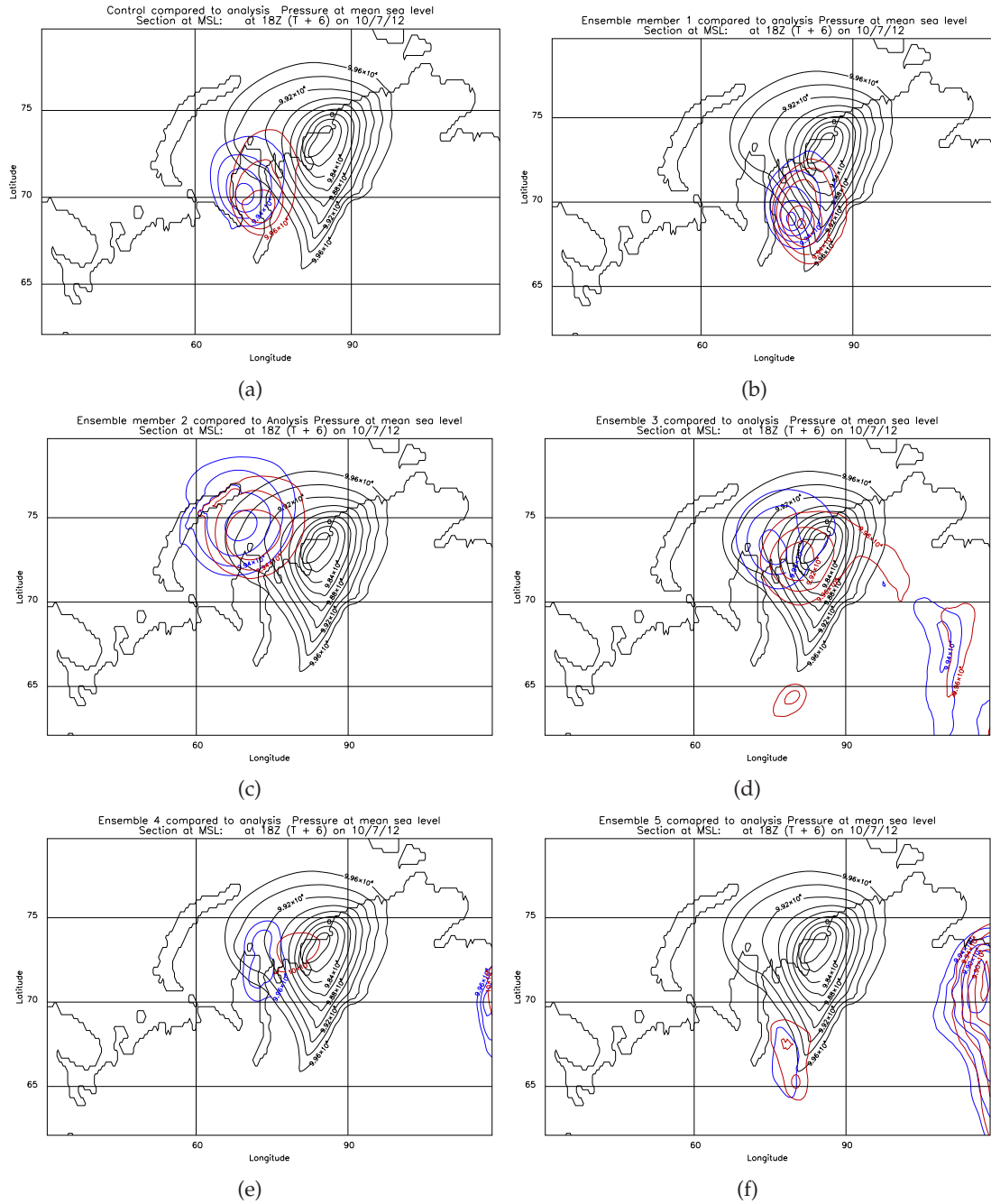
Figure 6.31: Analysis PMSL at 18 UTC 10 July 2012 contours at 980 hPa to 996 hPa every 2 hPa. Each figure has the low pressure centre of each corresponding member of EN-MCS and EN-NOMCS. Blue contours are members of EN-MCS and red contours are the members of EN-NOMCS for (a) control, (b) member 1, (c) member 2, (d) member 3, (e) member 4 and (f) member 5.
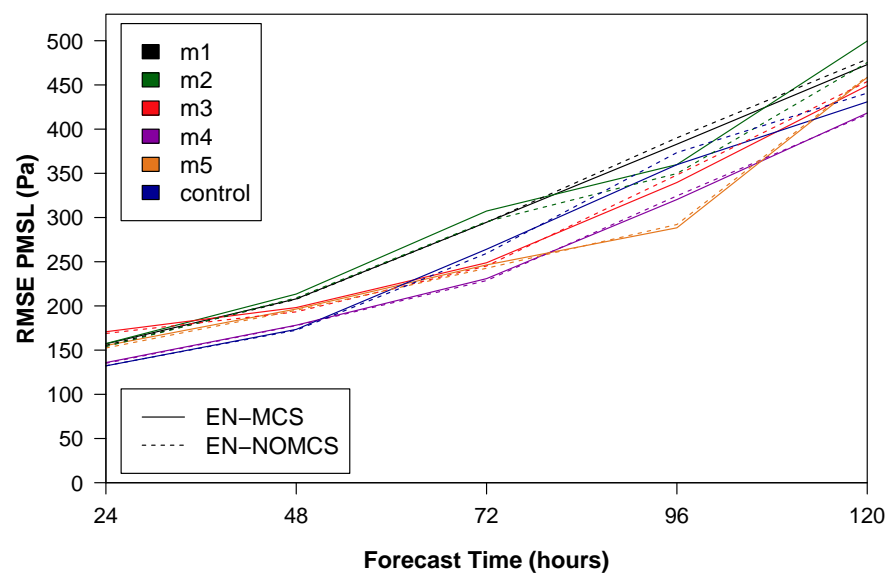
Figure 6.32: Root mean squared error (RMSE) for PMSL 18 UTC 6 July 2012 to 18 UTC 10 July 2012. Each ensemble member from EN-MCS (solid lines) and EN-NOMCS (dashed lines) compared to the analysis (member−analysis).

6.6   Conclusions

This Chapter has examined the impact that PV structures associated with a mature MCS has on the downstream forecast after 5 days by adding MCS perturbations into an ensemble to determine if the results found in Chapter 5 are robust. The aim of the Chapter was to answer the question posed in Section 1.1: How does the representation of an MCS affect forecast evolution and forecast skill (compared to analysis) for the synoptic-scale forecast downstream from the MCS? To answer this question the hypothesis from Section 5.1.1 (investigated in Chapter 5) was expanded to include a further two hypotheses described in Section 6.1. The conclusions of this Chapter will now be discussed in terms of the hypotheses posed.

Hypothesis: The MCS perturbations have a consistent impact on the forecast evolution (in an ensemble).

Previous studies have looked at the impact of perturbations on the synoptic scale or in cyclones and tropical cyclones (Grams and Archambault, 2016; Beare *et al.*, 2003; Quinting and Jones, 2016) but have never specifically studied the impact that perturbations related to mesoscale, thunderstorm structures may have on the downstream forecast. Similarly to what was found in Chapter 5 for one simulation, for an ensemble simulation these MCS perturbations have been shown to cause differences (in PV, PMSL and windspeeds). These differences in PV, PMSL and windspeed initially grow on the convective scale associated with the MCS and the UK cyclone before growing to impact the synoptic scale (entire northern hemisphere) downstream after 5 days. The differences in PV, PMSL and windspeeds follow synoptic scale patterns of ridges and troughs, with most of the differences occurring along ridge boundaries.

MCS perturbations cause differences in the thermodynamic and dynamical structures compared to the simulations without perturbations (in terms of PV, windspeed, geopotential height, PMSL and potential temperature). These differences initially grow on the convective scale associated with where they are added to the model (where the two MCSs are occurring) and then impact the cyclone which formed over the UK on 6 July (this was also found in Chapter 5). For the first 30 hours the magnitude of the differences in PMSL decrease as the simulations react to the MCS perturbations by dampening them out (for PV the differences remain fairly constant for the first 30–36 hours). After

this time the spatial area of influence of the differences grows from influencing the UK and France to impacting Scandinavia by 48 hours as the differences are carried along a Rossby wave guide downstream of where the MCS perturbations are initially introduced to the simulation. Similarly to Tan *et al.* (2004) and Zhang *et al.* (2003) who studied error growth for convection parametrized models, it has been shown that errors grow slowly at first over the first 30 hours of the forecast before increasing steadily following the same 3 stage difference growth that they found. By 120 hours into the forecast the differences cover the entire northern hemisphere, with the largest differences occurring at a ridge boundary over eastern Europe.

As was found in Chapter 5 for a deterministic simulation, in the ensemble simulations with the MCS perturbations the eastward movement is slower, with each member of EN-MCS having a low pressure centre over northern Russia after 5 days further west than in the corresponding EN-NOMCS members (Figure 6.31(a)–(f)). This slower eastward movement is due to the MCS perturbations creating a stronger gradient in PV at the ridge boundaries which amplifies the ridges to the north west and accelerates the jet streak. Low-PV air is injected higher up into the troposphere in the ridge changing the circulation patterns and strengthening the divergent outflow which amplifies the ridge causing the slower eastward progression. This was similarly found by Grams and Archambault (2016), Quinting and Jones (2016) and Riemer *et al.* (2008) when studying the impact of tropical cyclones in model simulations by comparing against similar simulations with the tropical cyclone removed.

Rodwell *et al.* (2013) also noted that MCSs (and diabatic physics) play an active role in the evolution of the synoptic-scale trough slowing down the eastward progression of the wave. Bosart and Lackmann (1995) when studying Hurricane David that impacted the USA in 1979 described "tropopause uplifting" associated with diabatic and advective warming. As the gradient in PV is strengthened at the ridge boundary the largest differences in PV downstream were collocated with the location of the ridge boundary between the members of EN-MCS and EN-NOMCS. This created negative PV differences along the ridge boundaries showing that the lower-PV air is amplified further north west in the EN-MCS members along with the PV being lower or more negative in these members than in the EN-NOMCS members. These negative PV differences were also found by Grams and Archambault (2016) and the magnitude of these differences is similar to

this study with them finding a maximum negative difference of 7 PVU after 108 hours, whereas here 10 PVU differences were found after 120 hours. The spatial scale of these negative PV differences is similar as well.

Adding MCS perturbations leads to the deepening of the low pressure system downstream over northern Russia after 5 days (by up to 3 hPa) in some members (control, member 2 and 4) similarly as to Gray (2001). This deepening occurs in members where the MCS produced in the model due to the MCS perturbations added is strongest (in terms of precipitation and PV) with the simulations having the largest amount of rainfall associated with the two MCSs (Figure 6.7(a),(c) and (e); and greatest difference between the members of EN-NOMCS in terms of amount of rainfall). In other members (member 1 and 3) the low pressure is shifted to the west due to the MCS perturbations. In member 5 the low pressure centre was less deep (994 hPa in EN-NOMCS and 995 hPa in EN-MCS) and was located too far south in both simulations. The effect of convection and moist processes created by the MCS perturbations has the biggest impact on the growth of the differences over time. In members where a strong MCS was created (in terms of heavier rainfall than in the corresponding member without the MCS perturbations) the differences grew largest. In the member where no MCS was created in either the perturbed or unperturbed forecast (member 5) there were fewer differences (in terms of PV, PMSL and windspeed) after five days. This has been found in previous studies; Zhang *et al.* (2003) and Tan *et al.* (2004) found that lack of moisture due to there being little or no convective activity led to smaller error growth. Therefore, the effects of moisture have been found to create a larger growth of differences downstream.

Differences have been found to persist downstream from the initial MCS and change the forecast of the low-pressure system downstream this could have an impact on the forecasting downstream; Rodwell *et al.* (2013) found that UK and European forecast busts are created due to the poor forecasting of MCSs in the USA. The addition of MCS perturbations into the ensemble forecast could thus have a beneficial effect on the downstream forecast. When the MCS is not represented in the simulations (member 5 of EN-MCS and EN-NOMCS) the low-pressure centre forms too far south and was not as deep compared to the analysis (by up to 15 hPa where the low pressure centre forms; 995 hPa compared to 980 hPa in the analysis) but there was less variation between the location of the low pressure centre between the members of EN-NOMCS and EN-MCS in this case. This is

consistent with the findings of Rodwell *et al.* (2013) that found poor forecasts of MCSs over the USA caused forecast busts downstream in Europe in the days ahead. This provides evidence for the importance of representing the MCS on producing a successful downstream forecast as the other members which eventually produce an MCS have the cyclone in a better location downstream. None of the 12 members produce as deep a low pressure centre as the analysis shows though (988 hPa was the deepest pressure in member 1 of EN-MCS compared with 980 hPa in the analysis). However, the addition of the MCS perturbations deepens the low-pressure centre over northern Russia downstream giving a better comparison of the depth to the analysis than without the MCS perturbations.

Hypothesis: The MCS perturbations lead to enhanced ensemble spread compared to the corresponding initial condition perturbation ensemble and/or new forecast evolutions.

There are clear differences (in PV, PMSL and windspeed as well as an increase in RMSD values over time) between the corresponding members from EN-MCS and EN-NOMCS showing that the MCS perturbations create different forecast evolutions. Although different realisations of the forecast are produced through the addition of the MCS perturbations there is little impact on the variability of the ensemble from adding the MCS perturbations shown through the range of RMSD values remaining similar between both ensembles. This suggests that the addition of the MCS perturbations creates a systematic effect on the model in that it leads to differences that grow due to the convection and associated circulation patterns. However, these systematic changes are relatively small in comparison to the impact on the forecast evolution arising from the IC perturbations. The RMSD member–member comparison values saturate after 5 days for PV but not PMSL due to PV being an inherently noisy field. PV is a noisy and small-scale field so small differences in PV that occur at the start of the simulation do not produce larger RMSD values as the differences move further apart. PMSL on the other hand has RMSD values that continue to grow over time as it is a less noisy and is a large-scale field so overlap occurs to begin with so as differences grow over time separation occurs causing RMSD values to continually grow. When comparing all 12 members to each other the variability in RMSD values (for member–ensemble mean comparison) is shown to increase by 0.05 PVU (at 18 UTC 10 July) which is approximately a 10% increase in the

range when the members of EN-MCS and EN-NOMCS are compared separately.

The CR for PV and precipitation are lower (by 0.025) when comparing all 12 members to each other instead of the members of EN-NOMCS and EN-MCS separately showing that the MCS perturbations create a slightly larger spread overall when comparing all members together. The increased spread created by the MCS perturbations could be useful for operational ensemble forecasting since these forecasts often do not have a large enough spread to include important potential realisations of the forecast, particularly of extreme events. Comparing all 12 members shows that there are more possible forecast outcomes with the MCS perturbations than without them since there is an increased spread in CR.

FCP calculations show that the ensemble members are more similar to the corresponding member from the other ensemble (EN-MCS members compared to EN-NOMCS) than to their respective control showing that the IC perturbations cause more differences between the forecasts than the MCS perturbations. FCP calculations show that similarly to RMSD, PV saturates by 5 days. For FCP calculations at 500 hPa at a threshold of 1 PVU the member–control comparisons saturate to a point where the differences between the forecast become equivalent to comparing to random forecasts.

When comparing the forecasts to the corresponding analyses, RMS error values are reduced (for 5 of the 6 members) by the addition of the MCS perturbations but only slightly (after 3 days; 2.27% maximum; Table 6.1). This reduction is sensitive to the IC perturbations that were initially used with the member of the ensemble which most closely matches the analysis (the control, with or without MCS perturbations) giving the most improvements in RMS error value when the MCS perturbations are included (2.27%). This beneficial impact on forecast errors suggests that the slower eastward movement of the ridges in the members of EN-MCS yields a beneficial impact on the forecast downstream (in terms of PMSL). These percentage differences in RMSD between the members of EN-MCS and EN-NOMCS compared to the analysis are small throughout the 5 day forecast though. Thus, more case studies are required before it can be concluded that these MCS perturbations improve the downstream forecast predictability.

In summary, the MCS perturbations create differences in PV, PMSL and windspeed downstream that grow on the convective scale, over the first 30 hours around the MCS

and UK cyclone, before growing rapidly onto the synoptic scale to cover the entire north-
ern hemisphere after 5 days. The main differences in PV, PMSL and windspeeds develop
along Rossby wave ridges as the greater amount (and larger magnitude) of negative PV
anomalies at tropopause level in the MCS perturbations members leads to an amplifi-
cation of the ridges which consequently slows down the eastward movement in these
members. The MCS perturbations, thus, produce further realisations of the downstream
forecast which could be beneficial to operational forecasting, along with slightly increas-
ing the ensemble spread.

Chapter 7

Conclusions and future work

7.1 Conclusions

This thesis has been aimed at determining how convection associated with MCSs is represented in convection-permitting and convection-parametrizing models and the impact that differences in the representation of the MCS (between the convection-permitting and convection-parametrizing models) has on the downstream forecast. Three main questions have been studied:

1. What are the mesoscale and synoptic-scale structures of PV anomalies generated by MCSs?

2. How is the forecasting of MCSs affected by the representation of convection in NWP models (whether convection is parametrized or permitted by the model) and what are the associated PV structures produced?

3. How does the representation of an MCS affect forecast evolution and forecast skill (compared to analysis) for the synoptic-scale forecast downstream from the MCS?

This thesis has been split into four research Chapters. Chapter 3 and 4 investigated questions 1 and 2, respectively. Chapter 5 and 6 both investigated the third question. The conclusions from each Chapter based on the questions posed above will now be discussed before the contributions of this thesis and implications to the field are presented. Finally some ideas for potential future work are discussed.

7.1.1 Case studies

Chapter 3 investigated Question 1 from 7.1 using four MCS case studies. These four case studies reveal that for UK and western European MCSs the PV structure differs (Figure 3.30) to those documented in the USA (Fritsch *et al.*, 1994; Houze, 2004). The main

difference in the PV anomaly structure is that in the MCSs in this study a negative PV anomaly forms above the middle level positive PV and is spread either side of the positive PV anomaly. Each of the four case studies had a horizontal extent of 60 km which is much less than the larger 250 km suggested by Houze (2004), but MCSs occurring in USA tend to have stronger CAPE associated with them than those that occur in western Europe so are likely to impact a larger area. This can also lead to weaker convection (and less deep) in these European MCSs which could account for the weaker divergent outflow of negative PV at upper-levels than in USA MCSs.

Each case study had a maximum positive PV anomaly of 4–5 PVU at 500–600 hPa and negative PV anomalies above and to the side of this positive PV anomaly of -1.5 PVU above 500 hPa and up to the tropopause (approximately 250 hPa). All four cases occurred in a Spanish plume type environment in which a layer of warm dry air is advected north-eastwards from the Spanish plateau ahead of a synoptic-scale upper-level trough to the east of the UK and/or France causing moist air to be trapped below a layer of dry air. The level at which the dry air occurred varied between the cases though but all of the cases had convection which triggered after an increase in CAPE over several hours due to forced ascent through positive vorticity advection associated with the upper-level trough and low-level warm advection.

The 5 July 2012 case was chosen as the principle case to investigate for the rest of the thesis because two MCSs developed (both triggering over the south of France). The MCS which impacted the southeast UK is then affected by the development of a cyclone on 6 July 2012 over the UK. The impact of the representation of this MCS on the subsequent forecast of the cyclone therefore became a question to address with the research.

7.1.2 Representation of MCSs and associated PV structures in convection-permitting and convection-parametrizing NWP models

Chapter 4 investigated Question 2 from 7.1 using the case study from 5 July 2012. To examine this question the MetUM was used to simulate a convection-parametrizing Global model and convection-permitting Euro 4 km, UKV and France 1.5 km models for a 24 hour forecast period (00 UTC 5 July 2012 to 00 UTC 6 July 2012) for the 5 July 2012 case study.

The Global model failed to represent the MCS at its mature stage (18 UTC) even

though it did produce rainfall at the time of triggering (convection and rainfall seen at 09 UTC). It is thought this could be because the Global model may have removed the instability too quickly (or did not have enough instability) from the convection scheme and the convection scheme was inherently unable to model the upscale development of the MCS. The UKV model produces an MCS too early because convection formed very close to the southern boundary causing the location of the MCS to be too far west by 18 UTC. Negative PV anomalies also occurred at 250 hPa level over the east coast of the UK at 18 UTC which did not occur in the other simulations as they were further east still. This meant that the rainfall produced in the UKV model was too far west in comparison to reality and windspeeds were altered.

The MetUM was configured with a domain covering France with a 1.5 km grid spacing. The France 1.5 km simulation of the 5 July 2012 case was to encompass the area over which the MCS initially developed in the south of France as well as where it matures further north. The purpose of this France 1.5 km simulation was to examine whether an extension of the high resolution domain over which the MCS develops improves the forecast of the MCS, in comparison to the UKV model, which has the same resolution but misses the initial development of the MCS because its domain does not extend into southern France.

The MCSs produced by the convection-permitting simulations (Euro 4 km, France 1.5 km and UKV) produce stronger windspeeds, precipitation and larger negative and positive PV anomalies in association with the MCS in comparison to the MCS produced in the convection-parametrizing Global simulation. The convection-permitting models create heavier precipitation (by up to 20 mmhr^{-1}) due to their finer representation of convection (because the effect of convection is not averaged over an entire grid box unlike in the convection-parametrizing simulations). Hence individual storms can be represented leading to stronger updraughts and hence stronger windspeeds and associated PV anomalies. The convection-permitting models create smaller cells of rainfall (due to the more localised representation of convection). Here it was found that the Euro 4 km creates large cells of intense precipitation whereas the 1.5 km models produce cells that are too small. These findings were also found in previous studies (Lean *et al.*, 2008; Barrett *et al.*, 2016). The France 1.5 km model was found to have a better representation of the rainfall produced by the MCS in terms of location and magnitude compared to the

UKV model when looking at rainfall radar.

Convection-permitting models create greater magnitude upper-tropospheric (250 hPa) negative PV (lowest-value PV: UKV; -15 PVU, France 1.5 km; -15 PVU, Euro 4 km: -15 PVU) than the convection-parametrizing models (Global; 0 PVU). Convection-permitting models also create higher magnitude positive PV anomalies at middle-levels and tropopause level (France 1.5 km; 24 PVU, Euro 4 km 24 PVU, UKV; 18 PVU) in comparison to the convection-parametrizing models (Global; 4 PVU, NAE; 5 PVU). These stronger positive and negative PV anomalies in the convection-permitting configurations are a consequence of the explicit representation of convection on the grid.

The higher magnitude negative and positive PV anomalies still persist after coarse graining the convection-permitting simulations to 100 km and comparing the results to the convection-parametrizing Global simulation once also coarse grained to 100 km resolution. Differences in the PV structures between models will have an associated impact on the circulation patterns due to their influence on the static stability and larger scale circulation patterns (Gray, 2001). The representation of convection between the convection-permitting and convection-parametrizing simulations related to the MCS produce the largest differences in PV after coarse graining at tropopause level (up to 5 PVU difference at 250 hPa–350 hPa). The large differences in PV at upper-levels between the convection-permitting and convection-parametrizing models are due to negative PV anomalies produced in the convection-permitting models persisting after coarse graining (although reduced to -1 PVU from -15 PVU) which do not occur in the Global model. These negative PV anomalies in the coarse grained convection-permitting simulations are associated with differences in the windspeed, potential temperature and geopotential height (up to 24 m difference in geopotential height, 5.5 K in θ and 12 ms^{-1} in windspeed by 18 UTC) between these simulations and the Global model.

The pattern and structure of PV distributions at tropopause elevations is the key to achieving a successful forecast in some cases (Fehlmann and Davies, 1997) as it is this level which influences the downstream forecast most. The PV distributions at tropopause level have been found to be important after coarse graining since stronger magnitude negative PV anomalies still occur in the convection-permitting models which have associated impacts on the circulation patterns and potential temperature. These stronger negative PV anomalies cause the upper-level trough to develop further west

than in the convection-parametrizing models (and there is a north-westerly flow associated with the MCS, compared to a northerly flow in the Global model) due to ridge amplification in the convection-permitting models. The negative PV at upper-levels in the convection-permitting simulations generate different associated wind and temperature perturbations than in the convection-parametrizing simulations. At upper-levels the background winds are also stronger than at middle-levels where the positive PV anomalies are produced therefore there is a larger impact on the downstream flow due to the gravity waves moving away from the perturbations produced by the anomaly quicker at upper-levels.

Differences in PV, windspeed, rainfall and geopotential height between the convection-permitting and convection-parametrizing simulations grow in magnitude and spatial area from triggering at 09 UTC 5 July to 18 UTC 5 July. These differences initially grow at the convective scale where the two MCSs develop/mature in the simulations due to localised diabatic heating and moisture forcing the differences to grow (Zhang *et al.*, 2003). These convective scale differences have been found in previous studies to grow 10 times quicker in convection-permitting simulations than in convection-parametrizing simulations (Hohenegger and Schlar, 2007) suggesting that any differences between the Global model and the Euro 4 km, France 1.5 km and UKV simulations relating to the representation of the MCS could lead to large magnitude differences between the forecasts after a short amount of time.

For this case study, the Global model does not represent the MCS at 18 UTC whereas the convection-permitting simulations do. Once the convection-permitting simulations are coarse grained they still represent the MCS while the coarse grained Global model does not. This accounts for most of the differences in PV, geopotential height, rainfall and windspeeds that develop showing the importance of the ability to represent moist processes on error growth between simulations. It is these moist weather phenomena (such as MCSs) that have been shown to lead to large-scale flow modification of the Rossby wave pattern creating the potential for forecast busts (Rodwell *et al.*, 2013; Davies and Didone, 2013; Teubler and Riemer, 2016). Hence, the Global model is missing important processes.

The PV structure of the MCS is better represented by the coarse grained convection-permitting simulations than the convection-parametrizing simulation (represents the

low–negative PV at upper-levels). Due to the improved representation of PV in the convection-permitting simulations an MCS develops in these simulations even after coarse graining which does not develop in the Global simulation. Thus, as was found by Gray (2001) and Fehlmann and Davies (1997), the addition of these PV structures into the simulation which misrepresents the MCS and associated PV structure may have a beneficial impact on the forecast. Adding coarse grained convection-permitting PV structures associated with the MCS into the convection-parametrizing model may help produce a better representation of the downstream forecast (Rodwell *et al.*, 2013). Therefore, determining the impact that convection-permitting PV anomalies associated with MCSs have on the downstream forecast in convection-parametrizing simulations became the next question to address.

7.1.3 Downstream influence of MCSs in NWP models: deterministic simulations

Chapter 5 investigated Question 3 from 7.1. MCS perturbations of potential temperature (θ), zonal wind (u) and meridional wind (u) were calculated at 18 UTC as the difference between the coarse grained Euro 4 km model (averaged to 25 km grid spacing) and the Global model. The variables θ, u and v winds are used as perturbations to account for changes to the environmental flow due to PV anomalies which form in association with the MCS. MCS perturbations are calculated at 18 UTC when the MCS was mature to take into account the difference in the PV structures associated with the MCS, between the convection-permitting (Euro 4 km model) and convection-parametrizing (Global model) models. MCS perturbations were calculated for all model vertical levels, just upper levels (250 hPa–350 hPa), middle levels (450 hPa–750 hPa) and upper levels multiplied by a factor of three to investigate the implications on the downstream forecast depending on what vertical levels the perturbations are added. These MCS perturbations were added to the Global model (at T+18; when the MCS was mature) to investigate what impact the difference in PV structures associated with the MCS (which in Chapter 4 were found to persist after coarse graining the convection-permitting models) between the coarse grained Euro 4 km and Global models has on the downstream flow over a 5 day forecast.

The largest influence on the downstream forecast occurred when MCS perturbations

were added over all model vertical levels (instead of just at upper levels of 350 hPa–250 hPa or middle levels of 750 hPa–450 hPa). The perturbations at upper levels had more influence on the growth of differences in PV, geopotential height and PMSL than the perturbations added at middle levels though because of their impact on the tropopause-level winds. The perturbations added at upper-levels were larger magnitude though so this may have had an impact. The amplitude of the perturbations added had an impact on the magnitude of the differences downstream. However, the location of sensitivity to PV can be different to the amplitude of PV (Beare *et al.*, 2003) therefore this may be an important factor on the results and would be interesting to investigate in future work. Pomroy and Thorpe (2000) found that upper-level negative PV anomalies induce larger perturbations in wind and temperature than lower-tropospheric positive PV anomalies. These larger induced perturbations in wind and temperature (anticyclonic circulations and cold anomaly) associated with the negative PV anomaly is thus the likely reason why upper-level negative PV anomalies associated with the MCS produce larger difference growth downstream than the positive PV anomalies at middle-levels produce. In addition to this the background winds at upper-levels are stronger than at middle-levels due to the jet stream and this will cause differences at this level to grow more quickly away from the initial perturbations.

When the MCS perturbations were multiplied by a factor of 3, differences downstream were larger. The spatial influence of the differences (in PV, PMSL, windspeed) is not affected by the MCS perturbations used. The growth of differences downstream in geopotential height perturbations has a resemblance to Figure 5 of Beare *et al.* (2003) with negative and positive differences developing around the area where perturbations are added which grow in spatial scale and magnitude away from the initial input area. When MCS perturbations were added at all levels the MCS and UK cyclone were best represented in terms of magnitude and location of precipitation.

Differences (in PV, PMSL, geopotential height, windspeeds) between the perturbed and unperturbed simulations grow slowly over the first 30 hours (seen in RMSD calculations of PV and PMSL) due to the model's reaction to the addition of the MCS perturbations by dampening them out. This slow growth in RMSD values (for PV and PMSL) over the first 30 hours in convection-parametrized model was also found by Tan *et al.* (2004) and Zhang *et al.* (2003). Initially differences grow on the convective-scale sur-

rounding the MCS and cyclone over the UK. The differences then grow more rapidly and spread onto the synoptic scale and by 5 days into the simulation affect the entire northern hemisphere, with differences at upper levels developing along ridge boundaries. Each simulation with MCS perturbations included had a slower eastward progression downstream compared to the unperturbed simulation with the magnitude of the perturbations having an impact on how slow the eastward progression is.

7.1.4 Downstream influence of MCS perturbations: ensemble simulations

Chapter 6 continued the investigation of Question 3. from 7.1. To continue this investigation an ensemble approach was developed whereby two ensembles were produced. One with initial condition perturbations (EN-NOMCS) and the other with initial condition perturbations and MCS perturbations (EN-MCS). In Chapter 5 MCS perturbations added over all model levels were shown to give the best representation of the MCS and UK cyclone, along with a larger difference growth downstream. Therefore, MCS perturbations were added at all model levels in this Chapter. Both ensembles were simulated for a 5 day period.

All of the members of EN-MCS and EN-NOMCS created differing forecasts in terms of PV, precipitation, windspeed and PMSL. The differences (in PV, PMSL and windspeeds) between corresponding members of EN-MCS and EN-NOMCS were smaller than the differences in the members of the individual ensembles showing that the IC perturbations cause more of an impact on the forecast than the MCS perturbations. The MCS perturbations lead to an improved representation of the rainfall associated with the MCS (on 5 July) and the cyclone (on 6 July) in terms of location and amount in the members of EN-MCS in comparison to the members of EN-NOMCS (except member 5 does not produce the MCS). Differences between the corresponding members of EN-MCS and EN-NOMCS grow slowly for the first 30 hours (for PV and PMSL) as they grow on the convective-scale associated with the two MCSs and the UK cyclone.

After 30 hours differences grow rapidly onto the synoptic scale to cover the whole northern hemisphere by 5 days. In some members the differences (in PV, PMSL and windspeed) grow to larger magnitude (after 5 days) seeming to be dependant on the representation of the MCS and UK cyclone on the first day of the forecast with member 5 having the smallest difference growth due to not representing the MCS on 5 July in either

EN-MCS or EN-NOMCS (showing the importance of moist processes on the growth of errors). PV anomalies are known to impact on the levels below or above them by action at a distance therefore the mid-level PV anomalies impact on the upper-levels and the upper-level anomalies impact on the mid-levels.

The differences in PV, windspeed and PMSL created between the members of EN-MCS and EN-NOMCS are collocated to the location of the upper-level Rossby wave ridges. The MCS perturbations lead to a strengthening of the PV gradient at the boundary of the ridge, creating negative PV differences at this level (up to 7 PVU), and divergent outflow created by diabatically generated ascent and associated latent heat release (Grams and Archambault, 2016) due to the convection in the MCSs. The ridges in EN-MCS are also amplified to the north west accounting for the slower eastward progression of the weather systems in the members of EN-MCS. This slower eastward progression and ridge building was also found in Grams and Archambault (2016), Quinting and Jones (2016) and Riemer *et al.* (2008) related to tropical cyclones and extratropical cyclones.

In all members of EN-MCS the low-pressure system that develops to the north of Russia over the Kara sea after 5 days is shifted to the west in comparison to the members of EN-NOMCS, giving the members of EN-MCS worst positioning when compared to analysis. In three of the members the low-pressure centre is also deepened downstream from the MCS compared to the EN-NOMCS member (by up to 3 hPa; low of 989 hPa) which produces a more realistic central pressure to the analysis (980 hPa). This improvement in the depth of the low-pressure centre in these members of EN-MCS suggests that adding these MCS perturbations could be beneficial on the downstream forecast by improving the predictability. These three members had the best representation (in terms of location and amount of rainfall in comparison to radar) of both the MCS and cyclone which occurred on 5 and 6 July, respectively and was improved over the forecast produced by the corresponding member of EN-NOMCS. These members of EN-MCS also produced the most rainfall in association with the two MCSs occurring on 5 July suggesting the importance of moist processes on the development of downstream differences. The slower eastward movement of the low-pressure centre in the members of EN-MCS is due to lower-PV air at upper-levels leading to a higher tropopause height in these members due to diabatic outflow and ridge building.

Member 5 of both EN-NOMCS and EN-MCS does not represent the MCS at all (no rainfall produced). This leads to the smallest differences in PV, windspeeds and PMSL after 120 hours due to the lack of convective activity as the differences are initialised. This has been found in previous studies by Zhang *et al.* (2003) and Tan *et al.* (2004) who found that lack of moisture due to there being little or no convective activity led to smaller error growth. The low pressure centre of member 5 of EN-NOMCS and EN-MCS is not as deep as the other members (995 hPa) and is located too far south in comparison to not only the other members of EN-MCS and EN-NOMCS but also to the analysis. Representing the MCS is therefore an important influence on the downstream forecast of the low pressure centre 120 hours ahead (similar results were found by Rodwell *et al.* (2013) and Gray (2001)).

The RMSD values (for PV and PMSL) between EN-NOMCS and EN-MCS is similar when comparing the members to the control of each ensemble. When comparing members of EN-MCS to members of EN-NOMCS there are large differences in RMSD (up to 0.9 hPa PMSL and 1.3 PVU PV) but these differences in RMSD are smaller than when comparing the member to the control (maximum RMSD values of 2.25 PVU PV and 3.5 hPa PMSL). The MCS perturbations therefore create fewer differences between the simulations than the IC perturbations. Comparing all 12 members to each other shows that the variability is increased (in terms of RMSD) compared to the variability for the members of EN-MCS and EN-NOMCS separately, especially when comparing all members to the control of EN-NOMCS which increases the variability by approximately 1.5 hPa for PMSL. The largest variability in member–member comparisons of PMSL is found in the three members that deepen the low-pressure system downsteam due to the better representation of the MCS in the EN-MCS members. The RMSD and FCP calculations for PV saturate after 5 days due to it being a noisier field whereas PMSL does not saturate after 5 days.

Including MCS perturbations could improve ensemble forecasting of downstream events by increasing the ensemble spread (found a reduction in CR values when all 12 members are compared) and increasing the amount of forecast realisations produced since the MCS perturbations create differing forecasts in EN-MCS to the corresponding members of EN-NOMCS and in some cases improve the forecast of the downstream low-pressure centre (in terms of depth, not positioning). The MCS perturbations have

been shown to improve the RMS errors in PMSL downstream (in 5 of the 6 members after 3 days) with the largest improvement of 2.27% in the control member which had a deepening of the low-pressure centre. An improvement in RMS error values occurs once the low-pressure system begins to develop after 3 days downstream.

7.2   Contributions

This thesis has contributed to the understanding of how MCS are represented by convection-permitting and convection-parametrizing NWP models and the structure of the PV anomalies produced. This understanding was then used to investigate the impact that the differing representations of the convection in MCSs between the convection-permitting and convection-parametrizing models has on the downstream forecast and how this impacts the robustness of the forecast. The main contributions produced in this thesis are now detailed:

1. Previous literature has documented that the PV structure of MCSs includes a positive PV anomaly in middle-levels and a near zero or negative PV anomaly at upper levels (Fritsch *et al.*, 1994; Houze, 2004). In this thesis, by analysis of four case studies of MCSs occurring in western Europe, a consistent PV structure has been found through simulations at 12 km, 4 km and 1.5 km grid-spacing. A positive PV anomaly at middle-levels (700–400 hPa) with a negative anomaly at upper-levels and to either side of the positive anomaly (250 hPa–500 hPa) has been found (Figure 3.30). The magnitudes of these anomalies vary dependant on the grid-spacing of the model used.

2. The use of a larger domain convection-permitting model extending into France and Spain, including the area of convective triggering associated with MCSs may improve the forecast of MCSs over the UK. Evidence for this was found through the France 1.5 km model (similar to the UKV model but displaced further south) creating a better forecast of the MCS studied than the UKV model, in terms of the location and magnitude of rainfall and the wind direction compared to reality.

3. A coarse-graining technique was developed for use in Chapter 4 (see Section 2.3) to compare the convection-permitting and convection-parametrized models by averaging them to the same comparable 100km grid spacing. Other grid spacing sizes

could be utilised. This allowed for a direct comparison between the models and was later used in Chapter 5 and 6 to coarse grain the Euro 4 km wind and temperature fields to the Global 25 km grid spacing to gain an understanding of the impact the MCS created in the convection-permitting Euro 4 km simulations has on the downstream forecast simulated by the convection-parametrizing Global model.

4. When convection-permitting MCS PV structures (which have stronger magnitude negative and positive PV anomalies) are coarse grained to a comparable resolution as the convection-parametrizing simulations, stronger negative and positive PV anomalies still exist in the coarse grained convection-permitting models which do not exist in the coarse grained convection-parametrizing models. These strong PV anomalies have associated changes in the windspeed surrounding them, particularly at upper-levels (tropopause height) which has an impact on the downstream flow as the background winds are stronger at this level. Negative PV anomalies at upper-levels are not generated in the convection-parametrizing simulation. This is the first study to determine if these PV structures associated with MCSs can have an impact on the downstream development. Many studies have been conducted into the impact of differences between models in the simulation of large-scale systems such as tropical cyclones or cyclones but not for mesoscale, thunderstorm structures such as MCSs, to see if these persistent differences after coarse graining, impact the downstream forecast, since spatially it impacts a very small scale to begin with. Horizontal dipoles of PV produced in the convection-permitting simulations create stronger magnitude positive and negative anomalies after coarse graining is implemented than in the convection-parametrizing simulation.

5. Upper-level PV structures associated with MCSs have the largest influence on the downstream development. When MCS perturbations are added to Global model simulations the largest impact on the forecast occurs when perturbations are added over all levels, however, upper-level perturbations appear to have the strongest effect when comparing upper-levels to middle-level perturbations (which contradicts an earlier study by Gray (2001), that found middle-level PV structures were found to have the largest impact on the forecast downstream).

6. This is the first study in which PV structures associated with real MCSs (rather than idealised MCSs) have been used to perturb a weather forecast. Previous stud-

ies have looked at the impact of adding random noise or statistical ICs into the models (but not directly related to an MCS) instead of a physically sensible structure such as the PV from an MCS as has been done in this study. This adds the wind and temperatures associated with the PV structure of the MCS into the model which accounts for real physical error in the model. Gray (2001) added idealised perturbations of PV to a forecast by assuming that the upper-level PV anomaly was 0.1 PVU between 150 hPa to 350 hPa and the middle level anomaly was 2 PVU between 475 hPa to 625 hPa. This study has shown that these magnitudes are not typical of the negative and positive PV anomalies which form in MCSs when convection is explicitly represented in the models and more appropriate values should be approximately -1 PVU at upper-levels to 5 PVU at middle levels (these values are taken from the results found in Chapter 3 using the 12 km NAE model but these values were found to be larger when smaller grid-spacing was used).

7. It has been shown that MCSs can impact the downstream flow evolution over 5 days by enhancing the upper-tropospheric ridge structure and consequently affecting the location and depth of a downstream cyclone (in the case study the cyclone was deeper and further west in the ensemble members with a representation of the MCS).

8. It has been shown that MCSs impact the thermodynamic and dynamical flow around them and this persists downstream from the MCS event. In the past the impact of cyclones or large scale Rossby waves has been studied and has been shown to impact the flow downstream but small scale structures such as MCSs or thunderstorm structures have not been studied in terms of their downstream influence (except for the Gray (2001) idealised study).

9. It is not just the MCS PV perturbations themselves that are important for the downstream forecast but whether or not an MCS then evolves in the Global model after the perturbations are added (as defined by precipitation). This was found by the member which does not produce an MCS causing the fewest differences downstream providing evidence for representing MCSs in the forecast to produce an accurate downstream forecast.

10. It has been shown that, for this case study, adding MCS perturbations significantly

changes the ensemble forecasts between the corresponding members with and without perturbations. However, these MCS perturbations cause smaller differences than the IC perturbations. This is probably because the IC perturbations are added over the whole globe rather than the MCS perturbations that were added within a relatively much smaller geographical area.

11. MCS perturbations create a wider range of more differing realisations of the downstream forecast. Development of further forecast evolutions due to the addition of MCS perturbations is shown by an increased range in the RMSD values for 250 hPa PV and PMSL (whether doing member–member or member–control comparisons) and an increase in the ensemble spread when all members are compared (defined by a reduction in the correspondence ratio; spread is not increased when comparing the members of EN-MCS and EN-NOMCS separately). The spread for the noisier fields (e.g. PV at 500 hPa) tends to stop increasing (saturates) as the displacements and amplitude changes at each pixel become comparable to the scales of the features. For smoother fields such as PMSL the spread is still increasing by day 5 because the field represents larger-scale smoother variability for which similarities between members (when using a grid-scale metric) can be retained for longer.

12. The error of the ensemble compared to analyses is improved at days 4 and 5 when MCS perturbations are included, although it is made somewhat worse up to day 3. This is showing that the MCS perturbations can affect the forecast error as well as the spread and in this case the perturbations acted more beneficially later in the forecasts. The forecast errors were reduced in the EN-MCS cases compared to the EN-NOMCS cases after day 3 when the low pressure system begun to develop downstream from where the MCS originated.

In the above contributions point 1 was found in Chapter 3. Points 2, 3 and 4 were found in Chapter 4. Point 5 was found in Chapter 5. The rest were found in Chapter 6. These contributions have implications to the field which will now be discussed.

7.3   Implications

The implications of this thesis on mesoscale modelling and MCS forecasting is split into the PV structure of western European MCSs, the impact these PV structures have in the convection-permitting and convection-parametrizing models and the downstream predictability of forecasts based on their representation of MCSs

7.3.1   PV structure of western European MCSs

The PV structure of MCSs occurring in UK and western Europe has never been investigated before, with the majority of the research being focused on the PV structure of USA MCSs based on satellite imagery rather than NWP modelling (Fritsch *et al.*, 1994; Houze, 2004; Raymond and Jiang, 1990; Bartels and Maddox, 1991; Bosart and Sanders, 1981). A strong positive PV anomaly is found in middle levels with a negative anomaly spread out at tropopause level either side of the positive PV anomaly. The magnitude of the positive and negative anomalies depends on whether the model is convection-permitting or convection-parametrizing. The convection-permitting models allow for stronger negative and positive anomalies to form due to the localised latent heating from convection. A similar PV anomaly structure related to UK MCSs was found by Done *et al.* (2006); with a positive anomaly in mid-levels and a negative lens of PV at tropopause level. However, this study was based on hydrostatic convection-permitting 12 km grid spacing simulations therefore it was likely that now that the MetUM is nonhydrostatic it could have had an impact on the results.

Now that the typical PV structure of western European MCSs has been established it could potentially be used operationally in forecasts to improve the representation of MCSs in the models. Operationally, it could be potentially implemented by inputting idealised PV structures. The potential ideas for use of the PV structures in operational forecasting are described in Section 7.4.2.

7.3.2   PV structures in convection-permitting and convection-parametrizing simulations

Differences between the PV structures associated with MCSs produced in convection-permitting and convection-parametrized models persist after coarse graining to compa-

rable resolution. This has implications on the windspeeds and pressure patterns even on the comparable resolution. This creates differing forecasts with the coarse grained convection-permitting models producing a better representation of the MCS than the convection-parametrized model. This has implications for forecasting of MCSs as it has an effect on the convection produced by the model and thus the MCS is represented better in terms of location and magnitude of rainfall produced in the coarse grained convection-permitting models.

The differences in the PV structures of the coarse-grained convection-permitting and convection parametrizing models are largest at upper levels (350-250 hPa). The 350–250 hPa level is where the negative PV anomalies associated with MCSs are not represented by the convection parametrization scheme in the convection parametrizing models. This is perhaps not surprising since the convection parametrization is not designed to represent individual storms. The largest feedback on the larger-scale circulation patterns occurs at upper levels near the tropopause at jet-stream level Done *et al.* (2006). Therefore, understanding the structure of the typical negative PV anomalies at upper levels in MCSs is important both for a conceptual understanding of the errors that might be present in a forecast if an MCS is poorly represented and to modify a forecast (manually or in an automated way) by introducing a better representation of the upper-level structure.

7.3.3 Downstream predictability

This research has shown the importance of representing the MCS on the development of the downstream forecast (particularly on the low-pressure system produced). In this study, coarse-grained wind and temperature perturbations associated with the explicit representation of an MCS in an ensemble of convection-permitting model forecasts were injected into Global model forecasts. These perturbations caused differences to the forecasts (in PV, PMSL and windspeed) and to the ensemble spread (shown through a reduction in the correspondence ratio for PV and precipitation). The upper-level perturbations had more of an impact than perturbations added at middle-levels which is particularly important for Global model forecasts of MCSs which seem to misrepresent the PV structure at upper-levels associated with MCSs and create no negative (and sometimes not even near zero PV) PV anomalies.

It is thought possible that a similar approach of adding perturbations in wind and temperature associated with the MCS could be used in an operational ensemble forecast system. Taking the Met Office system as an example, a convection- permitting ensemble could be run for 6–12 hours with boundaries and initial conditions supplied by MOGREPS-G forecasts. Then PV structures from the convection-permitting forecasts could be inserted (as wind and temperature perturbations) into the equivalent MOGREPS-G members to provide additional members and an additional source of ensemble spread, based on physical processes, that could not otherwise be obtained. The hope would be that this approach could be simulated sufficiently quickly to provide a better indication of the possible impact of deep convection on forecasts 3–5 days ahead. The objective is not necessarily to try to improve any individual forecast because it is known that there will be uncertainties and errors in the convection-permitting simulations that provide the perturbations, but rather to give MOGREPS-G a better opportunity to produce a more realistic spread. Since Rodwell *et al.* (2013) found that forecast busts downstream from the USA over UK and Europe are largely influenced by poor forecasting of MCSs over the USA, a good place to try this approach would be over the US with the aim of achieving better 3–5-day MOGREPS-G forecasts for the UK region. It may also be possible to introduce perturbations in a more idealised way in situations when the MOGREPS-G members are indicating the possibility of deep convection through the convection-parametrization scheme.

It must be noted that a limitation of the Euro 4 km model is that the convection tends to be overactive therefore the negative PV simulated at upper-levels may be too strong. Therefore, it would be useful to determine the MCS perturbations from smaller grid-spacing simulations to then investigate the impact that these PV anomalies have on the downstream convection-parametrizing forecast (for example the France 1.5 km model).

7.4   Future work

This thesis has demonstrated the importance of a good representation of MCSs in weather forecast models, both for more realistic short-period weather forecasts (creating further realisations) and for representing the associated PV structures that can influence the larger-scale evolution of the subsequent longer-range forecasts. However, it has also

revealed that there is further research required and a number of important questions which are posed from the results found in this thesis are discussed below.

In Chapter 3, a consistent structure for the four western European MCSs cases studied was identified, however, any firm assertions about the generality of these findings require further MCS case studies over Europe and elsewhere. This would allow for a more detailed analysis of why the negative PV anomalies occur to the sides of the positive PV anomaly at upper levels and whether this is a particular feature of western European MCSs or whether it is the same elsewhere in the world but as yet not documented. In addition, it would be interesting to determine whether all MCSs occurring over western Europe tend to be of a similar horizontal width and have similar magnitude PV anomalies (the magnitudes would be dependant on the grid spacing of the model used though).

Chapter 4, 5 and 6 are based on just one case study therefore it is important to understand how the coarse grained representation of convection related to MCSs in convection-permitting and convection-parametrizing models is affected for many more cases. It is reasonable to assume, from physical understanding, that the coarse-grained convection permitting models would still have stronger negative and positive PV anomalies which cause differences in the PV structures and hence differences in wind, temperature and rainfall, but it would be good to determine the typical magnitudes of the differences by studying many cases.

An investigation into the robustness of the downstream forecast in further case studies is also required, particularly for a variety of case studies in which the Global model did or did not represent an MCS. The convection-permitting ensemble used here only had six members, which is not as many as the approximately 10–20 used by operational centres. Simulations using ensembles with more members would be advantageous to be able to examine a greater variability of solutions to determine if that has an impact on the spread and usefulness of adding the MCS perturbations. It would be possible, in principle (cost permitting), to run with 18 members every 6 hours, for recent or new cases, using convection-permitting ensemble forecasts that are downscaled within MOGREPS-G.

Simulations could be initialised at earlier or later times relative to the MCS formation. That might mean trying 6 or 12 hours earlier (12 UTC or 18 UTC 4 July) for the 5 July

2012 case to see if this has an impact on the spread since in this thesis the simulations were initialised at 00 UTC 5 July 2012 at the time of the initial orographic convection. The process of adding MCS perturbations to the ensemble members could be repeated using the France 1.5 km model developed in Chapter 4 to create the MCS perturbations. The aim of repeating the process with the France 1.5 km model would be to determine if this has the same impact on the downstream predictability as creating them using the Euro 4 km model (Chapter 5 and Chapter 6) or whether it improves the predictability or increases the ensemble spread further (particularly because the Euro 4 km model has a tendency for overactive convection which could be a factor in the stronger negative PV anomalies at upper-levels associated with the MCS).

In Chapter 4 an improvement in the representation of the MCS and subsequent forecast was shown by using the France 1.5 km model over the UKV model since it was able to capture the triggering of the MCS unlike the UKV model. Further case studies should be investigated for the development of the initial triggering of MCS events using a larger version of the France 1.5 km model to determine if this model produces a better forecast of MCSs which impact the UK than the current UKV model (which has recently been extended further south into France but not into Spain). A few questions arise from this study that will require further research and are now discussed:

7.4.1   How do the type of perturbations impact the results of this study

Previous studies found that error growth is largely independent of the perturbations used (Zhang *et al.*, 2007). Leoncini *et al.* (2010) found that regardless of the perturbation used the RMS error values reached the same value at saturation; in a study where potential temperature perturbations were used at 0.01 K, 0.1 K and 1 K). Therefore, it is important to investigate whether the same results occur when different perturbations are used. The current study showed an impact from multiplying the perturbations by a factor of three, but that is probably an unrealistically large increase. It has been shown that the perturbations at upper-levels are more important than middle-levels for changing the evolution of a forecast and further examination of the differences between different levels for more cases would be valuable. The location of sensitivity to PV can be different to the amplitude of PV though (Beare *et al.*, 2003) therefore it is important to investigate not only how the amplitude impacts the downstream forecast but also where the PV

anomalies develop.

For this study temperature and wind perturbations were added as perturbations, in-line with an adjustment of the PV, but humidity perturbations could also be included or an investigation into the impact of separate perturbations of wind and temperature could be interesting. It would also be useful to know if the addition of perturbations over a period of time during the lifetime of the MCS (several hours) would make a difference, instead of using a single snapshot. This would allow for an investigation into if the particular perturbations used are important on the downstream differences which develop or if it is just that the magnitude of the perturbations is important, particularly at upper levels. An important question to ask is if this case study was hit with additional purely random noise if the same thing would happen that happens when the MCS perturbations are added or is it important that there are clear MCS structures being added to the model that are well represented in the convection-permitting models.

7.4.2 Could adding MCS perturbations to MetUM operational forecasts improve downstream forecasts

To assess the work in this study from a practical forecasting perspective the characteristic PV structure of UK and western European MCSs could be added as an idealised structure (potential idealised structure shown in Figure 7.1) into the operational Global model ensemble as it has been found that organised convection has thermodynamic and dynamical influences that can impact on the downstream forecast (Figure 7.1). As discussed earlier, the alternative approach would be to produce MCS perturbations from high resolution forecasts (as in this study) and then insert the MCS perturbations into the MOGREPS-G ensemble simulations when they are simulated operationally 6 hours later (Figure 7.2). This could be run using up to 18 ensemble members every 6 hours to provide an additional set of members with MCS perturbations.

Alternatively, the MCS perturbation ensemble members could be run in half of the members so that the ensemble is the same size and includes both MCS perturbed and unperturbed forecasts. A first step in an operational setup might be to perturb only a few members because otherwise it could be too computationally expensive. If either of these approaches were investigated it would enable a robust determination of whether adding MCS perturbations to the models could improve the spread downstream of ensemble

forecasts. An alternative approach could be to use a stochastic physics scheme in the data assimilation process that occurs to initiate the ensemble simulations to take account of the errors produced due to misrepresentation of MCSs. There was a similar method previously used in the MetUM MOGREPS-G simulations however it was retired as it was found to be of small benefit. This could be because it was based on the study of Gray (2001) which concluded that the mid-level PV anomalies had the largest impact on the downstream forecast and an upper-level PV anomaly of 0.1 PVU was used. The negative PV at upper-levels was therefore not accounted for in Gray (2001) and it is the negative anomaly at upper-levels that has been found in this study to be most important on the downstream forecast development.
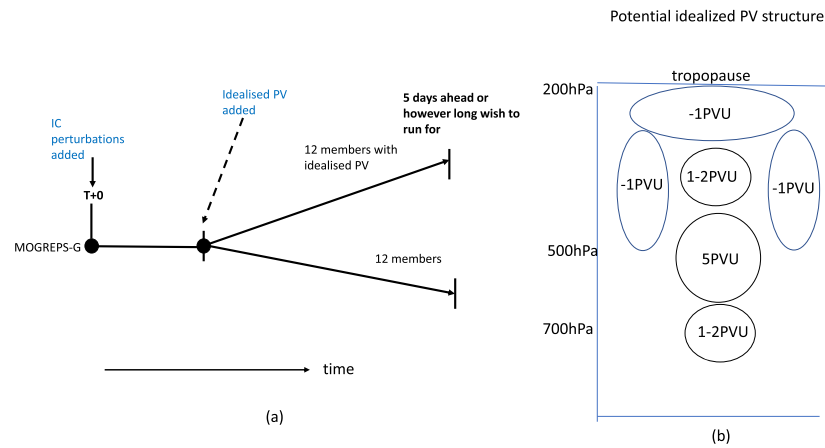

Figure 7.1: Operational model simulation set-up for future work proposal for idealised PV structure to then be added to MOGREPS-G ensemble simulations to represent the PV structure in MCSs better. The magnitude of the positive and negative PV anomalies in this figure is based on the findings from Chapter 3 for the NAE simulations.

Rodwell *et al.* (2013) found that misrepresentation of MCSs over the USA led to forecast busts downstream over Europe. There is the potential for extending this research to including MCS perturbations over the USA in the hope of improving the downstream forecasts over Europe 3–5 days later. This would benefit from further research into the PV structure of USA MCSs first, but that would not be essentially and could be an important way to improve forecasts downstream from the USA. Adding MCS perturbations in the USA forecasts would be especially worth trying now since the Met Office have recently set up and run convection-permitting forecasts over the US and North America. The hope would be that an ensemble such as MOGREPS-G might do better at getting
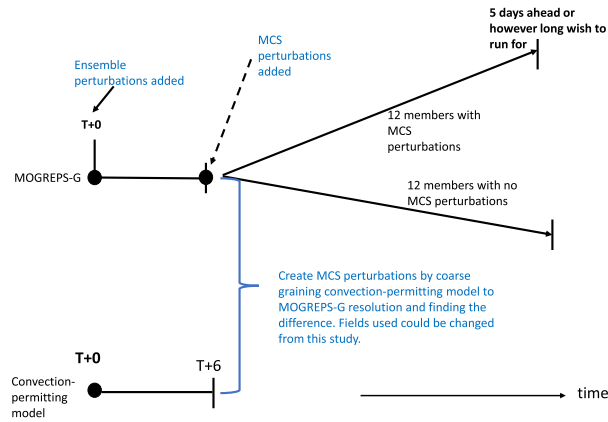
Figure 7.2: Operational model simulation set-up for future work proposal for a similar approach to this study but adding MCS perturbations to MOGREPS-G ensemble.

an earlier detection of changes in the possible forecast evolution (such as a change in the track or depth of a significant low pressure system) ahead of the deterministic global model forecast.

7.4.3   How is the MCS produced in the model determined by the synoptic-scale predictability?

Since MCSs have been shown to cause thermodynamic and dynamical impacts on the downstream predictability in the model simulations it is important to investigate how the synoptic-scale predictability influences the formation of the MCSs in the first place. For instance, the synoptic-scale forecast in the Global model of the case study in this thesis could have resulted in the misrepresentation of the MCS that impacted the UK on this day. Therefore, the forecast of the MCS is constrained by the accuracy of the forecast of the larger-scale pre-convective conditions. Further case studies using a larger number of ensemble members with different IC perturbations would be ideal to investigate this. The 6 members studied here, although show that the synoptic-scale patterns do have an impact on the MCS produced, are not sufficient to determine the influence that the larger-scale weather patterns have on the MCS produced in the model.

7.4.4 A more spatial or regime assessment of the predictability

The metrics used to determine the member to member variability and the ensemble spread are based on calculations at each model grid square. This does not take into account spatial differences between forecasts or changes in regimes or weather patterns. Further work could be done to evaluate the differences between ensemble members using spatial methods such as the Fractions Skill Score (Roberts and Lean, 2008) or to examine spatial anomalies in PMSL or even use types of regime classification. This would help to avoid the problem of error saturation in noisy fields and view the differences more like a forecaster would looking at weather charts.

References

Abel SJ, Shipway BJ. 2007. A comparison of cloud resolving model simulations of trade wind cumulus with aircraft observations taken during RICO. *Q. J. R. Meteorol. Soc.* **133**: 781–794.

Ambaum MHP. 2010. Thermal physics of the atmosphere. *Wiley-Blackwell* : 239pp.

Anderson CJ, Arritt RW. 2001. Mesoscale convective systems over the United States during the 1997-1998 El Nino. *Amer. Meteorol. Soc.* **129**: 2443–2457.

Arakawa A, Lamb VR. 1977. Computational design of the basic dynamical processes of the ucla general circulation model. *Methods of Computational Physics* **17**: 173–265.

Arakawa A, Schubert W. 1974. Interaction of a cumulus ensemble with the large-scale environment. Part I. *J. Atmos. Sci.* **31**: 674–701.

Arakawa A, Wu CM. 2013. A unified representation of deep moist convection in numerical modelling of the atmosphere- Part I. *J Atmos. Sci.* **70**: 1929–1953.

Augustine JA, Howard KW. 1991. Mesoscale convective complexes over the United States during 1986 and 1987. *Mon. Weather Rev.* **119**: 1575–1589.

Bannister R. 2007. Elementary 4D-Var: DARC Technical report No. 2. *DARC Technical report* **2**: 1–16.

Barrett AI, Gray SL, Kirshbaum DJ, Schultz DM, Jr JGF. 2016. The utility of convection permitting ensembles for the prediction of stationary convective bands. *Mon. Weather Rev.* **144**: 1093–1114.

Bartels DL, Maddox RA. 1991. Midlevel cyclonic vortices generated by mesoscale convective systems. *Mon. Weather Rev.* **119**: 104–118.

Beare RJ, Thorpe AJ, White AA. 2003. The predictability of extratropical cyclones: Nonlinear sensitivity to localized potential-vorticity perturbations. *Q. J. R. Meteor. Soc.* **129**: 219–237.

Bennett LJ, Browning KA, Blyth AM, Parker DJ, Clark PA. 2006. A review of the initiation of precipitating convection in the United Kingdom. *Q. J. R. Meteorol. Soc.* **132**: 1001–

1020.

Bishop CH, Etherton BJ, Majumdar SJ. 2001. Adaptive sampling with the ensemble trans-
form kalman filter. Part I: Theoretical aspects. *Mon. Weather Rev.* **129**: 420–436.

Bishop CH, Thorpe AJ. 1994. Potential vorticity and the electrostatics analogy: Quasi-
geostrophic theory. *Q. J. R. Meteor. Soc.* **120**: 713–731.

Bleaker S, Andre MJ. 1951. On the diurnal variation of precipitation, particularly over
central U.S.A. and its relation to large-scale orographic circulation systems. *Q. J. R.
Meteorol. Soc.* **77**: 260–271.

Bloom SC, L L Takacs AMS, Ledvina D. 1996. Data assimilation using incremental anal-
ysis updates. *Mon. Weather Rev.* **124**: 1256–1271.

Bonner WD. 1968. Climatology of the low level jet. *Mon. Weather Rev.* **96**: 833–850.

Bosart LF, Lackmann GM. 1995. Postlandfall Tropical Cyclone Reintensification in a
Weakly Baroclinic Environment: A Case Study of Hurricane David (September 1979).
Mon. Weather Rev. **123**: 3268–3291.

Bosart LF, Sanders F. 1981. The Johnstown Flood of July 1977: A Long-Lived Convective
System. *J. Atmos. Sci.* **38**: 1616–1642.

Bowler NE, Arribas A, Mylne KR, Robertson KB, Beare SE. 2008. The MOGREPS short-
range ensemble prediction system. *Q. J. R. Meteorol. Soc.* **134**: 703–722.

Brandes EA. 1990. Evolution and Structure of the 6-7 May 1985 Mesoscale Convective
System and Associated Vortex. *Mon. Weather Rev.* **118**: 109–127.

Brooks HE, Doswell CA. 1993. New technology and numerical weather prediction- a
wasted opportunity? *Weather* **48**: 173–177.

Brown JM. 1979. Mesoscale unsaturated downdrafts driven by rainfall evaporation: a
numerical study. *J. Atmos. Sci.* **36**: 313–338.

Browning KA, Hill FF. 1984. Structure and evolution of a mesoscale convective system
near the British Isles. *Q. J. R. Meteorol. Soc.* **110**: 897–913.

Bryan GH, Wyngaard JC, Fritsch JM. 2003. Resolution requirements for the simulation
of deep moist convection. *Mon. Weather Rev.* **131**: 2394–2416.

Carlson TN, Ludlam FH. 1968. Conditions for the occurence of severe local thunder-
storms. *Tellus* **20**: 203–226.

Chagnon J, Gray S. 2009. Horizontal potential vorticity dipoles on the convective storm
scale. *Q. J. R. Meteorol. Soc.* **135**: 1392–1408.

Charney JG, Phillips NA. 1953. Numerical integration of the quasi-geostrophic equations

for baroptropic and simple baroclinic flows. *Journal of Meteorology* **10**: 71–99.

Chen S, Frank WM. 1993. A Numerical Study of the Genesis of Extratropical Convective Mesovortices. Part I: Evolution and Dynamics. *J. Atmos. Sci.* **50**: 2401–2426.

Chen YL, Li J. 1995. Large-scale conditions favourable for the development of heavy rainfall during TAMEX IOP 3. *Mon. Weather Rev.* **123**: 2978–3002.

Clark P, Roberts N, Humphrey L, Ballard SP, Charlton-Perez C. 2016. Review Convection-permitting models: A step-change in rainfall forecasting. *Meteorol. Appl.* **23**: 165–181.

Clark PA, Browning KA, Forbes RM, Morcrette CJ, Blyth AM, Lean HW. 2014. The evolution of an MCS over southern England. Part 2: model simulations and sensitivity to microphysics. *Q. J. R. Meteorol. Soc.* **140**: 458–479.

Clayton A. 2012. Incremental analysis update (IAU) scheme. *Unifed model documentation paper No.31* **4**: 1–27.

Cohen AE, Coniglio MC, Corfidi SF, Corfidi SJ. 2007. Discrimination of mesoscale convective system environments using sounding observations. *Wea. Forecasting* **22**: 1045–1062.

Cotton WR, Lin M, McAnelly RL, Tremback CJ. 1989. A Composite Model of Mesoscale Convective Complexes. *Mon. Weather Rev.* **117**: 765–783.

Cullen MJP. 1999. The use of dynamical knowledge of the atmpshere to improve nwp models. *ECMWF Seminar Proceedings: Recent Developments in numerical methods for atmospheric modelling* : 418–441.

Davies CA, Trier SB. 2007. Mesoscale Convective Vortices Observed during BAMEX. Part I: Kinematic and Thermodynamic Structure. *Mon. Wea. Rev.* **135**: 2029–2049.

Davies HC, Didone M. 2013. Diagnosis and Dynamics of Forecast Error Growth. *Mon. Weather Rev.* **141**: 2483–2501.

Davies T, Cullen MJP, Malcolm AJ, Mawson MH, Staniforth A, White AA, Wood N. 2005. A new dynamical core for the met office's global and regional modelling of the atmosphere. *Q. J. R. Meteorol. Soc.* **131**: 1759–1782.

Davis CA. 1992. Piecewise Potential Vorticity Inversion. *Journal of Atmos. Sci.* **49**: 1397–1411.

Davis CA, Emanuel KA. 1991. Potential vorticity diagnostics of cyclogenesis. *Mon. Weather Rev.* **119**: 1929–1953.

Davis CA, Galarneau TJ. 2009. The Vertical Structure of Mesoscale Convective Vorticies.

J. Atmos. Sci. **66**: 686–704.

Dirren S, Didone M, Davies HC. 2003. Diagnosis of "forecast-analysis" difference of a weather prediction system. *Geophys. Res. Lett.* **30**: 2060.

Done JM, Craig GC, Gray SL, Clark PA, Gray MEB. 2006. Mesoscale simulations of organized convection: Importance of convective equilibrium. *Q. J. R. Meteorol. Soc.* **132**: 737–756.

Done JM, Craig GC, Gray SL, Clark PA. 2012. Case-to-case variability of predictability of deep convection in a mesoscale model. *Q. J. R. Meteorol. Soc.* **138**: 638–648.

Edwards JM. 1996. Efficient calculation of infra-red fluxes and cooling rates using the two-stream equations. *J. Atmos. Sci.* **53**: 1921–1932.

Edwards JM, Slingo A. 1996. Studies with a flexible new radiation code I: Choosing a configuration for a large-scale model. *Q. J. R. Meteorol. Soc.* **122**: 689–719.

Eisenstat SC, Elman HC, Schultz MH. 1983. Variational iterative methods for nonsymmetric systems of linear equations. *SIAM J. Numer. Anal.* **20**: 345–357.

Emanuel KA. 1994. Atmospheric Convection. *Oxford Uni. Press* : 592pp.

Ertel H. 1942. Ein Neuer hydrodynamischer Wirbelsatz. *Met. Z.* **59**: 271–281.

Evensen G. 1994. Sequential data assimilation with a nonlinear quasi-geostrophic model using Monte-Carlo methods to forecast error statistics. *J. Geophys. Res.* **99**: 10 143–10 162.

Fehlmann R, Davies HC. 1997. Misforecasts of synoptic systems: Diagnosis via PV retrodiction. *Mon. Weather Rev.* **125**: 2247–2264.

Fehlmann R, Quadri C, Davies HC. 2000. An Alpine rainstorm: Sensitivity to the mesoscale upper-level structure. *Weather forecasting* **15**: 4–28.

Flack DLA, Gray SL, Plant RS, Lean HW, Craig GC. 2017. Convective-scale perturbation growth across the spectrum of convective regimes. *submitted* .

Fritsch J, Chappell C. 1980. Numerical prediction of convectively driven mesoscale pressure systems. Part I: Convective Parameterization. *J. Atmos. Sci.* **37**: 1722–1733.

Fritsch JM, Brown JM. 1982. On the generation of convectively driven mesohighs aloft. *Mon. Weather Rev.* **110**: 1554–1563.

Fritsch JM, Kane RJ, Chelius CH. 1986. The contribution of mesoscale convective weather systems to the warm season precipitation in the United States. *J. Clim. Appl. Meteorol.* **25**: 1333–1345.

Fritsch JM, Maddox RA. 1981. Convectively driven mesoscale weather systems aloft.

Part I:Observations. *J. Appl. Meteor.* **20**: 9–19.

Fritsch JM, Murphy JD, Kain JS. 1994. Warm Core Vortex Amplification over Land. *J. Atmos. Sci.* **51**: 1780–1807.

Galarneau TJ, Bosart LF. 2009. Baroclinic Transition of a Long-Lived Mesoscale Convective Vortex. *Mon. Weather Rev.* **137**: 562–584.

Gebhardt C, Theis SE, Paulat M, Bouallegue ZB. 2011. Uncertainties in COSMO-DE precipitation forecasts introduced by model perturbations and variation of lateral boundaries. *Atmos. Research* **100**: 168–177.

Gerard L, Piriou JM, Brozkova R, Geleyn JF, Banciu D. 2009. Cloud and precipitation parameterization in a meso-gamma-scale operational weather prediction model. *Mon. Weather Rev.* **137**: 3960–3977.

Goodliff M, Amezcua J, Leeuwen PJV. 2015. Comparing hybrid data assimilation methods on the Lorenz 1963 model with increasing non-linearity. *Tellus A: Dynamic Meteorology and Oceanography* **67**: 1–13.

Grams CM, Archambault HM. 2016. The key role of diabatic outflow in amplifying the midlatitude flow: a representative case study of weather systems surrounding western north Pacific extratropical transition. *Mon. Weather Rev.* **144**: 3847–3869.

Grant ALM. 2001. Cloud-base fluxes in the cumulus-capped boundary layer. *Q. J. R. Meteorol. Soc.* **127**: 407–421.

Grant ALM, Brown AR. 1999. A similarity hypothesis for shallow-cumulus transports. *Q. J. R. Meteorol. Soc.* **125**: 1913–1936.

Gray M. 2001. The impact of mesoscale convective-system potential vorticity anomalies on numerical-weather-prediction forecasts. *Q. J. R. Meteorol. Soc.* **127**: 73–88.

Gray MEB, Marshall C. 1998. Mesoscale convective systems over the UK, 1981-97. *Weather* **53**: 388–395.

Gregory D. 1995. A consistent treatment of the evaporation of rain and snow. *Mon. Weather Rev.* **123**: 2716–2732.

Gregory D, Rowntree PR. 1990. A mass-flux convection scheme with representation of cloud ensemble characteristics and stability dependent closure. *Mon. Weather Rev.* **118**: 1483–1506.

Gregory D, Wilson D, Bushell A. 2002. Insights into cloud parametrization provided by a prognostic approach. *Q. J. R. Metorol. Soc.* **128**: 1485–1504.

Gregory J. 1999. Representation of the radiative effects of convective anvils. *Hadley Centre*

Technical Note 7, Meteorological Office, FitzRoy Road, Exeter, EX1 3PB .

Griffiths M, Thorpe AJ, Browning KA. 2000. Convective destabilization by a tropopause fold diagnosed using potential-vorticity inversion. *Q. J. R. Meteorol. Soc.* **126**: 125–144.

Hanley KE, Plant RS, Stein THM, Hogan RJ, Nicol J, Lean HW, Halliwell C, Clark PA. 2015. Mixing-length controls on high-resolution simulations of convective storms. *Q. J. R. Meteorol. Soc.* **141**: 272–284.

Hohenegger C, Schlar C. 2007. Atmospheric predictability at synoptic versus cloud-resolving scales. *Bull. Amer. Meteor. Soc.* **88**: 1783–1793.

Holton JR. 1992. An introduction to dynamic meteorology. *publ. Academic Press* .

Hoskins BJ, McIntyre ME, Robertson AW. 1985. On the use and significance of isentropic potential vorticity maps. *Q. J. R. Meteor. Soc.* **111**: 877–946.

Houze RA. 1977. Structure and Dynamics of a Tropical Squall-Line System. *Mon. Weather Rev.* **105**: 1540–1567.

Houze RA. 1993. Cloud dynamics. *Int. Geophys. Ser.* **53**: 334–404.

Houze RA. 1997. Stratiform Precipitation in Regions of Convection: A Meteorological Paradox? *Bull.Am. Meteorol.Soc.* **78**: 2179–2196.

Houze RA. 2004. Mesoscale Convective Systems. *Rev.Geophys.* **42**: 43pp.

Houze RA, Smull B, Dodge P. 1990. Mesoscale Organization of Springtime Rainstorms in Oklahoma. *Mon. Weather Rev.* **118**: 613–653.

Inness P, Dorling S. 2013. Operational Weather Forecasting. *Wiley-Blackwell* : 231pp.

Johnson RH, Bartels DL. 1992. Circulations associated with a mature-to-decaying mid-latitude mesoscale convective system. Part II: Upper-level features. *Mon. Weather Rev.* **120**: 1301–1320.

Johnston EC. 1981. Mesoscale vorticity centers induced by mesoscale convective complexes. *M. S. thesis, University of Wisconsin* : 54 pp.

Johnston RH, Chen S, Toth JJ. 1989. Circulations associated with a mature-to-decaying midlatitude mesoscale convective system. Part I: Surface features - heat bursts and mesolow development. *Mon. Weather Rev.* **117**: 942–959.

Kain JS, Coauthors. 2008. Some practical considerations regarding horizontal resolution in the first generation of operational convection-allowing NWP. *Wea. Forecasting* **23**: 931–952.

Kain JS, Fritsch JM. 1992. The role of the convective 'trigger function' in numerical forecasts of mesoscale convective systems. *Meteorol. Atmos. Phys.* **49**: 93–106.

Kalman RE. 1960. A new approach to linear filtering and prediction problems. *Transactions of the AMSE - Journal of Basic Engineering* **82D**: 35–45.

Kane RJ, Chelius CR, Fritsch JM. 1987. Precipitation Characteristics of Mesoscale Convective Weather Systems. *J. Climate Appl. Meteor.* **26**: 1345–1357.

Lean HW, Clark PA, Dixon M, Roberts NM, Fitch A, Forbes R, Halliwell C. 2008. Characteristics of High-Resolution Versions of the Met Office Unified Model for Forecasting Convection over the United Kingdom. *Mon. Weather Rev.* **136**: 3408–3424.

Leoncini G, Plant RS, Gray SL, Clark PA. 2010. Perturbation growth at the convective scale for CSIP IOP18. *Royal Meteorological Soc.* **136**: 653–670.

Lewis MW, Gray SL. 2010. Categorisation of synoptic environments associated with mesoscale convective systems over the UK. *Atmos. Res.* **97**: 194–213.

Liang AG, Fritsch JM. 1993a. Mesoscale convective complexes in Africa. *Mon. Weather Rev.* **121**: 2254–2263.

Liang AG, Fritsch JM. 1993b. Mesoscale convective complexes over the Indian monsoon region. *J. Climate* **6**: 911–919.

Liang AG, Fritsch JM. 1997. The global population of mesoscale convective complexes. *Q. J. R. Meteorol. Soc.* **123**: 389–405.

Liang AG, Fritsch JM. 2000. The Large-Scale Environments of the Global Populations of Mesoscale Convective Complexes. *Mon. Weather Rev.* **128**: 2756–2776.

Lock A, Edwards J. 2012. UM Documentation Paper 24: The Parametrization of Boundary Layer Processes. *Met Office, FitzRoy Road, Exeter, Devon, EX1 3PB* .

Lock AP. 2001. The numerical representation of entrainment in parametrizations of boundary layer turbulent mixing. *Mon. Weather Rev.* **129**: 1148–1163.

Lock AP, Brown AR, Bush MR, Martin GM, Smith RNB. 2000. A new boundary layer mixing scheme. part i: Scheme description and single-column model tests. *Mon. Weather. Rev.* **128**: 3187–3199.

Lorenz EN. 1969. Atmospheric predictability as revealed by naturally occurring analogues. *J. Atmos. Sci* **26**: 636–646.

Maddox RA. 1980. Mesoscale convective complexes. *Bull.Am. Meteorol.Soc.* **61**: 1374–1387.

Maddox RA. 1983. Large-scale meteorological conditions associated with mid-latitude, mesoscale convective complexes. *Mon. Weather Rev.* **111**: 1475–1493.

Maddox RA, Rogers DM, Howard KW. 1982. Mesoscale convective complexes over the

United States during 1981- annual summary. *Mon. Weather Rev.* **110**: 1501–1515.

Mapes B. 1993. Gregarious Tropical Convection. *J. Atmos. Sci.* **50**: 2026–2037.

Mapes B, Houze RA. 1995. Diabatic Divergence Profiles in Western Pacific Mesoscale Convective Systems. *J. Atmos. Sci.* **52**: 1807–1828.

Martin JE. 2006. Mid-Latitude Atmospheric Dynamics: A first course. *Wiley* : 324pp.

McAnelly RL, Cotton WR. 1989. The Precipitation Life Cycle of Mesoscale Convective Complexes over the Central United States. *Mon. Weather Rev.* **117**: 784–808.

McCallum E, Waters AJ. 1993. Severe thunderstorm over south-east England, 20/21 July 1992: Satellite and radar perspective of a mesoscale convective system. *Weather* **48**: 198–208.

Menard RD, Fritsch JM. 1989. A mesoscale convective complex-generated inertially stable warm core vortex. *Mon. Weather Rev.* **117**: 1237–1261.

Miller RA, Fritsch JM. 1991. Mesoscale convective complexes in the western Pacific region. *Mon. Weather Rev.* **119**: 2978–2992.

Morel C, Senesi S. 2002a. A climatology of mesoscale convective systems over Europe using satellite infrared imagery. I: Methodology. *Q. J. R. Meteorol. Soc.* **128**: 1953–1971.

Morel C, Senesi S. 2002b. A climatology of mesoscale convective systems over Europe using satellite infrared imagery. II: Characteristics of European mesoscale convective systems. *Q. J. R. Meteorol. Soc.* **128**: 1973–1995.

Morris TN. 1986. The Spanish plume-testing the forecaster's nerve. *Meteorol. Mag.* **115**: 349–357.

Panagi PM, Dicks EM. 1997. Met Office Unified Model data, Diagnostics, Graphics programs and other observational data available from the JCCM through the aegis of the Universities Weather Research Network UWERN. *JCCM Internal Report* **69**.

Pearson KJ, Lister GMS, Birch CE, Allen RP, Hogan RJ, Woolnough SJ. 2014. Modelling the diurnal cycle of tropical convection across the 'grey zone'. *Q. J. R. Meteorol. Soc.* **140**: 491–499.

Petch JC. 2006. Sensitivity studies of developing convection in a cloud-resolving model. *Q. J. R. Meteor. Soc.* **132**: 345–358.

Plant RS, Craig GC, Gray SL. 2003. On a threefold classification of extratropical cyclogenesis. *Q. J. R. Meteor. Soc.* **129**: 2989–3012.

Pomroy HR, Thorpe AJ. 2000. The evolution and dynamical role of reduced upper-tropospheric potential vorticity in intensive observing period one of FASTEX. *Mon.*

Weather Rev. **128**: 1817–1834.

Quinting JF, Jones SC. 2016. On the impact of tropical cyclones on rossby wave packets: A climatological perspective. *Mon. Weather Rev.* **144**: 2021–2048.

Raymond DJ, Jiang H. 1990. A Theory for Long-Lived Mesoscale Convective Systems. *J. Atmos. Sci.* **47**: 3067–3077.

Riemer M, Jones SC, Davies CA. 2008. The impact of extratropical transition on the downstream flow: An idealized modelling study with a straight jet. *Q. J. R. Meteor. Soc.* **134**: 69–91.

Roberts N. 2000. The relationship between water vapour imagery and thunderstorms. *Met Office tech. report* **110**: 1–40.

Roberts NM. 2003. The impact of a change to the use of the convection scheme to high-resolution simulations of convective events. *Met Office Tech. Rep.* **407**: 30 pp.

Roberts NM, Lean HW. 2008. Scale-selective verification of rainfall accumulations from high-resolution forecasts of convective events. *Mon. Weather Rev.* **136**: 78–97.

Rodwell MJ. 2006. Comparing and combining deterministic and ensemble forecasts: How to predict rainfall occurrence better. *ECMWF Newsletter* **106**: 17–23.

Rodwell MJ, Magnusson L, Bauer P, Betchtold P, Bonavita M, Cardinali C, Diamantakis M. 2013. Characteristics of occassional poor medium-range weather forecasts for Europe. *Bull. Amer. Meteorol. Soc.* **94**: 1393–1405.

Rogers RF, Fritsch JM. 2001. Cyclogenesis from Convectively Driven Amplification of Midlevel Mesoscale Convective Vortices. *Mon. Weather Rev.* **129**: 605–637.

Romero R, Ramis C, Alonso S, Doswell C, Stensrud D. 1998. Mesoscale model simulations of three heavy precipitation events in the western Mediterranean region. *Mon Weather Rev.* **126**: 1859–1881.

Rotunno R, Klemp JB, Weisman ML. 1988. A theory for strong, long-lived squall lines. *J. Atmos. Sci.* **45**: 463–485.

Sachinananda M, Zrnic DS. 1986. Differential propogation phase-shift and rainfall rate estimation. *Radio Sci.* **21**: 235–247.

Schiesser HH, Houze RA, Huntrieser H. 1995. The mesoscale structure of severe precipitation systems in Switzerland. *Mon. Weather Rev.* **123**: 2070–2097.

Selz T, Craig GC. 2015. Upscale error growth in a high-resolution simulation of a summertime weather event over Europe. *Mon. Weather Rev.* **143**: 813–827.

Skamarock WC, Smolarkiewicz PK, Klemp JB, Smith RB. 1997. Preconditioned

conjugate-residual solvers for Helmholtz equations in nonhydrostatic models. *Mon. Weather Rev.* **125**: 587–599.

Smith RNB. 1990. A scheme for predicting layer clouds and their water contents in a general circulation model. *Q. J. R. Meteorol. Soc.* **116**: 435–460.

Smolarkiewicz PK, Margolin LG. 1994. 'variational elliptic solver for atmospheric applications. *Technical Report LA-12712-MS, Los Alamos, USA* .

Smull BF, Augustine JA. 1993. Multiscale Analysis of a Mature Mesoscale Convective Complex. *Mon. Weather Rev.* **121**: 103–132.

Smull BF, Houze RA. 1985. A midlatitude squall line with a trailing stratiform region of a midlatitude squall line. *Mon. Weather Rev.* **113**: 117–133.

Smull BF, Houze RA. 1987. Dual-doppler radar analysis of a midlatitude squall line with a trailing region of stratiform rains. *J. Atmos. Sci.* **44**: 2128–2148.

Staniforth A, Cote J. 1991. Semi- lagrangian schemes for atmospheric models - a review. *Mon. Weather Rev.* **119**: 2206–2223.

Staniforth A, White A, Wood N, Thuburn J, Zerroukat M, Cordero E, Davies T, Diamantakis M. 2006. Joy of U.M. 6.3 model formulation. Unified Model documentation paper 15. *Met Office, FitzRoy Road, Exeter, UK, EX1 3PB* .

Stein THM, Hogan RJ, Clark PA, Halliwell CE, Hanley KE, Lean HW, Nicol JC, Plant RS. 2015. The Dymecs Project: A statistical approach for the evaluation of convective storms in high-resolution NWP models. *Amer. Meteorol. Soc.* : 939–951.

Stensrud D, Manikin G, Rogers E, Mitchell K. 1999. Importance of cold pools to NCEP mesoscale Eta model forecasts. *Wea. Forecasting* **14**: 650–670.

Stensrud DJ, Bao J, Warner TT. 2000. Using Initial Condition and Model Physics Perturbations in Short-Range Ensemble Simulations of Mesoscale Convective Systems. *Mon. Weather Rev.* **128**: 2077–2107.

Stensrud DJ, Fritsch JM. 1994. Mesoscale Convective Systems in Weakly Forced Large-Scale Environments. Part III: Numerical Simulations and Implications for Operational Forecasting. *Mon. Weather Rev.* **122**: 2084–2104.

Stensrud DJ, Wandishin MS. 2000. The correspondence ratio in forecast evaluation. *Wea. Forecasting* **15**: 593–602.

Stratton R, Willet M, Derbyshire S, Wong R. 2012. Convection Scheme: Unified Model Documentation Paper 27. *Met Office, FitzRoy Road, Exeter, EX1 3PB, United Kingdom* .

Swann H. 2001. Evaluation of the mass-flux approach to parameterizing deep convec-

tion. *Q. J. R. Meteorol. Soc.* **127**: 1239–1260.

Talagrand O, Courtier P. 1987. Variational assimilation of meteorological observations with the adjoint vorticity equation. 1. Theory. *Q. J. R. Meteor. Soc.* **113**: 1311–1328.

Tan ZM, Zhang F, Rotunno R, Snyder C. 2004. Mesoscale predictability of moist baro-clinic waves: Experiments with parameterized convection. *J. Atmos. Sci.* **61**: 1794–1804.

Tang Y, Lean H, Bornemann J. 2013. The benefits of the met office variable resolution NWP model for forecasting convection. *Meteorol. Appl.* **20**: 417–426.

Teubler F, Riemer M. 2016. Dynamics of rossby wave packets in a quantative potential vorticity-potential temperature framework. *J. Atmos. Sci.* **73**: 1063–1081.

Thorpe AJ, Emanuel KA. 1985. Frontogenesis in the presence of small stability to slant-wise convection. *J. Atmos. Sci.* **42**: 1809–1824.

Trier SB, Davies AC. 2007. Mesoscale convective vortices observed during BAMEX. Part II: Influences on secondary deep convection. *Mon. Weather Rev.* **135**: 2051–2075.

Velasco I, Fritsch JM. 1987. Mesoscale convective complexes in the Americas. *J. Geophys. Res.* **92**: 9591–9613.

Wandishin MS, Stensrud DJ, Mullen SL, Wicker LJ. 2008. On the predictability of mesoscale convective systems: Two-dimensional simulations. *Wea. Forecasting* **23**: 773–785.

Wandishin MS, Stensrud DJ, Mullen SL, Wicker LJ. 2010. On the Predictability of Mesoscale Convective Systems: Three-Dimensional Simulations. *Mon. Weather Rev.* **138**: 863–885.

Warner TT, Hsu HM. 2000. Nested-model simulation of moist convection: The Impact of coarse-grid parameterized convection on fine=grid resolved convection. *Mon. Weather Rev.* **128**: 2211–2231.

Wilkinson J. 2012. UM Documentation Paper 26: The Large-Scale Precipitation Scheme. *MetOffice, FitzRoy Road, Exeter, Devon, EX1 3PB* .

Wilson D, Morcrette C. 2011. The large scale cloud scheme and saturated specific humid-ity. *Met Office, FitzRoy Road, Exeter, Devon, EX1 3PB* .

Wilson DR, Ballard SP. 1999. A Microphysically based precipitation scheme for the UK Meteorological Office Unified Model. *Q. J. R. Meteorol. Soc.* **125**: 1607–1636.

Young MV. 1995. Severe thunderstorms over south-east England on 24 June 1994: A forecasting perspective. *Weather* **50**: 250–256.

Yu X, Lee TY. 2010. Role of convective parameterization in simulations of a convection

band at grey-zone resolutions. *Tellus A* **62**: 617–632.

Yuter SE, Houze RA. 1998. The natural variability of precipitating clouds over the western Pacific warm pool. *Q. J. R. Meteorol. Soc.* **124**: 53–99.

Zhang D. 1992. The Formation of a Cooling-induced Mesovortex in the Trailing Stratiform Region of a Midlatitude Squall Line. *Mon. Weather Rev.* **120**: 2763–2785.

Zhang DL, Fritsch JM. 1987. Numerical simulation of the mesoβ-scale structure and evolution of the 1977 Johnstown flood. Part II: Inertially stable warm-core vortex and mesoscale convective complex. *J. Atmos. Sci.* **44**: 2593–2612.

Zhang DL, Fritsch JM. 1988. Numerical sensitivity experiments of varying model physics on structure, evolution and dynamics of two mesoscale convective systems. *J. Atmos. Sci.* **45**: 261–293.

Zhang F, Synder C, Rotunno R. 2003. Effects of moist convection on mesoscale predictability. *J. Atmos. Sci* **60**: 1173–1185.

Zhang FC, Bei N, Rotunno R, Snyder C, Epifanio C. 2007. Mesoscale predictability of moist baroclinic waves: Convection-permitting experiments and multistage error growth dynamics. *J. Atmos. Sci.* **64**: 3579–3594.

Zhang FC, Synder C, Rotunno R. 2002. Mesoscale predictability of the "surprise" snowstorm of 24-25 january 2000. *Mon. Weather. Rev.* **130**: 1617–1632.

Zhu H, Thorpe A. 2006. Predictability of extratropical cyclones: The influence of initial condition and model uncertainties. *J. Atmos. Sci.* **63**: 1483–1497.